ON-LINE REFUELING FOR THE ADVANCED HIGH TEMPERATURE REACTOR

A Dissertation
Presented to
The Academic Faculty

By

Pietro Avigni

In Partial Fulfillment
Of the Requirements for the Degree
Doctor of Philosophy in Nuclear and Radiological Engineering

Georgia Institute of Technology

May, 2017

ON-LINE REFUELING FOR THE ADVANCED HIGH TEMPERATURE REACTOR

Approved by:

Dr. Bojan Petrovic, Advisor
Nuclear and Radiological Engineering Program
School of Mechanical Engineering
Georgia Institute of Technology

Dr. Ivan Maldonado
School of Nuclear Engineering
University of Tennessee

Dr. Alexander Alexeev
School of Mechanical Engineering
Georgia Institute of Technology

Dr. Graydon Yoder
Reactor and Nuclear Systems Division
Oak Ridge National Laboratory

Dr. Dingkang Zhang
Nuclear and Radiological Engineering Program
School of Mechanical Engineering
Georgia Institute of Technology

Date Approved: March 10, 2017

ACKNOWLEDGEMENTS

I would like to thank my advisor Dr. Bojan Petrovic for his guidance and support during the entirety of this project. Also, I thank the other committee members, Dr. Alexander Alexeev, Dr. Graydon Yoder, Dr. Ivan Maldonado and Dr. Dingkang Zhang for their time and involvement in the completion of this work.

I would like to acknowledge my colleagues, Timothy Flaspohler, Giovanni Maronati, Michael Huang and Kyle Ramey for their help and support.

Some of the work performed in this project has been funded by US Department of Energy under the Nuclear Energy University Program (NEUP) Project 12-3870, under Prime Contract No. DE-AC07-05ID14517; project title: "Fuel and Core Design Options to Overcome the Heavy Metal Loading Limit and Improve Performance and Safety of Liquid Salt Cooled Reactors".

TABLE OF CONTENTS

Acknowledgements iii

List of Tables viii

List of Figures ix

Symbols and Abbreviations xv

Summary xvi

1. Introduction and background information 1

1.1. Problem description 1

1.1.1. Description of the reactor and technologies 1

1.1.2. Problem statement 5

1.1.3. Proposed solution 6

1.2. Review of previous work: design and modeling approach 10

1.2.1. Refueling procedure for standard AHTR 10

1.2.2. Thermal hydraulic, neutronic and mechanical analysis of the AHTR 11

1.3. Methodology 12

1.3.1. High level description of the problem 12

1.3.2. Specific approaches 13

1.3.3. Computational methods 14

2. Thermal-hydraulic characteristics of assembly replacement operation 16

2.1. Thermal-hydraulic phenomena involved in the refueling process 16

2.1.1. Methodology 16

2.1.2. Methodology: some considerations and issues 19

2.2. Considerations on thermal hydraulics of coolant channel and fuel plate 21

2.2.1. Assumptions and approximations 21

2.2.2. Plate-wise steady state thermal characteristics 25

2.3. Fuel assembly thermal hydraulic characteristics 28
2.3.1. Steady state flow and temperature distributions 31
2.3.2. Flow at outlet of assembly 35
2.3.3. Transient temperature distribution in the assembly 37
2.3.4. Assembly transfer from reactor core to spent fuel pool 41
2.4. Flow in the channel of the removed assembly 42
2.4.1. Modeling approach 42
2.4.2. Assembly extraction simulations 45
2.4.3. Mass flow rate in the channel during assembly extraction 48
2.5. Flow characteristics in the lower plenum 55
2.5.1. Flow distribution in the lower plenum: modeling approach and steady solution 57
2.5.2. Time-dependent flow distribution in the lower plenum 62
2.6. Flow characteristics in the upper plenum 66
2.6.1. Flow distribution in the upper plenum: modeling approach and steady solution 67
2.6.2. Time-dependent flow distribution in the upper plenum 73
3. Neutronics modeling for online refueling 77
3.1. SCALE neutronics model 78
3.1.1. Components of the AHTR SCALE model 78
3.1.2. Input file creation process 84
3.1.3. Preliminary testing for the SCALE core model 88
3.1.4. Parameters for depletion calculations 91
3.2. Methodology for reference core calculations 92
3.2.1. Assembly depletion simulations 93
3.2.2. Assembly criticality calculations 96
3.2.3. Correlation between burnup and equivalent enrichment 98
3.2.4. Estimation of reference core configuration 102

3.3. Reactivity variation during the refueling transient 110
3.3.1. Removal of a spent fuel assembly 111
3.3.2. Insertion of the fresh fuel assembly 115
3.3.3. Core neutronic feedback 117
3.4. Refueling and control strategy 119
3.4.1. System response to uncontrolled reactivity variation due to online refueling 120
3.4.2. Replacing speed and frequency 122
3.5. Fuel cycle and refueling patterns 123
4. Mechanical analysis and refueling procedure options 125
4.1. Mechanical analysis 126
4.1.1. Mechanical stability of the refueling operation 126
4.1.2. Design alternatives for reducing lift force on assembly 130
4.1.3. Force as a function of elevation 135
4.1.4. Hold-down mechanism 137
4.2. Potential refueling strategy 143
5. Cost modeling 146
5.1. Introduction 147
5.2. Models and methodology for the economic analysis 148
5.2.1. Assumptions 148
5.2.2. Price of uranium 149
5.2.3. Simplified fuel cycle cost model 152
5.3. Preliminary evaluations on the economic model 157
5.3.1. Cost of assembly fabrication 159
5.3.2. Parametric studies 161
5.4. Considerations on refueling outages 169
5.4.1. Refueling machines 171

5.5. Considerations on maintenance outages 172
5.6. Potential economic advantages from online refueling 173
6. Integration, future work and conclusions 176
6.1. Integration of various aspects 176
6.2. Future work 178
6.3. Conclusion 180
7. Appendix 181
7.1. MATLAB input: plate-wise axial heat conduction 181
7.2. MATLAB input: 3D assembly flow and temperature distributions 190
7.3. Visual Basic input: assembly channel pressure drop as function of mass flow rate 205
7.4. MATLAB input: creation of SCALE full core model input file 211
7.5. MATLAB input: 2D fission density plotting from SCALE output 236
References 245

LIST OF TABLES

Table 1-1. Scope of the work....7
Table 2-1. Coolant properties....23
Table 2-2. Mesh size function and mesh properties....45
Table 2-3. Gap friction pressure drop [Pa] as function of channel mass flow rate and assembly elevation....49
Table 2-4. Bypass channel mass flow rate [kg/s] as function of channel mass flow rate and assembly elevation....50
Table 2-5. Channel friction pressure drop [Pa] as function of channel mass flow rate and assembly elevation....50
Table 2-6. Power interpolation coefficients as function of elevation....52
Table 2-7. Parameters for interpolation functions of coefficient A and exponent B....53
Table 2-8. Mesh characteristics....57
Table 2-9. Simulation characteristics....59
Table 2-10. Mesh characteristics....68
Table 2-11. Simulation characteristics....70
Table 3-1. Parameters for depletion curve fitting....95
Table 3-2. Parameters for the fitting curve of k versus enrichment....97
Table 3-3. Parameters for the enrichment vs burnup fitting function....100
Table 5-1. Average spot uranium prices since 2006 [35]....149
Table 5-2. First guess parameters for fuel cost model....158
Table 5-3. Online refueling savings for different initial fuel enrichments....159
Table 5-4. Reference parameters for baseline cost calculation....160
Table 5-5. Cost shares for fuel assembly fabrication....160
Table 5-6. Reference parameters for calculation of online refueling cost advantage....173
Table 5-7. Online refueling cost advantage results for 19.75% initial enrichment....174
Table 5-8. Online refueling cost advantage results for 9% initial enrichment....174

LIST OF FIGURES

Figure 1-1. AHTR vessel and core configuration (left) [2]; AHTR fuel assembly configuration (right) 2
Figure 1-2. Reference AHTR core and vessel dimensions 3
Figure 2-1. Temperature difference between the 2D and 1D solution 22
Figure 2-2. Friction factor as a function of the elevation 24
Figure 2-3. Temperature (left) and heat transfer coefficient (right) as function of elevation in the active portion of the coolant channel 26
Figure 2-4. Graphite thermal conductivity as a function of temperature for various irradiations 27
Figure 2-5. Maximum fuel temperature for average assembly as a function of graphite thermal conductivity 27
Figure 2-6. Mesh for the fuel plate 29
Figure 2-7. Typical materials distribution for the fuel plate, showing the graphite meat (blue), the fuel stripes (light blue), the coolant channels (brown), the support (orange) and the box (green) 29
Figure 2-8. Temperature distribution of the average fuel plate 31
Figure 2-9. Horizontal temperature [°C] distribution at axial location of maximum fuel temperature 33
Figure 2-10. 3D temperature [°C] distribution for one third of the active part of the fuel assembly 34
Figure 2-11. Mesh details for the 2D CFD simulation of the flow at the outlet of the assembly channels 36
Figure 2-12. 2D vorticity contours for six time steps, 0.2 seconds spaced 37
Figure 2-13. Temperature [°C] distribution at the end of the control rod insertion and 30 min after the control rod insertion and assembly extraction into upper plenum 39
Figure 2-14. Time evolution of maximum (orange) and minimum (blue) temperatures for axial average assembly power density after the assembly extraction into upper plenum 40
Figure 2-15. Time evolution of maximum (orange) and minimum (blue) temperatures for assembly (axial average assembly power density) in argon atmosphere (after 1 min in salt) 42

Figure 2-16. Fluid volume details and mesh [the solid geometry represents the fluid volume between the lower support plate and the lower face of the assembly].....44
Figure 2-17. CAD model configuration for various time steps. As the time increases, the height changes to simulate the extraction 46
Figure 2-18. Pathlines colored by velocity magnitude [m/s] 47
Figure 2-19. Power interpolation coefficient A as function of elevation of the extracted assembly 53
Figure 2-20. Power interpolation exponent B as function of elevation of the extracted assembly 53
Figure 2-21. Friction pressure drop in the free channel as function of mass flow rate.....54
Figure 2-22. Channel mass flow rate as function of assembly elevation.....55
Figure 2-23. Lower plenum CAD models: reduced (37 assemblies) and full version (253 assemblies).....56
Figure 2-24. Mesh for small version (top) and full version (bottom) of the lower plenum model59
Figure 2-25. Lower plenum velocity streamlines colored by velocity magnitude (front view) 61
Figure 2-26. Lower plenum velocity streamline colored by velocity magnitude (back and bottom view).....61
Figure 2-27. Assembly extraction velocity and elevation as function of time 63
Figure 2-28. Mass flow rate for the channel of the extracted assemblies and for the rest of the channels in the core.....64
Figure 2-29. Horizontal velocity magnitude contours at different elevations before and after the assembly extraction.....65
Figure 2-30. Upper plenum CAD models: reduced (19 assemblies, left) and full version (253 assemblies, right) 66
Figure 2-31. Mesh and mesh partitioning (lower-right frame) for the upper plenum model.....69
Figure 2-32. Pathlines colored by velocity magnitude (left) and contours of velocity magnitude (right) [m/s].....72
Figure 2-33. Pathlines colored by temperature (left) and contours of temperature (right) [K].....72
Figure 2-34. Core outlet radial temperature profile 73
Figure 2-35. Upper plenum velocity magnitude (left) and temperature (right).....76
Figure 3-1. Distribution of fuel kernels in the fuel stripe matrix, as modeled in SCALE 79

Figure 3-2. Detail of horizontal cross section of two fuel plates, as modeled in the SCALE model 80
Figure 3-3. SCALE model of the fuel assembly (horizontal cross section) 81
Figure 3-4. Horizontal (left) and vertical (right) cross section of the SCALE core model. Each ring is modeled using a different unit.....82
Figure 3-5. 3D view of the SCALE core model; assemblies are grouped in three radial rings and one assembly is partially extracted 83
Figure 3-6. Sample core fission density (arbitrary units) plot representing the power distribution for a 10 rings model. 87
Figure 3-7. Uncertainty as a function of number of generations 89
Figure 3-8. Uncertainty as a function of number of particles per generation.....90
Figure 3-9. Simulation time as a function of number of units.....90
Figure 3-10. Depletion curve for 9% initial enrichment 93
Figure 3-11. Depletion curve for 19.75% initial enrichment 94
Figure 3-12. Interpolated depletion curves for 9% (left) and 19.75% (right) enrichment 96
Figure 3-13. k versus enrichment data and fitted values.....97
Figure 3-14. Equivalent enrichment versus burnup data and fitting curve for 9% (left) and 19.75% (right) enrichment 99
Figure 3-15. Two-ring full core model configuration.....100
Figure 3-16. Fission density vs radial ring for the depleted and equivalent cores 101
Figure 3-17. Guessed normalized radial burnup profile, 1.3 peaking factor.....104
Figure 3-18. Reactivity vs average burnup for specific normalized profile.....105
Figure 3-19. Normalized radial fission density profile for various average burnup values in GWd/ tHM 106
Figure 3-20. Critical fission power density profile; average burnup equal to 59 GWd/ tHM 106
Figure 3-21. Burnup profile calculated from multivariate regression 108
Figure 3-22. Fission density profile derived from regression burnup profile 109
Figure 3-23. 10-rings full core model and locations of element replacement (2^{nd}, 6^{th} and 10^{th} ring in left, center and fight frame, respectively).....110
Figure 3-24. Reactivity variation for control rod insertion and assembly extraction at internal core location for spent fuel.....112

Figure 3-25. Reactivity variation for control rod insertion and assembly extraction at intermediate core location for spent fuel 112
Figure 3-26. Ratio of fission density of assembly portion with control rod over average fission density of assembly without control rod (left) and ratio of assembly power as function of elevation over static assembly power (right) 114
Figure 3-27. Reactivity variation for control rod insertion and assembly extraction at internal core location for fresh fuel 116
Figure 3-28. Reactivity variation for control rod insertion and assembly extraction at intermediate core location for fresh fuel 117
Figure 3-29. Reactivity variation for control rod insertion and assembly extraction at external core location for fresh fuel 117
Figure 3-30. Multiplication coefficient k as function of fuel temperature for various coolant temperatures (900K in blue, 1000K in orange, 1100K in gray) 118
Figure 3-31. Reactivity evolution during the on-line refueling operation at intermediate core location (6^{th} ring), assuming inactive control system and no thermal feedback.....119
Figure 3-32. Uncontrolled (without feedback) and total (with feedback) reactivity as a function of time.....121
Figure 3-33. Reactor power variation due to uncontrolled online refueling operation.....121
Figure 3-34. Replacing cycle (days) as a function of enrichment and packing fraction for the 253 batches cycle (on-line refueling).....122
Figure 4-1. Shear stress as a function of the elevation in the core.....129
Figure 4-2. Options for increasing control rod dimensions.....131
Figure 4-3. Downward force as a function of the fuel plate thickness. 132
Figure 4-4. Flow rate reduction (left) and core temperature rise (right) as function of coolant channel width, for reference assembly configuration 134
Figure 4-5. Flow rate reduction (left) and core temperature rise (right) as function of coolant channel width, for reference assembly plus 200 kg weight.....135
Figure 4-6. Internal, bypass and total mass flow rates in the channel as a function of extraction elevation 136
Figure 4-7. Total force and its components acting on the assembly as a function of extraction elevation 137

Figure 4-8. Fuel assembly grappling collar, upper core support plate and control rod drive mechanism details [2].....138
Figure 4-9. Fuel assembly locking mechanism; extraction sequence.....141
Figure 4-10. Fuel assembly extraction procedure.....145
Figure 5-1. UF6 and SWU spot prices since 2006 [reference UxC].....149
Figure 5-2. Uranium spot and long term prices in the last 5 years [36].....150
Figure 5-3. Fuel cost for 2-batch and online refueling as function of UF6 price (left) and SWU price (right).....151
Figure 5-4. Burnup ratio (left axis) and loss with respect to infinite batches (right axis) as function of number of batches.....155
Figure 5-5. Fuel cost as a function of number of batches for 19.75% (left frame) and 9% (right frame). The cost for online refueling is represented by the asymptotic yellow line.....158
Figure 5-6. Fuel cost as function of fabrication cost for online and 2-batches fuel cycle for 19.75% initial enrichment.....162
Figure 5-7. Fuel cost reduction from 2-batches to online refueling as a function of fabrication cost.....163
Figure 5-8. Fuel cost shares (fabrication and other costs) for online and 2-batches cycle as a function of the fabrication cost.....163
Figure 5-9. Fuel cost (left) and cost shares (right) for different number of batches as a function of the refueling outage cost.....164
Figure 5-10. Optimal number of batches as a function of refueling outage cost for high cost (up to $90 million, left) and low cost (up to $100,000, right).....166
Figure 5-11. Optimal fuel cost as a function of refueling outage cost, minimized with respect to the number of batches.....167
Figure 5-12. Total number of assemblies needed over the reactor lifetime (60 years) as a function of the number of batches.....168
Figure 5-13. Loss due to shutdown or reduced power time as a function of the outage power level.....170
Figure 5-14. Loss due to shutdown or reduced power time as a function of the outage duration.....171
Figure 5-15. Loss due to maintenance outage as a function of the outage duration and cost.....172

Figure 6-1. Integration of modeling aspects.....176

SYMBOLS AND ABBREVIATIONS

AHTR	Advanced High Temperature Reactor
CAD	Computer-Aided Design
CFD	Computational Fluid Dynamics
DOE	U.S. Department of Energy
DRACS	Direct Reactor Auxiliary Cooling System
FHR	Fluoride-salt-cooled High-temperature Reactor
FLiBe	Lithium Fluoride and Beryllium Fluoride molten salt
HTC	Heat Transfer Coefficient
LRM	Linear Reactivity Model
LWR	Light Water Reactor
MDM	Moving and Deforming Mesh
MHC	Molybdenum Hafnium Carbide
MSR	Molten Salt Reactor
NEUP	Nuclear Energy University Program
ORNL	Oak Ridge National Laboratory
RANS	Reynolds-Averaged Navier-Stokes
SAS	Scale-Adaptive Simulation
SWU	Separative Work Unit
TRISO	Tristructural-Isotopic particle
UCO	Uranium Oxycarbide
UDF	User-Defined Function
URANS	Unsteady Reynolds-Averaged Navier-Stokes
wrt	With respect to

SUMMARY

This work aims to resolve the low heavy metal loading and fuel utilization issues of the Advanced High Temperature Reactor (AHTR) by means of a novel technique based on an online refueling approach.

The thesis starts with a general introduction of the AHTR technology and its characteristics, followed by a description of the general design limitations derived from the use of a very specific combination of fuel and moderator materials. The introduction illustrates the proposed solution consisting of the online refueling approach, as well as the methodology that has been developed and used to study it. Due to the novelty of the solution proposed in this work, a new methodology has been defined and developed and its features are presented here. The second chapter describes the thermal hydraulic modeling and simulation work that has been performed for the characterization of the steady state and transient behavior of the core during the online refueling. The third chapter analyzes the neutronic modeling that simulates the reactivity variations of the core during the transient, and provides some general information on the fuel cycle and the neutronic characteristics of the core. The fourth chapter discusses new solutions that aim to make the online refueling approach viable, related to the mechanical aspects, operational procedures and design modifications. The fifth chapter provides an overview of the economic modeling and a preliminary evaluation of the economic benefits produced by the implementation of online refueling. The novel refueling approach improves fuel economy and reduces fuel cycle cost, and thus constitutes an enabling technology toward commercialization of AHTRs; the conclusion of the work provides a summary of the various aspects integrated into a global view with a perspective on the future work that is originated by this study.

1. INTRODUCTION AND BACKGROUND INFORMATION

The Advanced High Temperature Reactor (AHTR) is a Fluoride-cooled High-temperature Reactor (FHR) moderated by graphite and carbonaceous materials and fueled by TRISO particles embedded in fuel plates ("fuel planks"). The combination of these technologies results in a very reliable and safe source of high temperature energy usable for electricity or process heat production. One of the design aspects that potentially offers opportunities for a significant improvement is the relatively inefficient use of nuclear fuel due to low heavy metal loading in the core and necessity for larger moderation volumes; this work aims to resolve this aspect by the implementation of an online refueling technique.

The online refueling offers several potential advantages over the conventional multibatch refueling, such as a potential increase of the fuel discharge burnup and overall fuel cost reduction, but it also brings several challenges, such as more complicated operational procedures and safety aspects. This work provides an overview of the most significant aspects, and shows how this relatively unexplored, novel multi-physics approach could be deployed to improve the FHR reactor technology.

1.1. Problem description

This work is based on the Advanced High Temperature Reactor design and its reference TRISO fuel configuration. This combination of technologies, namely TRISO fuel, high temperature salt as coolant and graphite as moderator, requires methods for fuel utilization improvement, that can be obtained either through fuel design optimization, or techniques to better utilize the current fuel design, such as online refueling. This section provides a brief description of the main features of this reactor technology, in order to provide the basis for the analysis of the online refueling.

1.1.1. Description of the reactor and technologies

The Advanced High Temperature Reactor (AHTR) being considered in this study is a Fluoride-Salt-cooled High-temperature Reactor (FHR) developed by ORNL. This reactor design is based

on a hexagonal prismatic fuel elements 6.0 meters tall. It is moderated by graphite and the fuel form is a dispersion of TRISO particles into a graphite matrix [1]; the active portion of the assembly is 5.5 m, and 25 cm of the reflector material is added at the top and bottom of each plate. The core is made of 252 assemblies (the central, 253rd assembly will most probably be used for instrumentation purposes) and each hexagonal assembly contains 18 vertical fuel plates. Each fuel plate has a central graphite support layer and two lateral fuel stripes that are close to the coolant channel, in order to facilitate the heat removal process. The reference fuel enrichment for the initial design was 19.75%, but designs with lower enrichments have been evaluated [2], particularly the 9% option. The thickness of the fuel stripes is also subject to optimization, and the reference value is 0.62 cm each. Figure 1-1 shows a view of the vessel and the core on the left, and the horizontal cross section of a single assembly on the right side. Further details and dimensions are provided below (Figure 1-2) and in Section 3.1.

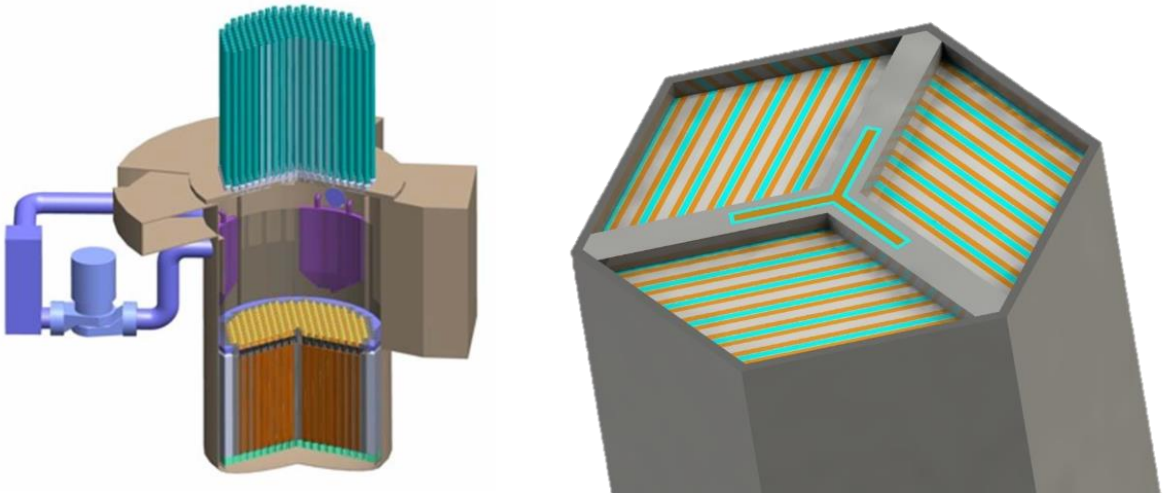

Figure 1-1. AHTR vessel and core configuration (left) [2]; AHTR fuel assembly configuration (right)

1.1.1.1. Nuclear power plant design and technologies

The design of the reactor considered in this work is a 3400 MWth core immersed in FLiBe; the inlet and outlet temperatures are 650°C and 700°C respectively and the nominal coolant flow is on the order of 28000 kg/s, or about 14 m^3/s.

From a neutronics perspective, the salt is a slightly moderating substance with low absorption cross section. From a thermal standpoint, the salt has the following properties:

- The density is about 1950 kg/m3 at the reference temperatures, about twice the density of water at room temperature. Its variation with respect to temperature is on the order of -0.5 kg/m^3/K, which makes it very interesting from the passive safety point of view.
- The thermal conductivity is about 1.1 W/m/K.
- The specific heat is about 2415 J/kg/K, about half the specific heat of water at room temperature; note that since the salt mass density is twice that of water, the resulting volumetric heat capacity for salt is similar to that of water.
- The dynamic viscosity is about 0.006 Pa*s (substantially larger than water) and it decreases with increasing temperature.
- The Reynolds number of the flow through the assemblies is about 10000, whereas typical Re numbers for LWRs are on the order of 50000. The flow is turbulent but not far from the transition region.

The use of FLiBe as the coolant and graphite as the moderator is a relatively well explored design approach and the core technologies are derived from the Molten Salt Reactor (MSR) technology experience [3].

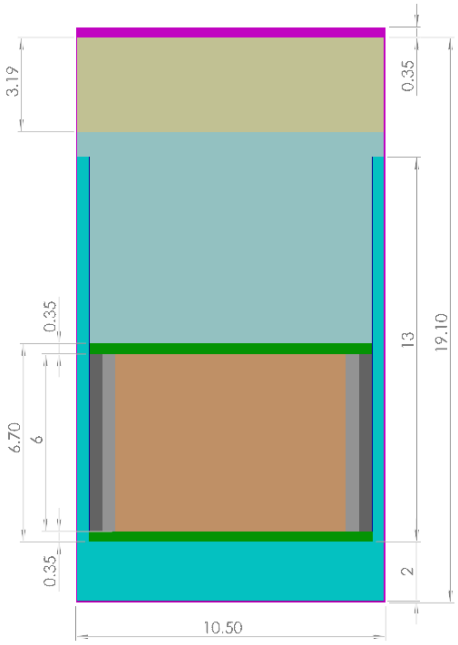

Figure 1-2. Reference AHTR core and vessel dimensions

1.1.1.2. Core and fuel features

The core of the AHTR is composed of 253 hexagonal blocks, surrounded by a ring of replaceable reflector assemblies and another ring representing the permanent reflector, which protects the barrel and the vessel from irradiation. The fuel assemblies measure 45 cm face-to-face and are supported by an internal carbon-carbon composite structure and an external hexagonal box, holding the 18 fuel plates together (Figure 1-1, right frame). The flow channels, 21 per assembly, are 7 mm wide, except for the 6 of them, the first and the last one in each third of the assembly, which are only 3.5 mm thick because they cool down only half of the fuel plate; this parameter has been minimized in order to maximize the volume available for moderation without compromising the cooling capability. The control rod is Y-shaped and inserted into a Y-shaped slot in the center of the support structure; each assembly has its own control rod in the reference design.

Each of the 18 fuel plates is about 2.55 cm thick and it contains two fuel stripes, one on each side of the plate. The reference thickness for the fuel stripe is 0.62 mm, but this parameter strongly depends on the fuel design optimization results, and on the manufacturing process, which has not yet been explored on a large scale. The remaining parts of the fuel plate are the central graphite support structure and the 1 mm thick cladding; the thickness of the support is complementary to the fuel stripe thickness with respect to the fixed total fuel plate thickness of 2.55 cm.

The fuel stripe contains TRISO fuel particles, substantially identical to the particles developed as part of the Advanced Gas Reactor (AGR) program. The uranium oxycarbide kernel (428 μm diameter) is surrounded by 3 protective layers that provide mechanical support for the integrity of the particle and retain fission gasses; the overall diameter of one particle is estimated to be around 847 μm. The particles are randomly distributed in the fuel stipe, but usually modeled as regularly distributed within a cubic lattice for computational purposes; the consequences of this approximation have been analyzed in other works. Further details on the modeling of this type of fuel are given in the neutronic section.

1.1.1.3. FHR reactors: common features

The Liquid Salt Reactor technology has been going through a strong development in the last decade, it appears to be a very promising technology for the future of nuclear power generation.

Several designs have been developed, including a small modular version [4], a pebble bed version [5] and prismatic assembly based versions, such as the AHTR. Even though they are different designs with different capabilities, they all deploy the same base technology, which is the use of FLiBe as coolant and TRISO particles as fuel; as a consequence, they all share the same basic issues, including the low heavy metal loading of the core.

The pebble bed version of the FHR family is going to be built and tested in China in the next few years [6] and it is going to be the first step toward the full development of the FLiBe technology in the nuclear field. This design addresses the issue of low heavy metal loading using an approach that is very similar, from a conceptual standpoint, to the online refueling approach presented in this work. In fact, the pebble bed design allows the continuous replacement of pebbles in the core, similarly to what would happen in an online refueling approach, without having, however, a full control on the location of the newly inserted fuel. Of course, in this case, the portion of the core that is replaced is much smaller and it can be performed much more quickly than the case of the AHTR, but still some basic concepts and issues are shared between the two designs.

1.1.2. Problem statement

The AHTR reference core design is based on a traditional batch refueling approach, which requires to shut down the reactor and replace/reshuffle a certain amount of fuel assemblies in the core at a specific frequency. Several options have been evaluated in the design process, in order to maximize the lifetime of a single batch and optimize the use of fuel. However, the relatively short cycle and poor fuel utilization are intrinsic features of this family of reactors with the traditional refueling approach, due to the low heavy metal loading in the core and insufficient moderation. The low heavy metal loading is mainly due to the use of TRISO fuel, leading to a low density of fissile material in the core. The insufficient moderation derives from the use of graphite as a moderator: carbon is a very good moderator but requires a large volume in order to completely thermalize the neutrons; in contrast with this, the dimension of the core is limited by economic aspects. It must be noted that the heavy metal loading and the moderation are competing aspects: an increase of the heavy metal loaded into the core would reduce the amount of volume available for moderation, and vice versa.

Since the fuel is expected to be more expensive than the fuel of light water reactors, poor fuel utilization may challenge the economic viability of the AHTR.

1.1.3. Proposed solution

The overarching objective of this work is the development of a novel approach to refueling that will eliminate or at least ameliorate the problem presented in the previous section.
The approach that has been analyzed in this work is the continuous on-power refueling, or online refueling. The refueling procedure is performed at full power or at almost full power (the reactor is not shut down) and a single assembly is removed and replaced in each refueling operation. Refueling of a small group of symmetrically located assemblies at a time (in brief succession) has also been considered.
The online refueling can represent a concrete solution to the problem and provide substantial improvements with respect to the following aspects:

- Elimination of cycle length issues. There is no need to shut down the reactor every few months to refuel, since the refueling is continuous and on-power. This reduces the number of outages during the reactor lifetime and the outage costs (only maintenance outages would be needed).
- Improved moderation with limited repercussion on the outage cost. It is possible to reduce the amount of heavy metal loading and thus optimize the moderation provided by graphite. This results in improved fuel utilization.
- Continuous refueling provides intrinsic improvement of the fuel utilization, allowing toachieve higher discharge burnup, i.e., better fuel utilization.
- Several factors result in a reduction of the fuel cycle cost.
- Salt-cooled reactors require the refueling to be performed at high temperature, in order to maintain the salt liquid. Performing the refueling on-power (at least partial) can represent an advantage from this standpoint.

The online refueling presents several challenges, on the thermal, neutronic and mechanical level; these challenges will be presented in the following sections and analyzed in this work. Despite these challenges, the online refueling represents a potentially appropriate solution to the AHTR fuel utilization issues.

1.1.3.1. Global objectives and scope of the work

The overall objectives and scope of the work (Table 1-1) are:

- Evaluate and confirm the stability of the core during the on-power refueling operations. The core of the AHTR has negative reactivity feedback so it is expected to adapt well to the change in power and temperature during the transient.
- Show that the system is capable of maintaining the thermal margin of the fuel plate temperature and ensuring the coolability of the core and the assembly.
- Verify the flow stability and the mechanical feasibility of the transient.
- Analyze the economic advantages/disadvantages resulting from the implementation of the on-line refueling.

This analysis requires establishing new specific models and a methodology; this innovative approach has been developed in this work.

Table 1-1. Scope of the work

Neutronics	• Develop full core model (CR insertion, depleted assembly extraction and a fresh assembly insertion) • Evaluate reactivity evolution wrt time and position of assembly • Evaluate power distribution in core and assembly wrt time • Evaluate reactivity feedback • Control rod maneuvering
Thermal-hydraulics	• Steady 2D and 3D flow velocity and temperature distribution for the assembly and the plenums • Analysis of TH models and best approaches for full core simulation • Evaluation of potential simplifications for TH models • Develop full core model for transient simulation
Mechanical	• Analysis of issues deriving from moving a large assembly in an active core • Assessment of required mechanisms for maneuvering the assembly • Evaluate potential design alternatives
Economics	• Develop model for evaluation of economic viability • Quantify fuel cycle cost advantages

The online refueling presents several challenges with respect to the neutronics, the thermal-hydraulics, the mechanical aspects, the actual refueling procedure and the economic viability.
With respect to the neutronics, the following aspects have been studied in this work:

- Development of a full core model for the AHTR for the evaluation of the reactivity response with respect to the control rod insertion, used fuel assembly extraction, and fresh fuel assembly insertion.
- Reactivity evolution with respect to the vertical position of the assembly being extracted from or inserted into the core.
- Power distribution in the core and in the removed assembly as a function of time.
- Reactivity feedback of the core in the fuel assembly removal/insertion transient scenario.
- Control rod maneuvering for the control of the power during the on-power (full power) or almost on-power transient.

With respect to the thermal-hydraulic aspects, the following objectives have been analyzed:

- Analysis of the steady state 2D and 3D temperature and velocity distribution of the AHTR fuel assembly; flow distribution in the lower and upper plenum.
- Analysis of the thermal hydraulic models for the modeling of the flow in the assembly and the core. This aspect is developed starting from simple 2D channel cases all the way up to the core level.
- Evaluation of potential simplifications of hydraulic models for simulation of the entire system.
- Development of a full-core model or pseudo-full core model for the simulation of the fuel assembly removal transient.

This work also provides a general overview of the following mechanical and technical aspects:

- Analysis of the issues deriving from the moving of a 6.0 m tall fuel assembly in the core.
- Initial and general assessment of the mechanisms required for the maneuvering of the assembly.
- Evaluation of potential design alternatives for the improvement of the refueling procedure.

The economic section of this work has been devoted to the study of the following:

- Characterization of methodology for studying economics for online refueling.
- Evaluation of the fuel cycle cost advantages for the online refueling.

These several aspects have been partially integrated to provide a more complete view of the problem.

This work aims to provide an overall view of the problem, and the modeling issues of specific aspects of the problem are secondary objectives. Some of these aspects are relatively unexplored and this work will try to address them.

The general significance of this work involves the following outcomes:

- It will provide deeper insight into the refueling procedure of the AHTR, which allows a better utilization of nuclear fuel. This approach, even though it is relatively unexplored, represents an interesting option for improving the attractiveness of this type of nuclear plants.
- It will develop a method for the quantification of the advantages in the practical and economic viability of the on-line refueling.
- It will develop and describe the analysis and simulation process for this type of transient, which is challenging because of its multi-physics nature, i.e., the overall coupling of different aspects and the necessity of making specific assumptions and approximations.
- It will integrate different aspects from neutronics, thermal-hydraulics and mechanics into globally-coupled view of the problem.

This work aims to provide a comprehensive analysis of this problem. The ultimate significance of this work is in contributing to achieving a better utilization of nuclear fuel and making FHRs more economically viable.

This work is performed using funding received from the DOE Office of Nuclear Energy's Nuclear Energy University Programs (NEUP) and the objective of the project is the development of fuel and core design options to overcome the heavy metal loading limit and improve performance and safety of Liquid Salt Cooled Reactors [7]. Particularly, this work addresses the examination of an unconventional refueling strategy that improves fuel utilization and the related concepts/issues to facilitate such refueling.

This project supports the ORNL and DOE efforts in the development of the FHR reactor concept [8].

1.2. Review of previous work: design and modeling approach

The AHTR technology has been developed over the last decade and basic/limited analyses have been performed on the thermal-hydraulic properties of the assembly and the core, on the refueling approach and on the neutronic improvements provided by different refueling schemes.

1.2.1. Refueling procedure for standard AHTR

The reference AHTR design is based on a standard multibatch fuel cycle and several options for the number of batches to be used have been investigated.
The refueling approach for this type of fuel cycle has been designed and illustrated in previous AHTR design reports [2]. These reports explain the procedure that needs to be followed during a refueling operation and provide a mechanical and technical description of the components and parts that need to be developed in order to perform the refueling operation.
The refueling procedure in the current design is performed every 6 months and requires the reactor to shut down and the primary pump to reduce to 5% speed in order to prevent the assemblies from floating. The operation in the current design replaces 50% of the assemblies in a two-batch approach and the outage is expected to last 2 or 3 days.
The control rods are dropped into the assemblies that will be removed before starting the operation, and the guide tubes are extracted from the vessel; subsequently, the flange is shifted and the automatic robot is positioned above the core. Then the upper support plate is lifted and the spent assemblies are replaced with the fresh ones; once half of the assemblies is replaced, the operations are repeated in the reversed order and the reactor is restarted. The spent assemblies are transferred to a spent fuel pool through a transfer weir from the refueling lobe.
Several details are given in the reported documentation about the mechanisms that make this operation viable in a safe manner. Most of this work is compatible with the deployment of online refueling except for some adaptions required for easing the maneuvering of the assemblies in the upper plenum while the reactor is functioning.
As part of the previous work on the fuel cycle of the AHTR [1], neutronic analyses of the refueling schemes have been performed in order to investigate the base refueling approach, as well as the potential applicability of short interval batch refueling and viable refueling patterns. Baseline

studies have been performed for two-batches fuel cycles using different refueling patterns, namely circular patterns, shaped as pseudo-rings, or radial patterns, where equally burned assemblies are placed along different radii and different burnups alternate in the azimuthal direction. Further studies have been conducted for a higher number of batches, closer to the behavior of an online refueling approach behavior; these studies assume isotropic refueling pattern, with a specific degree of symmetry depending on the number of batches, because this pattern would minimize peaking factors across the core.

1.2.2. Thermal hydraulic, neutronic and mechanical analysis of the AHTR

The 1D analysis of the coolant channels in the fuel assembly has been performed in several analyses [1] in order to provide a basic understanding of the general properties of the AHTR core. Further analysis has been performed on the fuel assembly CFD modeling [9] and on the system modeling of the AHTR [10]. These studies provide a general overview of the AHTR behavior in operating conditions.

The refueling procedure has been analyzed in detail in the previous work [2]. This analysis provides an extensive description of the mechanical design of the core and the fuel assembly, and illustrates the procedure for refueling and the tools and mechanisms that are involved in the assembly replacement. Most of these aspects are fully compatible with the on-line refueling procedure and provide a good starting point for the mechanical analysis that needs to be performed for the on-line refueling.

On the neutronics side, some analysis of the refueling aspects has been performed in the previous work at ORNL [1]. This analysis examined the short interval batch refueling approach and provided a preliminary insight of the pseudo-online refueling, describing some possible refueling patterns.

Preliminary studies and initial setup for this work have been performed in the past year.

On the thermal-hydraulics side, the 3D analysis of the AHTR fuel assembly has been completed, as well as a preliminary assessment of the 2D on-line refueling transient. Part of this work also involved the understanding of the flow distribution in the channels, at the inlet and outlet of the assembly and in the plenums. This constitutes the basis for an appropriate modeling of the flow behavior and cooling capability of the AHTR during the transient.

On the neutronics side, an initial core model has been developed and tested. This model has been used for purposes relatively different from the study of online refueling, so it has been partially readapted and made suitable for the study of the online refueling neutronic characteristics.
On the mechanical side, the lift force on the fuel assembly has been evaluated. Further analysis has been performed in order to assess the mechanical stability of the assembly during the transient.
On the computational side, some time has been devoted to the understanding and improvement of the computational capabilities involving parallel meshing and simulations with Fluent.

1.3. Methodology

The investigation of the on-power refueling includes the following tasks:

1. Evaluation of the neutronics behavior during the control rod insertion, assembly extraction and fresh assembly insertion. The neutronic evaluations assume the steady thermal-hydraulic properties of the core are known.
2. Modeling of the flow in the AHTR core. The modeling involves the lower and upper plenum, the channels of the fuel assemblies and the overall core behavior. The thermal features of the system are added to the evaluations.
3. Integration of the thermal-hydraulics model with the core feedback and with the neutronic evaluations to simulate the system, starting from steady simulations and completing with a dynamic overview of the transient.

Beyond the basic modeling of physics involved in the online refueling, other technical aspects have been addressed that make the proposed approach more viable.

1.3.1. High level description of the problem

The assembly removal procedure is defined by many different aspects that will be analyzed at different levels. Some of these aspects are new and require the development of new approaches.
This procedure presents high-level issues from the neutronics standpoint; the reactivity presents relevant variations during the insertion of the control rod, the extraction of the burned element and the insertion of the fresh one. Also, the overall behavior of the core is a function of the temperature variation caused by the power change. These issues lead to the question of how to control the

reactivity during the refueling transient: we can let the reactor stabilize, thanks to the negative reactivity coefficient, or we can decide to keep the power constant by moving other control rods. The neutronic analysis aims to provide an answer to these issues. On the thermal-hydraulic side, the flow change will also strongly impact the core performance on a local and global level, plus it has impact on the neutronics through the temperature feedback. The thermal hydraulic modeling of the AHTR has to provide answers about the correct physical models to adopt in the simulations and at the same time its computational demand has to be minimized. The mechanical aspects are fundamental in order to make this solution possible, starting from the lift force due to the low density of graphite and ending with the issues about the hold down mechanism. These problematics will be analyzed first separately and then integrated as much as possible.

1.3.2. Specific approaches

The online refueling is a multiphysics problem involving neutronics, thermal hydraulics and mechanical aspects with a relation to economics. The interaction and resulting coupling of these components is more or less strong based on the particular aspect of the problem that is being analyzed. In general, it has been attempted in this work to decouple the phenomena as much as possible by making reasonable assumptions on the quantities that should be provided from coupled simulations; for this reason, the work is structured in separate sections for neutronics, thermal hydraulics, mechanical and technical aspects and economics. The links between different parts of the work are however highlighted in the specific parts of the work where they have been used.

The neutronic studies performed in this work are mainly focused on the creation of a basic full core model for Monte Carlo simulations and on the characterization of the behavior of the core reactivity during the refueling operations. These studies provide the basis for a better understanding of the online refueling behavior for more accurate or versatile modeling approaches that will be developed in the future, such as 2-step nodal models for the evaluation of refueling patterns and full core depletion. The neutronic studies performed in this work are integrated in a RELAP5 point kinetics model, accounting for thermal feedback, in order to evaluate the response of the system and assess potential reactivity control approaches for the online refueling.

The thermal hydraulic modeling is aimed at the characterization to the response of the flow following the removal of an assembly at full pump speed. The study of this problem has been

performed integrating basic monodimensional flow models with a more accurate CFD modeling of the plena and the channel of the removed assembly; the results produced by this analysis provide basic information on the flow variation through the core and the forces that are generated on the assemblies. This part of the work is relatively challenging in terms of computational resources required to characterize some flow details; this preliminary work is capable of providing this basic information, and it will be of interest for other modeling applications for the study of flow in the plena of the AHTR.

The core flow and neutronic behavior have an impact on the mechanical aspects and the technical procedure for the execution of the online refueling. The flow determines the force acting on the assembly while this is extracted from the core, so a series of basic calculations have been performed for the evaluation of the lifting effects; this study provides a preliminary assessment of the options for design modifications that allow the refueling operation to be performed safely without compromising the integrity of the reactor and its operation. Once the fuel assembly removal procedure has been defined, the various aspects have been partially integrated to provide a global picture of the transient.

A series of economic evaluations demonstrate the economic advantage coming from the implementation of the online refueling approach; these calculations are based on the linear reactivity model, while more accurate depletion models are being developed.

1.3.3. Computational methods

This work is based on computational simulation of the physics of the problem; it uses different simulation packages for the evaluation of the neutronic and thermal-hydraulic aspects.

From the neutronics standpoint, the KENO-VI Monte Carlo code integrated within SCALE6.1 is used; the code performs a multigroup evaluation and the double heterogeneity issue is addressed through the MCDancoff approach [11].

On the thermal-hydraulic side, for the CFD evaluations, the Fluent CFD code embedded in the ANSYS simulation package is used; the meshing is provided by the native Fluent solver or performed through the ANSYS Meshing software. System evaluations are performed by the RELAP5-3D code while simpler thermal-hydraulic calculations use a code written in MATLAB.

Thermal evaluations are also partly performed by the ANSYS Mechanical software provided in the ANSYS simulation package.

The 3D modeling uses Solidworks and the evaluation and presentation of the results is partly performed with Techplot.

The use of C is required for the coding of the Fluent User Defined Functions and the Scheme language serves for the Fluent Text User Interface and the batch execution from journal files.

2. THERMAL-HYDRAULIC CHARACTERISTICS OF ASSEMBLY REPLACEMENT OPERATION

2.1. Thermal-hydraulic phenomena involved in the refueling process

The online refueling consists of the removal of a fuel assembly from the core while the pumps are operating at a specified speed, which can be the nominal value (for full power) or an optimal reduced value with respect to nominal; as a consequence of this operation, after the assembly is lifted from the core to the upper plenum, the channel previously occupied by that fuel assembly is left empty, resulting in a substantial flow rate increase that affects the local as well as the global behavior of the core thermal hydraulics.

The nominal flow rate through the assembly channel in normal operating conditions is about 100 kg/s, and the estimated flow rate at the end of the transient (assembly completely extracted from its slot) is expected to be several hundred kg/s [12], resulting in a slight reduction of flow rate through the remaining assembly channels. This flow variation results in the variation of the temperature distribution in the core: this temperature distribution change is predicted to be small, a few degrees °C in the average core outlet temperature, but its effect on the power distribution through neutronic feedback mechanisms may not be negligible.

This section of the work addresses the impact of the flow change on the core thermal hydraulic performance and temperature distribution, which will be subsequently linked to the neutronics models to study the power evolution of the core during the transient. In order to obtain a good evaluation of these effects in transient conditions, a good understanding of the behavior of the flow in the core is needed.

2.1.1. Methodology

The study of the thermal hydraulic behavior of the AHTR core for the online refueling operation represents a somewhat unconventional problem. Therefore, a specific analysis methodology has been developed. As part of this methodology, several computational tools have been used in support of the thermal hydraulic evaluations, including both system codes (RELAP [13] and

TRACE [14]) and computational fluid dynamics (CFD) codes (Fluent [15]). The system codes have been generally used for the modeling of the entire system in its complexity, while CFD has been applied to the simulation of flow distribution of specific parts of the system.

The process of characterization begins with the comprehension of the basic flow properties and features of the coolant in steady state conditions at different levels (channel, assembly, plenums, core) and terminates with the characterization of the time dependent temperature and flow distribution in the channel of the removed assembly.

This work cannot be performed by using system codes only. In fact, system codes allow a simple representation of the hydraulic systems and are very effective when the system is at the same time complex but based on components that can be described by relatively simple correlations or components that show a simple flow configuration.

System codes cannot easily simulate systems with moving parts, such as the assembly that is lifted in its channel, and for this reason they require input from CFD or experimental evaluations for a correct representation of this aspect. Another issue that is not negligible when using system codes is their limited capability of simulation of 3D flows. The systems evaluations presented in this work are therefore integrated and supplemented by information provided through CFD analysis (Fluent).

The fluid dynamics and CFD analysis has been developed starting from the characterization of the flow features of various zones of the AHTR assembly and core in steady conditions. In reference to the single channel steady state analysis, the following studies have been performed:

- Evaluation of heat conduction in the fuel element [18]. It has been shown that the axial heat conduction in the fuel plate can be neglected in most cases, since the fuel stripe is thin, on the order of 6 mm. The radial monodimensional modeling of the fuel plate can then be considered extremely accurate if there is no need to capture the assembly hot spots.
- Evaluation of the flow velocity distribution in the channel [18]. A comparison has been made between the full 3D channel flow and 2D approximation that neglects the flow dependence on the horizontal location, parallel to the fuel plate, and it has been shown that the flow can be modeled as infinite 2D rectangular channel flow.
- Evaluation of flow properties and correlations [18]. Correlations for heat transfer and friction factor have been determined, specific for Flibe.

The work on the single channel and plate provided the basis for the analysis of the fuel element, a hexagonal prismatic channel comprising 18 fuel plates. This analysis has been performed on a 3D level [18], in parallel with the work performed at ORNL [9].

At ORNL a full CFD and heat conduction model of the fuel assembly has been developed, whereas reference [18] presents a simplified approach which neglects axial conduction and models the flow using heat transfer and friction correlations. The full CFD assembly analysis is a relatively large problem from a computational standpoint, whereas the simplified approach is more feasible in terms of computation and it is still able to provide accurate information about flow distribution, making it suitable for use in a larger domain such as the core.

The thermal hydraulic analysis of the AHTR core is a relatively large problem that cannot easily be addressed using only CFD, because the range of scales involved in the flow distribution would require very large meshing. CFD has been used for characterization of the flow in the plena, and the core flow distribution has been computed using friction and heat transfer correlations in RELAP. This combination can provide adequate understanding of the flow distribution in the AHTR core. This aspect completes the full core steady state analysis and constitutes the basis for the study of the assembly removal.

Several approximations have been introduced in order to simulate the extraction of the assembly in the upper plenum, which will be explained in the following sections.

A 2D analysis of the transient has been performed [19]; this analysis is mainly intended to investigate a potential approach for studying this problem, while the numerical results of this simulation play only a minor role. This analysis used a coupling of boundary conditions approach based on user defined functions in Fluent, plus dynamic meshing for the modeling of the motion of the assembly.

The coupling of boundary conditions is a general approach that allows coupling of the CFD solver with input from external sources (for example other thermal-hydraulics codes) or within the model itself. This approach allows modeling of specific components of the system by the use of simple correlations that the user can implement in C language; in this case this approach was used to model the flow for the intra-assembly channels through correlations derived from previous analyses [18].

The dynamic meshing has been used to model the motion of the assembly in the core. Fluent has the capability of changing and adapting the mesh in order to perform time-dependent dynamic

simulations. This feature however can only be used with tetrahedral meshing, which is not the preferred meshing type for the CFD modeling of the AHTR developed so far, and requires a lot of computational resources when applied to a 3D problem.

These tools successfully allowed the simulation of the extraction of the assembly in 2D configuration, but revealed to have excessive requirements on computer resources for direct application to the 3D assembly removal. For this reason, a simplified quasi static approach has been used, based on the assumption that the transient is slow with respect to the characteristic flow time scale.

2.1.2. Methodology: some considerations and issues

The removal of the fuel assembly from the AHTR core represents a somewhat unconventional problem and as such presents specific issues and challenges and thus requires specific considerations; the most relevant are listed in this section.

1. Flow-related considerations:
    a. Vortex shedding at assembly outlets. The flow at the outlet of the assembly is represented by several parallel jets (Figure 2-12) that interact with each other, making the solution unstable. A secondary consequence of this aspect is the need for a relatively fine mesh at the assembly outlet that becomes prohibitive if this phenomenon needs to be captured on a full core level.
    b. Transient formulation of unsteady models. All RANS turbulence models have been formulated for steady configurations, so they might not be accurate in predicting the solution in unsteady configurations. However, in this case the transient is supposed to be slow with respect to the flow characteristic time, so the URANS models are almost certainly acceptable. A way to confirm their validity would be experimental validation, which is not easily applicable in this case.
    c. Quasi-static approach. Full 3D dynamic meshing simulation of the assembly removal is not practical in our case, so the adoption of a quasi-static approach has been necessary in order to simulate the transient. Note that the amount of coolant in the assembly channel in nominal condition is about 300 kg; with a 100 kg/s mass flow rate; the coolant present in the assembly channel is completely replaced every

3 s. This time scale is noticeably smaller (one to two orders of magnitude) than the expected time required for extracting or inserting the assembly, which is at least 1 min.

d. Choice of turbulence model. Several options are available in Fluent for the modeling of turbulence; since the flow is only slightly turbulent and it is constrained by solid walls (fuel plate surfaces), the kω model is the primary choice and the kε realizable model is the best alternative.

2. Computational aspects:
    a. Problem dimension. The characteristic dimensions for the flow span a very broad range, from 7 mm for the coolant channel thickness to 6 m for the fuel assembly height. Such wide range can easily result in prohibitive computational requirements, if assumptions for the simplification of the problem are not adopted.
    b. Parallel simulations. Even though a full CFD model of the system cannot be made, the use of the parallel capabilities of Fluent, associated to adequate simplification of the problem, can be capable of providing meaningful solutions. The use of parallel version of Fluent requires part of the input to be parallelized.
    c. Meshing and post-processing. Since the problem is large and parallel, the meshing and post-processing also have to be performed in parallel. In particular, since data loading time is large, the use of automated execution scripts is necessary.
3. Limitations on the use of system codes (RELAP):
    a. Moving parts. Since system codes are not capable of simulating moving parts, the use of more flexible CFD tools is needed. The integration of these tools with the system code provides an appropriate configuration for simulating this problem.
    b. Accurate modeling of geometrical features. System codes are based on the use of basic thermal hydraulic correlations that are derived from strong simplification of the original problem. This is a limiting factor in this case, where more complicated geometrical features need to be modeled.
    c. Accurate 3D flow modeling. System codes cannot provide accurate 3D flow modeling, but only macroscopic 3D flow distributions neglecting specific geometrical features.

The analysis approach for the online refueling is developed keeping in mind these considerations and limitations. Some of these limitations can be overcome simply by increasing the available computational capabilities, but this aspect is beyond the scope of this work, which aims to provide a general approach more than an accurate solution to specific problems.

2.2. Considerations on thermal hydraulics of coolant channel and fuel plate

The steady state analysis of the flow and temperature distribution for the coolant channel and the fuel plate has been performed in order to provide a basic characterization of the operational configuration of the fuel assembly.

2.2.1. Assumptions and approximations

Several assumptions can be made on the flow and temperature distribution:

- The axial component of heat conduction can be neglected in the evaluation of the temperature distribution of the thermal structures in the fuel assembly.
- The fluid (Flibe) can be considered incompressible with constant properties.
- The coolant channel is a parallelepiped but the transversal dimension is substantially smaller than the other two dimensions, so the channel can be approximated as a 2D rectangular channel for CFD purposes.
- Fully developed flow solution can be used in the coolant channels for the calculation of heat transfer and friction factor, not accounting for entrance length effect.

2.2.1.1. Axial heat conduction

The fuel plate of the AHTR is a 3D conducting structure, but the heat conduction prevails in one direction. The error that results in treating the heat conduction as monodimensional has been estimated. If the axial heat conduction is negligible, a much simpler treatment of the heat conduction is allowed, substantially less computationally demanding. Since the temperature gradient in the vertical direction is 1000 times smaller than the one in the horizontal one, the axial heat conduction is expected to be negligible.

In order to demonstrate this assumption, the monodimensional approach is compared to a 2D approach that accounts for axial conduction. The modeled domain is a section of the fuel plate, with z being the vertical direction (from inlet to outlet of the core) and x being the horizontal direction (from the centerline of the graphite meat to the surface in contact with the coolant).

The solution of the heat conduction has been performed using a 2D finite volume approach, that in the case of the 1D approximation neglects the heat conduction in the z direction.

The problem has been solved using a MATLAB code [Appendix 7.1]; the solution of the 1D linear system is obtained through the matrix inversion function provided by MATLAB, while the solution for the 2D model is obtained through a Gauss-Seidel iterative procedure.

Figure 2-1 shows the temperature difference between the two solutions.

As expected, the 2D solution is lower where the temperature is higher and higher where the temperature is lower, because of slightly enhanced heat conduction. The maximum temperature difference is 0.003°C, which is completely negligible, considering for example the uncertainties in k. Moreover, using the 1D solution would mean being conservative. Similar considerations hold for the coolant temperature: a little more power is delivered where the coolant is colder and a little less where the coolant is hotter, but the difference is absolutely negligible, of the order of 10^{-4} °C.

The 1D approach for the evaluation of the axial plate temperature distribution is very close to the 2D solution and it is conservative; it substantially reduces the computational requirements, which makes it desirable for highly computationally demanding applications.

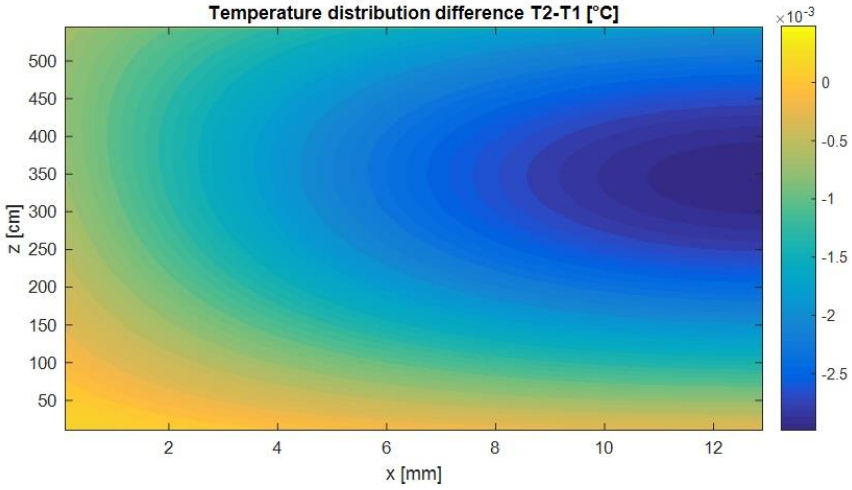

Figure 2-1. Temperature difference between the 2D and 1D solution

2.2.1.2. Coolant properties

The AHTR uses FLiBe as a coolant. The properties of this salt are relatively well known and the most recent formulas for the interpolation of experimental data are provided in reference [20]. This fluid can be approximated as incompressible and most of the properties are not strongly dependent on the temperature. For analysis purposes, many times it is easier to assume a fluid with constant properties. Table 2-1 provides the average value and uncertainty for specific properties in the operating temperature range of the AHTR, with particular focus on the interval between 650 and 700°C.

Table 2-1. Coolant properties

Property	Mean	Uncertainty of data	Deviation from mean
Mass Density [kg/m3]	1950.0	0.05%	0.36%
Dynamic viscosity [Pa*s]	6.0	20%	6.08%
Thermal conductivity [W/(m*K)]	1.1	15%	0.66%
Heat capacity [J/(kg/K)]	2416.0	2%	0%
Volumetric heat capacity [J/(m3*K)]	4.71e6	-	0.36%

2.2.1.3. 3D channel to 2D channel simplification

The coolant channel is a parallelepiped with a transversal dimension (distance between plates) substantially smaller than the other two dimensions. The flow solution for the full 3D channel model and the 2D rectangular channel model have been computed using Fluent and compared in order to prove the validity of the 2D approximation.

The velocity distribution of the 3D solution requires more space to reach the fully developed region and, at the centerline, it is slightly higher than the solution of the 2D case. This is due to the fact that the velocity of the flow is smaller for locations close to the short sides of the channels.

Similarly, looking at the fully developed velocity profile, the curve for the 3D solution is higher (at the centerline) compared to the one of the 2D solution. The maximum velocity is 2.31 m/s for the 3D case and 2.28 m/s for the 2D case. The slope of the curve at the edges is about 2% different from one case to the other.

Since the two channels have different hydraulic diameter, an appropriate indicator for the difference between the two cases is the friction factor, which is shown in Figure 2-2. The two friction factors, in the central region, are very close; the difference is about 0.8%. Moreover, the 2D friction factor is higher, so the 2D approximation can be considered conservative.

It should also be noted that the difference is even more negligible in that interval where the 2D solution is developed and the 3D solution is still developing. This means that for the evaluation of the fully developed solution a relatively short length can be considered, reducing the computational demand.

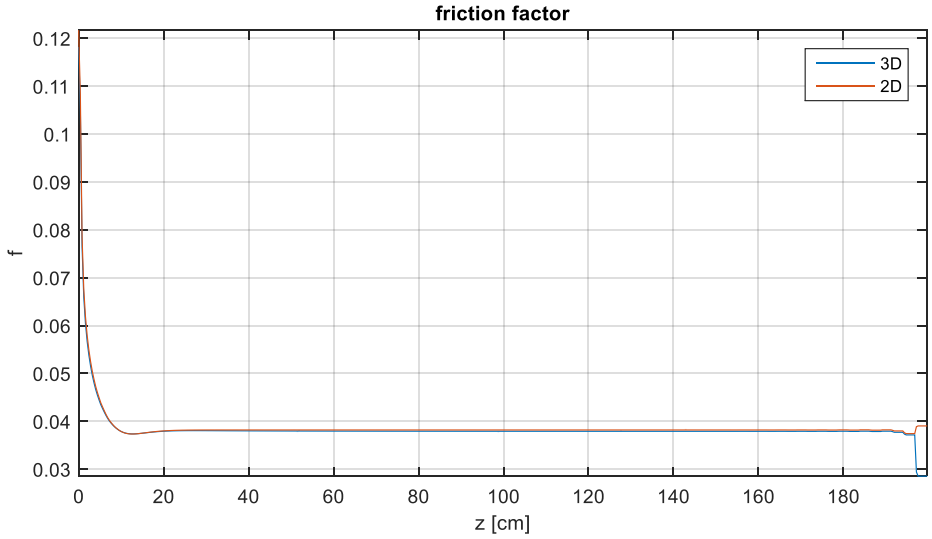

Figure 2-2. Friction factor as a function of the elevation

2.2.1.4. Coolant channel friction factor correlation

The friction factor for fully developed flow in various flow regimes has been investigated using Fluent and the 2D coolant channel model. The friction factor correlation is needed for the calculation of the flow distribution in the AHTR assembly. Note that the values for the transitional regime have been obtained by interpolation between the upper extreme for the laminar regime and the lower extreme for the turbulent regime.

The overall behavior of the skin friction coefficient can then be expressed as:

$$f = \begin{cases} \dfrac{24}{Re} & Re < 2000 \\ 4.2721e-7 * Re + 0.011146 & 2000 < Re < 4000 \\ 2.821096 * Re^{-0.710987} + 0.00510267 & Re > 4000 \end{cases} \quad (1)$$

2.2.1.5. Coolant channel heat transfer correlation

Similarly to the friction factor correlation, the heat transfer coefficient correlation has been computed from the fully developed flow solution as a function of the Reynolds number. Note that the values for the transitional regime have been obtained by interpolation between the upper extreme for the laminar regime and the lower extreme for the turbulent regime.

The overall behavior of the Nusselt number as a function of Reynolds can be summarized as follows:

$$Nu = \begin{cases} 8.2353 & Re < 2000 \\ 0.0228 * Re - 37.265 & 2000 < Re < 4000 \\ 0.0378 * Re^{0.8752} & Re > 4000 \end{cases} \quad (2)$$

2.2.2. Plate-wise steady state thermal characteristics

A series of preliminary studies of the thermal hydraulic features of the assembly at the level of coolant channel and fuel plate has been performed to evaluate the nominal operating conditions. Figure 2-3 shows the temperature and heat transfer coefficient profiles of the coolant along the active portion of the average coolant channel. The average heat transfer coefficient is about 7500 W/m²K, derived from a Reynolds number of about 7300, which corresponds to about 1.9 m/s mean flow velocity.

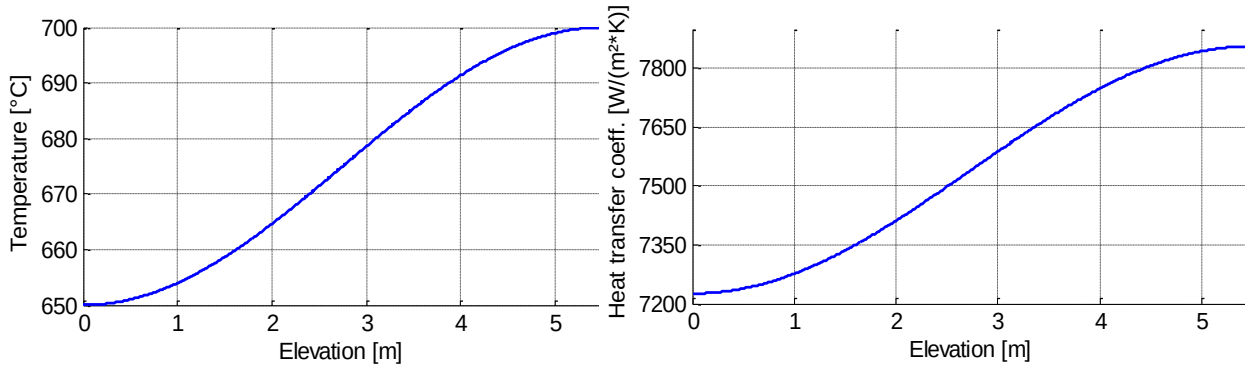

Figure 2-3. Temperature (left) and heat transfer coefficient (right) as function of elevation in the active portion of the coolant channel

The flow along the rectangular channels can be appropriately modeled using 1D correlations; specific flow details at inlet and outlet of rectangular channel require more advanced evaluations to be properly characterized. In particular, the flow distribution of the flow at the outlet of the parallel channels at the assembly level generates unstable vortex interaction that needs to be characterized via CFD.

Looking at the thermal characteristics of the fuel plate, the temperature profile is strongly affected by the thermal conductivity of graphite in irradiated conditions. The typical profile is parabolic with maximum temperature at the interface between the graphite meat and each fuel stripe. The maximum temperature depends on several factors, mainly the fission density distribution and the burnup distribution. However, the thermal limit for TRISO fuel is notably high, maintaining even the most peaked fuel assemblies far from unsafe conditions.

2.2.2.1. Thermal conductivity of graphite

Thermal calculations of the fuel assembly and plates depend on the thermal conductivity of graphite. Figure 2-4 shows the thermal conductivity of graphite as a function of temperature for various irradiations; the conductivity remains above 20 W/(m*K) even for high neutron fluence.

Figure 2-5 shows the maximum fuel temperature as a function of graphite thermal conductivity, assumed to be uniform within the fuel plate. Since the conductivity will always be larger than 20 or 30 W/(m*K), even for deteriorated conditions at high irradiation, the maximum fuel temperature will increase but, most probably, it will not challenge the integrity of the fuel. The maximum

temperature increase, going from unirradiated conditions (100 W/(m*K)) to low conductivity condition (20 W/(m*K)) is on the order of 70°C.

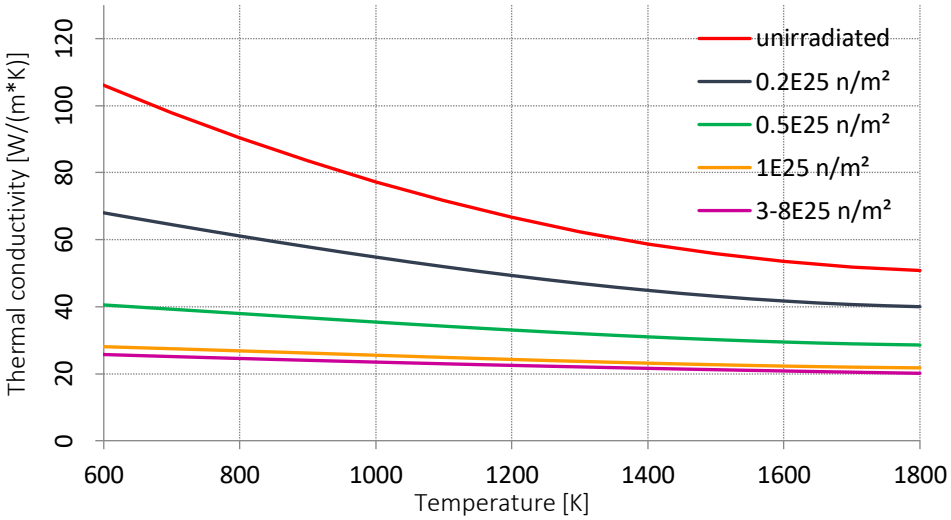

Figure 2-4. Graphite thermal conductivity as a function of temperature for various irradiations

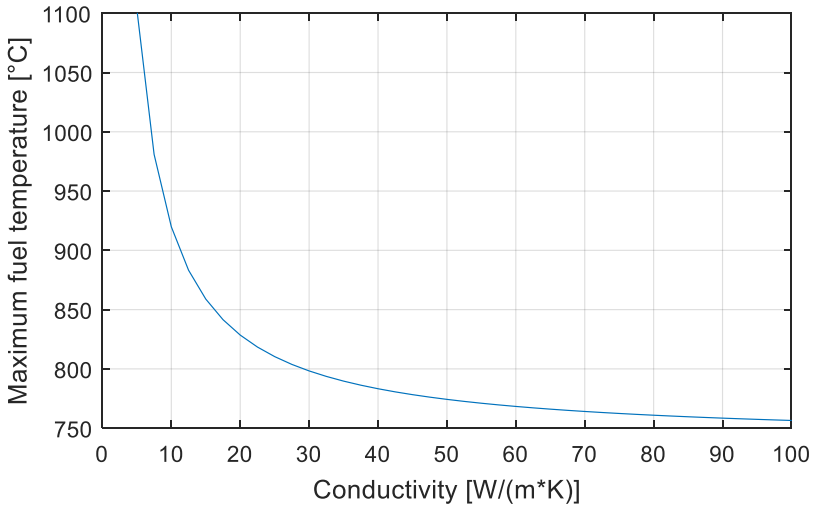

Figure 2-5. Maximum fuel temperature for average assembly as a function of graphite thermal conductivity

2.3. Fuel assembly thermal hydraulic characteristics

The work on the single channel and plate presented in section 2.2 laid the ground for the analysis of the fuel assembly. The objectives of this analysis are the following:

- Evaluate flow distribution within the fuel assembly, particularly how the flow splits between the 21 internal channels (6 of which are half the nominal thickness), and the bypass channel surrounding the fuel assembly outer box.
- Evaluate the temperature distribution in the fuel assembly with particular focus on the localization of the hot spots and heat removal properties.

The modeling approach is based on MATLAB and a code has been developed that performs the calculation of the coolant properties and the temperature distribution within the fuel assembly. The calculation of the coolant properties is based on the assumption that each coolant channel can be treated as a monodimensional channel and the flow is fully developed at every location. This assumption is not completely valid at the extremes of the channel but the channel is substantially longer than the entrance length, so little error derives from making this assumption. On the other side the temperature distribution of the plate is calculated on a 2D horizontal cross section of the assembly, and this methodology is valid since the axial conduction component can be neglected, as described in section 2.2.1.1. The calculation begins at the base of the assembly and ends at the assembly outlets; at each axial step the new coolant temperature is obtained by computing the heat flux from the lower axial step. The code [Appendix 7.2] is based on the following outline:

1. The mesh is defined. Figure 2-6 shows part of the mesh, particularly the portion of the horizontal cross section that represents a single plate. Note that the mesh presented in the figure is substantially coarser than the one used for the calculations, for illustration purposes. A triangular mesh has been implemented, since it fits well with the hexagonal geometry of the assembly. Equilateral triangles have been used for simplicity in the equations' derivation, even if this choice requires particular attention in order to accurately represent the body. The dimensions of the cross section in fact are slightly adjusted in order to correctly fit the mesh: the boundaries of different materials lie perfectly on the sides of specific triangles.

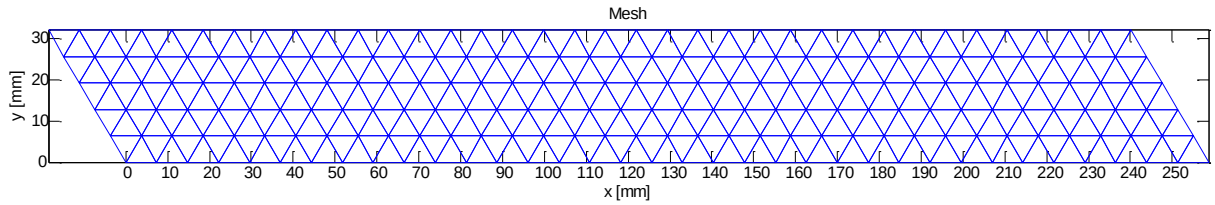

Figure 2-6. Mesh for the fuel plate

2. Definition of matrices for the following quantities:
    a. Direction of the triangle. For each node the direction (upward or downward) of the triangle is recorded;
    b. Distribution of materials. Figure 2-7 shows the material distribution for the plate: green for the box wall, blue for the fuel plate (light blue for the fuel stripe), orange for the support structure and red for the coolant. Note that the cladding is neglected.
    c. Power density distribution. The heat is deposited only in the plates, particularly in the two light blue stripes we can see in the previous figure. Also, considering the axial distribution of the power, a chopped cosine profile has been used for the study (with a 1.3 peaking factor), but the model is capable of modeling any kind of profile. Also note that the model assumes uniform horizontal power distribution (along the x axis), neglecting neutronic power peaking factors. The conclusions derived from this models are then due only to purely thermal hydraulic effects and not neutronic effects.
    d. Thermal conductivity of the materials.

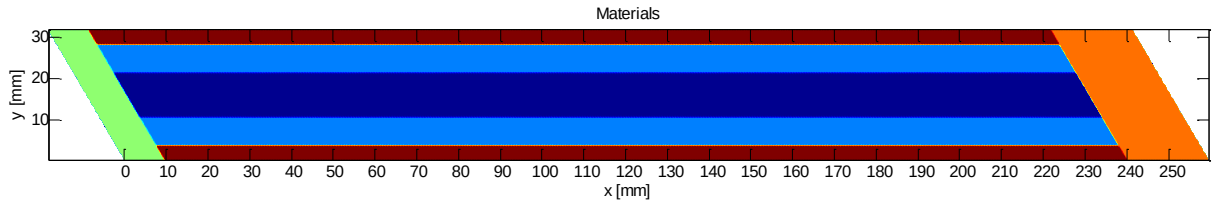

Figure 2-7. Typical materials distribution for the fuel plate, showing the graphite meat (blue), the fuel stripes (light blue), the coolant channels (brown), the support (orange) and the box (green)

3. Evaluation of the boundary connections for every triangle. Since the finite volume method is implemented, the classification of how each triangle exchanges energy with the neighboring cells is needed. The model allows for three types of boundary connections:
    a. Insulated face. No power is transferred through the boundary.
    b. Convection. The face is connected to a certain channel at a given temperature. The heat transfer coefficient is provided by the heat transfer correlation presented in section 2.2.1.5.
    c. Conduction. The thermal conductivity of graphite (about 15 W/m*K) has been used.

    The boundary connections are used to build the matrix of the linear system that has to be solved in order to provide the temperature distribution. Also, a conductive connection has been modeled between the right and upper wall, in order to preserve the symmetry of the system.
4. Evaluation of the flow velocity for the internal channels. The total flow through the system is fixed; the ratio of the external and internal flow with respect to the total flow is defined in the input, while the splitting of the flow among the 7 internal channels is determined by the total pressure drop along the channels, which is the same for all of them. The correlations presented in section 2.2.1.4 have been used to evaluate the friction coefficient. The velocity of the flow in the 2 small channels (lower and upper) is about 1.5 m/s and the velocity in the other five channels is about 2 m/s.
5. The last step consists of the iterative procedure that provides the axial distribution of the following temperatures:
    a. The temperature of the coolant at the inlet of the channels is given (650°C);
    b. The horizontal temperature distribution of the assembly is solved for that axial level;
    c. The power delivered to each channel is obtained by integration on the boundary nodes for every channel;
    d. The temperature of the coolant at the next axial step is evaluated through the following balance:

$$\dot{m}_{ch} * c_p * dT_c = \dot{q}' * dz \qquad (3)$$

    e. The procedure from point a is repeated until the top of the assembly is reached.

The modeling described in the previous paragraphs is capable of providing full 3D assembly evaluations, where the main approximations are the absence of axial heat conduction and the 1D modeling of the flow in the channels. This model has been used to calculate steady state temperature and flow distributions for the AHTR assembly.

2.3.1. Steady state flow and temperature distributions

The approach presented in the previous section is capable of providing the temperature distribution of a single plate, shown in Figure 2-8; this distribution has been obtained using 675°C for the coolant temperature of both the internal channels and the bypass channel, and 7500 W/(m²*K) for the heat transfer coefficient. Note that the yellow spot on the right part of the model is unphysical, due to the incorrect application of an insulated boundary condition, which neglects the heat flow through the support shape, to the adjacent third of assembly.

The temperature distribution in the central portion of the plate does not depend on the x location, so the maximum temperature can be evaluated, assuming no heat conduction in the x direction, by solving the 1D heat conduction equation. The solution of the conduction equation is shown in Eq. (4), where the maximum temperature is computed as a function of the power density q''', the fuel stripe thickness t, the heat transfer coefficient h and the conductivity k. The analytical result from this formula is in very good agreement with the numerical result of the 2D calculation, for which the maximum fuel temperature is about 783.5°C. Note that the temperature distribution of the support and the box is not correctly represented in this model, since the three-fold rotational symmetry of the fuel assembly is not correctly modeled in the single plate configuration.

$$T_{max} = T_c + q''' * \frac{t}{h} + \frac{q'''}{k} * \frac{t^2}{2} = 783°C \qquad (4)$$

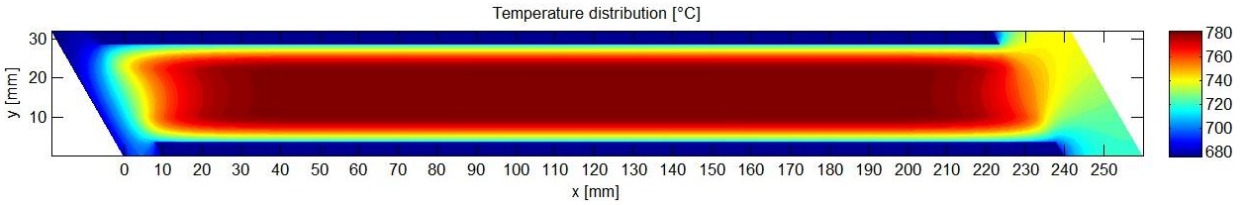

Figure 2-8. Temperature distribution of the average fuel plate

In order to capture the correct temperature distribution of the plates it is necessary to model at least one third (6 fuel plates) of the cross section and couple the boundary conditions for the two sides of the parallelogram that cut the support structure. This allows to retrieve information about the hot spots, and, coupled to the axial coolant temperature, allows to identify the highest fuel assembly temperature.

Figure 2-9 shows the temperature distribution for a horizontal cross section of the fuel assembly; the axial location at which this slice is taken is where the maximum fuel temperature is located, corresponding to about 3.25 m from the beginning of the active portion of the fuel element; this active portion is 5.5 m tall, so the maximum is located slightly above the mid plane.

Figure 2-10 shows the 3D temperature distribution of the fuel assembly. It is possible to notice that the maximum is not coincident with the mid plane but it is not far from it. Also, the two external plates, the one next to the support and the one next to the box, appear to be hotter than the remaining 4 plates.

This is further emphasized in Figure 2-10, where the 4 internal plates all have a very similar temperature distribution, while the top and the bottom one are 20°C hotter. The cause of this temperature difference is the reduced cooling capacity of the two thinner coolant channels, which are half the thickness of the standard channels, suggesting that the smaller channels, which should remove about half of the power that is removed by any other standard channel, in fact provide less-than-half cooling capacity than any other standard channel.

Notice that this is a purely thermal hydraulic effect,that has nothing to do with the power distribution, which in this case is assumed uniform everywhere. This temperature peaking effect would be even more important if a corrected, non-uniform power distribution, derived from neutronic considerations, was implemented. The moderation enhancement in proximity of the graphite support structure would generate a hot spot in the plate that is closest to the support structure, at a location near to the center of the hexagonal cross section [9].

Another aspect that should be noted looking at Figure 2-9 is the presence of heat flow from the right side to the top side of the parallelogram, indicating that the small channel next to the support structure (top) will have to remove more power than the small channel next to the box (bottom), thus being hotter and further increasing the hot spot in the internal fuel plates.

With respect to the axial coolant temperature distribution, the assumed 0.5% bypass flow results in very similar profiles for internal and bypass channels; the two smaller channel are 20 to 25°C

hotter than the other channels. One way to reduce the temperature for the smaller channels would be to increase their thickness by 33%: with this configuration the outlet temperature for all internal channels would match.

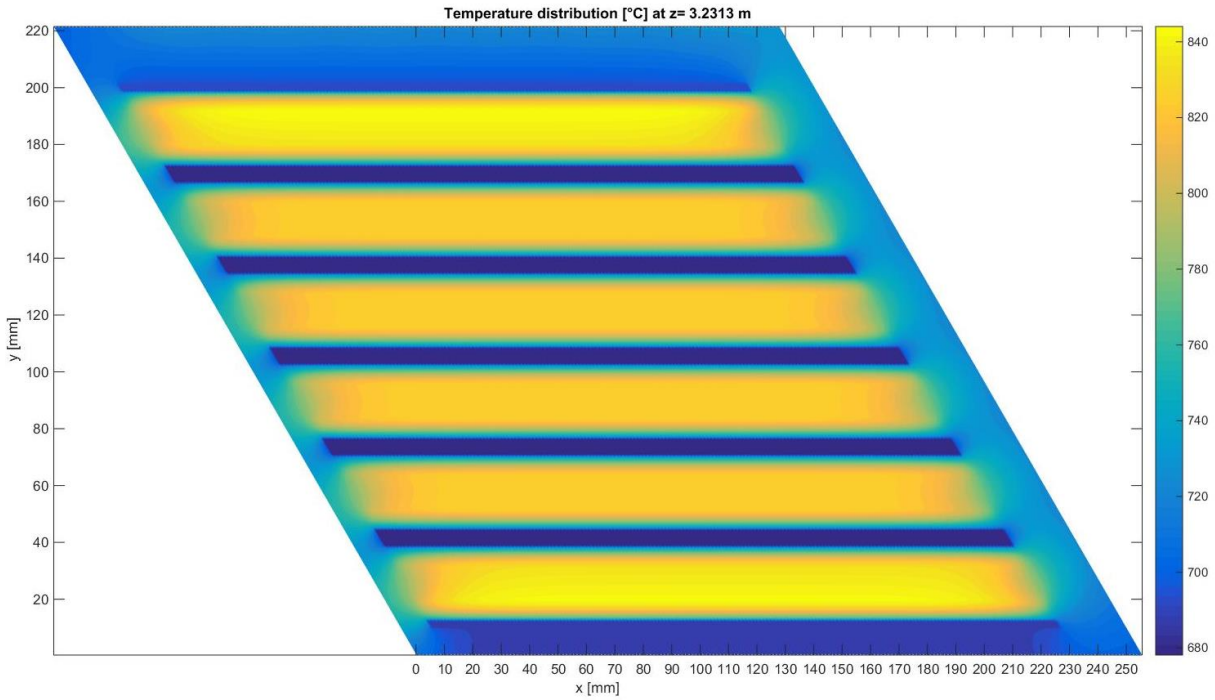

Figure 2-9. Horizontal temperature [°C] distribution at axial location of maximum fuel temperature

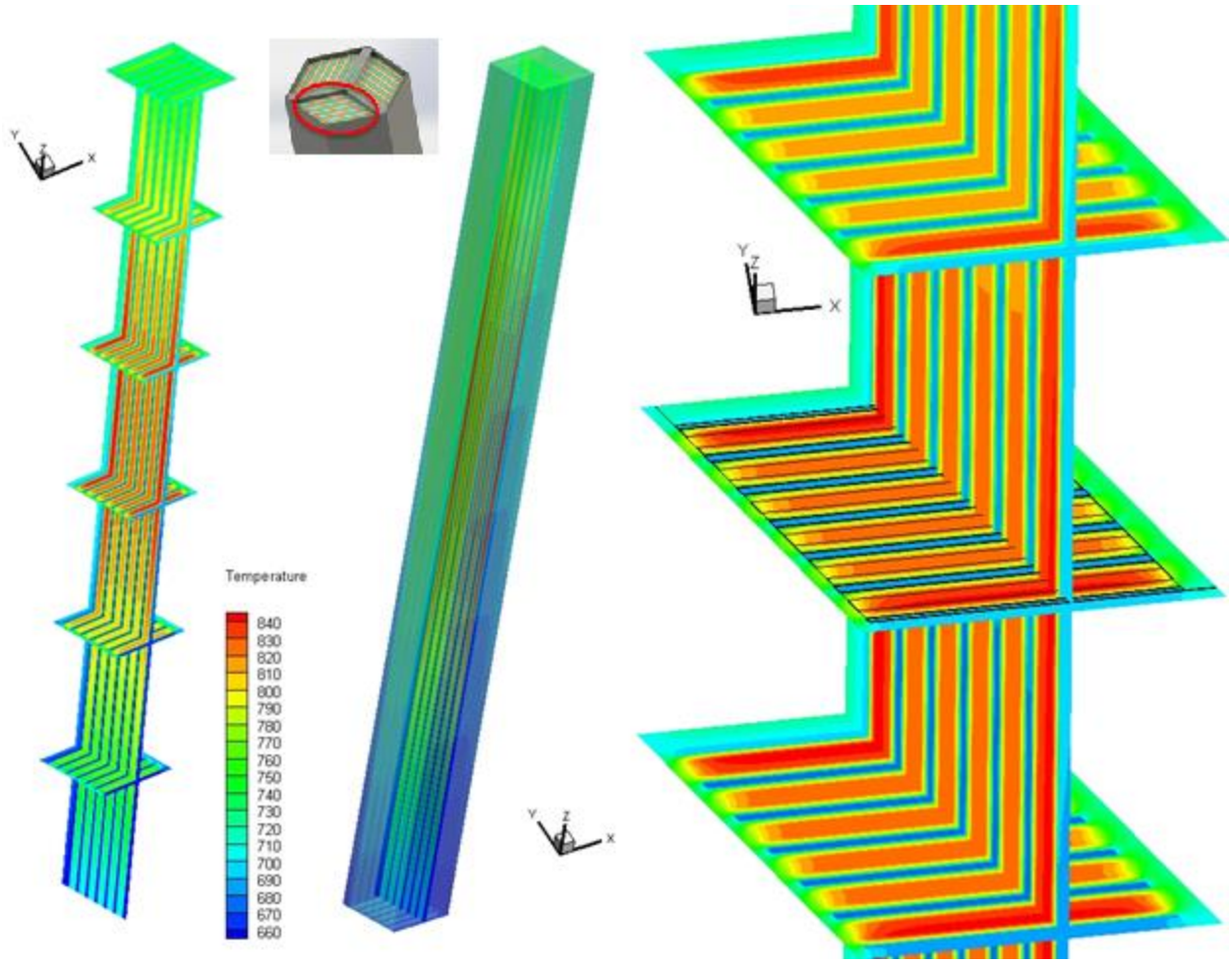

Figure 2-10. 3D temperature [°C] distribution for one third of the active part of the fuel assembly

The 3D analysis of the fuel assembly suggests that the fuel is substantially far from the thermal limit and the design allows adequate cooling of the system. Minor geometrical adaptions, such as the increase in the dimension of the two smaller channels, may help to reduce the peaking factors. The amount of bypass flow does not have a strong influence on the overall thermal distribution of the assembly and the absence of external flow results in a more uniform distribution; this option may be of interest in order to reduce the thermal stresses on the box and support structure.

2.3.2. Flow at outlet of assembly

The flow distribution within the fuel assembly is relatively simple since every channel is separated from each other. However, the flow at the outlet of the assembly shows more complicated features since each channel strongly interacts with the nearby parallel channels. The behavior of the flow at this location has been investigated using a bi-dimensional model; Figure 2-11 shows the model, as well as the meshing. Only one third of the assembly has been considered, for symmetry reasons, and the 2D section is vertical and orthogonal to the surface of the plates; 7 outlets are modeled, 5 standard channels and 2 external narrower channels. The model is a simplification of the real geometric configuration, but is able to capture the interaction between the flows from different channels.

The mesh for the problem is about one hundred thousand elements, the minimum and maximum mesh sizes are 0.07 mm and 1.4 cm, the growth rate is 1.5%. Boundary layers are modeled on all boundaries except the inlets and outlets, including the walls corresponding to the grappling collar that is located above the channel outlets.

Several turbulence models have been tested for modeling the flow, including the scale adaptive simulation (SAS) option; the wall is treated using the enhanced wall treatment option available in Fluent [16].

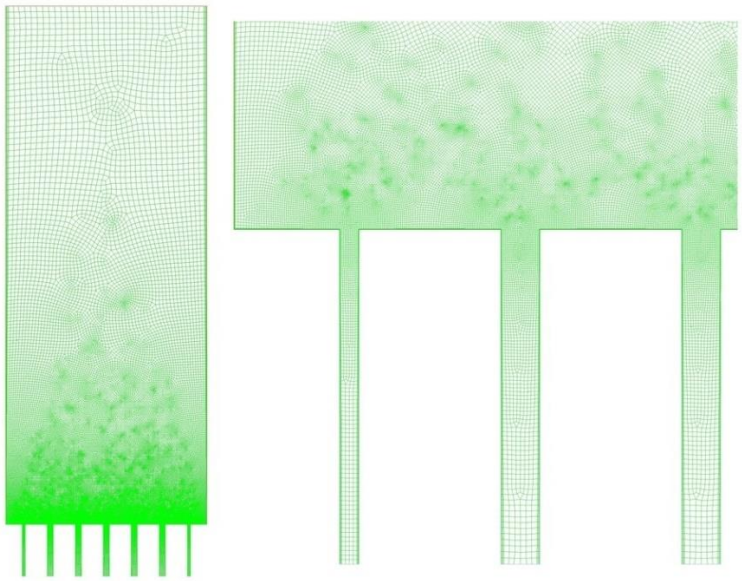

Figure 2-11. Mesh details for the 2D CFD simulation of the flow at the outlet of the assembly channels

The simulation has been run in transient mode, using time steps of 0.02 seconds. Figure 2-12 shows the vorticity contours for six consecutive time steps spaced 0.2 seconds. The solution is not steady and shows strong oscillatory interaction of the multiple jets exiting the top of the assembly.

A full 3D simulation of this phenomenon is not practical, having strong requirements on the computational side; as a consequence, it is not feasible to capture this aspect in a full 3D core simulation. In the remaining part of this work it is assumed that the flow at the outlet of the grappling collar, immediately preceding the upper plenum, can be considered uniform; and the portion of the duct between the outlet of the channels and the outlet of the grappling collar serves to make the flow more uniform. This assumption is also partially justified by the fact that the design of that portion of the assembly is at this stage of the design process only partially known.

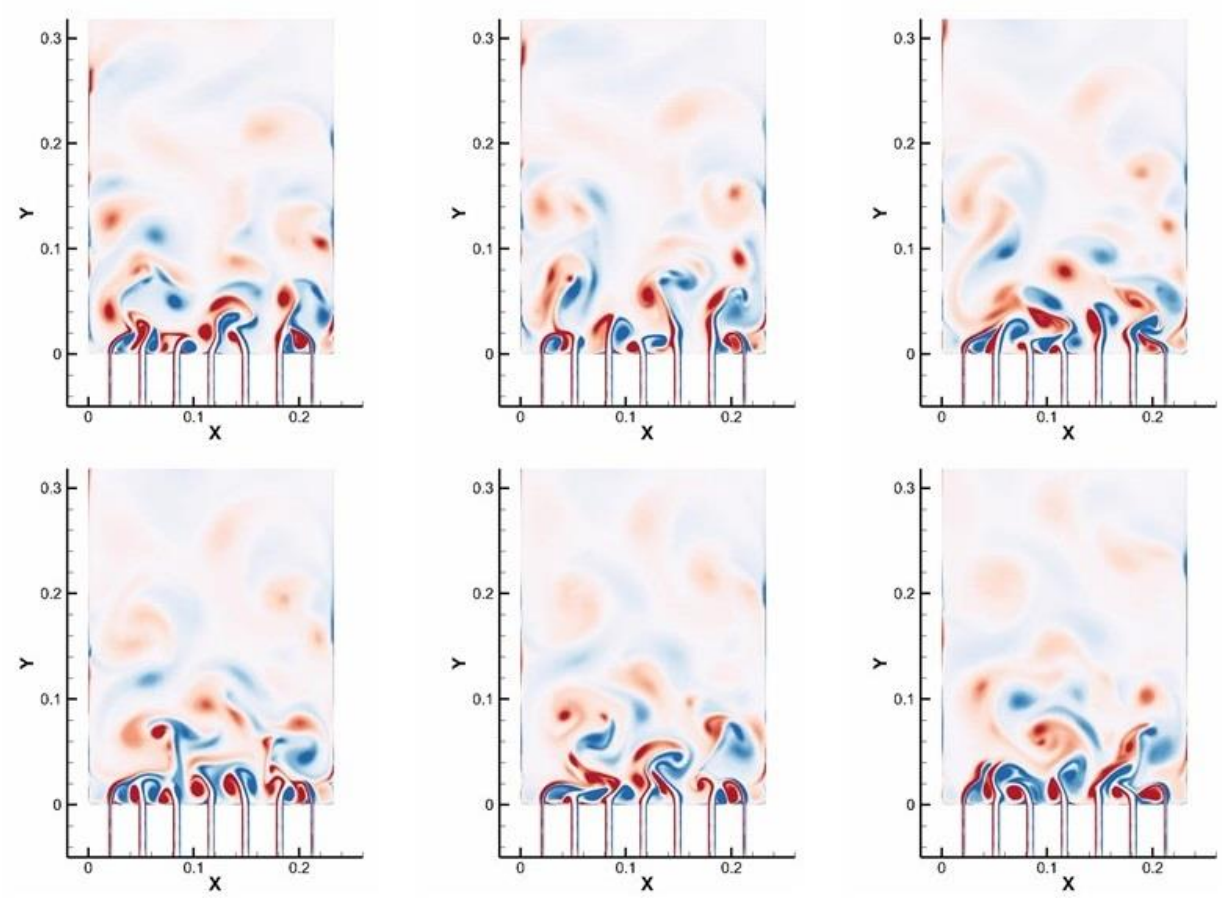

Figure 2-12. 2D vorticity contours for six time steps, 0.2 seconds spaced

2.3.3. Transient temperature distribution in the assembly

A preliminary study on the temperature evolution of the assembly as a function of time has been performed, in order to understand the time dependence of the temperature distribution. ANSYS Mechanical has been used to run the simulations. Since the objective of this study is not the full assembly temperature distribution, only a slice of the assembly has been considered, for simplicity; this assumption does not preserve the dimensionality of the problem but it is straightforward and not computationally intensive. Note that this assumption is partly justified by the absence of thermal axial conduction in the plates; the actual distribution depends on the axial power profile, but its behavior in time does not. This simulation assumes for simplicity flat axial power profile

(axial peaking factor equal to 1), and the maximum and minimum temperatures refer to the average axial power and not to the maximum axial density distribution.

The transient is simulated by a reasonable definition of the time dependence of the heat transfer coefficients and the power density. Reasonable values for the heat transfer coefficient are derived from the analysis presented in section 2.2, and the decay power is expressed as an exponential function. The simplified fuel assembly cross section model neglects the presence of the cladding and assumes that 100% of the power is deposited in the fuel stripes.

The heat generated in the fuel assembly is removed by two means: the heat transfer to the internal coolant channels and the heat transfer to the external bypass flow through the box. Convective transfer is modeled in both cases, by assuming appropriate values of reference temperature and heat transfer coefficient.

With respect to the external (bypass) channels, the reference temperature is constant and equal to 700°C, which is the average outlet temperature from the core; the heat transfer coefficient is chosen to be 200 W/m²K, which is comparable to the expected heat transfer coefficient to the external channels when the assembly is operating in steady conditions. The heat transfer coefficient is assumed to be constant. With respect to the internal channels, the reference temperature and heat transfer coefficient selected for the steady state conditions are 675°C and 7500 W/m²K respectively; the heat transfer coefficient decreases in time to simulate the flow reduction of the internal channels.

The power density for the steady state conditions is about 41.16 W/cm³, corresponding to the nominal power of the reactor.

In order to simulate the transient, the power is first reduced to 60% to simulate the control rod insertion, that takes 60 seconds, and subsequently the power decays exponentially following the typical power decay profile of uranium fuels [21]. Moreover, the flow reduction in the internal channels (modeled as a reduction of the heat transfer coefficient) is assumed to happen instantaneously right after the assembly removal begins. This is a very conservative assumption, but it is adequate for the purpose of this evaluation.

In summary the transient simulated in this section has the following structure:

1. From nominal conditions, the power is reduced to 60% for 1 min, with both the heat transfer coefficient (HTC) and reference temperature at nominal levels: 7500 W/m²K and 675°C for the internal channels, 200 W/m²K and 700°C for the external channels;

2. The internal HTC reduces to 100 W/m²K and the internal temperature increases to 700°C; this simulates fuel assembly extraction into the upper plenum.

Figure 2-13 shows the temperature distribution in the fuel assembly after the control rod is inserted (power drops to 60%) and the temperature distribution after the assembly is extracted and the flow through the channels reduces to a minimum level. The temperature in the assembly after the control rod insertion is on average lower, and the distribution remains unchanged with respect to the steady state conditions. At the end of the transient the temperature distribution drastically changes, due to the flow reduction through the internal channels; the distribution becomes more peaked towards the center of the plates, because the main active surfaces for heat removal are the box walls.

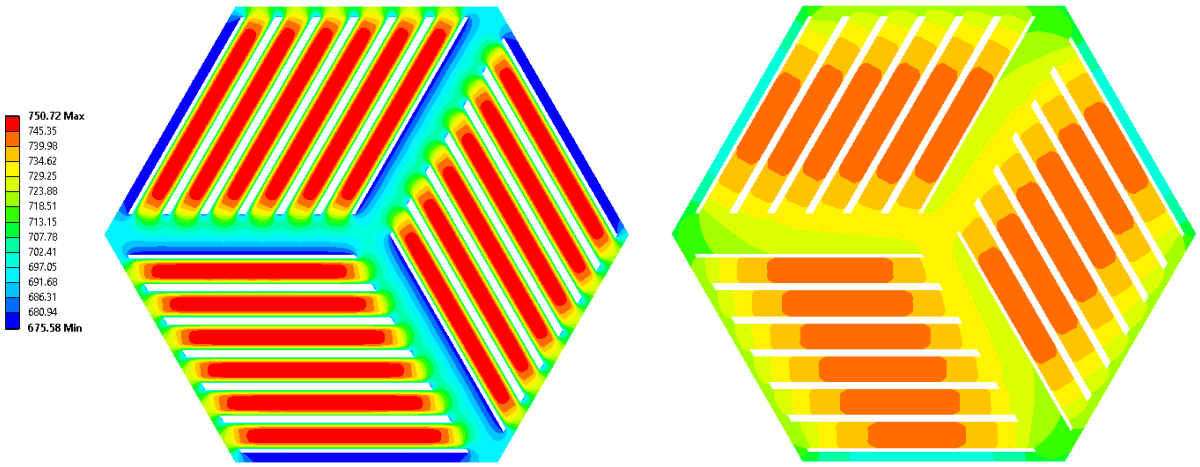

Figure 2-13. Temperature [°C] distribution at the end of the control rod insertion and 30 min after the control rod insertion and assembly extraction into upper plenum

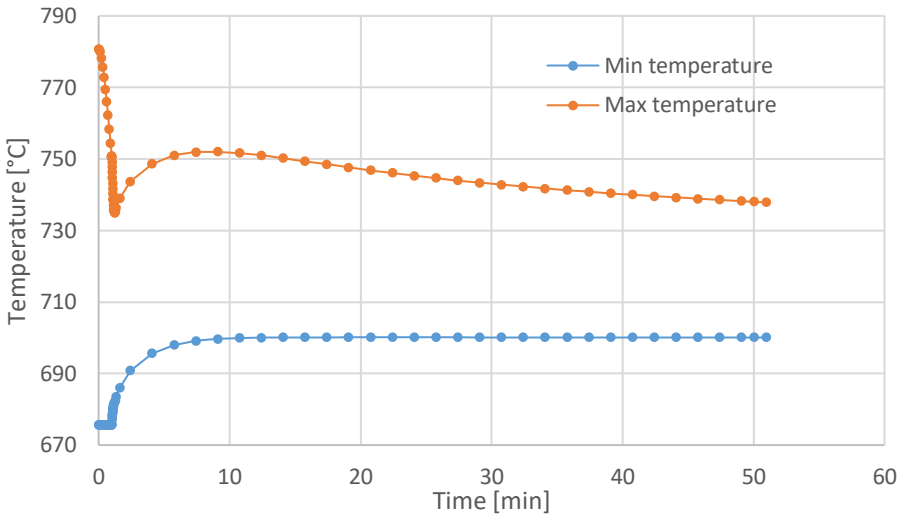

Figure 2-14. Time evolution of maximum (orange) and minimum (blue) temperatures for axial average assembly power density after the assembly extraction into upper plenum

Figure 2-14 shows the time dependence of the maximum and minimum assembly temperatures in the assembly cross section. The minimum temperature keeps increasing until it reaches a steady temperature around 700°C. As expected, the maximum temperature drops by 40°C after the control rod is inserted, then it reaches a maximum around 755°C, which is lower than the maximum in steady state conditions, and then decreases. Ideally, for infinite time, the temperature difference between the maximum and minimum temperature will reduce to zero, since the decay power keeps decreasing, but the assembly is extracted from the core long before the difference between the two temperatures becomes negligible. This simplified analysis shows that, as long as the assembly is maintained covered with salt, the temperature does not increase above the nominal values and the safety margins are not compromised.

2.3.4. Assembly transfer from reactor core to spent fuel pool

During the removal of the assembly from the core the temperature of the plates changes in time due to a series of factors; the maximum temperature needs to be maintained below the constraints in order to guarantee a safe operation. One particular concern is the temperature increase caused by the heat transfer reduction while the assembly is not covered in liquid salt; note that the transfer of the assembly from the core to the spent fuel pool through the refueling lobe implies residence of the assembly for some time in argon atmosphere.

In order to estimate the time available to perform safely the operation, ANSYS Mechanical [22] has been used to simulate a simplified transient simulation for the assembly transfer; the model used for this calculation is identical to the model presented in section 2.3.3.

The refueling sequence of events is simulated according to the following parameters:

1. From nominal conditions, the power is reduced to 60% for 1 min, with both HTC and reference temperature at nominal levels: 7500 W/m²K and 675°C for the internal channels, 200 W/m²K and 700°C for the external channels;
2. The internal HTC reduces to 100 W/m²K and the internal temperature increases to 700°C, for 1 min; this simulates the assembly while staying in the upper plenum. Note that the extraction is assumed to happen instantaneously;
3. Both internal and external HTC are reduced to 10% of the respective value: 10 and 20 W/m²K respectively; this simulates the assembly while located in Argon atmosphere at 700°C. Again, the extraction from upper plenum to Argon atmosphere is assumed to happen instantaneously.

Figure 2-15 shows the maximum and minimum temperatures for the average assembly. After the initial decrease due to the insertion of the control rod, the temperature increases, until, at about 2 hours, it reaches a steady value at 950°C (the plot only shows the first 30 min).

Assuming 850°C as a limiting temperature, the refueling operation can be performed safely as long as the duration of the assembly stay in Argon gas lasts less than about 20 min. Moreover, the duration of the stay in the upper plenum before the extraction into argon has only a minimal effect on the maximum fuel temperature.

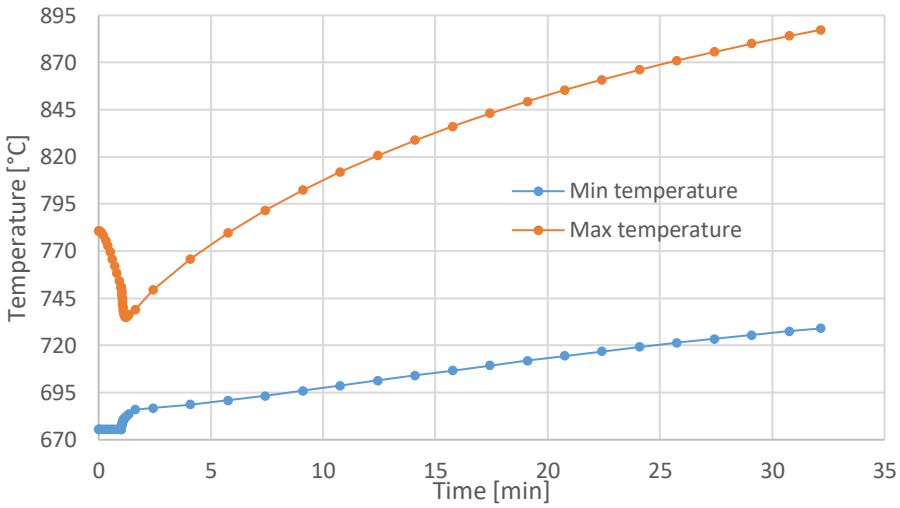

Figure 2-15. Time evolution of maximum (orange) and minimum (blue) temperatures for assembly (axial average assembly power density) in argon atmosphere (after 1 min in salt)

2.4. Flow in the channel of the removed assembly

After a general analysis of the steady state conditions and the time dependent response of the fuel channel and the assembly during the assembly extraction into argon, further studies of the time dependent flow distribution in the zone between the lower support plate and the removed assembly have been conducted. This part of the work is based on the use of Fluent as a simulation software, integrated with basic friction and heat transfer correlations for the modeling of certain boundary conditions.

The analysis of the flow in the channel of the extracted assembly is essential for the calculation of the flow distribution in the system, including lower and upper plenum, which is useful for the simulation of the time evolution of the core power and the assessment of the mechanical stability of the removal operation

2.4.1. Modeling approach

This section is devoted to the characterization of the flow distribution in the channel of the removed assembly; the analysis presented here focuses on the fluid zone that is enclosed by the lower

support plate and the lower face of the extracted assembly. the objective of this analysis is the characterization of the mass flow rate through the channel while the assembly is being extracted.
A full CFD transient simulation of this operation is relatively challenging; therefore, a few approximations have been adopted to simplify the analysis.
It is assumed that the transient can be treated as a sequence of steady state flow configurations; this assumption is valid if the transient is slow with respect to the fluid characteristic time (only a few seconds are needed to completely replace the amount of coolant in the channel of the assembly that will be replaced). Note that the flow adapts relatively rapidly to the movement of the assembly, on times of the order of less than 0.1s, and the only area where the flow oscillates very rapidly is the outlets of the assembly, as discussed in section 2.3.2. The quasi-static approach is then a reliable methodology.
Full 3D transient simulation of this transient is potentially feasible but would require computational capabilities that were not available for this work. In particular, the transient modeling is based on the use of moving and deforming meshing (MDM) functions that are available in Fluent, as well as other CFD software, and perform mesh adaption operations at every time step in order to simulate the motion of the assembly. This approach has been successfully demonstrated for a 2D configuration [19]; a few aspects that make this approach challenging for the 3D version of the problem are the fact that dynamic meshing in Fluent can only be applied to tetrahedral meshing (while the polyhedral is preferred in this case for better convergence) and the user control over mesh adaption is limited, leading to potentially very large meshes as the transient evolves. For these reasons the quasi-static approach has been selected.
All CFD simulations in this section have, as ultimate objective, the calculation of the steady state flow distribution for every specific geometric configuration. Some simulations however are conducted in transient mode, due to the presence of oscillations right after the top face of the lower support plate. The phenomenology of these oscillations is very similar to the vortex shedding that happens at the outlet of the assemblies, but it is partially constrained by the lower face of the extracted assembly. As a consequence, the transient behavior in this part of the system is more accentuated for configurations where the lower face of the assembly is already relatively far from the lower support plate.
This approach allows the CFD modeling of the volume between the support plate and the lower face of the assembly; the boundary conditions and the friction correlations complete the model by

coupling it to the behavior of the core. In particular, the boundary conditions at the inlets of the internal channels and the bypass channels are controlled by user-defined functions that couple the pressure at the two locations by computing a flow balance through the channels. This balance is based on the use of correlations and it is performed along the continuous path that follows the internal channels upward and then the bypass channels downward; this calculation allows to compute the correct flow splitting between the internal and bypass channels.

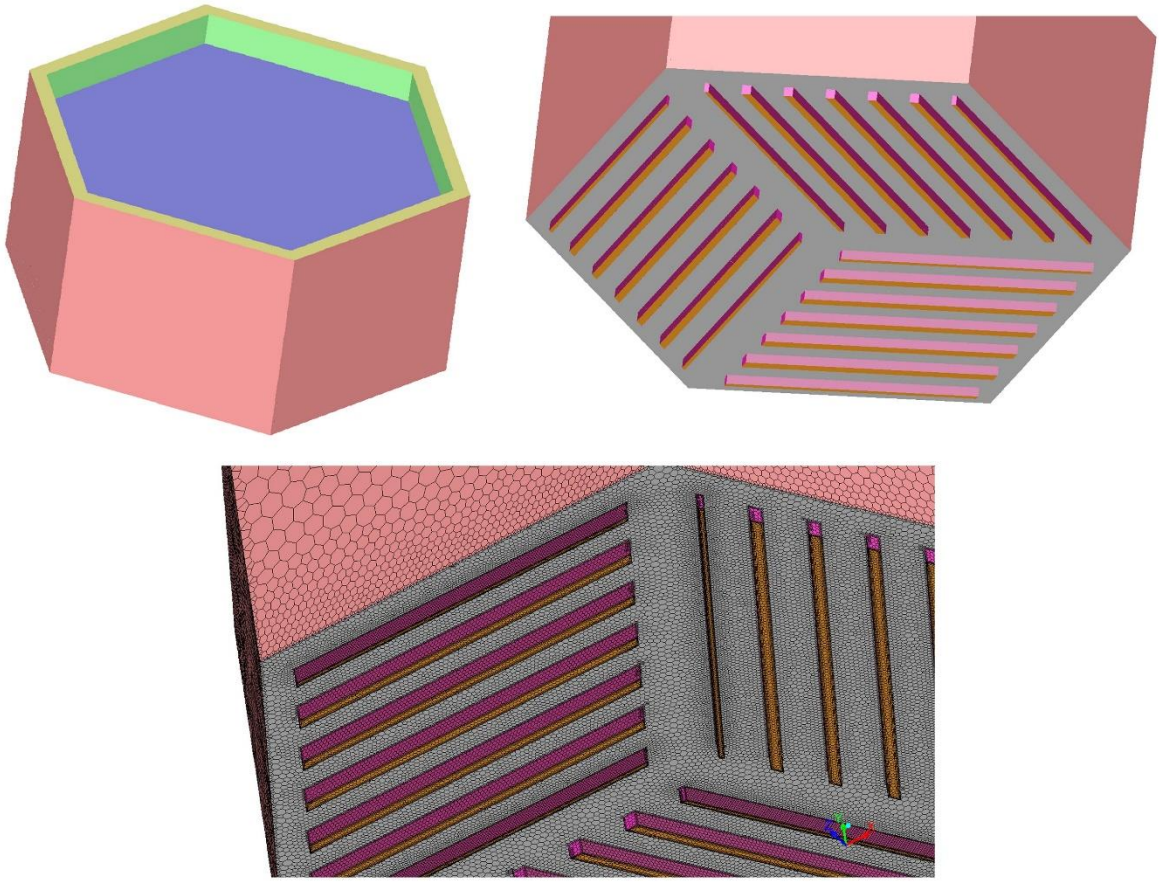

Figure 2-16. Fluid volume details and mesh [the solid geometry represents the fluid volume between the lower support plate and the lower face of the assembly]

2.4.2. Assembly extraction simulations

Assembly extraction simulations have been conducted using Fluent CFD simulation software. Figure 2-16 shows the graphical representation of the model. The model includes the entire zone between the upper surface of the lower support plate and the lower face of the extracted assembly, as well as partial modeling of the outlets from the lower plate, the inlets of the assembly and the inlets of the bypass channels. Figure 2-16 shows the model configuration for a specific time step, when the elevation of the assembly in its channel is about 20 cm. Several simulations have been run using different heights to simulate the extraction of the assembly; Figure 2-17 shows the CAD model for various assembly elevations: as the assembly is extracted, the volume of liquid becomes larger. Note that these models have been developed using SolidWorks.

Figure 2-16 also shows details of the mesh used for the simulation. The mesh is finer in proximity of the inlets and outlets of the model and it becomes coarser at internal locations. The final mesh is polyhedral, and it is generated in Fluent solver mode starting from a tetrahedral mesh with boundary layers, that has been previously generated in Fluent meshing mode. Table 2-2 lists the properties of the mesh generation process.

Table 2-2. Mesh size function and mesh properties

Minimum mesh size	0.15	cm
Maximum mesh size	1.5	cm
Growth rate	1.15	-
Number of boundary layers	3	-
Aspect ratio of first layer	8	-

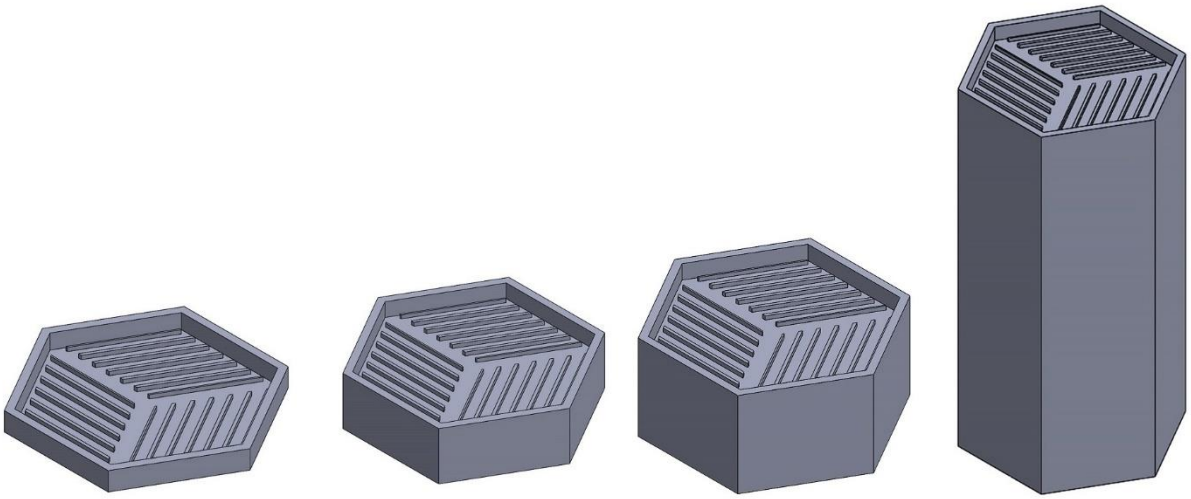

Figure 2-17. CAD model configuration for various time steps. As the time increases, the height changes to simulate the extraction

On the solver side, the k-ε realizable model has been used for turbulence [17], integrated with the enhanced wall treatment for the boundary layer.

UDFs have been used to compute pressure and velocity values for the boundary conditions. The boundary conditions are velocity-inlet for the lower support plate channels and pressure-outlet for the assembly internal channels and the bypass channels. The velocity at the inlets of the lower plate channels is fixed; the pressure at the two outlets is correlated using friction factor correlations presented in section 2.2.1.4, so that the flow in the channels does not need to be modeled in the CFD simulation. In detail, the UDF performs the following operations at the beginning of each iteration:

- The mass flow rate at the outlets of the internal and bypass channels is computed, and the average flow velocity is calculated;
- Using the average flow velocity, the pressure drop along the internal and bypass channels is computed; assuming that the pressure change along a path that flows through the bypass channel is the same as the pressure drop along a path that flows through an internal channel, the pressure difference between the two outlets is computed;
- The pressure at the outlet of the bypass channel is fixed at 0 Pa; the UDF computes the pressure at the outlet of the internal channels by summing the pressure at the outlet of the

bypass channel and the difference computed at the previous step; the UDF updates the pressure value for the boundary condition at the outlet of the internal channels.

This sequence of operations is performed at each iteration until a steady converged solution is obtained. Figure 2-18 shows the typical flow configuration in the channel of the extracted assembly at an elevation of 20 cm. The figure shows the pathlines colored by velocity magnitude. The pattern of the inlet channels is clearly visible, and we can notice that most of the fluid prefers to flow through the bypass channel for this specific elevation of the assembly.

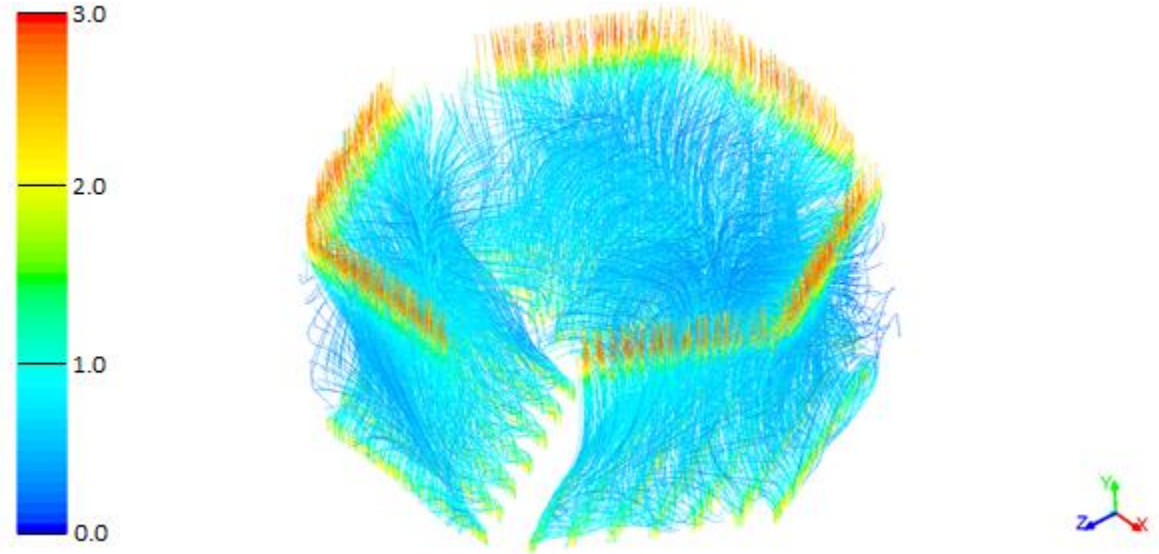

Figure 2-18. Pathlines colored by velocity magnitude [m/s]

2.4.3. Mass flow rate in the channel during assembly extraction

The CFD model presented in the previous section has been used to compute the mass flow rate behavior in time during the assembly extraction.

In order to compute the mass flow rate through the channel, a correlation that characterized the behavior of the flow in the channel of the removed assembly has been developed. This correlation has two input parameters, the elevation of the assembly and the total mass flow rate through the channel, and two output parameters, the pressure drop across the channel of the removed assembly and the fraction of total channel flow that flows through the bypass channels (complementary of the flow through the internal channels). This correlation is coupled to the rest of the core, that can be modeled by a single simple friction correlation, or, more in general, by a more complex RELAP5 system model. The coupling assumes that the total mass flow rate through the core is fixed by design at about 28000 kg/s and that the flow splits between channel and rest of the core in such a way that the pressure drops across the channel of the removed assembly and the rest of the core are the same. In other words, once the correlation is available, the fraction of flow that flows through the channel of the removed assembly is adjusted until the pressure drop through the channel of the removed assembly is equal to the pressure drop through the rest of the core. This calculation is performed iteratively, using the Excel solver, until the two pressure drops match and it is performed for several fuel assembly elevations, in order to fully characterize the mass flow rate through the channel of the removed assembly as a function of the elevation of the extracted element. Note that this approach does not account for the specific radial or azimuthal location of the assembly with respect to the core horizontal cross section.

The correlation that relates the total mass flow rate and the elevation to the pressure drop and the bypass mass flow rate has been developed by selecting specific values for the elevation, ranging from 2 mm (slightly lifted assembly) to 5.8 m (almost fully extracted assembly), and total channel flow rate, ranging from 110 kg/s (nominal flow) to 500 kg/s (expected upper bound on mass flow rate through the channel with assembly not completely extracted).

Table 2-3 and Table 2-4 show the gap friction pressure drop and the bypass channel mass flow rate, respectively, as a function of the total channel mass flow rate (horizontal) and the assembly elevation (vertical); a CFD simulation has been run for each couple of data points and the values of bypass flow rate and gap friction pressure drop have been recorded. Note that the gap pressure

drop is the friction pressure drop between the outlet of the channels in the lower support plate and the inlet of the bypass channels. These data have been processed in Excel and a Visual Basic function [Appendix 7.3] has been written, that computes the overall channel friction pressure drop from the inlets of the lower support plate channels to the top of the core (outlets of the bypass channels). The results of this calculation are presented in Table 2-5; the table shows the overall channel friction pressure drop as a function of the total channel mass flow rate and the assembly elevation. The colors of the table highlight the cells where the channel pressure drop is higher (red) or lower (green) than 60,000 Pa, which is a rough estimate of the expected core friction pressure drop for the AHTR core. This value remains meaningful for the online refueling transient, because the flow perturbation introduced by the extraction of one assembly has a limited effect on the average flow and friction pressure drop on the other assemblies.

Table 2-3. Gap friction pressure drop [Pa] as function of channel mass flow rate and assembly elevation

		Mass flow rate [kg/s]						
		110.65	120	150	200	300	400	500
Elevation [m]	0.002	41827.0	48063.0	70484.0	116993.0	-	-	-
	0.005	21415.0	24748.0	36760.0	61690.0	127236.0	-	-
	0.010	10068.0	11701.0	17499.0	29324.0	61311.0	105166.0	-
	0.050	3590.0	4234.0	6469.0	11544.0	26155.0	45454.0	-
	0.070	3133.0	3631.0	5572.0	10028.0	23092.0	41123.0	-
	0.100	2928.0	3381.0	5073.0	8611.0	18966.0	35863.0	-
	0.200	2417.0	2904.0	4389.0	7815.0	16174.0	27880.0	-
	1.000	2340.0	2732.0	4277.0	7282.0	15635.0	26968.0	-
	3.000	2667.0	3153.0	4990.0	8781.0	18900.0	31852.0	-
	5.000	3168.0	3714.0	5937.0	10563.0	22789.0	39116.0	59166.0
	5.800	3480.0	4072.0	6373.0	11355.0	24612.0	42098.0	64195.0

Table 2-4. Bypass channel mass flow rate [kg/s] as function of channel mass flow rate and assembly elevation

		Mass flow rate [kg/s]						
		110.65	120	150	200	300	400	500
Elevation [m]	0.002	26.47	28.38	34.41	44.42	-	-	-
	0.005	48.88	52.46	63.80	82.75	120.14	-	-
	0.010	62.66	67.51	82.55	104.95	157.00	205.68	-
	0.050	70.20	76.55	95.94	126.17	184.89	243.73	-
	0.070	70.29	76.77	96.47	127.13	186.67	246.04	-
	0.100	72.10	78.53	98.63	129.80	190.52	249.99	-
	0.200	72.92	79.30	99.80	130.94	192.76	254.24	-
	1.000	74.54	81.13	102.11	134.60	197.72	260.72	-
	3.000	78.59	85.40	107.01	142.27	208.76	275.46	-
	5.000	84.25	91.25	114.05	152.58	223.86	294.94	365.68
	5.800	87.68	94.40	117.60	157.06	231.76	305.28	378.44

Table 2-5. Channel friction pressure drop [Pa] as function of channel mass flow rate and assembly elevation

		Mass flow rate [kg/s]						
		110.65	120	150	200	300	400	500
Elevation [m]	0.002	47188.43	54161.35	79218.65	131053.82	-	-	-
	0.005	29720.62	34177.71	50199.85	83249.05	170104.71	-	-
	0.010	20803.47	23939.58	35036.22	56825.84	117897.63	198800.49	-
	0.050	15798.84	18363.20	27356.73	45665.44	94911.69	160269.89	-
	0.070	15333.64	17778.23	26556.64	44401.31	92544.82	157094.10	-
	0.100	15469.94	17879.13	26576.33	43787.65	90037.20	153872.12	-
	0.200	14989.89	17411.30	25965.39	42981.77	87514.59	147164.75	-
	1.000	14056.52	16264.07	24402.31	40299.68	82496.47	138791.44	-
	3.000	11863.28	13749.12	20651.20	34746.58	71554.54	120101.93	-
	5.000	9355.82	10816.24	16381.81	27929.53	58152.71	98411.93	148212.53
	5.800	8253.22	9533.96	14372.37	24584.62	51696.54	87565.93	132531.48

The data from Table 2-5 have been further analyzed in order to determine an analytical correlation for the calculation of the mass flow rate through the assembly channel. At each elevation, the dependence of the pressure drop on the mass flow rate has been interpolated (represented) using the following power function:

$$\Delta P = A * mflow^{B} \quad (5)$$

Where ΔP is the channel pressure drop, mflow is the channel mass flow rate, A is the interpolation coefficient and B is the interpolation exponent. This interpolation function shape is very accurate, providing a R^2 coefficient value very close to 1 for all elevations.

Equations (5), (6) and (7) provide a full analytical correlation between the total channel flow rate, the elevation and the channel friction pressure drop.

Table 2-6 shows the power interpolation coefficient and exponent as a function of the elevation of the extracted assembly.

An analytical fit for the two columns of Table 2-6 has been developed. The parameters of the fitting functions have been determined using the fitting tool app provided by MATLAB. This application allows to input a specific functional form and calculate the optimized parameters that best fit the data, according to available built-in algorithms [23].

The fit function for the coefficient A as a function of the elevation E is shown in equation (6) and the parameters for the interpolation are given in Table 2-7. This fit results in a R^2 value equal to 0.9999. Note that the functional form shown in equation (6) is a blend between a power function for small elevations and a linear function for larger elevations, and the term that includes the hyperbolic tangent serves as a blending function. Figure 2-19 provides a graphical representation of the interpolation function for the coefficient A, and highlights the power and linear functional behaviors for low and high elevations, respectively.

$$A(E) = (a * E^{-b} + c) + \frac{\left(1 + \tanh\left(f * (E - g)\right)\right)}{2} * \left(d * E + e - (a * E^{-b} + c)\right) \quad (6)$$

Similarly, an interpolation function has been developed for the exponent B as a function of the elevation E, using the following functional form:

$$B(E) = (a * E^2 + b * E + C) + \frac{\left(1 + \tanh\left(h * (E - k)\right)\right)}{2} * \left(d * E^2 + e * E + f - (a * E^2 + b * E + C)\right) \quad (7)$$

The parameters for equation (7) are given in Table 2-7; the R^2 value for this interpolation is 0.9848. A graphical representation of the interpolated exponent B as a function of the elevation is shown in Figure 2-20. In this case, the interpolation function is a blend of two parabolic functions (one for low and one for high elevation) and the blending function is still based on the hyperbolic tangent.

Equations (5), (6) and (7) provide a full analytical correlation between the total channel flow rate, the elevation and the channel friction pressure drop.

Table 2-6. Power interpolation coefficients as function of elevation

Elevation [m]	A	B
0.002	14.011	1.7253
0.005	7.8611	1.7496
0.010	5.4012	1.7524
0.050	3.3201	1.7994
0.070	3.0969	1.8074
0.100	3.5457	1.7802
0.200	3.6117	1.7711
1.000	3.2879	1.7772
3.000	2.4903	1.8001
5.000	1.6834	1.8324
5.800	1.4209	1.8410

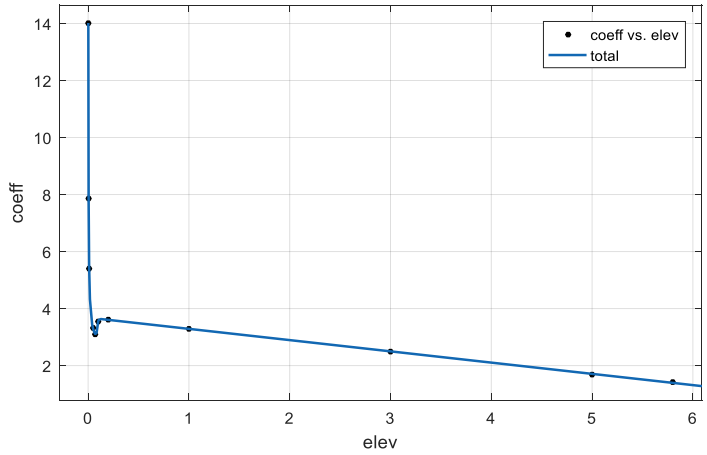

Figure 2-19. Power interpolation coefficient A as function of elevation of the extracted assembly

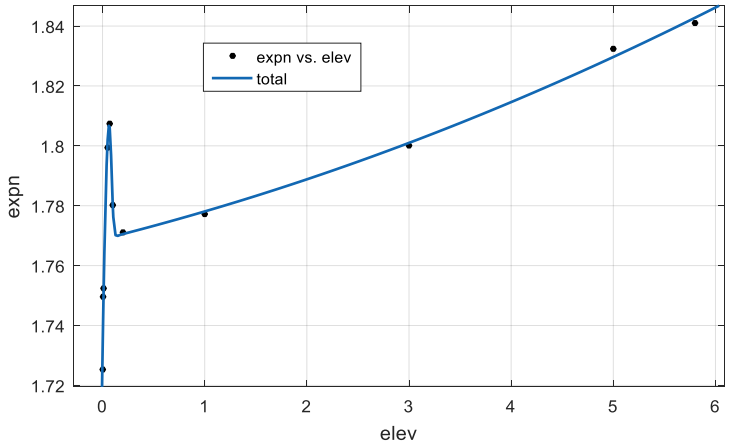

Figure 2-20. Power interpolation exponent B as function of elevation of the extracted assembly

Table 2-7. Parameters for interpolation functions of coefficient A and exponent B

Parameter	a	b	c	d	e	f	g	h	k
Coefficient A	0.05843	0.8497	2.541	-0.3947	3.683	100	0.09107	-	-
Exponent B	-14.11	2.159	1.73	0.000724	0.008554	1.769	-	44.15	0.09

CFD analyses have also been conducted to determine the behavior of the channel when the assembly has been completely extracted from the core. The modeling is analogous to the approach described in section 2.4.1, except that in this case there is no assembly in the channel, as well as no need to model bypass and internal flow. Figure 2-21 shows the calculated friction pressure drop

along the channel as a function of the channel mass flow rate. The functional dependence can be described by the following parabolic function:

$$\Delta P = 0.1396 * mflow^2 + 20.271 * mflow - 521.86 \quad (8)$$

The R^2 for this fitting is approximately 1.

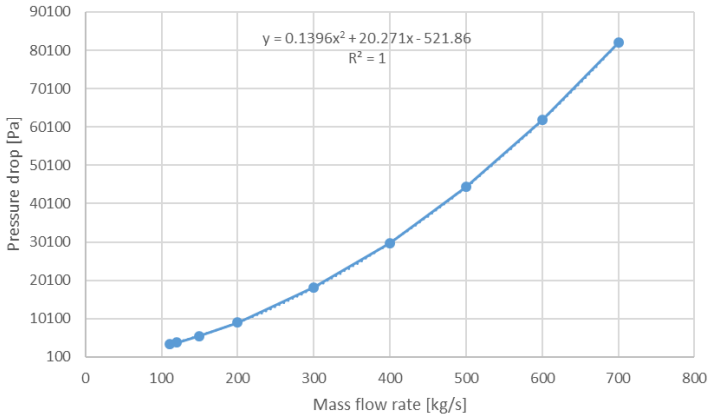

Figure 2-21. Friction pressure drop in the free channel as function of mass flow rate

Equations (5) and (8) have been used to compute the mass flow rate in the channel of the removed assembly as a function of the assembly elevation. This calculation has been performed for a set of selected values of elevation, using the Excel Solver to match the pressure drop across the core and the channel. In other words, the Excel solver adjusts the mass flow rate through the channel and, as a consequence, the mass flow rate through the rest of the core in order to minimize the difference between the friction pressure drops of the core and the channel of the assembly that is being extracted.

Figure 2-22 shows the resulting mass flow rate as function of elevation. This figure only shows the solution for flow when the element is at least partly inserted in the channel. The flow rate strongly increases from 110 to 270 kg/s during the initial 20 cm lifting, then the slope of the curve decreases, but the mass flow keeps increasing up to 360 kg/s. A strong increase also happens when the assembly is extracted from the channel, bringing the flow rate through the channel to about 620 kg/s.

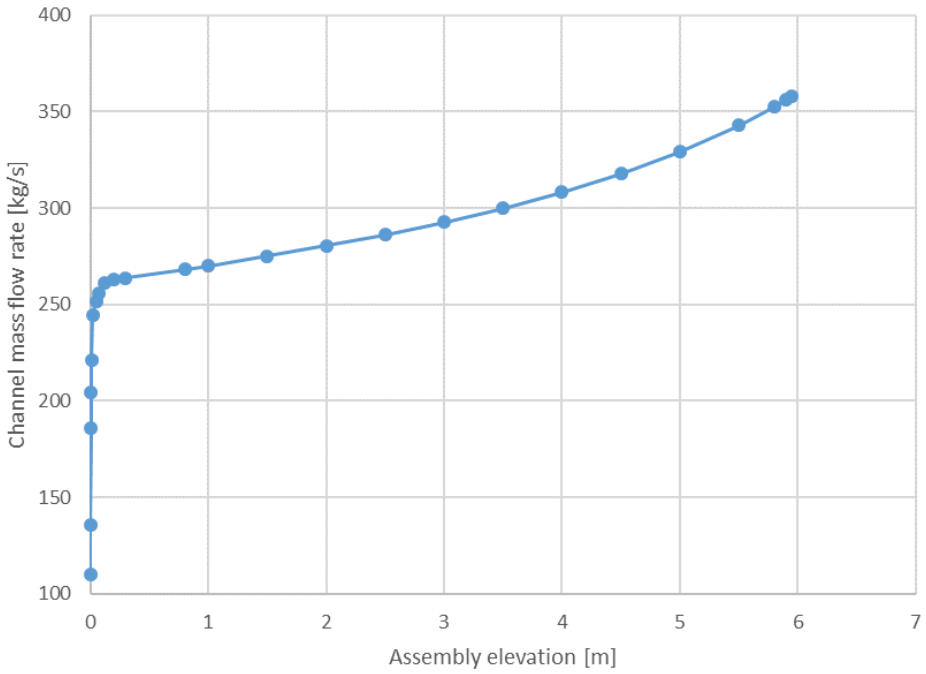

Figure 2-22. Channel mass flow rate as function of assembly elevation

2.5. Flow characteristics in the lower plenum

In order to simulate the behavior of the system in reaction to the extraction of the assembly, the results from the study on the mass flow rate in the channel as function of elevation or time have been used to model the flow in the lower plenum of the reactor.

Specifically, the mass flow rate and fluid conditions calculated from the work on the flow in the channel of the extracted assembly have been used as boundary conditions for the simulation of the evolution of the thermal hydraulic system during the removal of the assembly.

The simulation of the flow distribution in the lower plenum provided information on the behavior of the system in response to the increase of the mass flow rate in the channel of the removed assembly and the slight decrease of mass flow in the remaining assemblies.

The objective of the work is to demonstrate the limited effect of removing an assembly when the reactor is on-power and assess the feasibility of the online refueling.

This analysis has been developed in two subsections; the first section has been devoted to the development of the methodology using a version of the model that is smaller (smaller radius and lower number of assemblies) than the reference configuration; the second section has been devoted

to the application of the methodology developed in the first section to the simulation of the full lower plenum problem. Figure 2-23 shows the CAD models for the simplified (small) version of the AHTR lower plenum, using reduced dimensions and number of assemblies (36), and for the full version.

The reason for the use of this approach is the large amount of computational resources required for the solution of the full problem, making the development of the analysis approach on the smaller version of the problem necessary; in particular, some difficulties have been encountered in the graphical post-processing of the results from the full problem.

This section presents the smaller and full versions of the problem in an integrated manner, because many features are common to both, but the main differences will be highlighted as well.

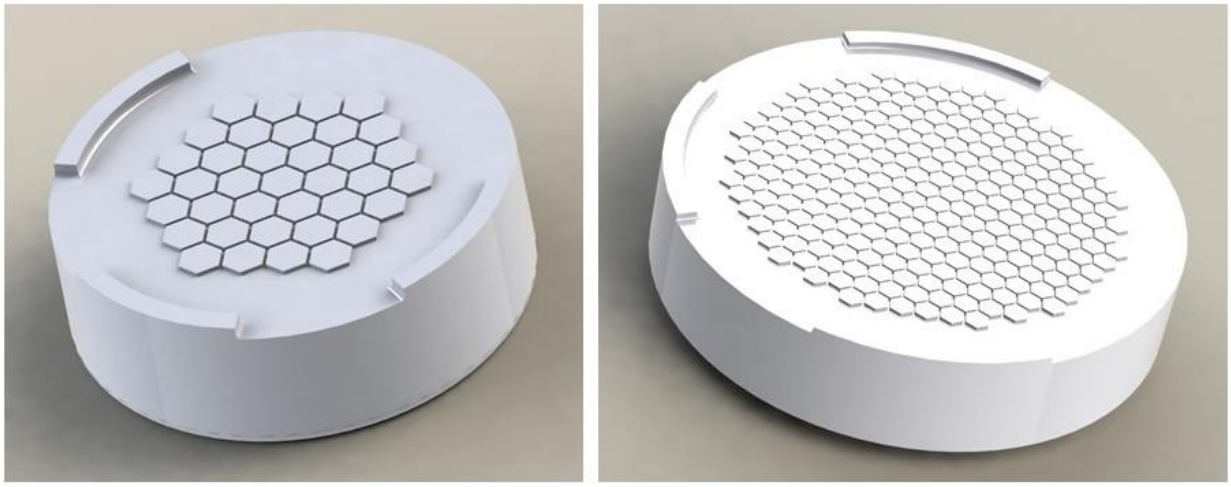

Figure 2-23. Lower plenum CAD models: reduced (37 assemblies) and full version (253 assemblies)

2.5.1. Flow distribution in the lower plenum: modeling approach and steady solution

Figure 2-23 shows the CAD models used for the simulation of the reduced and full problem. The figure shows the fluid volume being modeled and illustrates its boundaries. The inlets are represented by three partial downcomer sections where the coolant flows downward into the lower plenum; the outlets are partially modeled hexagonal assembly cross sections and all other surfaces are walls. Note that a full representation of the 21 internal assembly channels is not practical because it would make the mesh excessively large.

The mesh presented in Figure 2-24 has been used for the modeling of the flow in the lower plenum. The small and full versions of the problem both present similar meshing characteristics. Automatic tetrahedral mesh generation has been used in Fluent meshing mode, and it has been converted to polyhedral mesh in Fluent solver mode, in order to facilitate the convergence of the simulations.

Table 2-8 shows the characteristics of the mesh generated for the two versions of the problem; the size functions and the treatment of the wall boundary conditions is equivalent in both versions. Regarding the final mesh dimensions, the reduced problem mesh size is on the order of one million cells and the full problem is about five times larger (5 million cells); a factor of 5 is also present in the mesh memory usage, which is about 11 GB for the full version. Runtime is on the order of tens of minutes for a steady state calculation, and few hours for transient simulations.

Table 2-8. Mesh characteristics

Property	Reduced problem	Full problem	Units
Minimum mesh size	0.5	0.5	cm
Maximum mesh size	4.0	4.0	cm
Growth rate	1.15	1.15	-
Number of boundary layers	3	3	-
Aspect ratio of first layer	10	10	-
Mesh size	904749	5085520	#cells
Minimum orthogonal quality	0.161	0.108	-
Maximum aspect ratio	24.34	35.34	-
Mesh memory usage	1797	10731	MB

The turbulence model selected for the simulations is k-ε realizable and enhanced wall treatment is used for the wall boundary conditions; the convergence criterion for the residuals is 10-3 for all equations and no energy equation is solved since the temperature in the lower plenum, for this specific condition, is uniform and equal to 650°C.

Table 2-9 shows the configuration for the Fluent simulations run in parallel. The reduced problem has been run on 2 nodes and 16 parallel processes, resulting in 63000 cells per core; regarding the full version of the problem, the parallel simulation involved 5 nodes and 40 processes, resulting in about 129000 cells per core. Note that the cell density of the full problem is appropriate for the resources available, but the postprocessing has been relatively challenging due to the overall large dimension of the problem.

The simulation has been run in three steps:

1. Initial steady state simulation to obtain preliminary initial conditions (about 1000 iterations);
2. Intermediate transient simulation to further improve the initial conditions (few tens of seconds);
3. Transient simulation to simulate the flow change during the on-line refueling.

This section will present the results for the steady state conditions and the following section will illustrate some considerations on the transient simulation.

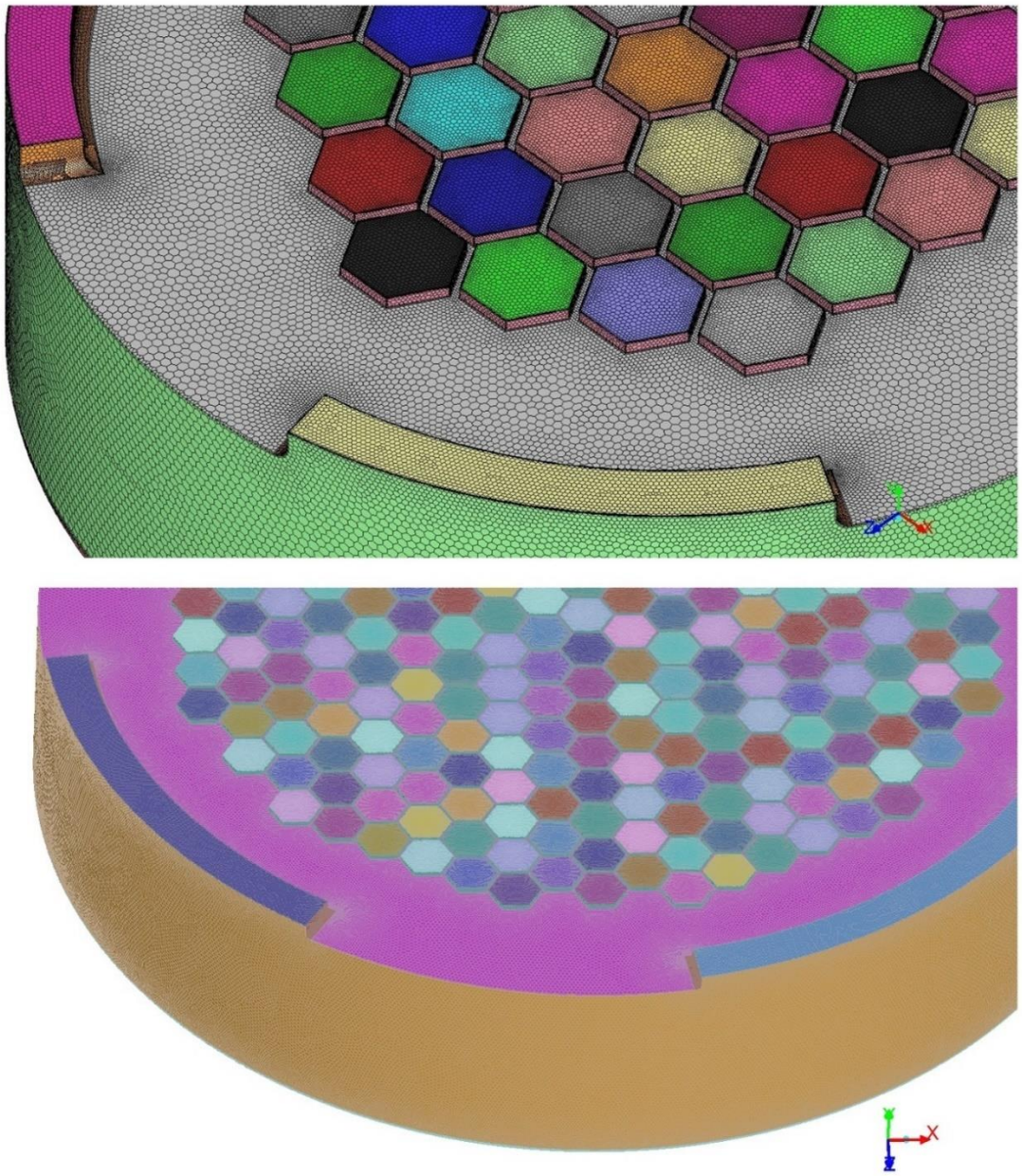

Figure 2-24. Mesh for small version (top) and full version (bottom) of the lower plenum model

Table 2-9. Simulation characteristics

Property	Reduced problem	Full problem	Units
Number of nodes	2	5	-
Number of processes	16	40	-
Mesh partitioning	63000	129000	cells/node

The inlet mass flow rate of the model is fixed by design and it is equal to the nominal mass flow rate of a single assembly multiplied by the number of assemblies included in the model; the mass flow rate is about 4000 kg/s for the reduced model and 28000 kg/s for the full model. The mass flow rate and the cross-sectional area of the downcomer region allow the calculation of the inlet downward velocity, which is 1.343 m/s and 2.753 m/s for the reduced and full model, respectively. With respect to the outlets (hexagonal faces of the assemblies), a pressure-outlet boundary condition has been implemented, with the target-mass-flow-rate option activated. This option allows the specification of a target flow rate value for a given boundary, that facilitates the convergence to the desired boundary flow distribution; for the steady state simulation the target mass flow rate is constant and equal to the average assembly mass flow rate, about 110 kg/s.

Figure 2-25 shows the velocity vector streamlines colored by velocity magnitude. The peak velocity is located in the downcomer section and large recirculation zones develop between consecutive downcomer sections as well as between each downcomer section and the inlets of the external ring of assemblies.

The flow distribution is compartmentalized in three regions, corresponding to the three downcomer sections; as a consequence, if, for example, the inlet temperature of one of the three downcomer sections decreases, due to a change of heat transfer capacity at the primary heat exchanger level, only one third of the assemblies (the ones closest to the specific downcomer section) will see a lower temperature, while the others will remain at nominal coolant temperature (at least for a few tens of seconds). Note that the model used for these calculation does not account for any flow mixing devices in the lower plenum, because the available preliminary design documents do not provide enough information.

Figure 2-26 shows the velocity vector streamlines from different perspectives (back and bottom view). The bottom view picture highlights that the flow in the lower plenum is clearly divided in three volumetric zones, one for each downcomer section. These three zones are not symmetric, because of the positioning of the downcomer inlets: the downcomer region is divided into 8 angular sections, of which 3 are the actual downcomer, 3 are DRACS heat exchanger regions, 1 is for the maintenance heat removal system and 1 is dedicated to the refueling lobe. The DRACS and maintenance areas are smaller, while the downcomer and refueling lobes are larger and positioned at 90° angular spacing, resulting in two downcomer sections facing one another and the remaining

downcomer section facing the refueling lobe. This geometrical configuration results in the flow configuration presented in Figure 2-26 and explains the asymmetry in the flow distribution.

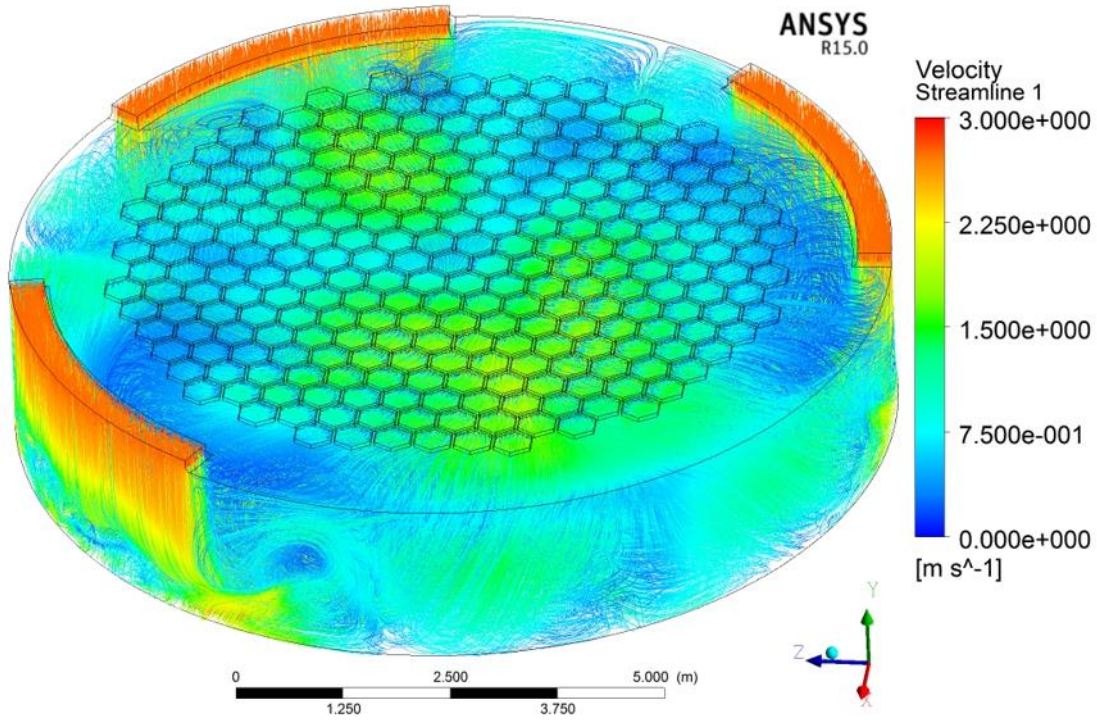

Figure 2-25. Lower plenum velocity streamlines colored by velocity magnitude (front view)

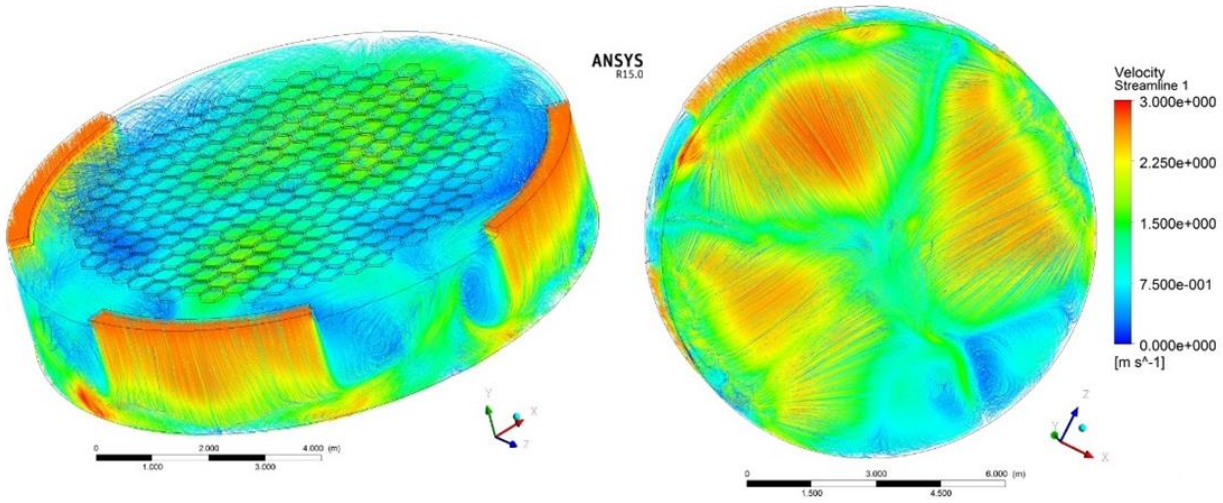

Figure 2-26. Lower plenum velocity streamline colored by velocity magnitude (back and bottom view)

2.5.2. Time-dependent flow distribution in the lower plenum

The results from the steady state simulation have been used as initial condition for the transient simulation of the assembly extraction. The structure of the simulation for the transient conditions remains mostly unchanged, except for a modification of the outlet boundary conditions that allows to account for the flow distribution variation caused by the assembly extraction.

The same pressure-outlet boundary condition as for the steady simulation has been implemented, with the target-mass-flow-rate option activated. However, the target mass flow rate is now computed from the results of section 2.4.3, for the channel of the extracted assembly, as well as the remaining channels.

In order to perform this calculation, a UDF has been developed in C, that computes the mass flow rate for each channel and sets the parameters of the outlet boundary conditions at every iteration. This UDF performs the calculation based on the following approach:

- The lifting velocity of the removed assembly is determined by the functional behavior shown in Figure 2-27 (blue line). The velocity increases from zero to a nominal value that is set by the operator, and then completes the extraction at a constant velocity. Note that a gradual increase in the lifting velocity helps to mitigate the sudden mass flow rate increase in the initial moments of the transient;
- As a consequence of this, the elevation of the assembly increases initially with a parabolic behavior, which becomes linear once the lifting velocity becomes constant. This behavior is illustrated in Figure 2-27 (orange line);
- The calculation of the elevation of the extracted assembly allows the calculation of the mass flow rate through the channel using the correlation developed in section 2.4.3;
- Once the mass flow rate through the channel of the extracted assembly is known, the mass flow rate through the remaining channels can be computed, since the total core mass flow rate is assumed to remain constant.

The UDF performs these calculations at every iteration and sets the target mass flow rate for each boundary based on this calculation.

Figure 2-28 shows the mass flow rate as a function of time for the channel of the extracted assembly and for the other channels. As previously mentioned, the flow change in the channel of the extracted element is substantial: the mass flow rate is about 6 times larger than the nominal

flow; however, this change has little effect on the average flow in the other channels, because the large increase of a single channel is compensated by a small decrease of the remaining 252 channels.

Note that the time dependence of the removal is directly related to the choice of the extraction velocity of the assembly. The speed chosen in this simulation is about 0.5 m/s, enabling the removal operation to be performed in less than 15s, but it is acceptable to choose a smaller value for the velocity.

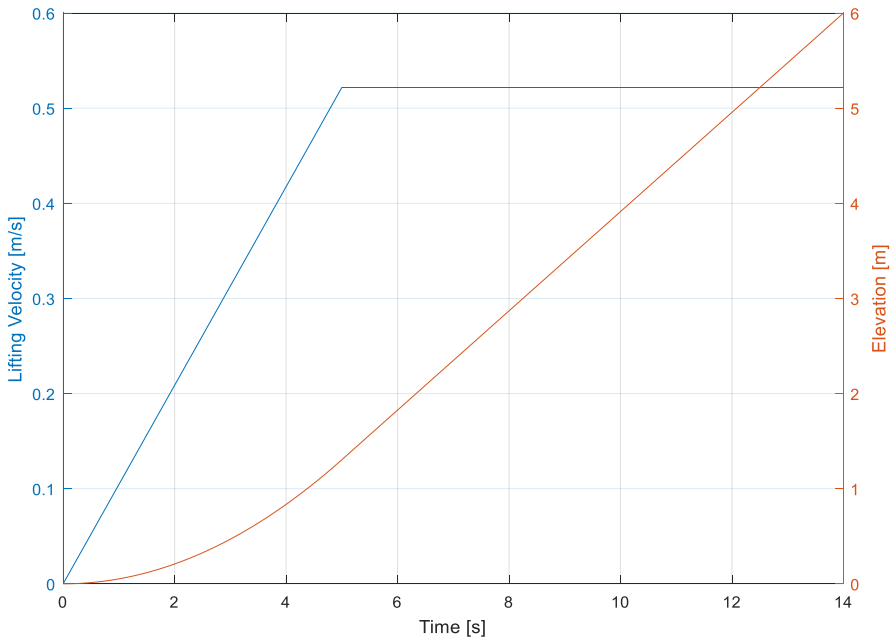

Figure 2-27. Assembly extraction velocity and elevation as function of time

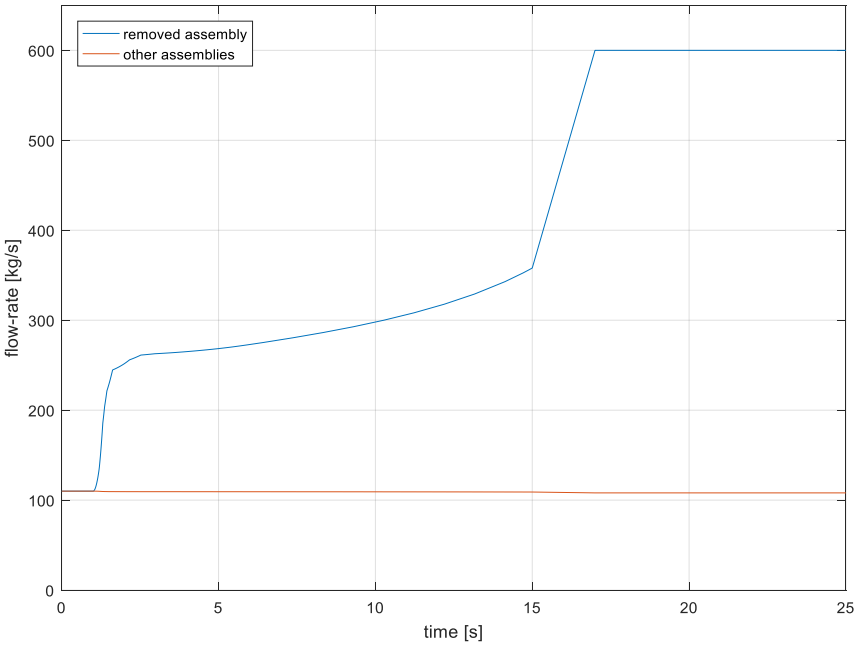

Figure 2-28. Mass flow rate for the channel of the extracted assemblies and for the rest of the channels in the core

The post-processing of the simulation data has been relatively challenging, due to the large dimension of the problem and the limited computational resources available, so graphical results have been generated only for the most significant time steps during the transient.

Figure 2-29 shows the velocity magnitude contours at the beginning (initial condition from the steady state solution) and at the end of the transient (assembly completely extracted). The contours are plotted for specific elevations in the lower plenum. The location of the assembly that is extracted from the core has been chosen randomly; the location for the simulation results presented in Figure 2-29 is at the 4th radial ring in front of the refueling lobe (red assembly in the lower right frame of Figure 2-29).

The extraction of the assembly at the specified location has little effect on the flow distribution in the lower plenum. For locations far from the lower support plate in the axial direction, the flow distribution is only slightly affected, and visible effects can only be detected for locations closer to the support plate, as illustrated in the two rightmost frames of Figure 2-29. The flow distribution at the inlets is uniform at the beginning of the transient, and it is perturbed at the end, in proximity of the removed assembly at distances less than few tens of cm from its inlet.

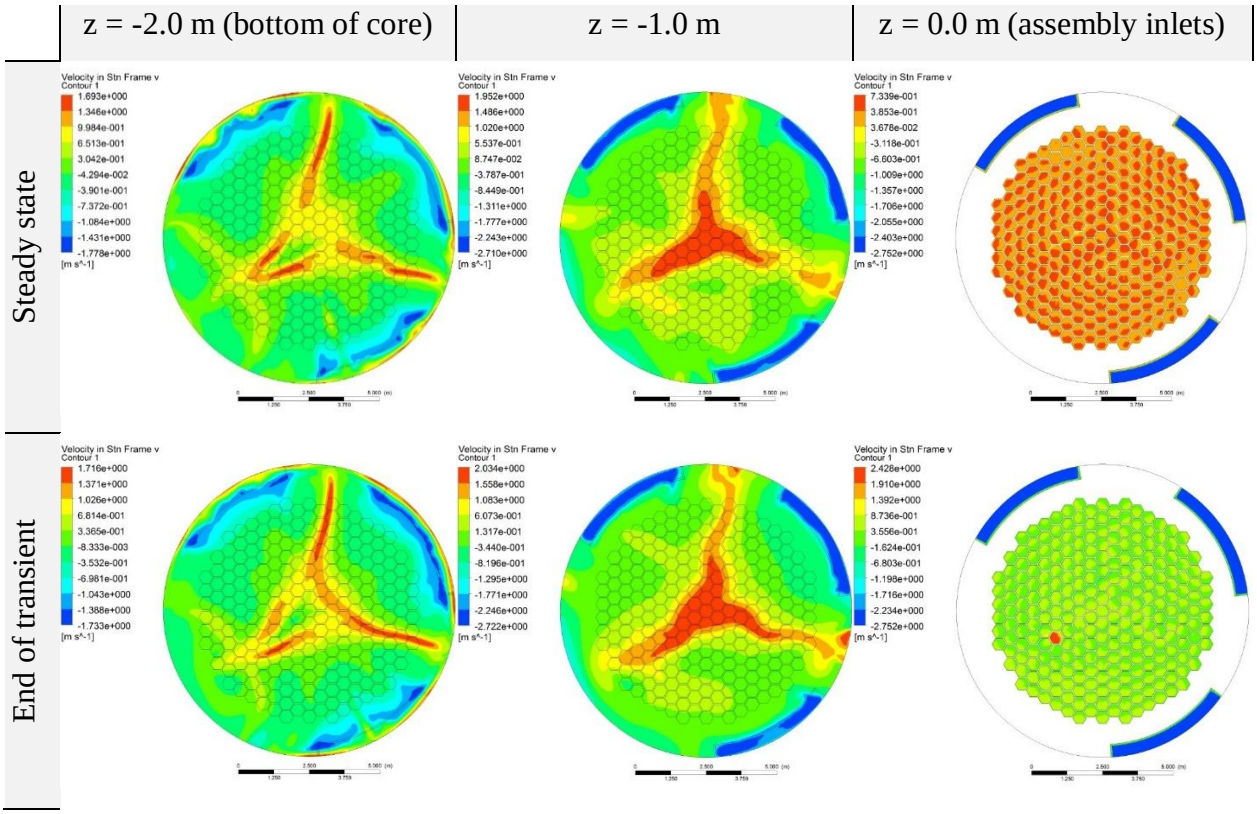

Figure 2-29. Horizontal velocity magnitude contours at different elevations before and after the assembly extraction

2.6. Flow characteristics in the upper plenum

The flow in the upper plenum has been simulated incorporating the results of analysis of the flow in the channel of the extracted assembly (Section 2.3.4), using it to compute the parameters for the inlet boundary conditions (fluid velocity normal to the boundary).

The simulation of the flow in the upper plenum has been developed to characterize the response of the flow and temperature distribution when the assembly is extracted from the core, and, ultimately, that this procedure is safe and can be performed without compromising the integrity of the reactor.

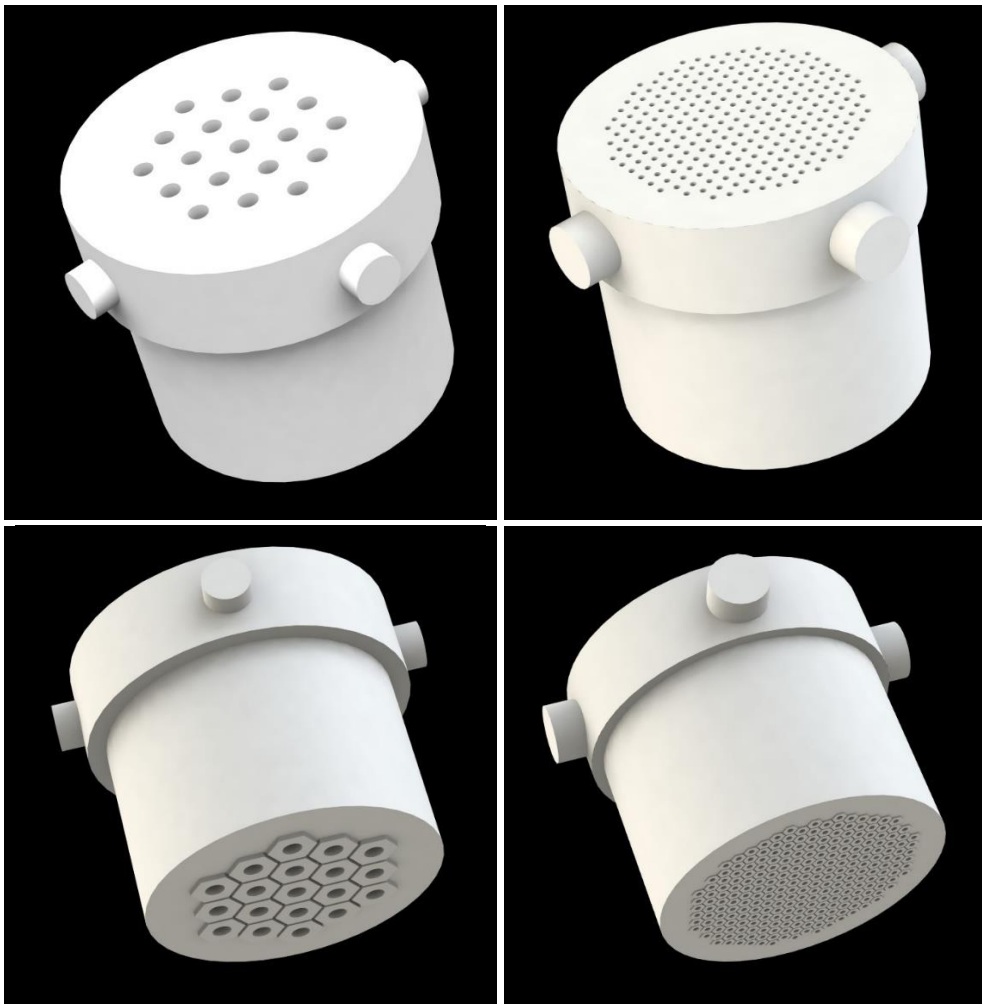

Figure 2-30. Upper plenum CAD models: reduced (19 assemblies, left) and full version (253 assemblies, right)

Similarly to the lower plenum case, the upper plenum analysis has been performed in two steps: the first step has been devoted to the development of the analysis methodology for a reduced version of the problem, comprised of 19 fuel assemblies and illustrated in the two left frames of Figure 2-30; the second step consisted of the application of the methodology to the full version of the problem, which is illustrated in the two right frames of Figure 2-30.
The reason for this approach is again the large computational requirements posed by the full version of the problem, which in this case, due to the dimensions of the upper plenum, is substantially larger than the lower plenum case.

2.6.1. Flow distribution in the upper plenum: modeling approach and steady solution

Figure 2-30 shows the CAD models for the simulation of the flow distribution in the upper plenum. The inlets are the hexagonal prismatic faces at the base of the cylinder and the outlets are three horizontal cylinders at the top of the vessel volume, each one associated to a separate heat exchanger loop. The fluid volume is vertically perforated by 253 control rod guide tubes, one for each assembly. Every surface other than the inlets and outlets is modeled as wall boundary condition.
Figure 2-31 shows the mesh for the upper plenum model, which is equivalent for both reduced and full problem version, except for the overall dimension:

- The two left frames show a detail at the upper support plate, where the assembly outlets are located;
- The top-right frame shows a detail at the upper plenum outlets;
- The bottom-right frame shows the mesh partitioning calculated by Fluent for parallel computation (white lines are boundaries of partitions on the surface of the model).

Automatic tetrahedral mesh generation has been performed in Fluent meshing mode, and the obtained mesh has been converted to polyhedral in Fluent solver mode.
Table 2-10 shows the mesh characteristics; the size functions are identical for both versions of the problem, as well as the properties of the boundary layers. The dimension of the mesh is 1.5 GB (less than 1 million cells) for the reduced problem and 42 GB (about 25 million cells) for the full problem; this number gives an indication of the computational power that is required to analyze

the problem and to post-process the results. The computational time is on the order of tens of minutes for a steady state solution and few hours for a transient solution.

Table 2-10. Mesh characteristics

Property	Reduced problem	Full problem	Units
Minimum mesh size	1.0	1.0	cm
Maximum mesh size	7.0	7.0	cm
Growth rate	1.08	1.08	-
Number of boundary layers	3	3	-
Aspect ratio of first layer	10	10	-
Mesh size	841767	25104557	#cells
Minimum orthogonal quality	0.167	0.164	-
Maximum aspect ratio	25.71	24.99	-
Mesh memory usage	1504	42112	MB

The turbulence model selected for the simulations is k-ε realizable and enhanced wall treatment is used for the wall boundary conditions; the convergence criterion for the residuals is 10^{-3} for all equations and 10^{-6} for the energy equation.

Table 2-11 the configuration for the Fluent simulations run in parallel. The reduced problem has been run on 3 nodes and 24 processors, allocating 37000 cells per node; the full version has been run on 14 nodes and 112 parallel processes for an average cell partitioning of 233000 cells per node. Note that the order of magnitude for an appropriate cell partitioning among parallel processes is few hundred thousand cells per core, for cores with 2 GB memory [24].

Similarly to the lower plenum case, the simulation has been run in 3 steps:

1. Initial steady state simulation to obtain preliminary initial conditions (about 1000 iterations);
2. Intermediate transient simulation to further improve the initial conditions (few tens of seconds);
3. Transient simulation to simulate the flow change during the on-line refueling.

The rest of the section will present the steady state results, and the transient results will be shown in the following section.

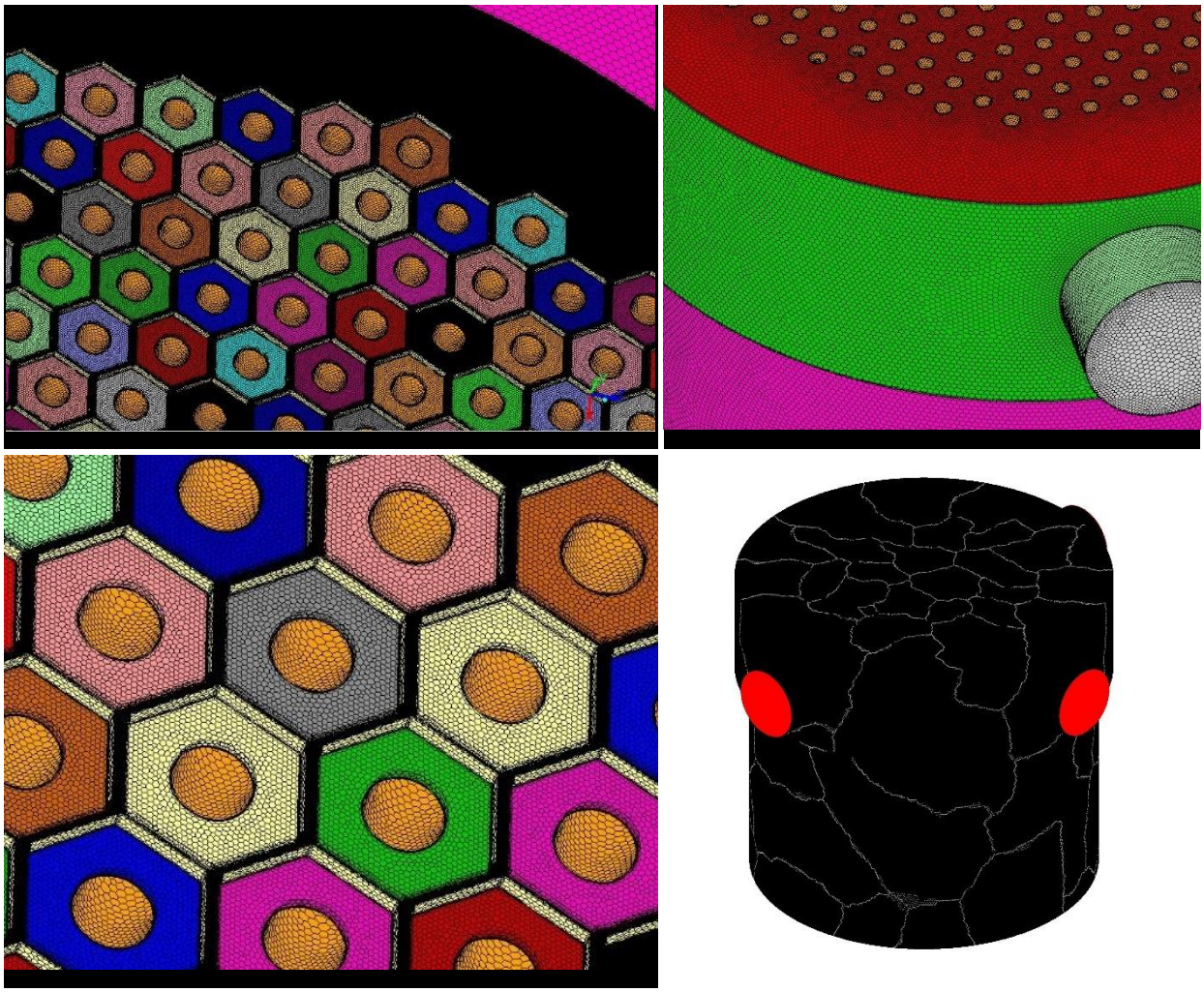

Figure 2-31. Mesh and mesh partitioning (lower-right frame) for the upper plenum model

Table 2-11. Simulation characteristics

Property	Reduced problem	Full problem	Units
Number of nodes	3	14	-
Number of processes	24	112	-
Mesh partitioning	37000	233000	cells/node

In order to compute the steady state solution, a velocity-inlet boundary condition has been modeled at the inlet faces, that are represented by the top hexagonal surfaces of the assembly; a pressure-outlet boundary condition has been selected for the outlets. The velocity at the inlet surfaces is normal to the boundary and it is computed from the mass flow rate, which is about 110 kg/s per assembly, resulting in a total mass flow rate of about 2090 kg/s and 28000 for the reduced and full version, respectively.

Figure 2-32 shows the pathlines colored by velocity magnitude (left frame) and contours of velocity magnitude (right frame) on horizontal planes at 3 axial locations in the upper plenum.

The flow velocity, that is uniformly distributed at the outlets of the assemblies, decreases as a function of the elevation in the upper plenum, due to the increased section area available for flow, and increases at the entrance to the 3 ducts that take the coolant to the respective primary heat exchangers. Note that the simulation assumes that the flow at the outlet of the grappling collar is uniformly distributed over the available surface; in reality the flow distribution at the outlet of the grappling collar is still influenced by the regular distribution pattern of the plates in the assembly. The flow in the upper plenum is compartmentalized in three regions, one for each heat exchanger loop; the presence of control rod guide tubes does not enhance the mixing of the flow. This aspect has a direct consequence on the average temperature of the flow entering the primary heat exchangers on the primary side:

- the assembly is removed at a certain radial and azimuthal location in the core that belongs to one of the three compartmentalized sections. The flow and temperature change due to the extraction of the assembly will then be seen mainly by that specific section and less by the remaining 2 sections;
- the remaining two sections will react to the change in the other section in a complementary way. In other words, if the assembly is extracted at a specific location, the associated primary loop will see a higher flow rate and a lower coolant temperature; the remaining

two sections will instead see a slightly reduced mass flow rate and, if the reactor power remains constant, a higher coolant temperature.

It can be concluded that the assembly extraction compromises the symmetry of the system on a neutronic and thermal standpoint; note also that enhanced flow mixing in the upper plenum is an important aspect for the appropriate functioning of the power loops.

Figure 2-33 shows the pathlines colored by temperature (left) and contours of temperature (right) on horizontal slices at three axial locations in the upper plenum.

The temperature distribution at the outlets of the core has been assumed to follow the parabolic profile presented in Figure 2-34 and described by equation (9):

$$T(r) = T_{min} + (T_{max} - T_{min}) * \left(1 - \left(\frac{r}{r_0}\right)^2\right) \quad (9)$$

Where Tmin=650°C, Tmax=750°C, r is the radial distance from the core axis and r0=8.45m (approximate core radius). Equation (9) is integrated with the Fluent solver using a UDF that computes the inlet temperature for each mesh point on the inlet boundary face surfaces and sets the appropriate parameters in the boundary condition definition.

Figure 2-33 shows the presence of recirculation zones in proximity of the cylindrical wall (barrel), where the fluid remains at low temperature; the planar temperature distribution remains unchanged throughout the upper plenum up to the outlets, where the pathlines bend to enter the primary piping.

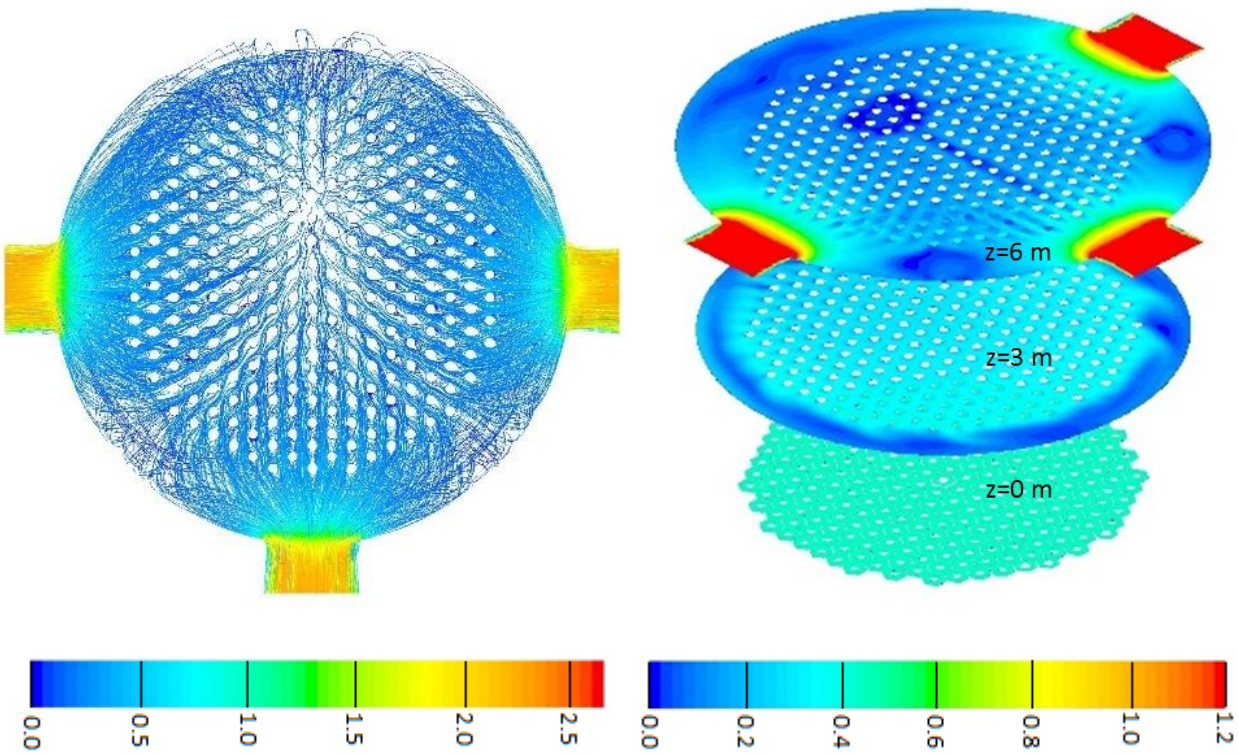

Figure 2-32. Pathlines colored by velocity magnitude (left) and contours of velocity magnitude (right) [m/s]

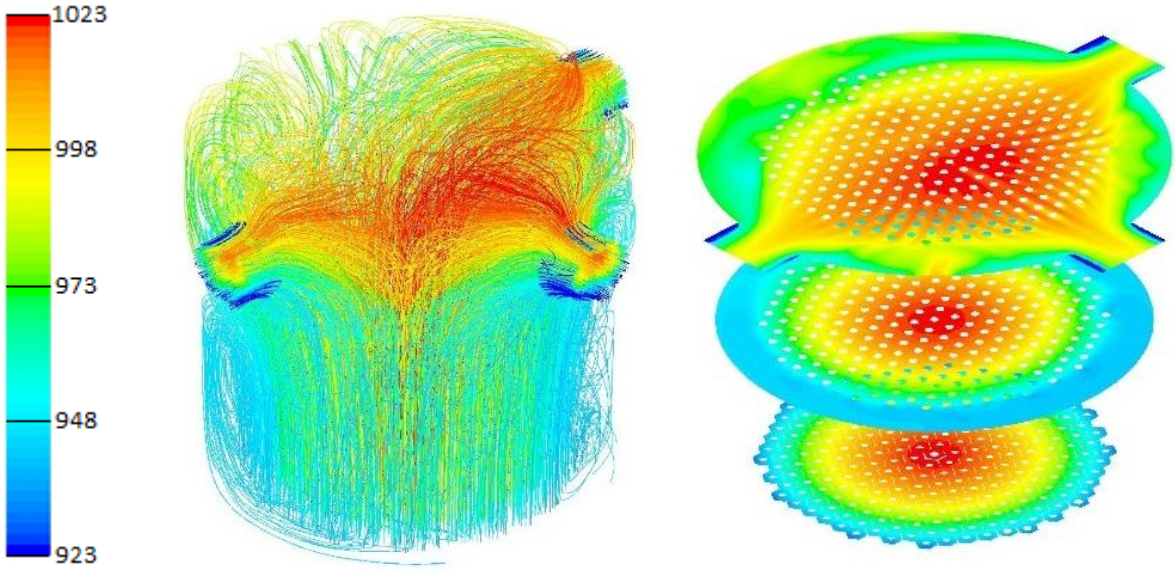

Figure 2-33. Pathlines colored by temperature (left) and contours of temperature (right) [K]

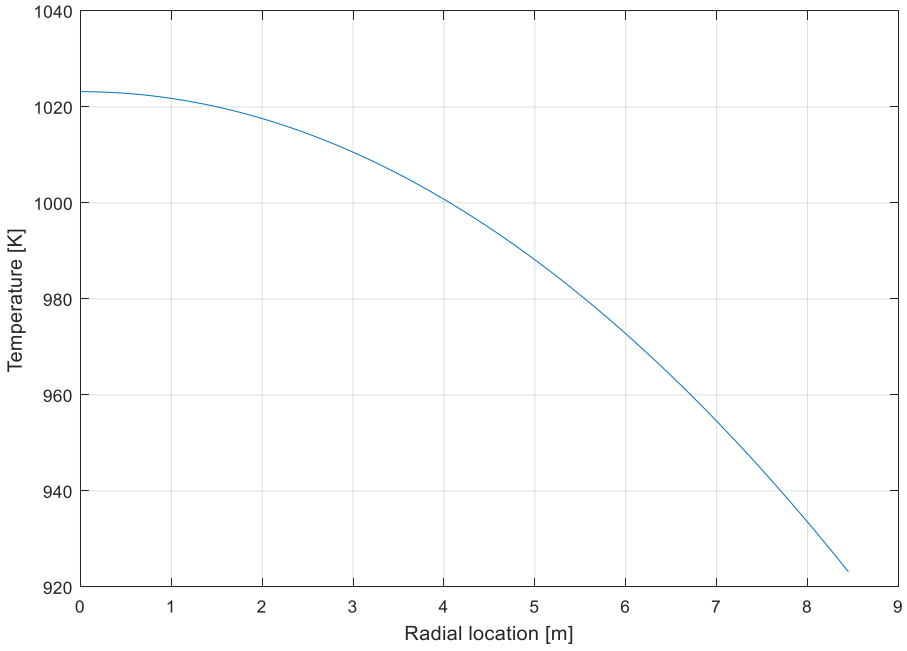

Figure 2-34. Core outlet radial temperature profile

2.6.2. Time-dependent flow distribution in the upper plenum

The transient problem represented by the removal of the assembly has been modeled by increasing the velocity of the flow at the outlet of the channel of the removed assembly according to the calculations performed in section 2.3.4. A more realistic approach would consist of the actual modeling of the motion of the inlet surfaces through the use of the moving/dynamic mesh (MDM) option available in Fluent. This approach has not been used here because of 2 reasons:

- The MDM option requires substantially larger computational capabilities, since the mesh, which is already relatively large (25 million cells), would have to be recalculated at every time step;
- The MDM option requires tetrahedral meshing; it is not compatible with the polyhedral mesh developed for the upper plenum. Reverting the polyhedral mesh back to tetrahedral would require a larger mesh in order to obtain the same level of convergence.

For these reasons, a simplified approach has been adopted, in which:

- The geometry and the mesh do not change in time;

- The insertion of the control rod is simulated with a reduction of the outlet temperature of the assembly that will be extracted from nominal to a reduced operation value;
- The extraction of the assembly is simulated by increasing the inlet velocity for the outlet surface corresponding to the assembly that is being extracted, without changing the geometry and the mesh.

This approach is not completely accurate on a local assembly level, because it does not model well the bypass and internal flow configuration, but it is capable of providing useful information on a global reactor vessel level.

The results from the steady state simulation have been used as initial condition for the transient simulation of the assembly extraction. The structure of the simulation is divided in two parts. The first part models the insertion of the control rod, by assuming that the outlet temperature of the selected assembly reduces to a lower value (650°C has been selected, even though the actual temperature will be somewhere between 650 and 700°C) over a 10 seconds period. The second part simulates the assembly extraction by increasing the inlet velocity at the selected assembly location over a period of time of about 20 seconds.

UDFs are used to implement the temperature change due to control rod insertion and the increased mass flow rate; in particular, the mass flow rate is calculated using the same UDF presented in section 2.5.2, and the inlet velocity is computed from it by knowing the surface of the assembly cross section and the fluid density.

The simulations have been run on several tens of cores, and a few hours are required for each step. The post-processing has been relatively challenging for the full problem, because the mesh is very large; even though Fluent allows parallel post-processing, the graphical data transfer process to the head node of our cluster required a lot of time, so it was not possible to develop movies from the auto-saved transient data. Results have only been plotted for specific time steps: the end of the control rod insertion process and the end of the assembly extraction.

Figure 2-35 shows the velocity magnitude and the temperature in the upper plenum for specific moments during the transient.

The effects of the control rod insertion on the flow distribution are negligible; this part of the transient only slightly affects the upper plenum temperature distribution, only along the path of the flow that is ejected from the channel of the selected assembly; also the local temperature mixing effects tend to homogenize the temperature towards the top of the upper plenum.

At the end of the transient the effects of the assembly extraction are more evident. The pathlines clearly show a peak in flow velocity for the flow that exits the selected channels. Following these pathlines, the velocity tends to decrease when the flow approaches the top of the vessel, and then they increase, before entering the outlet piping. This decrease in flow velocity in the top part of the vessel enhances the flow mixing, locally homogenizing the temperature distribution, as shown in the lower-right frame of Figure 2-35.

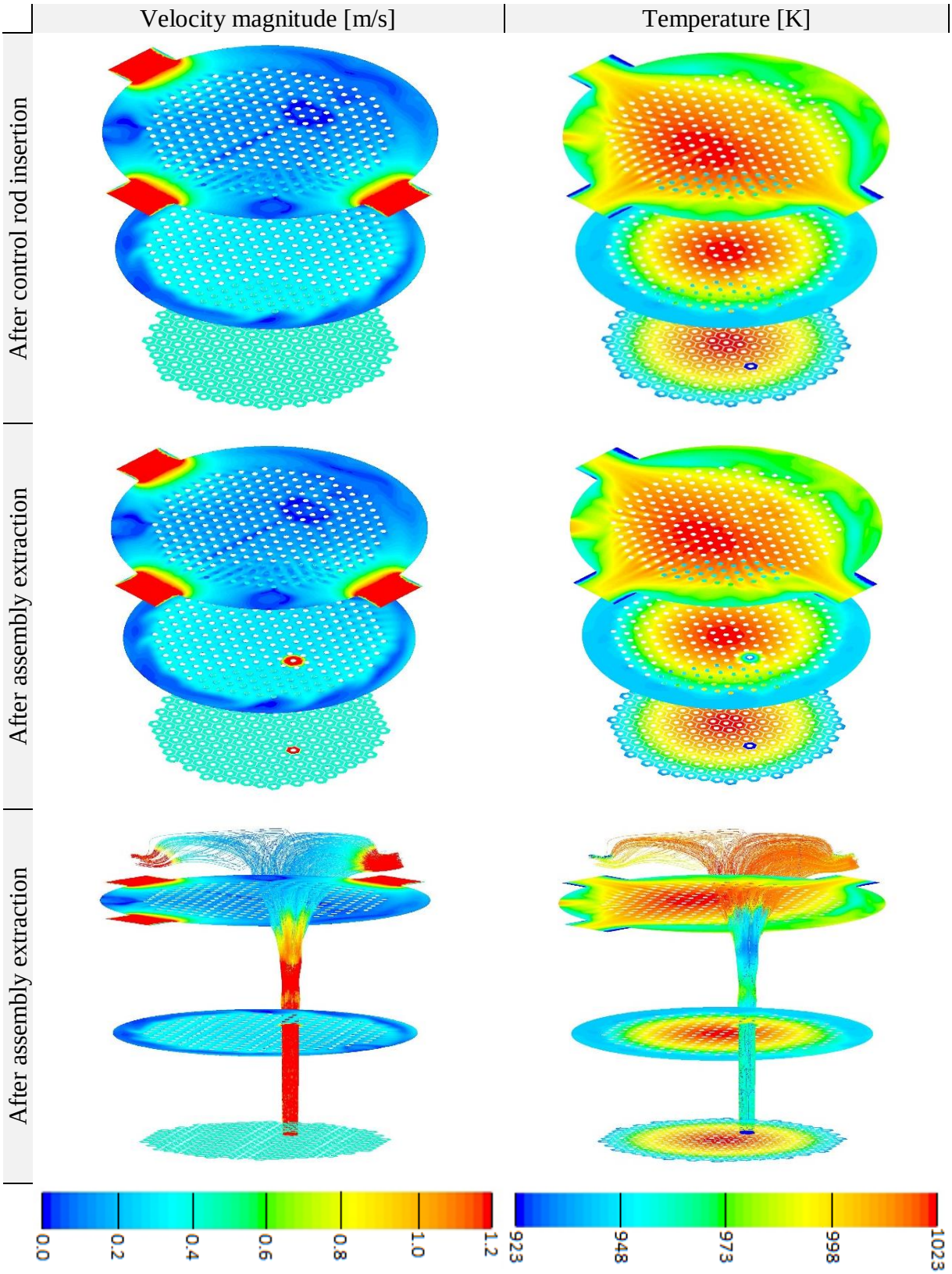

Figure 2-35. Upper plenum velocity magnitude (left) and temperature (right)

3. NEUTRONICS MODELING FOR ONLINE REFUELING

The online refueling, consisting of the replacement of a burned (spent) assembly with a fresh assembly while the reactor is operating, has consequences on the neutronics of the core that cannot be neglected in order to perform this operation safely.

The online refueling introduces two main aspects that are somewhat different from a standard multibatch fuel cycle on a neutronics level. The first difference is the specific refueling operation, that is performed at full power: this has an impact on the reactivity of the core and the control system needs to be designed to be able to deal with this variation. The second aspect, which is more complicated and only partially addressed in this work, is the completely different and new approach that needs to be developed for the characterization of the fuel cycle and the refueling patterns.

The neutronic studies performed as part of this work aim to provide a picture of the reactivity variations in the core during the single assembly replacement operation.

These studies are based on basic Monte Carlo models of the fuel assembly and the reactor core that have been used to perform several simulations of fuel depletion and criticality.

In order to facilitate the study of different core configurations for different core burnup distributions, a correlation based on reactivity conservation has been developed between the isotopics of a partially burned fuel assembly and an equivalent fresh fuel configuration with lower enrichment. This equivalence allowed the characterization of an approximated reference core configuration that has been used to study the characteristics of the reactivity evolution during the online refueling operation, constituted of the spent fuel assembly removal and the fresh assembly insertion.

The neutronic studies have been performed using mainly the SCALE code package, while the modeling is based on the work performed by Lewis [25], Kingsbury [26] and Huang [27]. Lewis developed a 2D core model that constituted the basis for the creation of the full core 3D Monte Carlo model developed in this work; he also provided the basic information for the modeling of the economics of the AHTR fuel. Kingsbury continued the work of Lewis, improving the modeling approach and its accuracy and enhancing the economics model. Huang provided useful

information about depletion calculation on AHTR fuel together with characterization of optimal fuel configurations and details on the Dancoff factor modeling approach.
This work provides a preliminary and general description of the neutronic characteristics of the online refueling approach and sets the basis for future works that will analyze various aspects in more detail.

3.1. SCALE neutronics model

The SCALE code package [28] has been used for the simulation of the neutronic properties of the core in the online refueling configuration. In particular, the Monte Carlo module KENOVI has been used for the calculation of the multiplication factor and the reactivity. The SCALE modeling approach is derived from the contribution of several modeling efforts intended to optimize the fuel design and utilization [31].

3.1.1. Components of the AHTR SCALE model

This section provides a general description of the various components of the AHTR core and how they are modeled in SCALE. The basic units that are illustrated here are the TRISO fuel particle, the fuel plate, the fuel assembly and the reactor core. This simplified model neglects those aspects of the design that do not affect the reactivity of the system, such as internals in the plenums or details of the configuration of the DRACS heat exchangers.

3.1.1.1. Fuel particle

The fuel particle is TRISO type [32]. The reference TRISO particle has 3 external layers that have several functions, such as maintaining the integrity of the particle and preventing the fission gases release to the coolant. From a modeling perspective it has been shown that these layers can be combined and homogenized with the graphite matrix without introducing substantial errors in the simulation process [25]; this approximation reduces the number of materials for which cross sections need to be calculated (reducing the preprocessing time of the simulation) and also reduces the number of surfaces that the neutron can potentially cross along his path, thus reducing the

computational time for the Monte Carlo portion of the calculation. The overall reduction in computational cost is on the order of factor of 2, maintaining the accuracy of the detailed calculation. The fuel particles are then modeled as simple spheres, immersed in the graphite matrix. The distribution of the particles in the thin fuel stripe is not fully known at this stage of the design, no experimental data are available yet to provide information about locations of particles one with respect to the other. It can be assumed that particles have a random distribution in the matrix; however, SCALE does not provide an option for modeling a random distribution of particles, so a reference cubic lattice has been assumed for this calculation (Figure 3-1); the effect of assuming a specific particle distribution instead of a random one has been evaluated in other works [34] and it can be considered acceptable for the purpose of this work.

The TRISO particles lattice pitch is on the order of 1 mm, corresponding to a packing fraction of 40%; the diameter of the kernel (uranium oxycarbide) is about 0.427 mm.

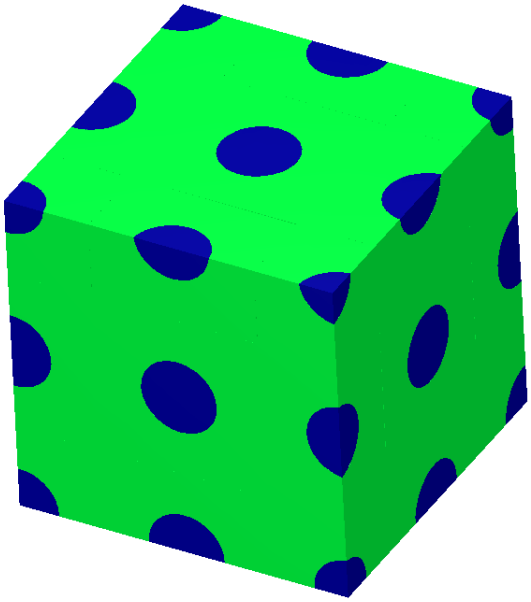

Figure 3-1. Distribution of fuel kernels in the fuel stripe matrix, as modeled in SCALE

3.1.1.2. Fuel plate

Figure 3-2 shows the configuration of the fuel plates in the horizontal cross section of the assembly. The TRISO fuel is embedded into a graphite (carbonaceous) matrix that forms the fuel stripe (green) and two fuel stripes are present in each fuel plate, one for each side. The heat produced in

the fuel stripe is transferred to the coolant (pink) through a 1 mm thick plate cladding (red). The structure is supported by the internal portion of the plate, named graphite meat. In this work, a specific fuel configuration has been selected, for which four layers of particles have been modeled for each fuel stripe; note that this is not necessarily the optimal fuel configuration for maximum fuel utilization; an optimal fuel design can be developed once the basis for the online refueling approach is established.

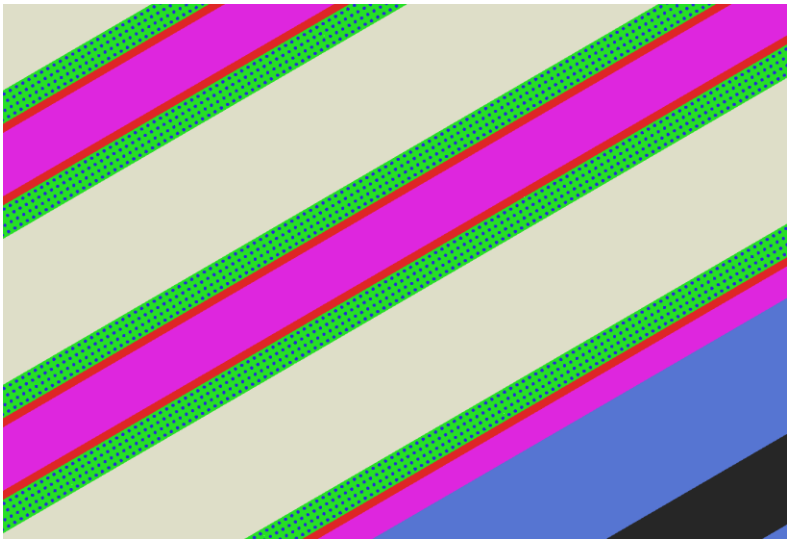

Figure 3-2. Detail of horizontal cross section of two fuel plates, as modeled in the SCALE model

3.1.1.3. Fuel assembly

Figure 3-3 shows the horizontal cross section of the fuel assembly. The model does not include very specific details of the geometry such as spacers but captures the overall structure of the assembly.

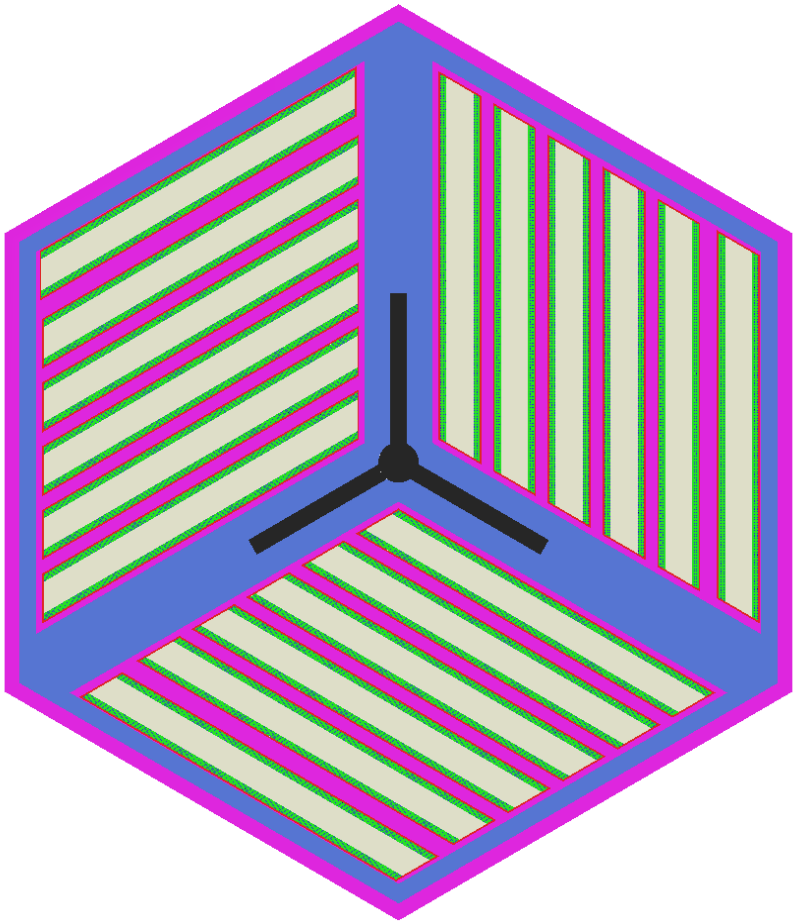

Figure 3-3. SCALE model of the fuel assembly (horizontal cross section)

3.1.1.4. Core

Figure 3-4 shows the horizontal cross section of the core model. This model includes a central assembly location plus the nine radial rings; two rings of graphite assemblies model the radial permanent and replaceable reflector, respectively. The boundary of the reflector is delimited by the core barrel, followed by downcomer. The model is completed by the vessel wall, that has a void boundary condition at the external surface. In the axial direction, the model includes the support plates and the plena as well as the assemblies in the core with the respective control rods. Figure 3-5 provides a 3D graphical representation of the core model, with a partially extracted assembly.

The central element can be modeled both as an assembly and as an instrumented element, reflecting alternative designs that have been considered in previous studies.

The radial distribution of elements based on enrichment, burnup, temperature distribution and other factors can be changed based on the specific needs and objectives of the simulation; for instance, if the assembly-wise radial fission density profile is needed, ten different assembly units can be defined, with different materials and temperatures.

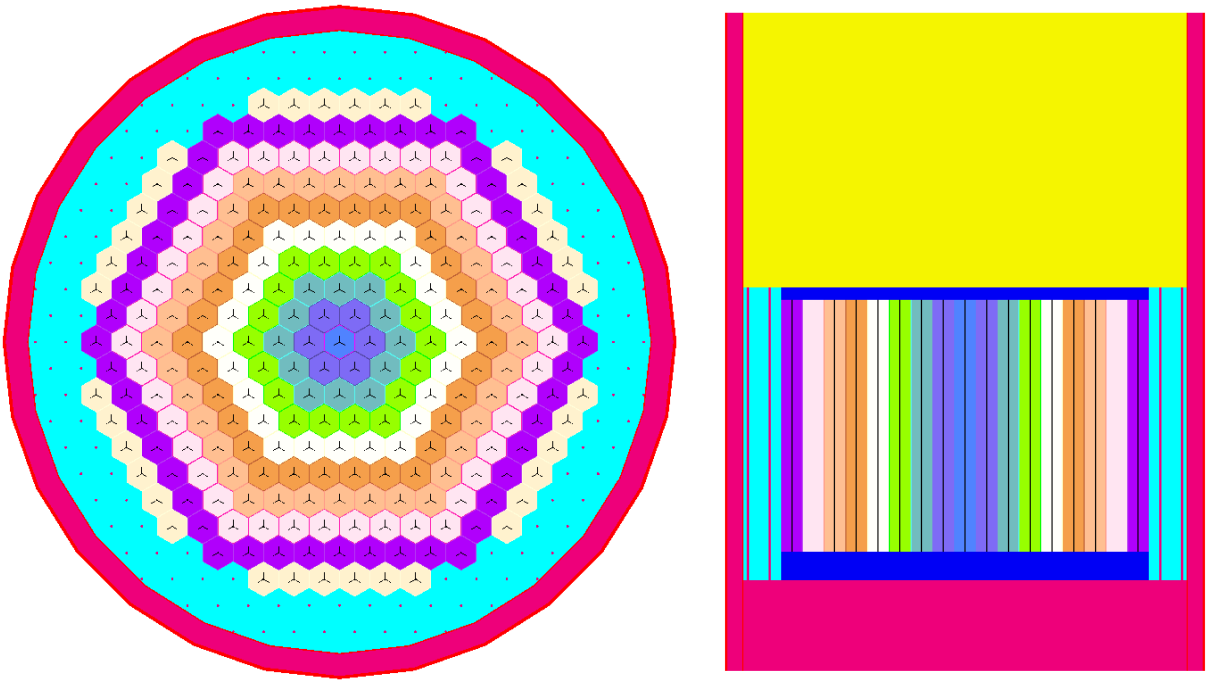

Figure 3-4. Horizontal (left) and vertical (right) cross section of the SCALE core model. Each ring is modeled using a different unit

Figure 3-5. 3D view of the SCALE core model; assemblies are grouped in three radial rings and one assembly is partially extracted

3.1.2. Input file creation process

The core model input file is created using an automated MATLAB process that builds the various parts of the model starting from a few sample elements assembled together [Appendix 7.4].
The sample elements are extracted from input files developed for other purposes such as fuel cycle and fuel assembly design optimization [33] and adapted to the creation of a 3D full core model.
The basic unit of each of these models is the assembly unit, which is constituted by 18 fuel plates distributed in three sub-channels and supported by the Y-shaped structure and the box wall (assembly channel wall); the definition of the assembly horizontal cross section in SCALE is relatively straightforward and can be obtained using holes and cubic arrays for the definition of the fuel stripe.
The fuel is of AGR-2 type; the enrichment can be set to the desired value based on the specific design. Note that different enrichments are being considered for the design: the initial design value is 19.75%, allowing the loading of a large amount of fissile material in the core but potentially too expensive for the current enrichment facilities; a second value that is being considered and that currently represents the reference design is 9%, which can be more easily and cheaply obtained at the current level of technologies and at the same time poses less challenges from the non-proliferation standpoint; finally an enrichment of about 5% should be considered, because it is more affordable and potentially viable in the online refueling consideration.
The assembly model is generally run in multigroup mode, because the continuous energy version cannot account for dependence on exact temperature of materials; this is due to the fact that the SCALE version used for this work (6.1 [29]) uses cross section libraries at specific temperatures (300, 600, 900, 1200 K) and can only interpolate in the multigroup mode. More recent versions of SCALE (6.2 and 6.2.1 [30]) have the capability of performing the data interpolation, but they were not available yet when these calculations were performed. Instead the McDancoff factor approach has been used, which allows to account for the multiple heterogeneity of the AHTR fuel in multigroup mode. The factor can be set in the celldata section of the SCALE input file; the typical values used for this study and derived from optimization processes performed in other work [33] is on the order of 0.88.
The simulations are run using the standard v7-238 cross section library and the csas6 module of KENOVI.

The assembly model is integrated into the full core model, based on the work performed by Lewis [25], who developed a 2D core model simulating a 10 cm thick slice of the core with mirror boundary conditions at the upper and lower faces. This model has been maintained in the horizontal (radial) plane but it has been expanded in the axial direction in order to account for axial distributions and the effect of axial reflectors, control rods and plena.
In the horizontal plane the location of different assemblies is defined by a hexagonal array that has a single axial layer; each unit allocated in the array contains the reference array as well as its corresponding section of axial reflectors and salt volumes in the lower and upper plenum.

3.1.2.1. SCALE input file creation script

The script [Appendix 7.4] that creates the SCALE input file is implemented in MATLAB and it can create a SCALE input file that includes the following sections:

1. Material composition. An assembly requires the definition of the fuel material, the homogenized matrix, the graphite meat and the cladding; the Flibe coolant and the graphite in the fuel block also must be defined. Support materials such as graphite in the reflector block and vessel steel are defined at the end of the core materials.
2. Cell data. A cubic lattice is used to describe the TRISO distribution in the fuel layer. A Dancoff factor approach has been developed in previous work, which allows a correct modeling of the cross sections with heterogeneous fuel [27].
3. Parameters. The initial testing aims to estimate the best values for number of generations, particles and skipped generations in order to balance minimizing the statistical uncertainty and the computation time.
4. Geometry and array specifications. This work, as previously mentioned, does not introduce a new modeling of the geometry, but tries to be as close as possible to the models developed in previous works for neutronic analysis purposes.

Several parameters can be defined in the input file creation process, based on the objective of the analysis, which can be one of the following:

- Determine properties of the power distribution in the core;
- Determine the effects on reactivity of the insertion of the control rods;
- Determine the effects on reactivity of the lifting (extracting) of one assembly.

The parameters that can be set by the user in the input file creation process are the following:

- Number of axial levels of each assembly unit;
- Number of radial rings, or, in general, assembly units;
- Number of materials for assembly definition (dependence on enrichment or temperature);
- Horizontal location of each assembly unit in the core;
- Axial elevation of an assembly in the core;
- Insertion of the control rod for each assembly.

The MATLAB script writes the input file for the KENOVI simulation, accepting the following input:

- General parameters: file name, check parameter (if 1, the check option in scale is activated), arrays parameter (if 0, the TRISO array is replaced with a homogenized layer of fuel material) and mesh parameter (if 1, the mesh is included in the input file).
- Material configuration. This is a matrix that has as many lines as the number of materials that will be written to the input file. Each material represents a possible assembly material configuration. The parameters that must be defined per each material are the temperatures of the fuel, cladding and coolant, as well as fuel enrichment. Note that temperatures are uniform over their respective regions.
- Definition of groups of elements. Each possible assembly location in the core is identified by a number (3 digits, the first one is the ring, from 0 to 10, the second and third digits represent the location in the ring, clockwise). Each location is filled with a unit type, represented by a unit ID. Each unit is defined later. This step allows the definition of the radial distribution of elements in the core.
- Definition of the unit types. This is a matrix, each line of which represents a unit, ordered by ID number. For each unit the following parameters are set: the elevation (in cm), the number of axial intervals and the presence of the control rod in each interval of the assembly.
- Definition of the unit properties. This is a cell array, of which each cell represents a unit, ordered by ID. For each cell two arrays are defined, that define the length and the material of each axial interval in that specific assembly.

With these parameters, the MATLAB script writes the SCALE input file in the following order: material compositions for the assemblies; material composition of the reflector, the plenums and

the barrel; cell data; parameters; geometry for each assembly, for each axial level; geometry for global unit (vessel, core, plenums); array of assemblies; array of TRISOs in each assembly; plots; boundary conditions (vacuum); grid. This procedure allows the creation of the input file for a specific configuration in a few seconds.

3.1.2.2. Data extraction from the SCALE output file

A MATLAB script for the extraction of the fission density distribution data from the SCALE output file has been developed (Appendix 7.5). This script is based on the use of a Monte Carlo approach for the sampling of points on the horizontal core cross section, to which a value of fission density is assigned based on the location; the unit-wise fission density values are extracted from the final portion of the SCALE output file and associated to the respective region in the core. A sample plot from a particular output file is presented in Figure 3-6. Note that each assembly is uniformly colored even though fission only happens in the assembly fuel stripes (in fact, only in fuel kernels).

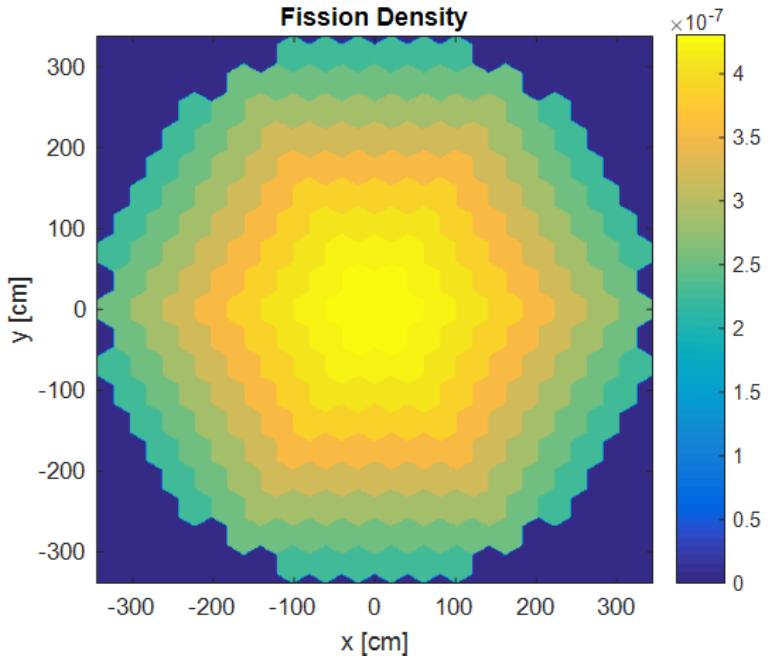

Figure 3-6. Sample core fission density (arbitrary units) plot representing the power distribution for a 10 rings model.

3.1.3. Preliminary testing for the SCALE core model

The SCALE core model has been tested in order to determine its correctness and the range for parameters that allows to run full core simulations and reduce the uncertainty to the required level. The reference model has been run for 100 generations of which 50 are skipped, and 100 thousand particles per generation. This reference case has been compared to variations in configuration in order to test the capability of the model. The parameters that are changed in order to test the capability of the model are the number of generations, the number of particles per generation, the number of materials used for the definition of the assembly units, the number of rings (or more in general the number of assembly units); the insertion of the control rod and extraction of the assembly have also been tested. This section presents the results of the preliminary testing.

The number of generations has been tested using a model with three radial rings having identical compositions; this model has been run for several values of total number of generations, of which half is skipped and the other half is active. Preliminary evaluations show that at least 100 generations should be skipped, with a few hundred thousand particles per generation, and a few hundred active generations should be run to achieve an uncertainty of around 10 pcm on the multiplication factor (Figure 3-7). For 100 generations and 100,000 particles per generation, the preprocessing time is about 1 hour and each generation takes 8 minutes; if the number of particles per generation is increased to 200,000 the calculation time for each generation increases to about 20 minutes.

The preprocessing time for the calculation of the cross section is strongly dependent on the number of materials or units used in the model and is not affected by the number of generations; in other words, the value obtained for this specific case, which is about 1h and 10m, is proportional to the number of rings modeled, 3 in this case. As expected, the functional behavior of the standard deviation goes with the inverse of the square of the number of generations (with the number of particles per generation held constant), so the number of generations required to obtain an uncertainty of 20 pcm is on the order of 100 active (200 total).

The number of particles per generation has been tested using 100 total generations and up to 500,000 particles per generation. Preliminary analysis shows that at least a few hundred thousand particles per generation should be used. The behavior of the standard deviation goes with the inverse of the square of the number of particles per generation, as expected, and the number of

particles per generations required to obtain a standard deviation of about 20 pcm is on the order of 200,000 (Figure 3-8).

The number of materials has been tested using a reference core model that has three different units for the radial rings and 1, 2 or 3 materials lists, each list representing a different type of assembly. The results show that the simulation time does not depend on the number of materials used in the model. This means that the preprocessing time can be directly related to the number of units used in the model, more than the number of materials lists used to define them; note that the number of materials indicates the number of mixtures used in the model and preprocessed before the Monte Carlo simulation.

The dependence on the number of rings (or units) has been analyzed using three models having 1, 3 and 10 rings respectively. The results show that the simulation time increases by about 40 min every time a new unit is added (Figure 3-9); we can probably also say that this increase is part of the preprocessing time and does not affect the calculation time of the histories of neutrons. Note that the number of rings is related to the number of integral assembly units (example: an assembly with 2 axial levels corresponds to 2 units). This is important in the decision process of how to discretize the core for specific simulations.

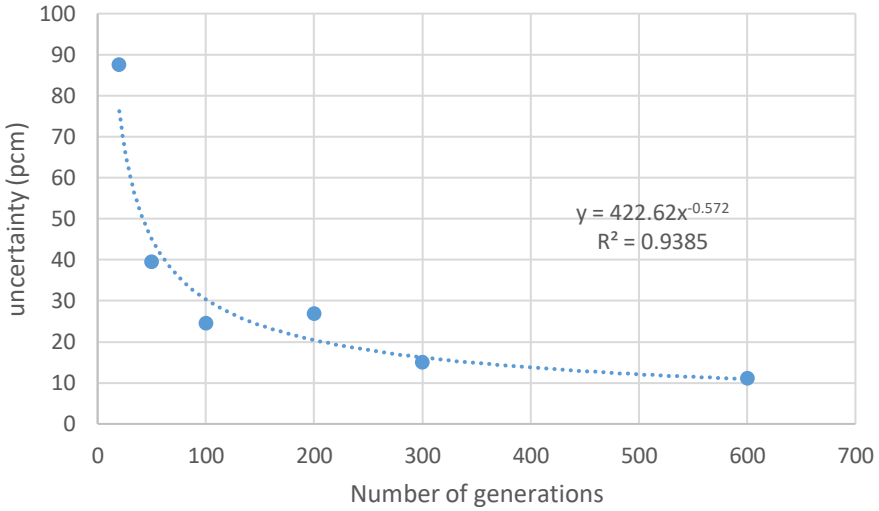

Figure 3-7. Uncertainty as a function of number of generations

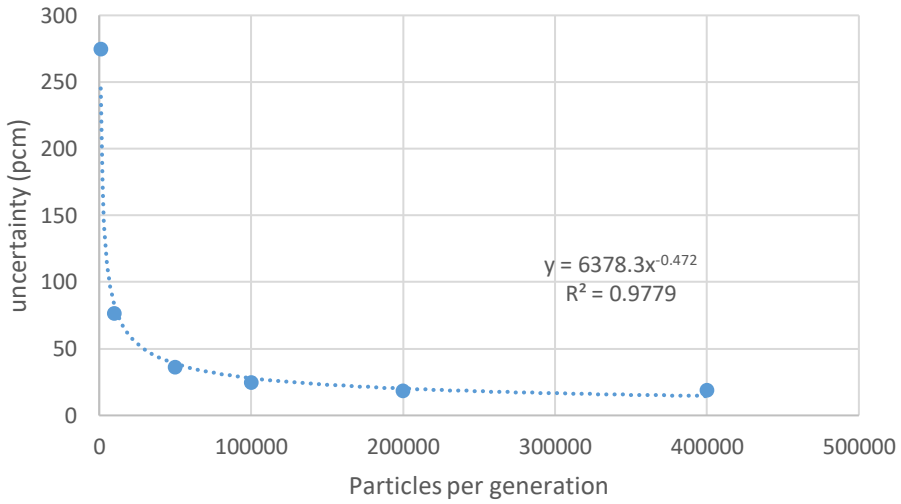

Figure 3-8. Uncertainty as a function of number of particles per generation

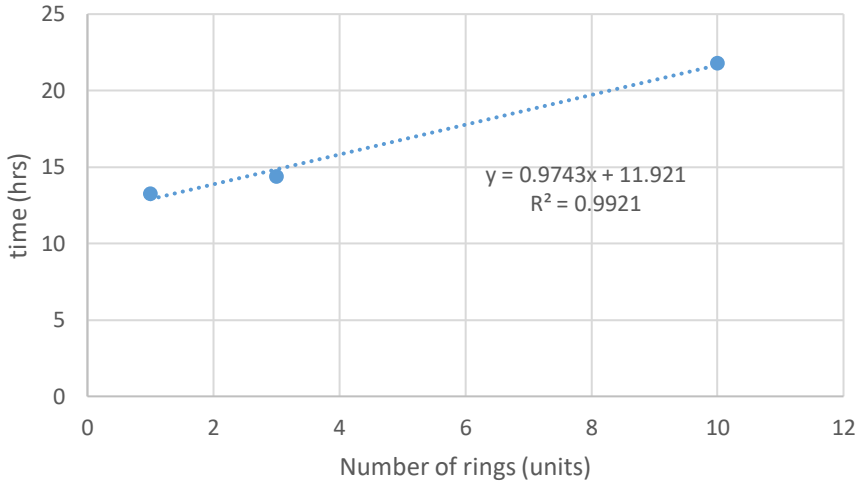

Figure 3-9. Simulation time as a function of number of units

The insertion of the control rod has been tested by calculating the reactivity at three insertion depths of the control rod of a specific element. More accurate studies will be shown later.

Three simulations have been run (100 generations, half skipped, 100000 particles per generation), with the control rod completely extracted, 50% inserted and completely inserted, respectively. The uncertainty is still relatively large if compared to the reactivity variation due to the insertion, but it is possible to get an impression of the behavior of reactivity as a function of the control rod

position. The order of magnitude of reactivity variation due to the insertion of the control rod from completely extracted to fully inserted is on the order of 100 pcm.
Similarly to the control rod case, three simulations have been run for the testing of the extraction of the spent element from the core, with the assembly completely inserted, 50% lifted and completely extracted from the core. Similar considerations are valid here, in the sense that the uncertainty is probably too large to derive an accurate correlation, but we can say that the complete extraction of the assembly from the core causes a decrease in reactivity of about 100 pcm.
These initial analyses, though the uncertainty is still pretty large, provide an overview and estimate of the order of magnitude of the reactivity variation for this transient. A deeper analysis is required to show the evolution and self-stabilization of the core accounting for all the involved factors and it will be described in the next sections.

3.1.4. Parameters for depletion calculations

The SCALE assembly model is used to run depletion calculation for evaluations of the reference or equilibrium core in order to determine the specific burnup conditions under which the online refueling operation is performed.
The depletion calculations are run using the t6-depl module in SCALE and maintaining the same parameters of the models used for criticality calculations presented in the previous sections. In particular, for the assembly model, 200 generations are run of which 40 are skipped, and 10,000 particles are used per generation in order to reach the required precision (40 pcm for the assembly depletion simulations).
For the depletion section in the input file, the power used for the fuel regions is 170.93 W/gHM, corresponding to the nominal AHTR power (3400 MWth) for the fuel configuration considered in this analysis (4 layers of TRISO particles per fuel stripe). The time step for burnup calculation is set at 2 days at the beginning of the simulation, and it increases up to 250 days after the first year at full power. The parameter nlib allows to increase the frequency of Monte Carlo calculations within a specific time step; nlib equal to 1 and 4 were tested and the difference was on the order of 8 days over the entire cycle length, which was considered negligible for the purposes of this work, so nlib=1 has been used for the simulations.

Regarding the number of nuclides considered for the burnup simulations, the parameter addnux was set at 2 and 3 for testing purposes, but the difference was found to be negligible for the purposes of this work, so addnux equal to 2 was selected for simplicity; the difference in terms of computational time between different addnux values is relatively small [27], consisting of a few percent increase for addnux equal to 3.
Several depletion simulations have been run using different enrichments and time step data, in order to calculate the reference conditions for criticality simulations.

3.2. Methodology for reference core calculations

The SCALE core model that has been described in the previous section and tested for several parameters has been used to perform evaluations of the properties of the AHTR core in online refueling configuration. After an appropriate evaluation of the distribution of enrichment and burnup in the reference core, the insertion of the control rod and extraction of the spent assembly have been simulated.
Since burnup simulations cannot be easily performed for a 3D core because of the amount of data that need to be tracked during the depletion of the fuel, the full core simulations that depend on the burnup of the assemblies have been run assuming that the isotopic composition of burned assemblies can be represented using fresh fuel with different enrichment. This assumption will be further illustrated in the following sections.
Once a relation between fuel burnup and enrichment is established, the fission density distribution can be computed for specific core configurations and the optimal core configurations can be extracted.
This approach seems to be the most viable because it allows to use a Monte Carlo code, which is accurate in terms of calculation of k, but does not require to run full core Monte Carlo depletion simulations, which would require large computational resources.
An alternative and more versatile approach for full core depletion simulations would consist of the use of nodal kinetics codes [34], once more reliable data about cross sections and few-groups approximations for the AHTR become available. These codes allow a much faster evaluation of a specific fuel cycle, once the refueling patterns are determined, potentially providing the basis for a true optimization of the fuel cycle for online refueling.

The current work instead focuses more on the development of Monte Carlo calculations for the online refueling operation, for which accurate information about the refueling pattern can be replaced by reasonable assumptions on the power profiles and the burnup distributions.

3.2.1. Assembly depletion simulations

Depletion simulations of the fuel assembly have been run for several enrichments in order to provide the data needed to generate a correlation between the burnup and the equivalent enrichment. Figure 3-10 and Figure 3-11 show the depletion simulations for 9% and 19.75% enrichment, respectively.

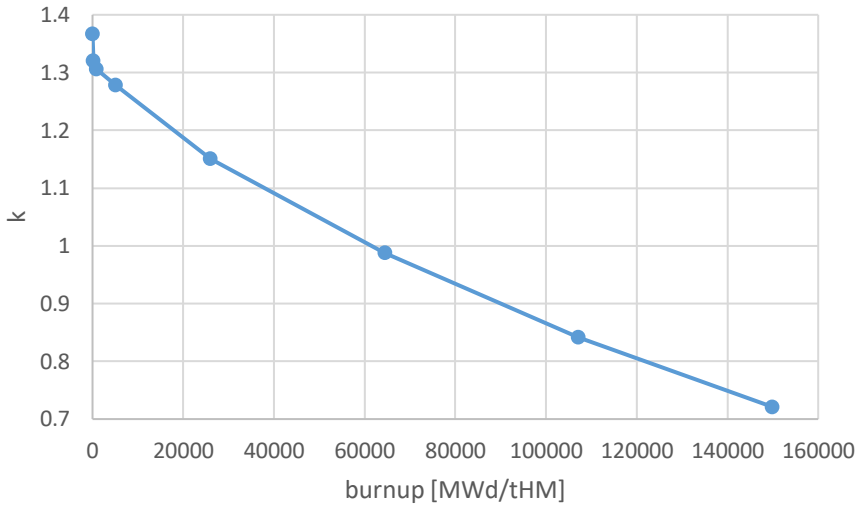

Figure 3-10. Depletion curve for 9% initial enrichment

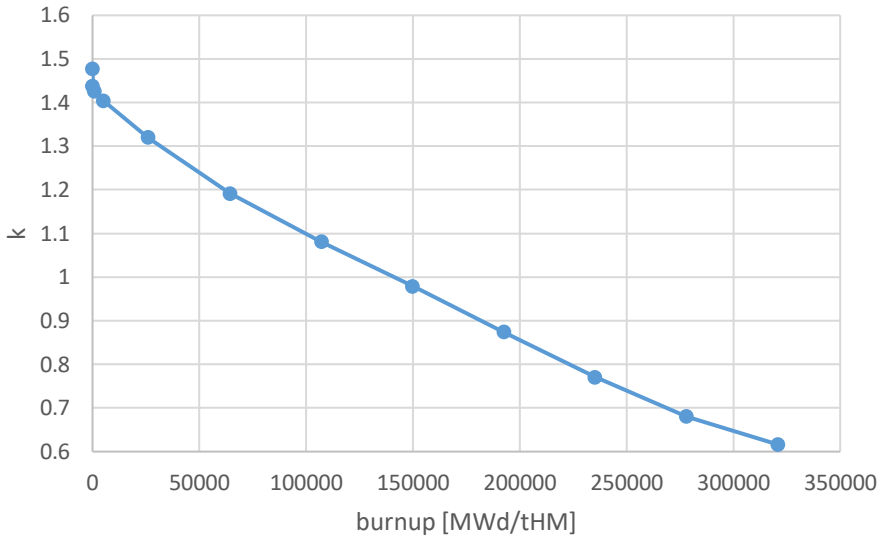

Figure 3-11. Depletion curve for 19.75% initial enrichment

Shorter burnsteps have been tested using a higher value for the nlib parameter in the depletion section of the input file; the nlib parameter sets the amount of intermediate calculations that are performed for a given burnstep. nlib equal to 1 provides adequate accuracy for this work. The parameter addnux is set to 2, as justified in previous sections; more nuclides should be included when the isotopic composition is relevant, while in this work the reactivity is of primary interest. The error in the cycle length using the specified burnstep data is on the order of 2%, which was considered acceptable for the purpose of the work; the cycle length is about 340 days and 820 days for the 9% and 19.75% enrichment, respectively. Note that the difference between the curve with higher discretization and the curve with lower discretization (high and low value for nlib parameter) increases for k equal to about 0.85, where the reactivity behavior cannot be well approximated with a linear function.

3.2.1.1. Regression of depletion data

The depletion data presented in the previous section have been interpolated using a specific fitting function the gives the k as a function of the burnup.
The interpolation curve for the 9% enrichment has the following form:

$$k(x) = a - b * x + d * \exp(-e * x) + f * \exp(-g * x) \quad (10)$$

Where k is the multiplication factor, x is the burnup in MWd/tHM. The parameters for the fitting curve are presented in Table 3-1. Similarly, for the curve for the 1975% enrichment, which will be used for the evaluation of power profiles, the following fitting curve has been used:

$$k(x) = \frac{a}{\left(\frac{x}{1e5} + b\right)^c} + d + e * x + f * \exp(-g * x) \quad (11)$$

Table 3-1. Parameters for depletion curve fitting

Enrichment	9%	19.75%
a	1.11	0.1691
b	2.642e-6	1.092
c	-	2.372
d	0.2029	1.293
e	2.302e-5	-2.239e-6
f	0.0538	0.0467
g	0.01085	0.0107
R^2	1.0	0.9999

The interpolation curves for the two enrichments are shown in Figure 3-12, along with the interpolation data. The curves have a linear component plus two decaying components, a steep exponential or hyperbolic component for low burnups and a more slowly decaying component for larger burnups. The error of the fitting curve with respect to the simulation data is relatively small, resulting in a very high R^2, as shown in Table 3-1

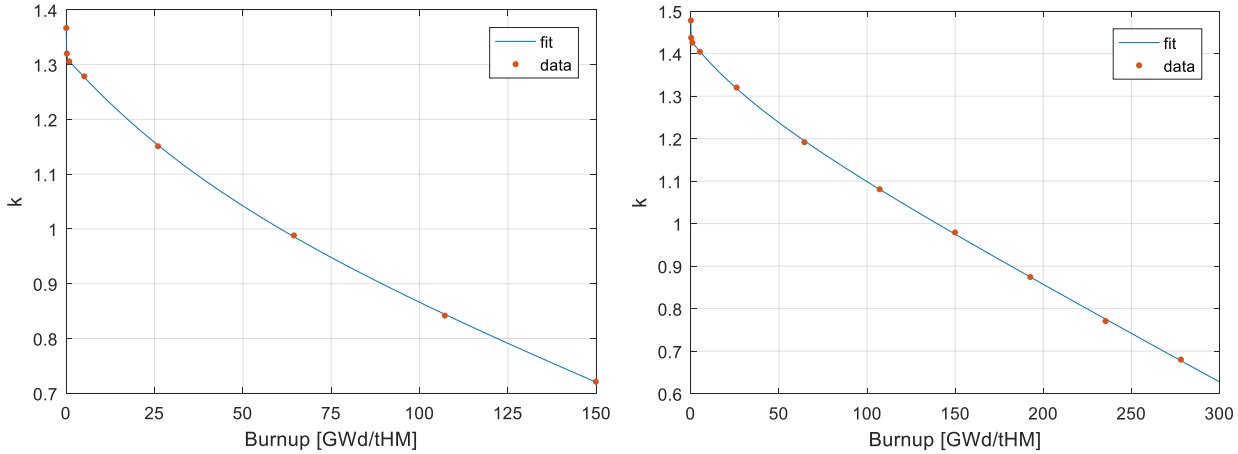

Figure 3-12. Interpolated depletion curves for 9% (left) and 19.75% (right) enrichment

3.2.2. Assembly criticality calculations

The multiplication factor has been computed for the reflected assembly as a function of the assembly enrichment. The ultimate purpose of this calculation is the determination of an analytical correlation between the burnup of a depleted assembly and the enrichment of an equivalent fresh assembly, whose fuel is fresh but at lower enrichment.

A series of enrichments between 1% and 19.75% have been selected and a single criticality calculation for fresh (zero burnup) fuel assembly has been run for each one of them. The results have been fitted with a specific analytical expression that minimizes the error with respect to the simulation data.

The fitting curve has the following form:

$$k(x) = a + b * x + c * x^2 + \frac{d}{x^e} \qquad (12)$$

Where k is the multiplication coefficient, x is the enrichment and the parameters are listed in Table 3-2. Figure 3-13 shows the simulation data as well as the corresponding data from the fitting curve. The matching between the simulation data and the fitting data is satisfactory. i.e., the points practically overlap.

Table 3-2. Parameters for the fitting curve of k versus enrichment

a	9.713
b	-3.496
c	5.631
d	-7.162
e	0.0498
R^2	1.0

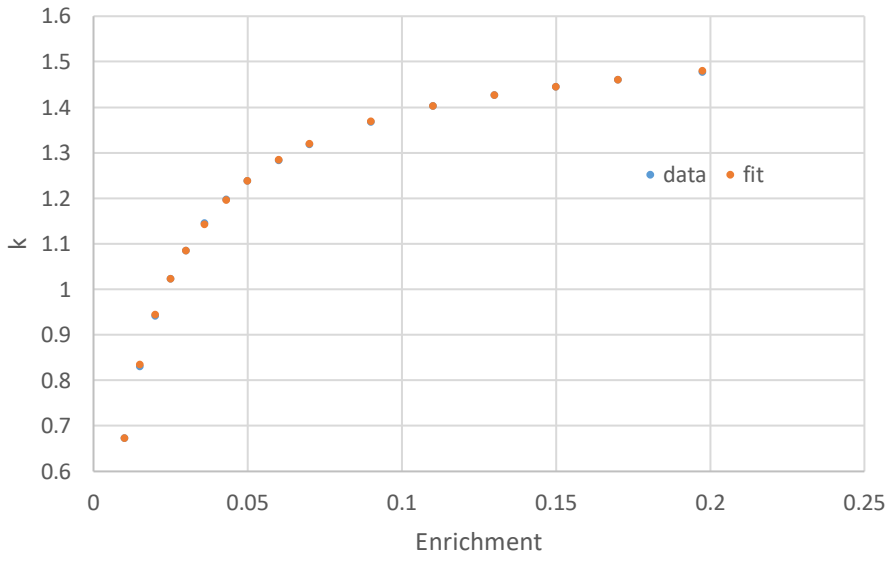

Figure 3-13. k versus enrichment data and fitted values

3.2.3. Correlation between burnup and equivalent enrichment

A correlation between burnup and equivalent enrichment has been developed based on the correlations presented in the previous sections. The correlation has been developed by assuming a specific set of burnup values and associating to them a set of equivalent enrichments in such a way that the k obtained from the burnup correlation is as close as possible to the k obtained from the enrichment correlation developed in the previous section. In other words, a correlation has been developed that, given a burnup value, returns the equivalent enrichment that produces the same k in a criticality calculation.

The specific approach followed to derive this correlation is the following:

1. A specific set of burnup values has been selected; 27 data points were considered in this analysis, so that all the features of the depletion curve can be described well by the interpolation. For each of these points, the k has been calculated using the burnup fitting function developed in section 3.2.1.1.
2. For each data point the equivalent enrichment has been guessed and the corresponding k has been calculated using the fitting function developed in section 3.2.2.
3. The cumulative absolute error is calculated by summing the absolute differences between the k from the burnup and the k from the guessed equivalent enrichment, which are computed for each data point.
4. Using the Excel Solver, the cumulative absolute error is minimized by changing the guessed values of the equivalent enrichment array. A set of equivalent enrichments is then obtained as a function of burnup.

The previously described operation has been performed for both the 9% and 19.75% enrichments. Figure 3-14 shows the correlation curves for 9% and 19.75% enrichment.

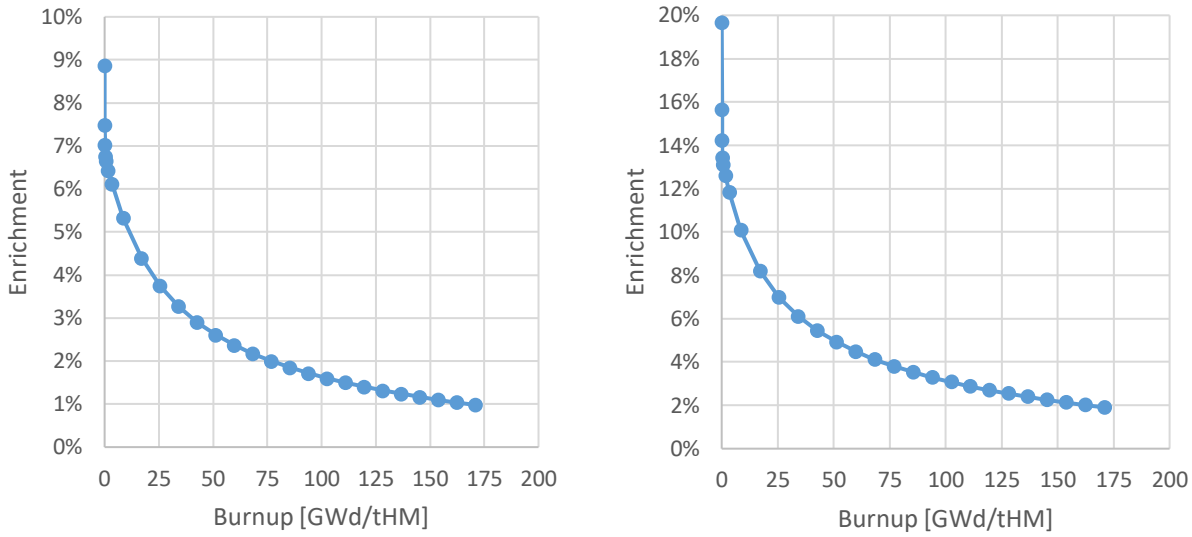

Figure 3-14. Equivalent enrichment versus burnup data and fitting curve for 9% (left) and 19.75% (right) enrichment

The curves described in the preceding paragraphs have been fitted using an approach similar to the one used in the previous sections.

The shape of the fitting function is the following:

$$enr(x) = \frac{a}{(x+b)^c} + d + e * \exp(-f * x) \qquad (13)$$

Where enr is the equivalent enrichment, x is the burnup in MWd/tHM and the parameters of the fitting function for the two enrichments are given in Table 3-3. A graphical representation of the fitting curves is given in Figure 3-14.

3.2.3.1. Verification of the correlation on full core simulation

The correlation between burnup and equivalent enrichment has been tested using the two-ring core configuration presented in Figure 3-15.

Table 3-3. Parameters for the enrichment vs burnup fitting function

Enrichment	9%	19.75%
a	63.39	6.684
b	2.223e4	1.103e4
c	0.6722	0.3913
d	-0.00785	-0.0396
e	0.01907	0.06108
f	0.01179	0.01227
R^2	0.9996	1.0

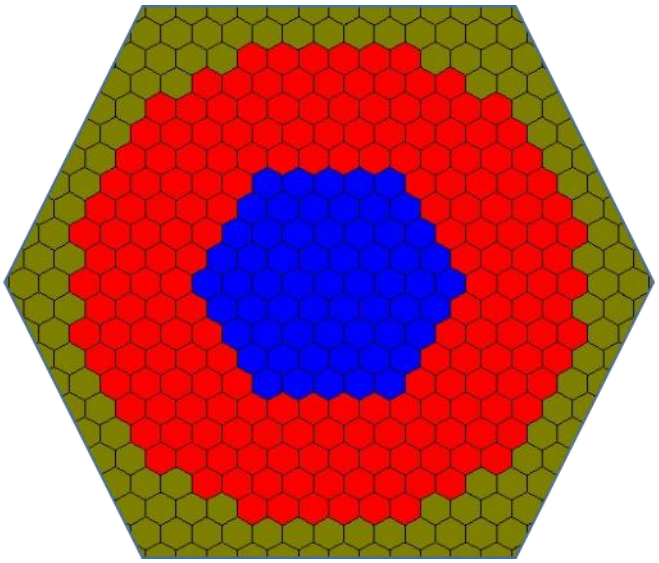

Figure 3-15. Two-ring full core model configuration

This core configuration is represented by two concentric assembly regions, the first region including rings 1 through 5 and modeling partially depleted fuel, and the second region including rings 6 through 10 and modeling fresh fuel. The geometry being the same, two versions of the problem have been studied; the depleted core version models the internal region of depleted fuel with full isotopics coming from depletion calculation of 9% enriched fuel at 59.1 GWd/tHM burnup; the equivalent core version instead models the internal ring as fresh fuel with 2.386%

enrichment, which is calculated from the mentioned burnup using the correlation developed in the previous section.

Both models have the same composition (fresh fuel) for the external ring and each ring is modeled using a specific unit.

The results of the simulation show that the overall error in reactivity is on the order of 250 pcm, which is not small but at the same time it is acceptable for the purpose of this analysis.

Figure 3-16 shows the fission density profiles for the depleted core and the equivalent core versions of the problem. The profiles have a similar shape and the overall structure is the same; note that uncertainties for fission data are not shown in the plot because they are relatively small with respect to the absolute fission density data, on the order of a few percent. The differences between the two versions become more evident at the interface between the two regions of high and low enrichment. Note that the assumed burnup of the internal region is relatively high, on the order of 59.1 GWd/ tHM.

Overall, the equivalent enrichment approximation seems to replicate well the general properties of the depleted core. Further work might provide full isotopics as function of burnup or full core depletion calculations might become more viable, thus allowing a more appropriate evaluation of the equilibrium cycle for online refueling; the approach presented in this section is considered adequate for the purpose of this work.

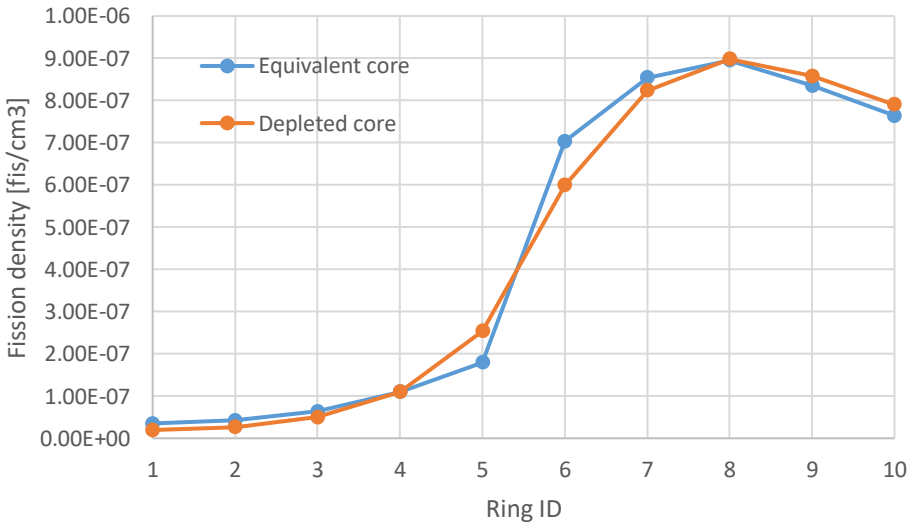

Figure 3-16. Fission density vs radial ring for the depleted and equivalent cores

3.2.4. Estimation of reference core configuration

The reference core configuration for the calculation of the reactivity changes during insertion of the control rod and subsequent extraction of spent elements has been estimated from general considerations on the power density distribution and a series of full core simulations based on guessed core burnup profiles.

The approach used to perform this task is based on a series of core burnup radial profiles derived from educated guesses; criticality calculations have been performed for each one of these profiles and the fission density has been extracted from the output files. All sets of derived data, except for the ones that are far from a flat radial fission density profile condition, have been analyzed using an ensemble learning technique to derive a burnup profile configuration that is close to critical conditions and results in a relatively flat power profile. This ensemble learning technique, performed using built-in MATLAB functions, allows to create an ensemble predictor based on training of observations and associated responses; in this case observations and responses are burnup/k and fission density distribution respectively, or vice versa. We have considered only the sets of data that are close to the specific desired condition (flat power profile) and in the vicinity of this condition the method can be applied.

The following sections will describe the calculation process for the burnup and fission density profiles, and how these sets of data are used to estimate a flat fission density profile condition for full core simulations.

The objective of this analysis is the determination of a burnup profile that provides almost flat fission density profile, which is assumed to be the operational condition for the AHTR in online refueling mode. It is important to note that this condition might not be optimal from the fuel utilization standpoint, but it guarantees more control on the thermal features of the assemblies, that are more uniform over the entire core. Also, the fission density profile will change during the operation and it will never be completely flat, so the calculations on reactivity changes during refueling operations don’t need to be performed in conditions of perfectly flat power profile.

3.2.4.1. Calculation of fission density profiles from burnup profiles

This section illustrates the approach used to compute specific fission density radial profiles given a specific burnup profile, for the estimation of the reference core configuration. The ensemble learning technique for the calculation of flat power profile configuration will be presented in the next section.

The procedure used for a calculation of a specific set of fission density profiles associated to burnup profiles is illustrated using a specific case as a reference. The approach is based on the following steps:

- A radial profile is guessed, assuming a certain peaking factor and slope of the curve. The profile is normalized to the number of assemblies per ring.
- A series of average burnups is selected, ranging from low to high burnup; low means below the critical configuration and high means above the critical configuration. The value of average burnup for which the configuration results to be critical is not known a priori, so a series of values needs to be selected in order to determine the critical conditions.
- The radial burnup profile is calculated by multiplying one of the selected average burnups and the guessed normalized profile; a burnup profile is obtained for each average burnup value.
- The burnup profile is converted into an equivalent enrichment profile using the correlation developed in section 3.2.3. A SCALE input file is generated from this equivalent enrichment profile for each average burnup value.
- The SCALE simulations are run; each simulation provides a value for k and a radial fission density profile.
- The multiplication factor k is plotted as a function of the average enrichment and the critical average burnup is found by interpolating the curve at zero reactivity.
- Once the critical average burnup is known, the critical fission density profile can be extracted from the results.

A specific example will be given here in order to show how this procedure works. This particular case assumes a 1.14 peaking factor (approximately) for radial burnup distribution and the functional shape shown in Figure 3-17. This burnup shape is peaked in the center, where the fission density would be expected to be higher with a uniform burnup profile; this profile is expected to

somewhat flatten the power profile. Note that only rings 8, 9 and 10 are below 1, because the number of assemblies for the outer rings is higher with respect to the number of assemblies in the internal ring; in other words, the profile is normalized accounting for the volume of fuel assemblies in each ring.

A series of average burnups is then selected, ranging from 40 to 79 GWd/ tHM, with 13 GWd/ tHM steps; the reference initial enrichment for the fuel used in this study is 9%. The profile of Figure 3-17 is then multiplied for each one of these values and 7 burnup profiles are obtained. These burnup profiles are converted to equivalent enrichment profiles, using the correlation derived in section 3.2.3, and a SCALE input file is created for each one of them. This process brings to the creation of a SCALE input file for each one of the average burnup values selected. At this point the Monte Carlo simulation is run.

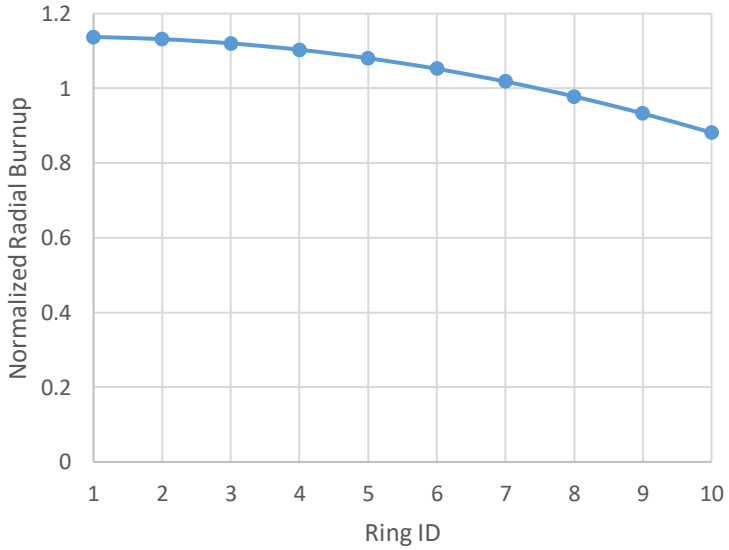

Figure 3-17. Guessed normalized radial burnup profile, 1.3 peaking factor

Each simulation (4 in this example) provides a value for k and a fission density profile that can be normalized.

Figure 3-18 plots the reactivity in pcm as a function of the average burnup values. The reactivity decreases as the burnup increases, as expected, and the critical configuration is obtained for burnup on the order of 56 GWd/ tHM.

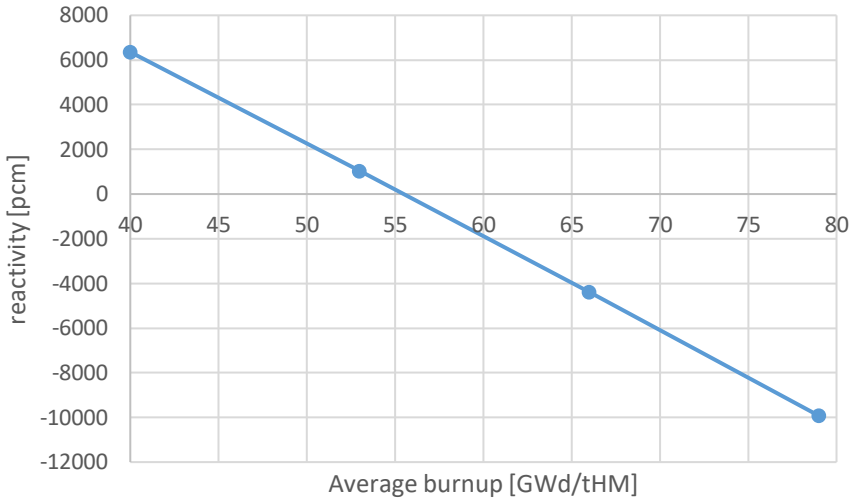

Figure 3-18. Reactivity vs average burnup for specific normalized profile

Figure 3-19 shows the normalized fission density profiles for various burnup values. We can notice that the peaking factor slightly decreases as the average burnup increases.

The critical power density profile is illustrated in Figure 3-20. The plot shows the presence of a flux depression in regions of lower burnup (external rings) where the average burnup of fuel is lower.

Further calculations have shown that lower burnups in the external rings are needed for more uniform power density distribution, as proven by the ensemble learning step that will be described in the following section.

The results demonstrate that, in order to achieve high discharge burnup, an optimal burnup distribution features highly burned assemblies at the edge of the core and more fresh assemblies in the center of the core. On the other side, this results in higher peaking factors.

For the 19.75% enrichment case, preliminary results show that local criticality is achieved due to the large amount of fissile material in the fuel.

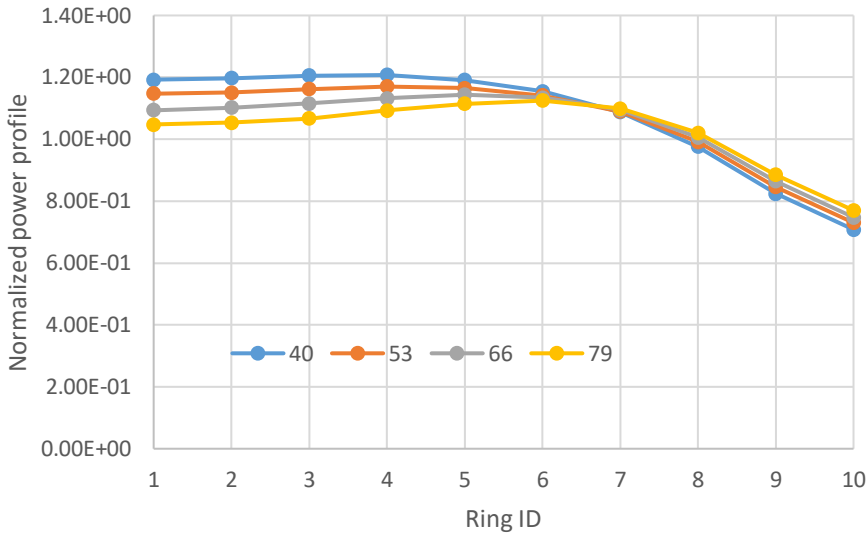

Figure 3-19. Normalized radial fission density profile for various average burnup values in GWd/ tHM

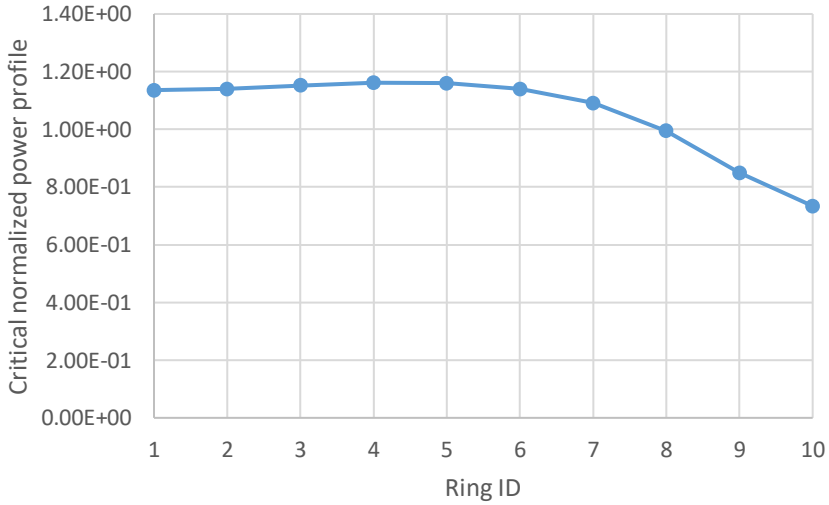

Figure 3-20. Critical fission power density profile; average burnup equal to 59 GWd/ tHM

This work assumes that fission power profile close to flat is a valid reference core configuration for performing the online refueling operations. The flat power profile condition will be analyzed in the following section.

3.2.4.2. Ensemble learning procedure for determination of flat power distribution configuration

Several groups of simulations of the type presented in the previous section have been run and a machine learning approach has been used in order to determine the burnup profile that would result in an almost flat fission density profile. This approach is not expected to provide the exact condition of flat power profile, because of several reasons, among which the non-linearity of the solution of the transport equation and the limited number of simulation data available, but it is expected to provide a configuration at least close to the desired condition.

The variables involved in the regression problem are the burnup profiles, the associated fission density profiles (not normalized) and the associated multiplication coefficients. Ensemble learning allows to correlate multiple inputs (burnup profile array) to multiple outputs (fission density array). The ensemble learning calculation has been performed on MATLAB using the built-in function *fitensemble*; this function takes as input the two variables to be correlated (in separate matrices), the number of learning cycles for the training process and the type of algorithm to be used for the regression; the method selected for this option is *bag*, required for regression problems. Note that the regression operations that involve the fission density profiles, use the non-normalized arrays, because of the need of being able to differentiate between two identical normalized profiles that have different k; for this reason the conclusions of this analysis are strictly specific for the set of parameters (number of generations and particles per generation) selected for the simulations that have been run as part of this work.

Since the objective of the analysis is the determination of the flat power configuration in critical conditions, the first step consisted of the identification of the flat fission density profile that provides k equal to 1. The regression function has been run using the fission density profile as input and k as output and the ensemble learning model has been computed. Then a series of flat fission density profiles has been created, each having a different average fission density value; for each of these profiles, the corresponding k has been computed by applying the regression model and the critical fission profile has been found for a fission density value of 4.9e-7 fis/cm^3.

Once the flat critical fission density profile has been identified, a second regression step has been performed, to compute the burnup profile corresponding to this fission density profile. the regression calculation had as input the fission density profile and as output the burnup profile. Once the regression calculation has been run, the ensemble learning model has been applied to the

flat critical fission density profile and the corresponding burnup profile has been found. Figure 3-21 shows the derived burnup profile, which is slightly peaked in the center of the core.

This profile has been verified on a full core SCALE simulation that provided the fission density profile presented in Figure 3-22. The plot shows that the fission density profile is not completely flat, but the peaking factor, on the order of 1.1 for the maximum and 0.8 for the minimum, is relatively low. Also note that the profile strongly depends on the ensemble used for training the data: more observations having low burnup in the periphery of the core would most likely improve the prediction

Keeping in mind that the power in the core of the AHTR during normal operation will not be completely flat, the burnup profile derived in this section has been considered appropriate for the analysis of the reactivity variations during online refueling operations, that will be presented in the following section.

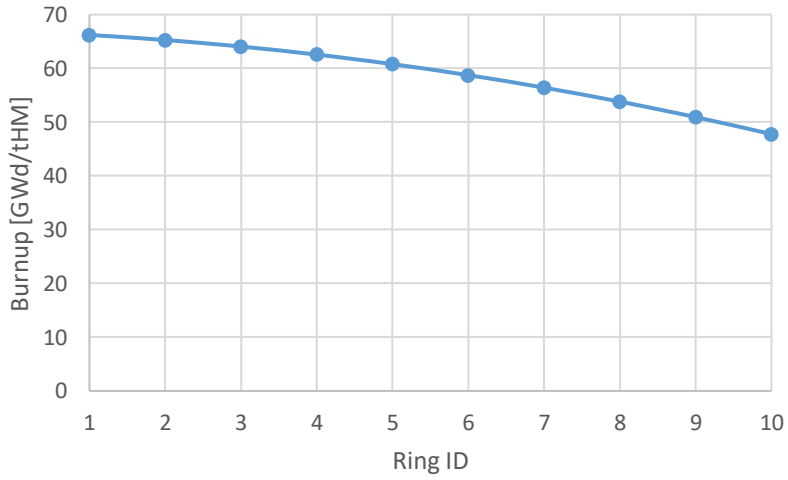

Figure 3-21. Burnup profile calculated from multivariate regression

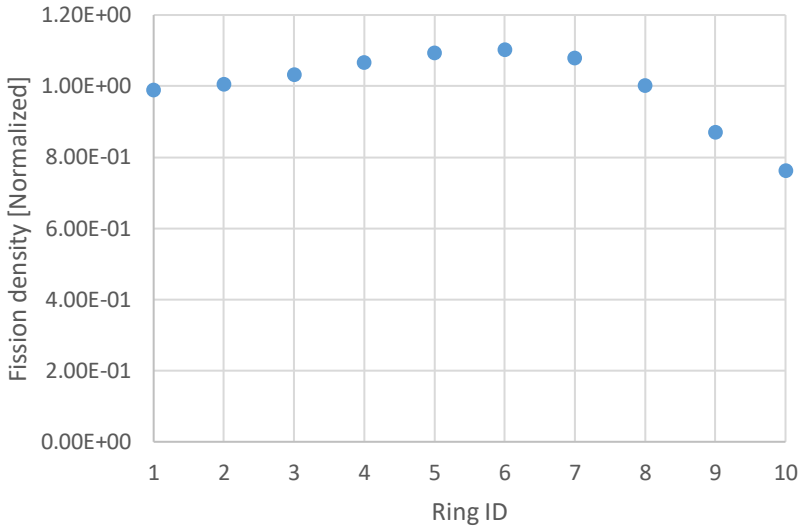

Figure 3-22. Fission density profile derived from regression burnup profile

3.3. Reactivity variation during the refueling transient

The reactivity variation due to the insertion of a control rod and extraction of an element from the core has been studied using the SCALE full core model illustrated in the previous sections. This model assumes 10 radial rings and the burnup profile presented in the previous section, derived from 9% initial enrichment. In order to assess the dependence of the reactivity variation on the position of the assembly in the core, identical simulations have been run with an element extracted at different radial locations; Figure 3-23 shows the three different core locations considered for these studies, along with the horizontal core cross section: the locations are the 1st, 6th and 10th ring, identifiable in the figures by a single assembly of different color, and named internal, intermediate and external, respectively. Note that the power profile considered in these studies is not completely flat in the radial direction; this factor has an influence on the radial dependence of the reactivity variations, but other factors come into play, such as the radial leakage and the moderation capability of the reflector rings.

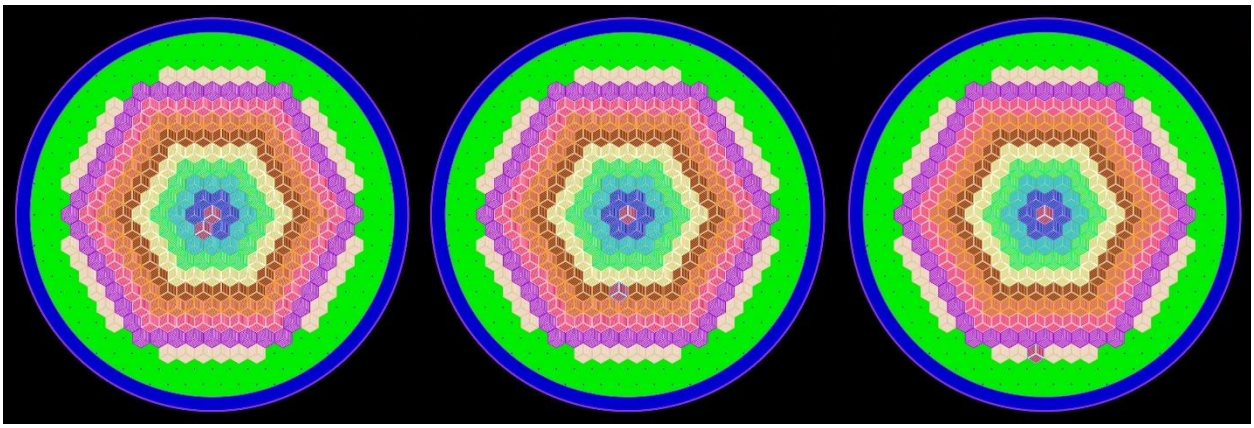

Figure 3-23. 10-rings full core model and locations of element replacement (2nd, 6th and 10th ring in left, center and fight frame, respectively)

The SCALE simulations have been run using a relatively large number of generations and particles in order to provide an acceptable statistical precision; the precision needed however may change based on the type of problem that is being simulated, so, for the same number of particles and generations, some problems show a very small relative uncertainty and some others show a larger relative uncertainty, making the interpretation of the results somewhat more challenging.

The number of generations used for these simulations is 260, of which 80 are skipped in order to converge the neutron source; the number of particles per generation is 100,000, which, combined to the total number of active generations, results in an average uncertainty on the order of 15 pcm. Two groups of simulations have been conducted, one with the intent of understanding the reactivity variations due to the insertion of the control rod into a spent fuel element and its extraction from the core, another one with the intent of analyzing the reactivity changes due to the insertion of a fresh fuel element into the core and the extraction of the control rod from it. Note that there is no difference in methodology between the two groups of simulations, because one can be seen as the reverse in time of the other and, since the SCALE simulations are static in time, they can be all executed at the same time with the same approach. The only difference is the use of a different burnup for the removed/inserted element.

3.3.1. Removal of a spent fuel assembly

The removal of a spent fuel assembly assumes that the assembly that will be removed from the core has a burnup of 100 GWd/ tHM, corresponding to an equivalent enrichment of 1.63%. Note that the type of fuel considered for this study, in its fresh configuration, has a discharge burnup of about 60 GWd/ tHM for a single-batch cycle (single assembly); in online refueling configuration this fuel would theoretically be capable of reaching about double the discharge burnup of the single-batch cycle, about 120 GWd/ tHM.

Figure 3-24 shows the reactivity variation for the control rod insertion and the assembly extraction for the internal core location. Figure 3-25 shows the same parameters for the intermediate core location. The results for the external core location are not reported here because they are very similar to the results for the internal core location.

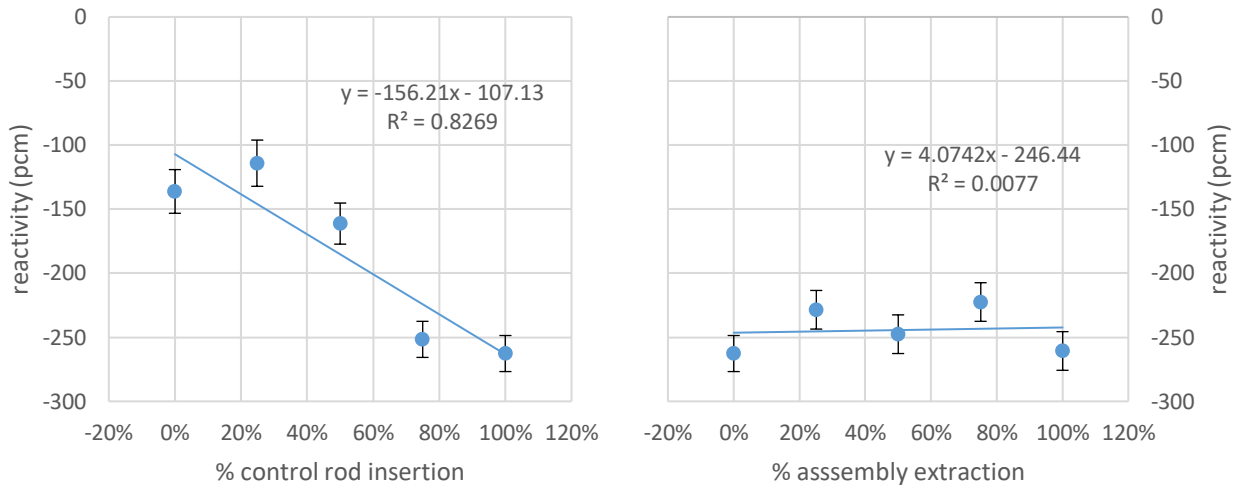

Figure 3-24. Reactivity variation for control rod insertion and assembly extraction at internal core location for spent fuel

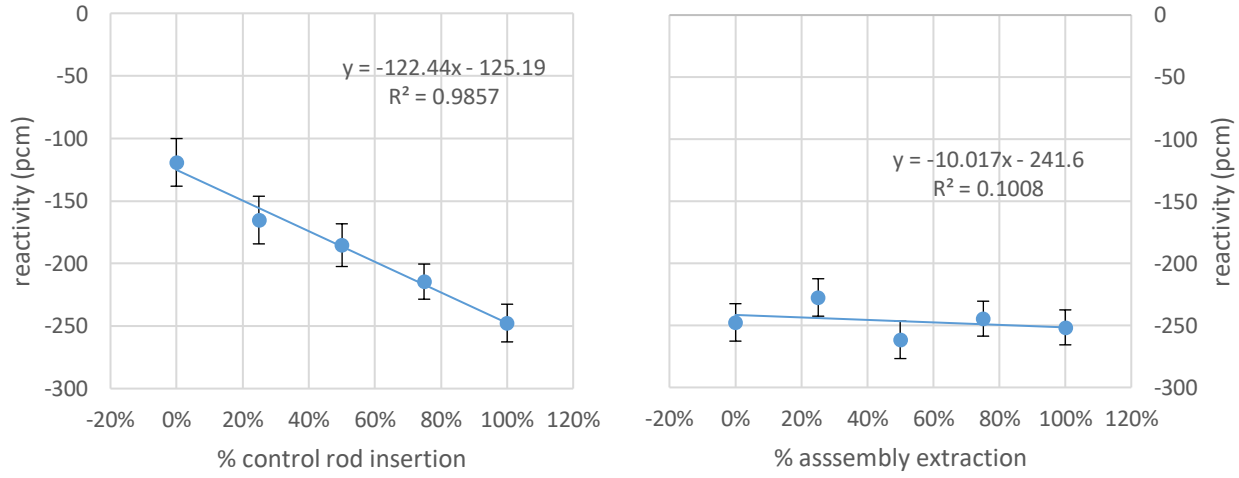

Figure 3-25. Reactivity variation for control rod insertion and assembly extraction at intermediate core location for spent fuel

Looking at the reactivity behavior for the internal core location (Figure 3-24), the insertion of the control rod in the spent assembly causes a reduction of reactivity on the order of 150 pcm, while the extraction of the spent assembly with control rod from the core does not cause a substantial reactivity variation. This behavior is somewhat expected since the spent fuel assembly has low reactivity; one might expect the reactivity to increase, because of the absorption potential removed from the core, but probably the moderation potential coming from the graphite in the assembly,

which is also removed from the core, counterbalances this effect, resulting in a zero net variation of reactivity. Note that the uncertainty in the results is still relatively large compared to the variations involved in this transition, especially for the assembly extraction case; however, it is small enough to allow a general understanding of the reactivity variations involved.

Considering the intermediate core location (Figure 3-25), the amount of reactivity extracted during the insertion of the control rod is about 125 pcm, while the extraction of the assembly still does not have consequences on the reactivity. The external core location, not reported here, has a very similar trend to the internal core location.

On a general level, it is possible to conclude that the insertion of the control rod in a spent assembly causes a decrease in reactivity of about 125 pcm with small dependence on the core location; the extraction of the assembly with the control rod inserted causes a negligible or easily controllable reactivity change, independently from the core location.

The left frame of Figure 3-26 shows the ratio between the average fission density in the portion of the assembly where the control rod is inserted and the average fission density of the assembly with the control rod completely extracted. The curve is slightly affected by the fact that the axial power profile is not uniform. The useful information that can be extracted from this plot is the fact that the insertion of the control rod causes a reduction of power to about 60% of the nominal value in the region that is affected by the specific control rod; this number is consistent with other types of reactors.

The right frame of Figure 3-26 shows the ratio between the power of the assembly (with control rod) being extracted and the power of the same assembly before beginning the extraction (which, from previous considerations, is about 60% of the nominal power before insertion of the control rod); as the assembly is extracted, the power decreases following a sinusoidal behavior, as expected. The residual power at the end of the extraction is about 3%, due to the neutron flux propagating out of the core.

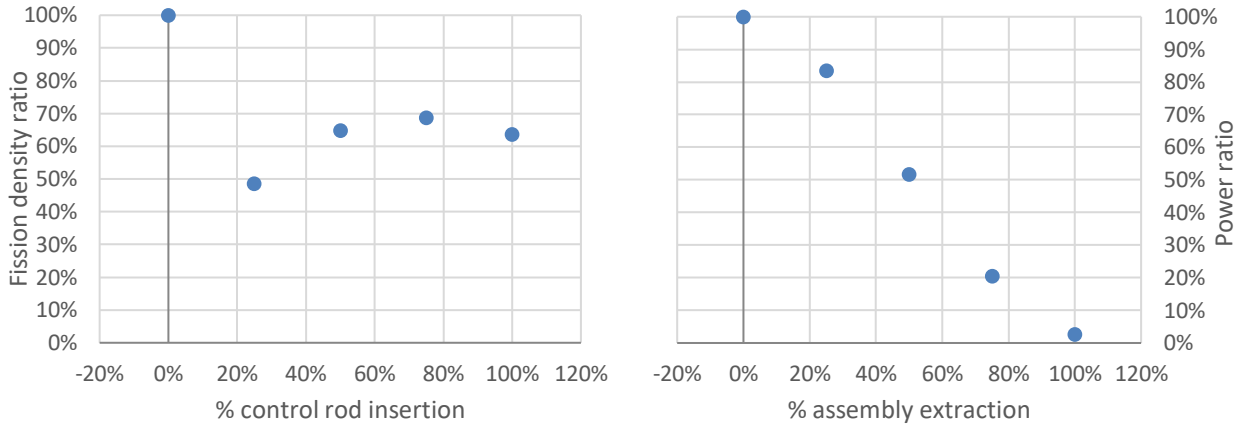

Figure 3-26. Ratio of fission density of assembly portion with control rod over average fission density of assembly without control rod (left) and ratio of assembly power as function of elevation over static assembly power (right)

3.3.2. Insertion of the fresh fuel assembly

Similar calculations have been performed for the insertion of a fresh fuel element in the core. The same approach and terminology have been used for this section, but for the fresh assembly insertion the operations are performed in the reversed order.

Figure 3-27, Figure 3-28 and Figure 3-29 show the result for fresh assembly insertion and control rod extraction for internal, intermediate and external core location, respectively.

Note that in fresh fuel conditions high reactivity variations are involved, so the uncertainty level provided by the simulations is now sufficiently low. All profiles have been fitted using a linear function to give a quick indication of the slope of the curve, but all plots clearly show a sinusoidal behavior, compatible with the expected non uniform axial power profile. As for the spent assembly removal case, both plots associated to the same location are identically scaled in the y direction and put one next to the other, to facilitate the comparison of the contributions of the fresh assembly and its control rod to the total reactivity change.

The contribution of the assembly insertion to the total reactivity change is about 25% of the total, while the main contribution, about 75%, comes from the extraction of the control rod from the element. A viable way of limiting this strong reactivity insertion during normal operation is a slow extraction of the control rod, in such a way that the strong reactivity excess of the fresh element can be diluted over the first days of the cycle; after the first days in the core, xenon will build up and the reactivity of the element will be reduced substantially and the control rod can be extracted or adjusted consequently.

The reactivity variations associated with fresh fuel are noticeably more substantial than the ones of the spent fuel and, unlike the spent fuel case, they seem to have a dependence on the radial location in the core, due to the non-uniform burnup profile. The reactivity insertion due to a fresh assembly insertion is 220, 250 and 150 pcm for the internal, intermediate and external ring, respectively; similarly, the reactivity insertion due to control rod extraction, which is more substantial, is equal to 550, 800 and 450 pcm for the internal, intermediate and external ring, respectively.

Similar simulations have been performed for the 19.75% enrichment case. In this case, results seem to suggest that the closer the fresh assembly is to the reflector, the higher will be its impact on the overall core reactivity. This effect is far less noticeable in the spent fuel assembly case and

its cause could be the advantage, in terms of reactivity, of the vicinity to the reflector region of the fresh fuel assembly.

This aspect highlights the importance that the reflector region, represented by the removable ring of graphite assemblies and the permanent reflector, has in determining the criticality of the system. From the online refueling perspective, the importance of the reflector region represents a supporting argument for the option of moving the control rods and the respective guide tubes from the active region of the core to the replaceable reflector ring, thus freeing up space in the upper plenum volume for the maneuvering of the assemblies during the online refueling operation.

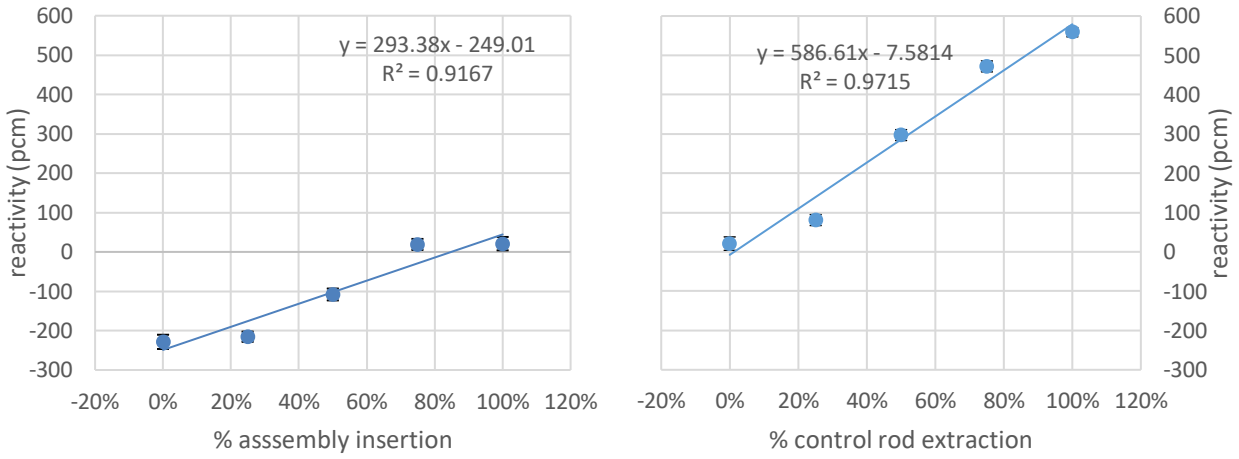

Figure 3-27. Reactivity variation for control rod insertion and assembly extraction at internal core location for fresh fuel

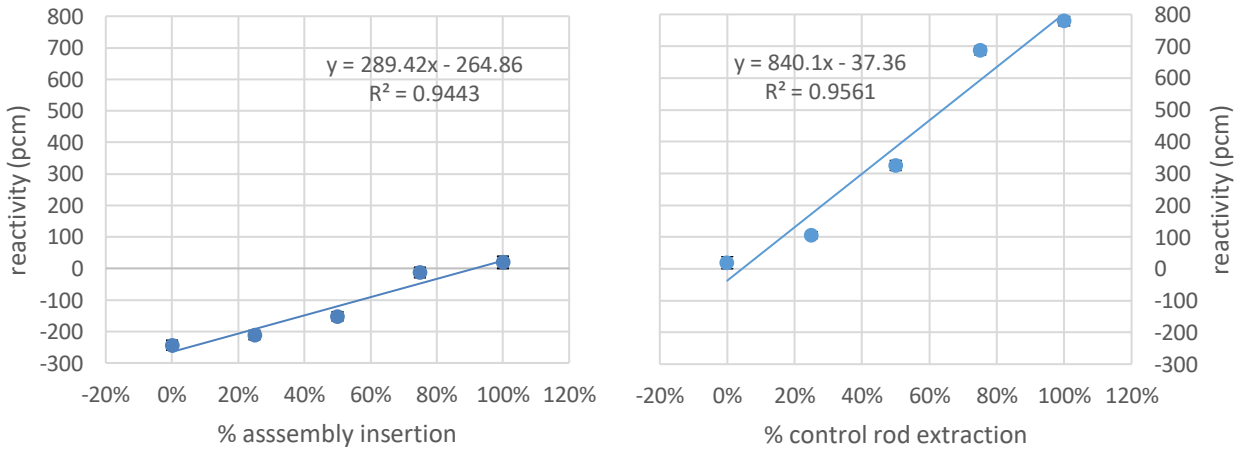

Figure 3-28. Reactivity variation for control rod insertion and assembly extraction at intermediate core location for fresh fuel

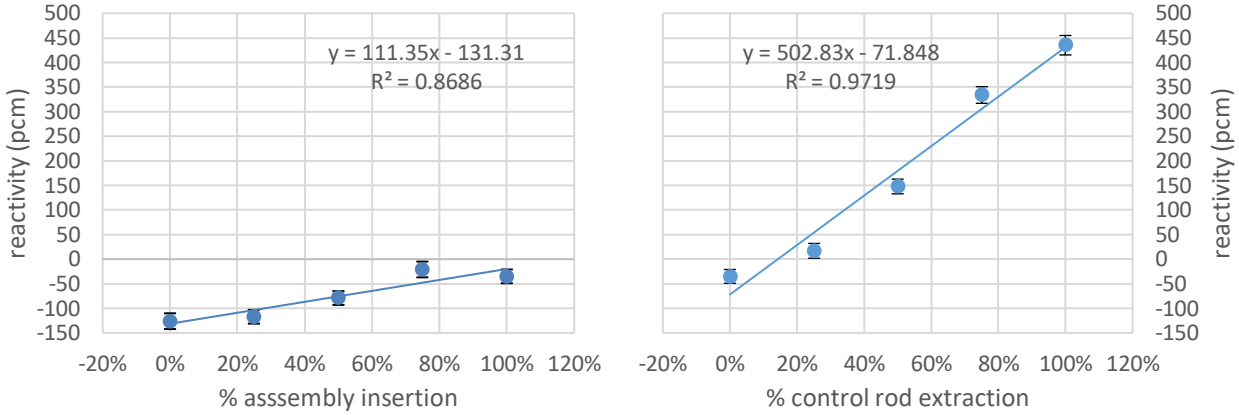

Figure 3-29. Reactivity variation for control rod insertion and assembly extraction at external core location for fresh fuel

3.3.3. Core neutronic feedback

The core neutronic feedback has been evaluated in previous works [12] and it has been integrated in this work in order to model reactivity variations derived from average core fuel and coolant temperature variations, including the changes in coolant density.

The neutronic feedback of the AHTR core is relevant for the calculation of the power evolution of the core and it has been implemented in the RELAP5 AHTR model for the simulation of specific transients [10].

The core feedback has been evaluated using a single assembly reflected model. The SCALE version that has been used for these calculations (v. 6.1.1, [29]) does not provide temperature interpolation for the cross sections in the continuous energy version of the problem, but only in multigroup mode. The cross sections in continuous energy mode are only available at discrete temperature values, typically 600K, 900K and 1200K; smaller discretization steps are needed for temperature dependence evaluations. For this reason, the multigroup approach has been used, based on the Dancoff factor model that was illustrated in previous sections.

The calculation of the reactivity feedback has been performed using 19.75% reference enrichment and a single simulation has been run for each selected combination of fuel and coolant temperature.

Ranges of investigated temperatures are 900-1500K for fuel temperature and 900-1100K for coolant temperature; the uncertainty obtained for this group of simulations is on the order of 10 to 15 pcm, which is accurate enough to provide the required information.

The results, shown in Figure 3-30, indicate that fuel temperature plays the major role in reactivity variation, as expected, whereas coolant temperature is far less influential; note that the dependence on coolant temperature includes the effects of coolant density reduction with temperature.

Reactivity coefficients have been calculated from the curves presented in Figure 3-30; the average coefficient for the fuel temperature is about -4.5 pcm/K and the mean value for the coolant temperature is about -0.5 pcm/K. Both coefficients are negative; the coolant temperature coefficient is close to 0, as expected, due to its moderation capabilities. Note that some studies have found positive coolant coefficients, but small enough to not compromise the safety of the reactor.

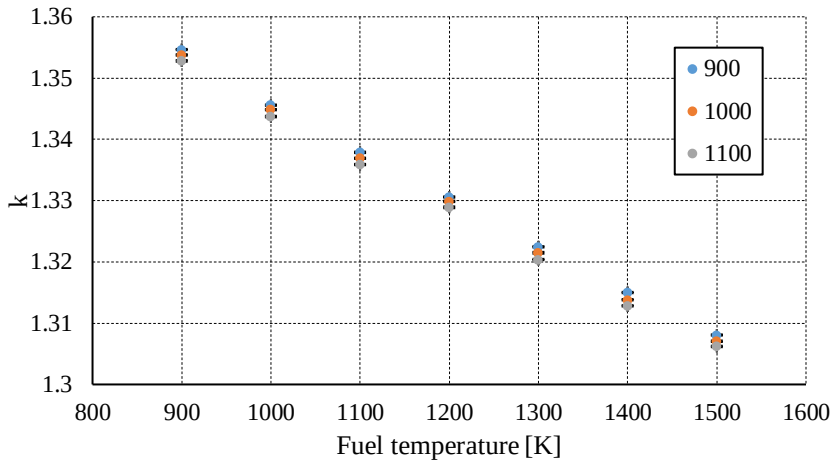

Figure 3-30. Multiplication coefficient k as function of fuel temperature for various coolant temperatures (900K in blue, 1000K in orange, 1100K in gray)

3.4. Refueling and control strategy

In the previous sections an illustration of the effects on reactivity due to assembly replacement has been given. Figure 3-31 provides a summary of the reactivity changes in pcm at an intermediate core location; the plot shows the reactivity variation for control rod insertion in the spent element, extraction of the spent element, insertion of the fresh element and extraction of the control rod. This curve assumes that the control system is inactive (positions of other control rods remain unchanged) and the thermal feedback does not react, and the initial xenon buildup is not accounted for; the purpose of the plot is to illustrate the overall contribution of the replaced assembly and its control rod that needs to be controlled during the online refueling operation. The main aspect that needs to be highlighted is the relatively small influence of the spent fuel compared to the insertion of the fresh fuel: the insertion of the fresh assembly with control rod brings a reactivity insertion of about 250 pcm, while the effects of the spent assembly extraction are on the order of 150 pcm.

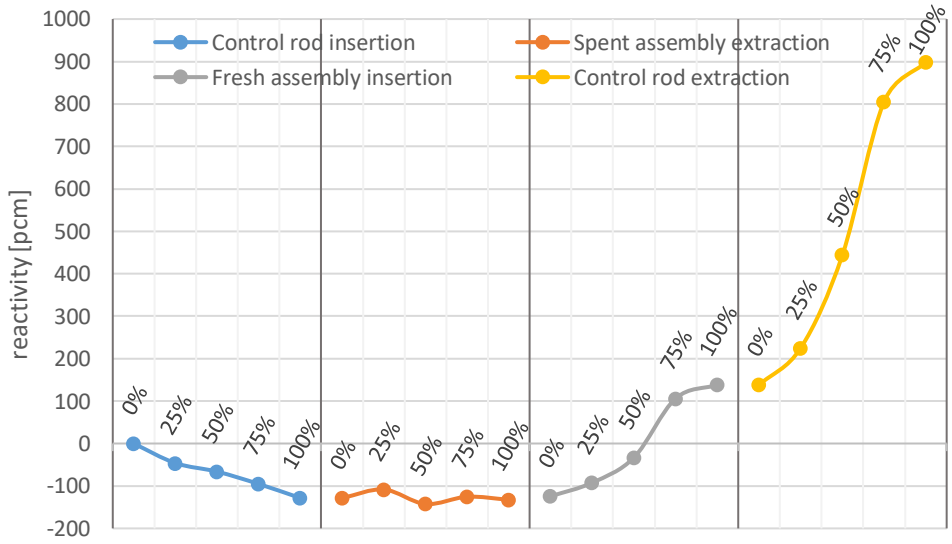

Figure 3-31. Reactivity evolution during the on-line refueling operation at intermediate core location (6th ring), assuming inactive control system and no thermal feedback

From a control standpoint, the extraction of the spent assembly does not require exceptional reactivity adjustments. On the other side, the insertion of the fresh element will most probably

require at least partial insertion of several control rods in other core elements. The procedure seems however feasible and facilitated by the action of the negative reactivity coefficients.
Moreover, note that the assembly modeling considered in this work does not include burnable poison, which would help to reduce the reactivity excess for the fresh fuel configuration.

3.4.1. System response to uncontrolled reactivity variation due to online refueling

The reactivity profile derived in the previous section has been implemented in a RELAP5 full reactor model [12] to assess the effectiveness of the core feedback and the response of the system to the specified reactivity variation, assuming that no control actions are performed during the operation except for the insertion/extraction of the selected fuel element and the respective control rod. Note that the intent of this section is to provide an estimate of the effects and not to assess a specific control approach.
The reactivity variation forced on the system is given in Figure 3-31; the sequence of events has been implemented as follows:

1. Control rod insertion: 60s; delay: 30s;
2. Assembly extraction: 90s;
3. Delay: 5 min; time needed to transfer burned element to pool and fresh element to core;
4. Assembly insertion: 90s; delay: 30s;
5. Control rod extraction: 4 min;

Figure 3-32 shows the uncontrolled reactivity (reactivity insertion without feedback) as a function of time as well as the total reactivity derived from the balancing effects of the neutronic feedback. Figure 3-33 shows the reactor power variation due to the reactivity change. Looking at the overall reactivity variation it is possible to identify four peaks: two are negative and due to the spent assembly removal, the other two are positive and due to the insertion of the fresh element. The power of the system decreases from 3.4 GW to 2.8 GW after removal of spent element, increases to 4.5 GW after the insertion of the fresh element and further increases to 8 GW (after a 9 GW peak) after the extraction of the control rod from the fresh element.
The most relevant contribution to the variation of power is the extraction of the control rod from the fresh element: such a large power increase might compromise the safety of the reactor. A control approach is then required to perform the operation safely; this approach can involve other

control rods, specific burnable poison design, or slow extraction of control rod from the fresh assembly.

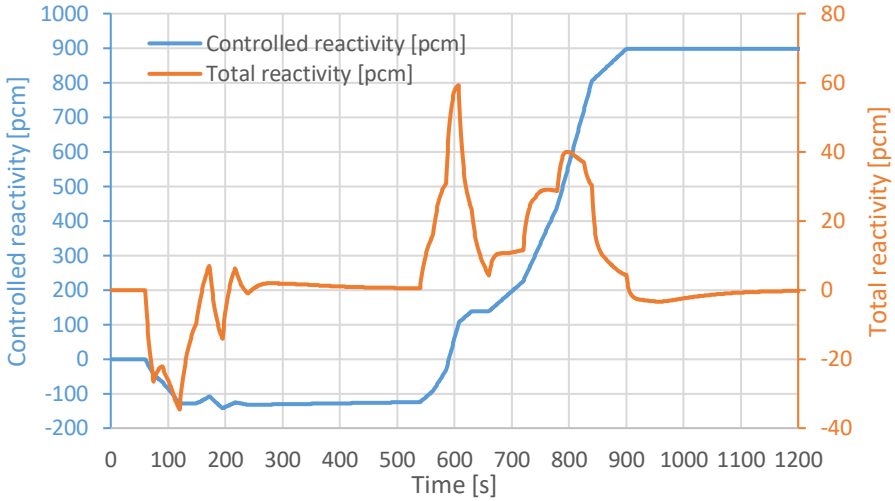

Figure 3-32. Uncontrolled (without feedback) and total (with feedback) reactivity as a function of time

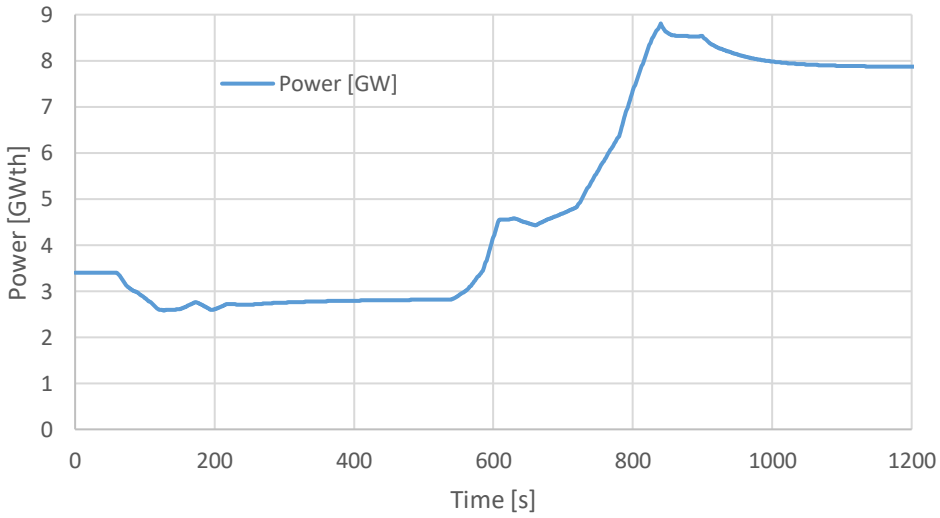

Figure 3-33. Reactor power variation due to uncontrolled online refueling operation

3.4.2. Replacing speed and frequency

Limitations on the fuel assembly removal frequency and speed come from different factors. The frequency of removal is primarily determined by the fuel configuration and the cycle length. The fuel assembly removal speed depends on the mechanical, thermal and hydraulic factors.

Considering the removal operations of the assembly from the core, the following steps will be performed: insertion of the control rod and adjustment of other control rods; removal of the control rod drive and adjustment of other control rod drives; lifting of the assembly in the channel; transfer of the assembly to the refueling lobe; repeat the same operations in the opposite order for the insertion of the fresh assembly. These operations, though very simple, require to be performed very carefully since the flow change is not negligible; also, the system could be compromised from a mechanical standpoint if parts of the system broke. The overall process is reasonably expected to require a maximum of a few hours to be completed, and potentially only a fraction of hour.

On the other side, the refueling frequency is limited by the amount of fuel that is loaded into each assembly. If less fuel is loaded (this helps to improve fuel utilization), the assembly burns faster and requires to be replaced more often. Figure 3-34 shows the replacing cycle (time between two refueling operations) as a function of fuel enrichment and packing fraction for the 253 batches cycle, representing the on-line refueling, for which one assembly is replaced at a time.

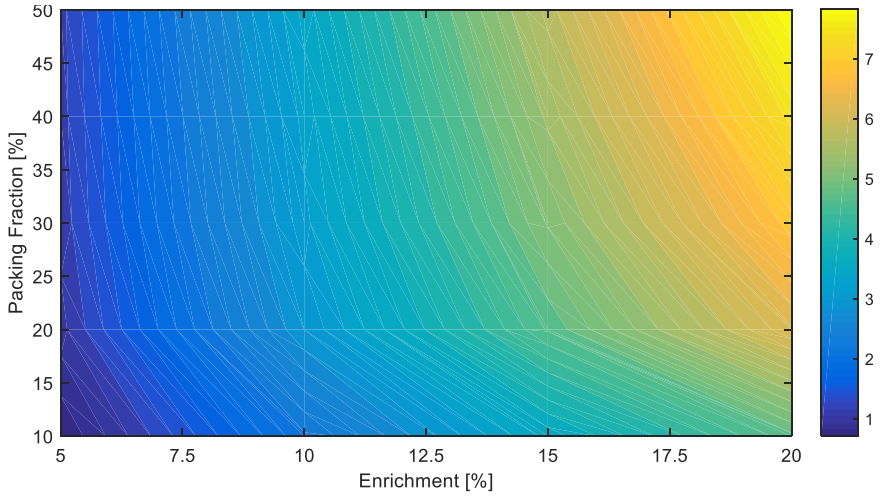

Figure 3-34. Replacing cycle (days) as a function of enrichment and packing fraction for the 253 batches cycle (on-line refueling)

Figure 3-34 shows that even for the lowest heavy metal loading configuration considered for the neutronic analysis [25] (5% enriched fuel with 10% packing fraction), the replacing frequency is of the order of 1 day. For the more reasonable values of packing fraction (greater than 20%) and 9% enrichment, the refueling interval increases to several days.

This analysis shows that a comfortable amount of time is available for performing safely the refueling operations; time margin is available in case the elements need to be let cool down (or up in case of fuel assembly insertion) in the upper plenum.

3.5. Fuel cycle and refueling patterns

The fuel cycle and the approach for the characterization of the refueling patterns for online refueling require a considerable computational effort in order to be analyzed properly. The limitations of the Monte Carlo calculations with respect to this application cis due to the large amount of data that need to be tracked for isotopics and the duration of the simulations for a specific required statistical precision. It is very challenging to simulate full core depletion tracking each assembly separately in a reasonable amount of time; moreover, since the refueling patterns and strategy are not known, a single depletion simulation is not sufficient to study the problem but multiple simulations would be needed, thus noticeably increasing the amount of calculations to be performed.

For the reasons listed in this section, full core depletion simulations have not been attempted. An alternative approach that will be explored in future work and that offers potential advantages in terms of calculation speed is the use of a 2-step procedure including a nodal kinetics codes, particularly NESTLE. A nodal model of the AHTR has been developed in previous work [34] and its features can be easily adapted to its use for online refueling. The substantial advantage of this approach is the small amount of time needed to obtain a solution for the flux distribution in the core, as well as fission density and power profiles, accounting for rod positions and depletion. The main disadvantage of a deterministic kinetics code is the need for accurate cross sections and parameters to be used in the solution of the neutron diffusion problem. This approach is very attractive for online refueling applications because it enables the simulation of different configurations in a relatively short amount of time, thus allowing to have a better understanding of fuel cycle and refueling patterns for online refueling.

Due to the amount of work for the calculation of parameters, such as cross sections or discontinuity factors accounting for fuel depletion, and the necessity of dealing with other aspects of the online refueling, this part of the study will be performed in future work. A few considerations on fuel cycle and refueling patterns can however be made, based on the neutronic studies performed so far.

The initial approach for refueling patterns that has been considered for online refueling is the replacement of the most burned assembly in the core. This approach poses the question on whether the core will reach an equilibrium condition or it will become unstable. This question can be answered only when nodal depletion tools become available, as explained in the previous paragraphs. Note that the assumptions made here is that the core cannot be reshuffled, but in principle an alternative refueling lobe design allowing the storage of more than one assembly at the same time would allow to reposition a partially burned assembly to another core location and then perform the refueling operation with fresh fuel. From a technical standpoint, this type of operation would be eased by the dislocation of the control rods to the reflector rings, freeing up space in the upper plenum. The ability to reposition elements in the core would allow to maximize the fuel utilization and at the same time have partial control on the power density distribution in the core.

Multiple elements can be replaced in the same refueling operation, assuming that the replacement of a single assembly requires a small amount of time. There are no substantial differences between replacing elements singularly or in small groups (e.g., of 3 or 6 symmertic assemblies) since, the individual assemblies will be anyway replaced singularly, one-by-one in short succession in this case.

4. MECHANICAL ANALYSIS AND REFUELING PROCEDURE OPTIONS

The online refueling presents several challenges from the mechanical standpoint and the sequence of operations that need to be performed in order to replace a fuel element while the reactor is operating potentially at full power.

Mechanical challenges derive mainly from the fact that the flow variations with respect to the steady conditions that happen during an online refueling operation are very substantial, on the order of few hundreds of kg per second with respect to the flow in the assembly channel. A second factor, that plays a fundamental role in the mechanical considerations relative to online refueling, is the buoyancy of graphite and structural materials, used to build the fuel assembly, in liquid Flibe.

Refueling procedure challenges derive from the fact that the current AHTR reactor core is designed for standard offline multibatch refueling and not for online refueling. Some aspects that need design updates or modifications in order to make online refueling a viable option are the control rod drive mechanisms, the upper core support plate and the distribution and control strategy of the control rods.

A refueling procedure needs to be developed by defining a sequence of operations that are performed to replace the fuel assembly and maintain the stability of the core.

4.1. Mechanical analysis

The mechanical analysis for the online refueling is aimed to the characterization of the mechanical stability of the assembly during the extraction from the core. The force acting on the fuel assembly as a function of the flow velocity is the reference parameter that drives the mechanical requirements on the maneuvering mechanisms. This force is affected by the buoyancy

4.1.1. Mechanical stability of the refueling operation

This section addresses the stability of the assembly during the refueling operation and provides an analysis of the force acting on a single assembly due to weight, buoyancy and flow.
An important phenomenon relative to FHR design is the fact that the density of nuclear-grade graphite and similar structural materials is lower than the density of Flibe at operating conditions, with the following consequences:

- In order to prevent fuel flotation during handling into the core (offline refueling), the fuel element must be designed so that its average mass density is fairly higher than the average density of the coolant.
- If the online refueling option is implemented, the weight of the fuel element must balance not only the static buoyant force (if it is present), but also the drag force due to the fluid flow. For the same reason, a hold-down (upper) plate is required during normal operation.

A basic monodimensional analysis has been performed to compute the various contributions to the overall force acting on the fuel assembly during operation. The typical design and geometry parameters for the AHTR are used in the calculation, starting with a nominal mass flow rate of about 110 kg/s per assembly channel, a total reactor power of 3400 MWth and a temperature rise across the core of about 50°C. Assembly flow parameters are evaluated from the design parameters, such as profiles of coolant velocity, viscosity, density, Reynold's number and friction factor as a function of the elevation in the core. The mass density and the friction factor are then extracted for the calculation of the force.
The total force acting on the fuel assembly is given by the following contributions:

$$F = F_w - F_b - F_d \quad (14)$$

Where F_w, F_b, F_d are absolute values of the weight, buoyancy and drag force, respectively, and the positive direction for F is downward: if F is negative, the fuel assembly will accelerate upward, if F is positive, the fuel assembly will be subject to a downward force. The following sections present evaluations of separated contributions to the overall force.

4.1.1.1. Weight force

The weight of the fuel element can be evaluated from the geometry and the mass density of the graphite and the control rod.

The density of graphite was assumed to be 1900 kg/m^3; this value is higher than typical values from literature for nuclear-grade graphite, which is about 1850 kg/m^3. The density of the graphite was assumed to be uniform and identical for support structure and fuel plate. Note that this assumption neglects the fact that uranium kernels of TRISO particles have substantially higher density than the other materials; uranium oxycarbide has a density equal to 10.8 g/cm^3, while graphite is on the order of 2 g/cm^3. This assumption is justified by the fact that the amount of heavy metal in a single fuel assembly is on the order of 80 kg, which is about 5% of the overall fuel assembly mass (about 1500 kg).

The density of the control rod is substantially higher, 10.28 g/cm^3 (design parameter, [1]). Despite the mass density of the control rod being higher with respect to graphite, the total volume occupied by the control rod is relatively small, about 2% of the total volume of the assembly, so the contribution of the control rod to the total mass might not be enough to counterbalance the lift force due to the flow.

The resulting average density for the fuel assembly is 2062 kg/m^3, which is higher than the average coolant density (about 1950 kg/m^3), but the margin is small, meaning that the total downward force due to the weight of the body will be almost completely canceled by the buoyancy in still coolant. The total weight of the assembly was found to be about 1530 kg.

4.1.1.2. Buoyant force

The buoyant force can be calculated from the total pressure difference between the inlet and the outlet faces of the assembly and the horizontal cross sectional area of the assembly.

The pressure difference is given by two contributions:

- The weight of the column of coolant between the inlet and the outlet
- The friction pressure drop

The first contribution, the hydrostatic pressure difference, is given by the following integral:

$$\Delta p_w = \int_H \rho * g * dz \qquad (15)$$

Where the density of the coolant is computed as a function of z.

The second contribution, the friction pressure drop, is given by:

$$\Delta p_f = \int_H dp_f \qquad (16)$$

Where the incremental friction pressure drop is provided by the use of an appropriate friction coefficient. In normal operating conditions, the typical values for these two quantities are about 0.6 and 1.0 bar, respectively.

The total buoyant force is given by:

$$F_b = S * (\Delta p_w + \Delta p_f) \qquad (17)$$

Where S is the horizontal cross sectional area of the fuel assembly (without the flow channels area).

The buoyancy effect is expected to increase with increasing mass flow rates, since the pressure difference between the inlet and outlet face of the assembly tends to increase.

4.1.1.3. Drag force

The drag force is the friction force exerted by the shear stresses on the walls of the channels due to the fluid flow through the assembly. The drag coefficient Cf, equivalent to the Fanning friction factor, is related to the Darcy friction factor f as follows:

$$Cf = f/4 \quad (18)$$

The shear stress can be computed from the drag coefficient using the following relationship:

$$\tau = Cf * \frac{1}{2} * \rho * v^2 \quad (19)$$

Where the density and velocity of the coolant as a function of z are provided from 1D hydraulic calculations. The previous equation provides the shear stress as a function of z.
The shear stress, in nominal operating conditions, depends on the elevation according to the following plot:

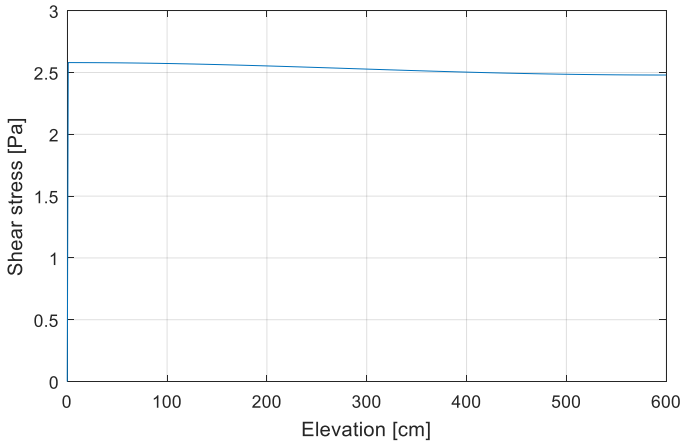

Figure 4-1. Shear stress as a function of the elevation in the core

As shown in Figure 4-1, the shear stress is pretty uniform along the elevation.

The shear stress represents the drag force per unit area, so the total drag force can be computed by integration of the shear stress over the lateral surface of the channels:

$$F_d = \int_S \tau * dS \qquad (20)$$

The overall force can be computed from equation (14).

4.1.1.4. Overall force on static fuel assembly

In nominal operating conditions the total force is -9194 N; the negative sign indicates that the fuel assembly, in absence of constraints, would move upward with an acceleration of about 6 m/s^2. For this reason, the upper plate is required in normal operating conditions.
The value of mass flow rate could be reduced until the resulting force on the assembly is equal to 0. A mass flow rate reduction of about 76.5% is needed in order to reach this condition. In other words, the mass flow rate in the core must be reduced to 23.5% of the nominal value in order to avoid the flotation of the assembly when the upper hold-down plate is removed. If a different approach is used in order to hold down the fuel assemblies during normal operation, this mechanism needs to be able to stand the force and momentum generated by the flow on the assembly that is unlocked from the support structures.

4.1.2. Design alternatives for reducing lift force on assembly

Several options are available for reducing the lift force on the assembly immersed in the flow. These options require design updates of the fuel assembly or of the AHTR operational parameters. One limiting factor of the current design is the fact that the average density of the assembly is comparable to the average density of the coolant, causing the assembly to float if only a small amount of flow is present. One obvious modification that would help prevent the floating would be higher average fuel assembly density; this can be achieved by intentionally designing the control rod (whose density is substantially higher than the density of graphite) bigger or longer. Note that the control rod is fully inserted in the element during its extraction from the core.

The dimensional increase might signify increased absorption, but this aspect can be mitigated by adjusting the composition of the MHC alloy (for instance decreasing the content of Hf).
The control rod length is equal to the length of the assembly, so the dimensions of the control rod can be increased in the horizontal plane, by increasing the horizontal length or thickness of each of the three branches, as shown in Figure 4-2.

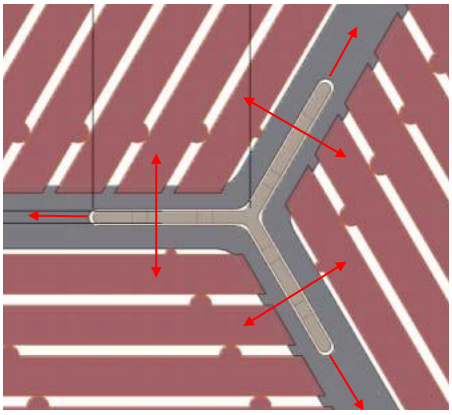

Figure 4-2. Options for increasing control rod dimensions

The dimensional increase of the control rod section needs to be compatible with the structural integrity of the Y-shaped support structure.
The weight of the standard control rod is about 150 kg, while the rest of the assembly is about 1400 kg. The equivalent weight that would be required to hold down the assembly in normal operating conditions is on the order of 1000 kg, which is not achievable by simply increasing the dimensions of the control rod. In other words, the dimensional increase of the control rod branches would help to hold the assembly down but would not be enough to counterbalance the drag of the flow during operating conditions. Other complementary approaches need to be investigated.
An alternative or supplementary way of adding weight to the assembly could be the addition of beryllium oxide to the fuel element structure, which would both increase the weight of the assembly and improve its moderation capabilities. However, increasing the overall assembly weight might not be desirable with respect to its maneuvering outside of salt, where a light element would be preferable; a good alternative to increasing the weight of the assembly is trying to reduce the upward forces causing the drag.

In the online refueling approach, heavy metal loading is not as limiting as in batch reload. If moderation and fuel utilization are not a limiting factor anymore, it is worth considering a higher cross sectional fraction for coolant flow. Note that the current reference design reduces the volume of coolant to the minimum required to maintain the temperature at a reasonable level in order to maximize the moderation capability. An increased cross section for the flow would result in reduced drag force on the assembly and improved maneuverability during refueling operations.
The following plot shows the downward force (positive if the force is directed downwards) as a function of the plate thickness, keeping the assembly box wall dimensions unchanged (larger fuel plate means thinner coolant gap and higher upward force).

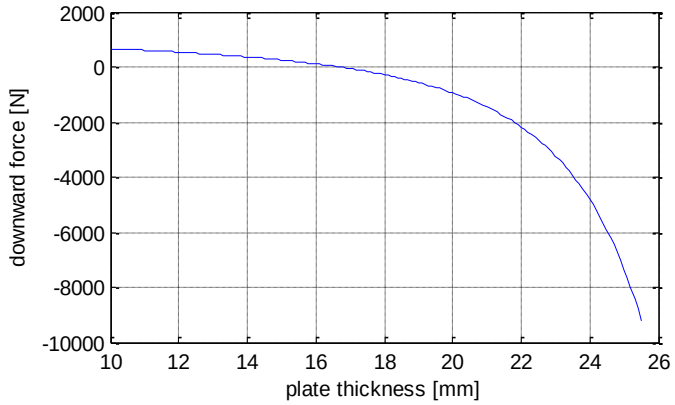

Figure 4-3. Downward force as a function of the fuel plate thickness.

The nominal plate thickness is 25.5 mm, corresponding to about 9000 N upward force (negative). This curve has been obtained assuming that the sum of the coolant gap and the fuel plate thickness remain constant, in order to preserve the overall dimensions of the assembly. The dimension of the fuel stripe is not relevant with respect to this calculation, since its density has been assumed to be similar to the density of graphite. However, probably a reduction of the fuel stripe thickness or packing fraction would be required if the plate dimension is reduced, in order to maintain adequate moderation capability.
Figure 4-3 shows that the upward drag force drops rapidly for thicknesses close to the nominal value (67% reduction for 2.5 mm variation) and, going from high to low plate thickness, the slope of the curve becomes smaller. The equilibrium point, at which the total force on the assembly at full power conditions is null, is obtained for plate thickness equal to 16 mm, about 10 mm less

than the nominal value. The nominal value for the coolant gap is 7 mm, which would become 17 mm if the dimension of the plate is reduced to the equilibrium point.

The reduced flow velocity obtained in this configuration results in smaller Reynolds number and worse heat transfer properties, but the salt heat transfer is relatively good, so this is not a limiting factor. Overall, this approach (increase of the coolant gap) seems to provide a very effective way of reducing the drag force on the assembly.

If the reduction of the coolant gap cannot be considered a viable option, because of moderation requirements, an alternative way of reducing the drag on the assembly would be a temporary reduction of the mass flow rate corresponding to a higher average core temperature rise. Note that the constraint on the core exit temperature derives from the compatibility of nickel alloys for piping with salt, which degrades substantially if the thermal limit is exceeded. If the temperature rise is limited in variation and time, the integrity of these alloys would probably not be compromised, but lack of information about behavior of nickel alloys beyond the known constraints makes it difficult to estimate a reasonable outlet temperature increase for the online refueling transient, which is directly linked to the flow rate and drag reduction.

Before an accurate examination of which of these options are the most appropriate for the online refueling, a better design for the hold down mechanism and the refueling operations needs to be developed, in order to identify the requirements for the fuel assembly parameters.

4.1.2.1. Flow rate reduction for enabling online refueling

The limiting case for enabling the online refueling operation is a 0 total force on the assembly when the upper support plate is removed from the core. A potential approach for reducing the force on the assembly is to increase the coolant channel width and at the same time reduce the core mass flow rate, which affects the drag force, until the total force on the assembly is 0.

Figure 4-4 shows the ratio between the modified and reference mass flow rate as a function of the coolant channel width; the right axis illustrates the variation of the core temperature rise resulting from the mass flow rate variation, assuming that the total core power is maintained constant.

For a 7 mm coolant channel, the flow ratio for zero force is about 28% of nominal, corresponding to a 180°C temperature rise of the coolant across the core. A 100°C temperature increase

(corresponding to 50% flow ratio) can be obtained by increasing the coolant channel width to about 10.4 mm (50% larger than reference design).

If the assembly weight can be increased by adding beryllium oxide at the bottom or by increasing the size of the control rod, both curves shift to the left. Figure 4-5 shows the same quantities described in Figure 4-4, with an additional weight of 200 kg added to the total assembly weight. In this configuration, increasing the coolant channel dimension to 10.7 mm (about 50% more than reference dimensions) provides zero resulting force without requiring a reduction of the mass flow rate or increase of the temperature rise.

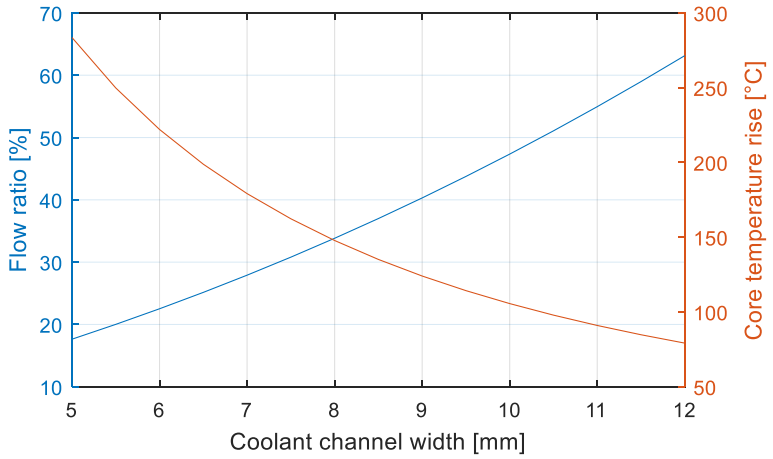

Figure 4-4. Flow rate reduction (left) and core temperature rise (right) as function of coolant channel width, for reference assembly configuration

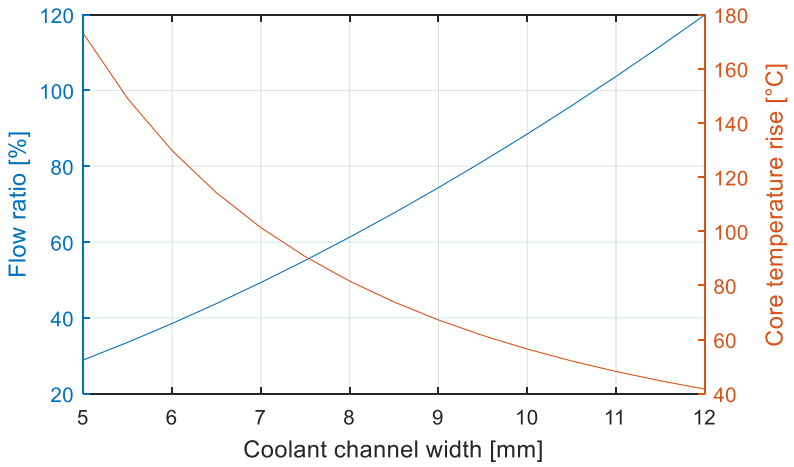

Figure 4-5. Flow rate reduction (left) and core temperature rise (right) as function of coolant channel width, for reference assembly plus 200 kg weight

4.1.3. Force as a function of elevation

The total force acting on the assembly as a function of the extraction elevation has been calculated, to provide a description of the mechanical requirements of the maneuvering devices during the assembly removal.

This calculation assumes the mass flow rate distribution calculated from the fluid dynamics model and presented in the thermal hydraulics section; the mass flow rate splitting between internal and bypass flow, as well as the overall channel mass flow rate, are plotted in Figure 4-6. Note that the contribution of the internal flow remains unchanged as a function of elevation, while the fraction due to bypass flow increases; the overall flow reflects the flow increase due to the reduced flow resistance through the bypass channel.

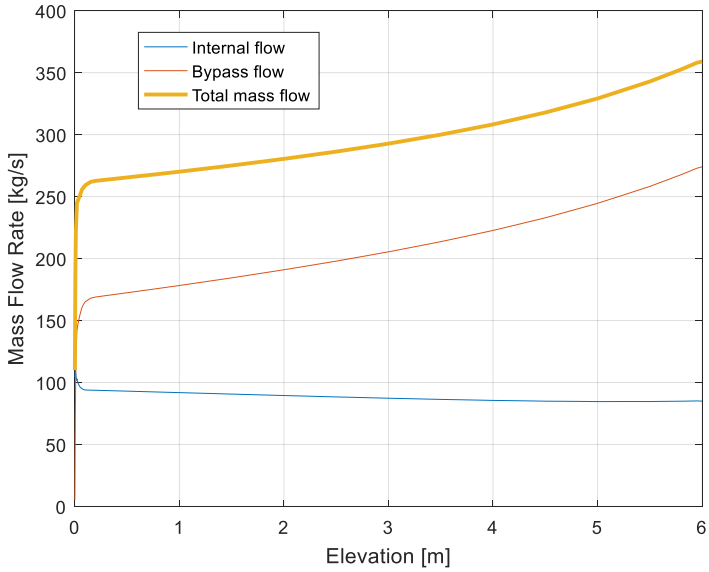

Figure 4-6. Internal, bypass and total mass flow rates in the channel as a function of extraction elevation

The calculation of the force on the assembly as a function of the elevation assumes the same approach that has been presented in section 4.1.1, considering different contributions to the overall force on the assembly. The drag force is given by two contributions, deriving from the two components of the mass flow rate presented in Figure 4-6. The internal drag comes from the integration of the friction along the entire elevation of the assembly, while the bypass drag only accounts for the friction in the range of elevations between the level of the assembly inlet and the level of the outlets of the upper support plate; this is the principal reason why the drag of the bypass flow tends to 0 as the assembly approaches the fully extracted condition.

Figure 4-7 presents the force contributions as well as the overall force as a function of the extraction elevation; the different contributions are plotted in absolute value. The plot shows that the weight (downwards) and the buoyancy (upwards) are the main components. Internal and bypass drag are comparable and have a minor effect on the overall force; as expected, the bypass friction reduces as the elevation of the assembly increases.

The overall force decreases with the assembly elevation, therefore the maximum force, representing the worse scenario, happens at the beginning of the assembly removal; the maximum vertical force on the assembly is on the order of 10000 N.

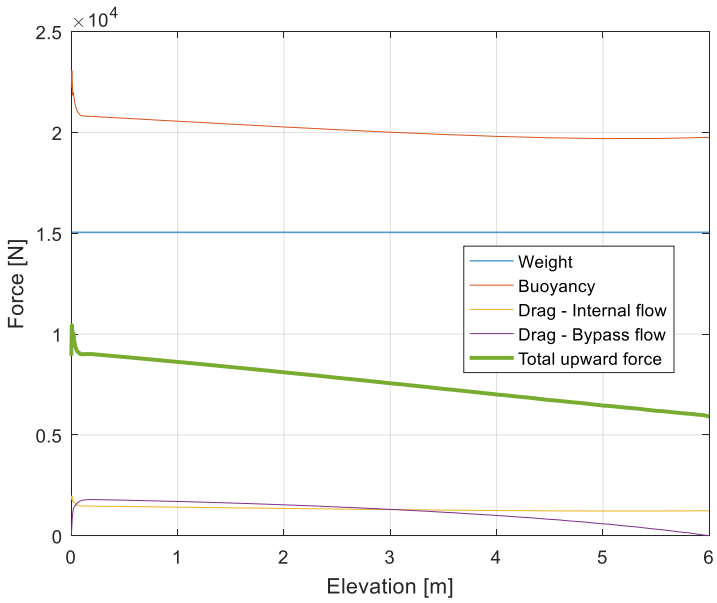

Figure 4-7. Total force and its components acting on the assembly as a function of extraction elevation

The vertical force generates a momentum on the support mechanism or the assembly removal arm, that needs to be compensated if no other support mechanisms are used in order to maintain the assembly straight during the refueling operation.

4.1.4. Hold-down mechanism

The current design of the AHTR features an upper core support plate that serves as a hold-down mechanism for the assemblies. Figure 4-8 provides a graphical representation of the upper portion of the fuel assembly, the grappling collar, which serves to remove the assembly during the refueling operations and locks the assembly into the upper support plate during normal operation. The upper core support plate, also shown in Figure 4-8, is a 35 cm thick support structure with hexagonal perforations where the grappling collar slips in and prevents the element from floating. Since the upper core support plate is a very large structure with limited support from the vessel, the control rod guide tubes are also used as a mechanism to hold down the assemblies during normal operation.

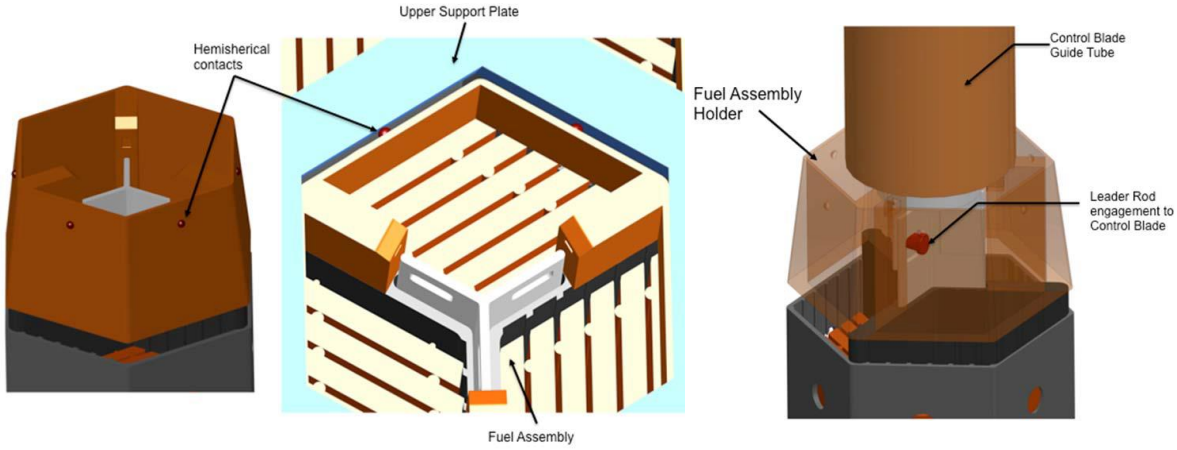

Figure 4-8. Fuel assembly grappling collar, upper core support plate and control rod drive mechanism details [2]

The current design of the upper core support plate and the configuration of the control rods and guide tubes is not compatible with the online refueling procedure for the following reasons:

- The assemblies cannot be singularly unlocked from their location; this would mean that the entire upper plate would need to be lifted for the removal of a single assembly;
- At full power and flow rate, with the upper support plate lifted, the assemblies cannot remain at their locations; instead they would be ejected rapidly in the upper plenum, due to buoyancy and drag. This aspect potentially raises safety issues if it is not resolved;
- At operating conditions, the upper plenum is densely populated by the control rod guide tubes (one per assembly), that would prevent transversal motion of assemblies, assuming that each assembly can be lifted singularly in the upper plenum;

Two principal issues are then identified to be resolved in order to make the online refueling a viable procedure:

- The design of the upper support plate needs to be modified in order to allow the replacement of a single assembly without affecting the mechanical stability of the others.
- The design and control approach for the control rods and guide tubes needs to be modified in order to allow the maneuvering of assemblies in the upper plenum at operating conditions, namely full power and nominal mass flow rate.

Ideally these design modifications should be minimal, in order to minimize their effects on the baseline thermal hydraulic and neutronic design of the AHTR.

4.1.4.1. Options for design modification of the hold-down mechanism

The design of the upper core support plate requires design modifications in order to allow the replacement of a single assembly. The current design locks the grappling collar of the assembly, which is also hexagon-shaped and has inclined sides, so that as the support plate is pushed down, the assembly cannot move in the horizontal plane (as well as vertical).

Since in the online refueling approach each assembly needs to be replaced singularly, the upper support plate needs to be replaced by a different locking approach, such as the one presented in Figure 4-9; this approach still requires the presence of a support plate, but the plate acts more like a support for the locking mechanisms.

The new design of the support plate only prevents the assembly from horizontal oscillation and it allows the assembly to slide in the vertical direction; for this reason, the sides of the hexagonal holes are now vertical and not inclined as in the original design. This implies that the sides of the grappling collar do not need to be inclined, instead they are a simple continuation of the box walls in the vertical direction.

The locking functionality is obtained through rotating wheels with three spokes, positioned at the center of triplets of assemblies, in an alternating manner, so that each hexagon has a rotating wheel at each of the three terminal locations of the respective Y-shaped support structure. The wheels allow the vertical motion of the assemblies when the spokes are aligned with the Y-shaped structure of the support plate, and prevent the assembly from moving in the vertical direction when the spokes overlap the Y-shaped support structure of the assembly. Note that the blockers have small effect (limited to the recirculation regions following the support structures in the vertical direction) on the flow in both the open and closed position. Three blockers contribute to lock down one assembly, each blocker with one spoke; since each blocker has three spokes, we can associate one blocker (three spokes) to each assembly.

During the online refueling, three blockers are rotated, so that the assembly can be extracted; this means that the nearby assemblies will be locked with only two blockers (i.e. two spokes), because the third one is switched to the unlock position. This requires that two blockers out of three are capable of entirely compensating the lift force. For safety reasons (in case one of the spokes breaks and another is involved in the refueling operation) it might be required that one spoke is capable of providing the entire balancing force.

One drawback of this approach is the fact that the entire lifting force for an assembly is counterbalanced by a blocker, which then will have strong requirements from the mechanical standpoint. Assuming that the blockers are capable of fulfilling their function, the entire core lifting force will ultimately be discharged on the upper support plate, which might need help from auxiliary support mechanisms in order to preserve its integrity, but this aspect is out of the scope of this work. Note that in the current AHTR design, this function is currently performed by the control rod guide tubes.

The configuration explained here is just a preliminary cartoon of how the separated locking mechanism may work, and more design details need to be defined for a practical deployment, but this level of detail is sufficient for approach illustration purposes. Some information that would help to improve the design of this approach is the definition of how these blockers are rotated, how they are locked in the required position and eventually replaced if they brake.

Other locking approaches are potentially applicable; for instance, locking mechanisms that act from the bottom of the core (from the lower support plate) would help to release some of the stress on the upper support plate, but they would probably be more complicated to design, since they would need the actuators to reach down into the lower plenum to operate them. Alternatively, the locking and supporting function could be performed by the control rod guide tubes only, but this would probably pose issues on the structural integrity of the tubes, which needs to be guaranteed because these tubes also perform a very important safety function.

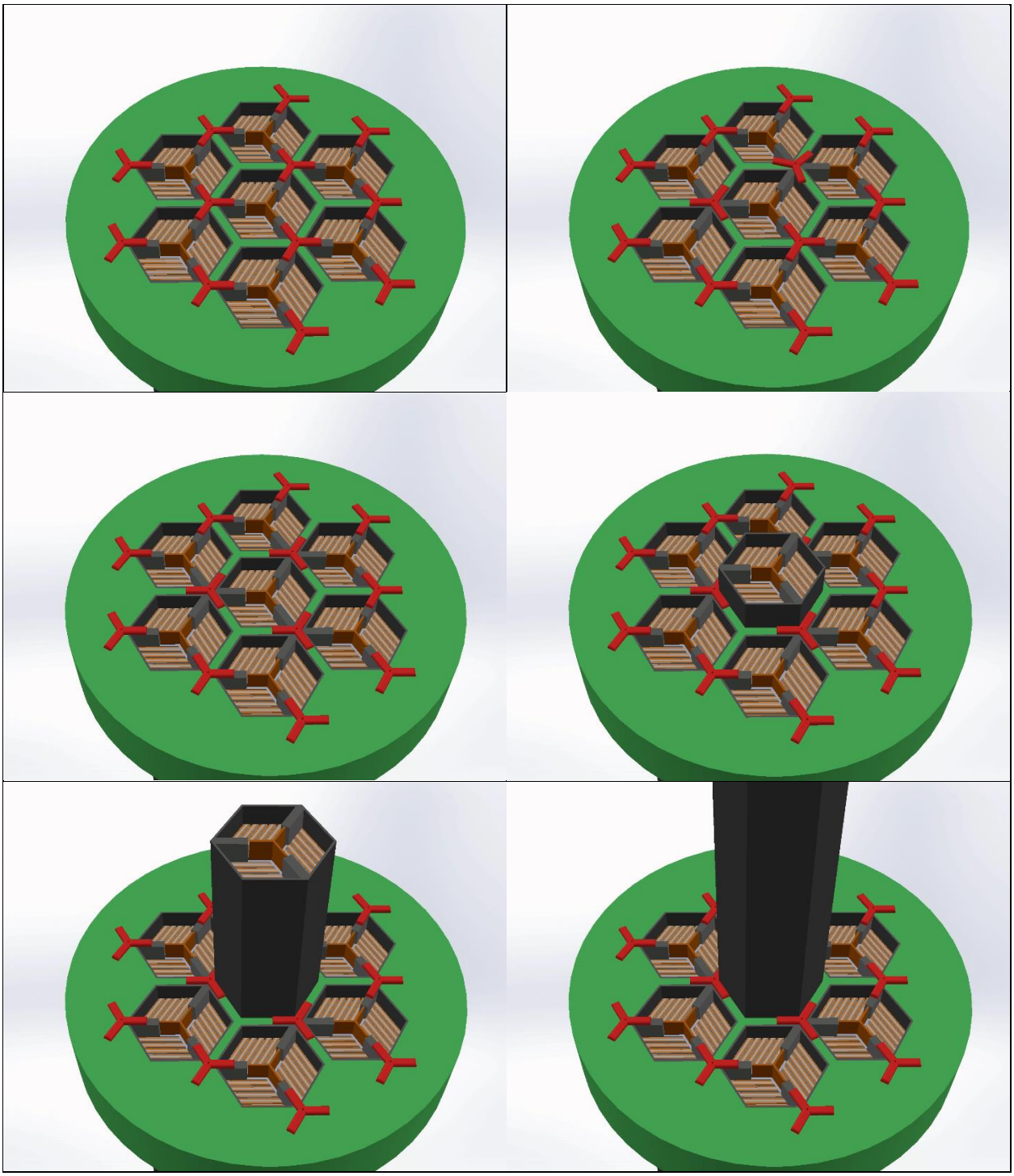

Figure 4-9. Fuel assembly locking mechanism; extraction sequence

4.1.4.2. Options for modifications to the control rod and control method design approach

Assuming that each assembly can be removed from and inserted into the core singularly, once the assembly is completely extracted in the upper plenum, it needs to be moved to the refueling lobe without interfering with the operation of the control rods and the guide tubes.

The current design features a control rod and a guide tube for each assembly, so the upper plenum in normal operation is densely occupied by the control rod guide tubes; each tube is about 20 cm in diameter and the distance between the centerlines of each tube is about 46.8 cm, so there is not enough space to allow the assembly to move in the upper plenum.

Several options for allowing the extracted assembly to move in the upper plenum can be explored.

- The control rod guide tubes that are located on the path between the assembly location and the refueling lobe are temporarily removed, in order to allow the assembly to be moved to the refueling lobe. The control rods of the extracted guide tubes can either be fully inserted in the assemblies or fully extracted with their respective guide tube, and the reactivity of the core needs to be adjusted accordingly. The arm that removes the assembly can rotate around the upper plenum in order to reach the minimum distance location from the extracted assembly and thus minimize the reactivity changes due to the extracted control rod guide tubes.
- The control rod and the guide tube design are reduced to a smaller diameter and the fuel assembly pitch is increased, so that the extracted assembly can be moved in the upper plenum without requiring to extract any guide tube. This option requires to modify the design of the assembly removal arm in such a way that the grappling mechanism in the upper plenum or Argon plenum can move on a honeycomb hexagonal pattern located at the median between nearby guide tubes. This pattern matches the configuration of the honeycomb-shaped upper support plate; this is necessary in order to allow the extracted assembly to move in between guide tubes without touching them. Note that the increased inter-assembly spacing could be filled with graphite instead of salt in order to increase the moderation capability, which is desirable for improving fuel utilization.
- The control rods are moved to the reflector region. This option allows to have an almost empty upper plenum (volume would be entirely filled with hot salt), so the grappling mechanism can be freely moved in the upper plenum. With respect to the transfer of the

assembly to the refueling lobe, if the spacing between the control rods is larger than nominal, the assembly can be transferred through the guide tubes in the reflector region without the need to lift the tubes. In alternative, some free space can be allocated in front of the refueling lobe and every assembly would be transferred to the refueling lobe through this space, regardless of the original location in the core. The lifting mechanism would be conceived as a circular crane-type mechanism that can transfer any assembly to a location in front of the refueling lobe, where a different mechanism grabs the fuel element and prepares it to be transferred to the pool.

With respect to the arm for maneuvering the assemblies in the upper plenum, since the flow would be relatively high during the operation, the mechanism needs to be capable to stand the momentum generated by the flow and the buoyancy. In other words, it might be necessary to have two grappling points, one at the top of the assembly and one at the bottom of the assembly, in order to prevent the assembly from departing from a vertical orientation.

4.2. Potential refueling strategy

A refueling procedure has been developed at a preliminary level. Several options are available with respect to how the refueling operation is performed, and each option has its own advantages and disadvantages. The procedure that is illustrated here is based on minimal modification of the upper plenum design, and other aspects such as reactivity control procedure might not be optimal; more appropriate approaches that require more substantial redesign of the core and reactivity control approach could be developed in the future. For instance, one design modification that would require substantial redesign but would make the online refueling approach more viable is the relocation of the control rods to the reflector region (which is acceptable in online refueling approach because the reactivity excess of the core will be substantially lower): this modification would allow easier handling of the fuel assemblies in the upper plenum, as mentioned in the previous section.

Figure 4-10 shows the sequence of operations for the removal of a single assembly; the insertion of the fresh assembly would be performed following the reversed sequence.

The vertical motion of the assembly is controlled by the control rod guide tube, that can be extracted or inserted in the upper plenum by an electric motor above the flange; the guide tube can be locked to and unlocked from the grappling collar.

The sequence of operations from the operating configuration consists of the following operations:

1. The control rod is inserted in the assembly and detached from the control rod drive tube;
2. The control rod guide tube mechanism is activated and the assembly is extracted to the upper plenum;
3. The control rod guide tubes that are located in between the assembly location and the refueling lobe are extracted from the upper plenum. The relative control rods can either be detached into the respective assemblies or extracted with the guide tube. The decision on whether a specific control rod needs to be extracted or left into the core needs to be made in such a way that the overall reactivity of the core remains sufficiently close to zero;
4. Once the path between the assembly and the refueling lobe has been cleared, the assembly is grabbed by a mechanical arm and pulled into the refueling lobe, where it can be transferred to the pool;
5. The sequence of operations is repeated in the reversed order for the insertion of the fresh assembly, and the core returns to normal operating conditions.

It should be emphasized that this approach minimizes the required design changes on one side, but makes the reactivity control approach during the refueling operation quite complicated. For the scope of this work the minimization of the design changes has been selected as the main priority with respect to other aspects.

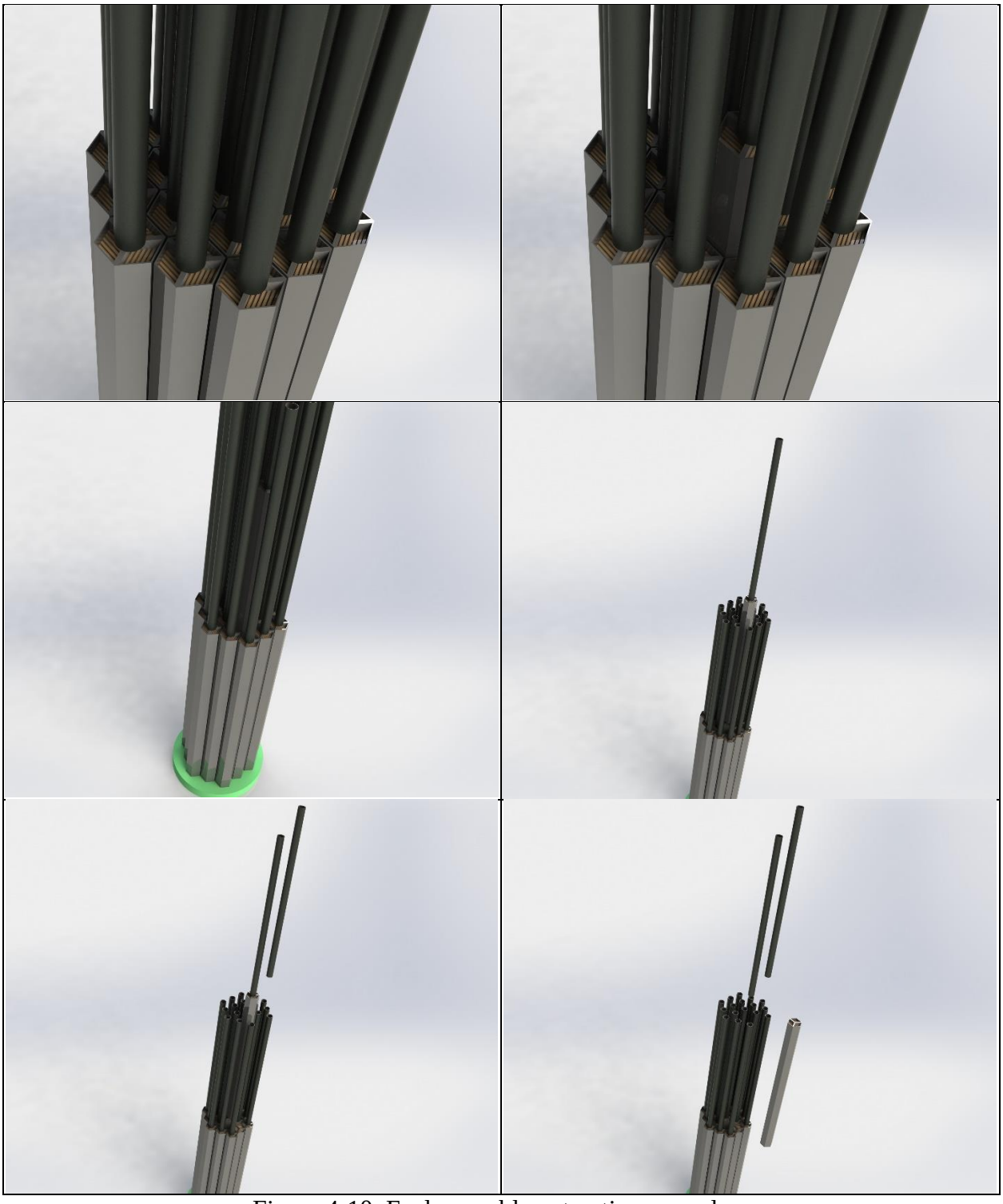

Figure 4-10. Fuel assembly extraction procedure

5. COST MODELING

A preliminary fuel cycle cost modeling for online refueling has been developed to determine the economic advantage over the standard multibatch fuel cycle options.

From the cost performance standpoint, online refueling differs from multibatch cycle in multiple aspects.

Online refueling has two main cost advantage factors over the standard multibatch refueling. The factor that has the major impact is the improvement of fuel utilization due to the substantial increase in assembly discharge burnup. A second factor directly affecting the fuel cost is the increased plant availability due to the fact that the reactor does not shut down during refueling operations; the effects of increased availability strongly depend on the amount of maintenance needed for the AHTR.

The refueling outage has a completely different dynamic, due to the fact that the reactor does not need to be shut down. The cost of the refueling outage is expected to be much lower (potentially negligible) for online refueling.

On the other side, refueling outages for multibatch refueling allow to perform maintenance of the reactor and the core while the reactor is shut down for refueling, limiting the expenses due to maintenance; this would not be possible for online refueling, because the reactor would be operating during the refueling outage, so planned maintenance outages (reactor shutdowns) would have to be scheduled at a specific frequency. In other words, online refueling would still need some shutdown time to perform maintenance operations, which would reduce the savings.

Further savings deriving from the implementation of online refueling involve the number of control rod and drive mechanisms and infrastructure regarding fuel enrichment and storage. The number of control rod drive mechanisms could potentially be reduced because the reactivity excess in online refueling conditions is smaller. The impact on infrastructure is determined by the potential use of 5% enrichment, which would allow a faster deployment of this technology; moreover, online refueling would reduce the amount of assemblies that need to be stored in the pools after being used in the core. Note that the resulting reduction of cooling power would not be as relevant as expected, because of the higher burnup of the discharged fuel.

5.1. Introduction

The modeling approach followed in this work is based on the studies performed by Lewis [25] and Kingsbury [26] on the reference AHTR fuel cycle. Lewis performed a preliminary analysis of the fuel cycle options associated with different packing fractions and enrichments in order to narrow down the fuel configuration selections and to help identifying the bounds to include the most attractive options for the fuel design. Kingsbury updated the preliminary model developed by Lewis using more accurate fuel depletion modeling and results.

The modeling approach is based on the linear reactivity model (LRM), which assumes that the reactivity of the fuel assembly has a linear dependence on fuel burnup. Non-linear reactivity model (NLRM) provides more accurate results. More advanced approaches could potentially be applied, for instance full core nodal methods or Monte Carlo codes, but they are not suitable for a preliminary analysis.

Online refueling is believed to offer potential economic advantages, despite the modifications to the reactor vessel and core design required to make it viable.

The fuel type selected for this study is a result of several initial fuel optimization studies [33] and it is based on 19.75% enrichment and about four TRISO particle layers for each fuel stripe (instead of the initial 7 layers), at 40% packing fraction. The analysis is applicable to other fuel configurations without need for major changes. The choice of enrichment is questionable, since it is relatively high with respect to current standards; however, this option represents the configuration that was originally selected for the AHTR design. The 9% option, representing the current baseline design, has also been considered in the neutronic studies, because it would allow continuous-process fuel fabrication. The 5% enrichment option has been taken into account because it would enable the use of the existing infrastructure for fuel fabrication, which is highly desirable from a cost perspective. For this study, the 19.75% option has been selected as reference and the other options have been considered during the calculation process; partial results and considerations are illustrated for 9% and 5% enrichment.

5.2. Models and methodology for the economic analysis

The methodology developed for the economic analysis of the online refueling is based on a simple approach and a set of assumptions that will be presented in the following paragraphs. This section presents the methodology that will then be used to perform parametric studies on the main cost parameters and to compare the fuel cost of multibatch and online fuel cycles.

5.2.1. Assumptions

Several assumptions have been made in the model development in order to facilitate the analysis and neglect those factors that are expected not to affect the conclusions of this analysis.
One of the main reasons why many of the following presented assumptions have been made is that this study is focused more on the comparison between online and multibatch refueling, than the actual accurate evaluation of fuel cost for online refueling, so some aspects that would otherwise be important are expected to essentially cancel out with respect to the comparison.
The main approximations are presented here:

1. Ignore time value of money.
2. Ignore losses during conversion and fabrication.
3. Use Linear Reactivity Model for evaluations on multibatch fuel cycles, including online refueling. Online refueling is assumed to be a multibatch fuel cycle with a number of cycles equal to the number of assemblies in the core (Plus other assumptions on costs of outages, etc.).
4. Account for refueling outages through the application of a fixed cost. Since an evaluation on the potential outage cost for the AHTR is not available, parametric studies on this parameter have been performed in order to identify the range of costs.
5. Assume prototypic outage and fuel fabrication cost values based on previous work [26].
6. Assume optimized fuel configuration derived from neutronic analysis. No further fuel design optimization has been performed after the economic analysis of the online refueling, even though a specific fuel design configuration exists that minimizes the fuel cost in this specific fuel cycle configuration. Note that the fuel configuration selected for this study has been guessed but it is believed to be close to an optimal fuel utilization condition.

5.2.2. Price of uranium

The cost of U3O8, its conversion to UF6 and the cost per separative work unit (SWU) have been estimated from the information provided online by Ux Consulting Company (UxC, [35]).

For simplicity the cost of uranium and the cost of conversion have been unified in a single converted uranium cost; in other words, UF6 spot price already includes the cost of uranium and the cost of its conversion to UF6.

Figure 5-1 shows the UF6 (uranium plus conversion) and SWU spot prices since 2006, on the left and right axis, respectively. The plot shows that the price of uranium has undergone substantial changes in the last decade and the trend for the most recent period of time is decreasing.

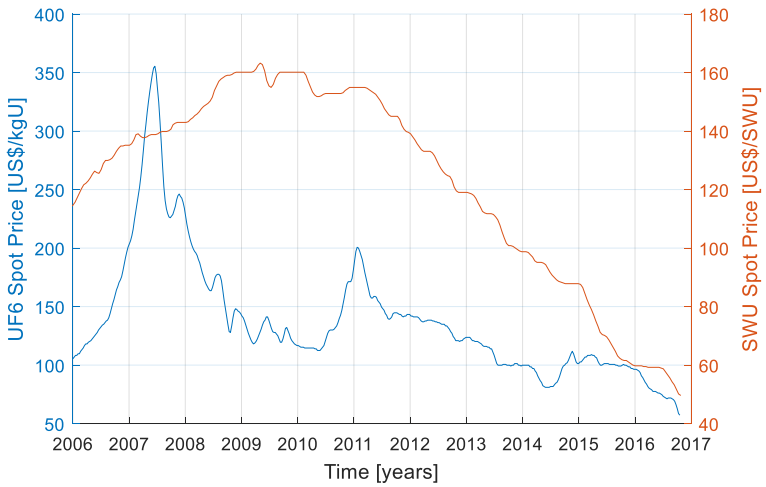

Figure 5-1. UF6 and SWU spot prices since 2006 [reference UxC]

For the scope of this work it has been decided to use the average prices in the last 10 years as reference prices for the calculation of the fuel cost. Table 5-1 shows the average spot uranium prices in the last decade, starting from 2006.

Table 5-1. Average spot uranium prices since 2006 [35]

UF6 average price	104.26	US$/kgU
SWU average price	92.75	US$/SWU

Since utilities need long term uranium supply, the spot price is not the actual cost paid by the utility, which is usually replaced by a long term contract price that is slightly different with respect to the spot price, typically but not necessarily lower. Figure 5-2 shows the spot and long term prices of uranium in the last 5 years. The plot clearly shows that the long term price in the last 5 years has been 20% higher than the spot price; on the other side, this trend is typical of the recent times only, when the price of uranium has been falling substantially with respect to the first decade of the 21st century.

As mentioned previously, this work uses the average spot price in the last 10 years, instead of the long term price; this assumption is justified by the fact that the difference between the two prices is not substantial.

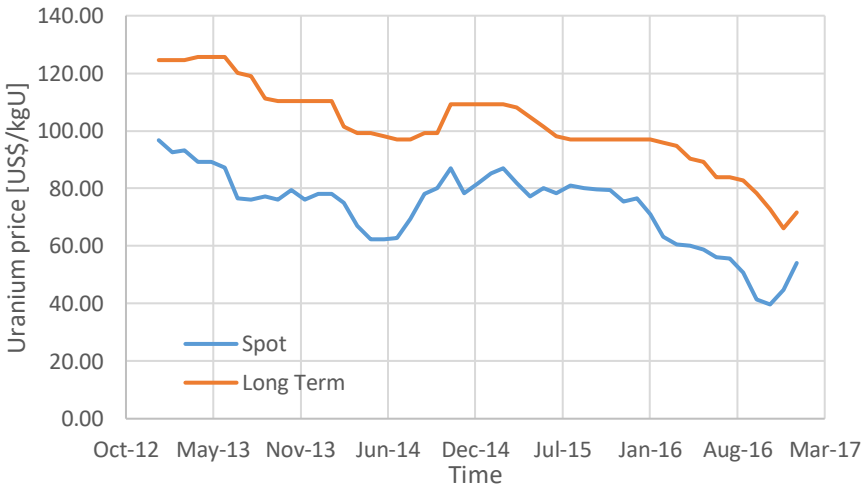

Figure 5-2. Uranium spot and long term prices in the last 5 years [36]

Fixed values have been assumed in this work for uranium and enrichment price, but their variability in time is substantial, as shown in Figure 5-1. Figure 5-3 shows the dependence of the fuel cost on the price of uranium and enrichment in the range of 10 to 150 $/kgU and $/SWU, for uranium and enrichment respectively. The plots show a similar trend for the two quantities, with price of SWU being slightly more influential than uranium price on the final fuel cost; note that, as one of the two prices increases, the overall difference in terms of cost between 2-batch and online cycle becomes larger.

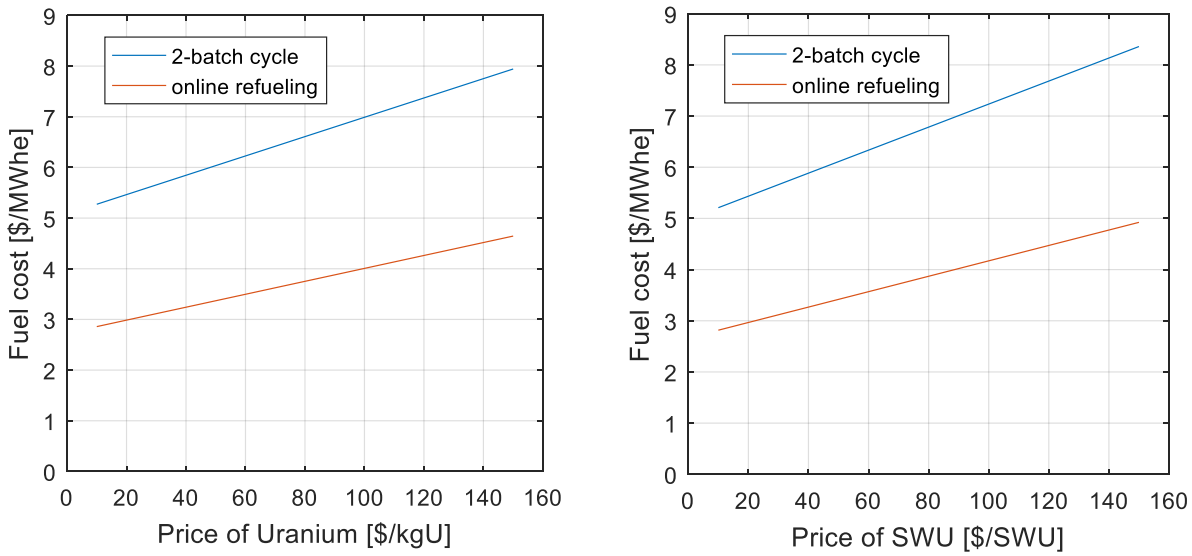

Figure 5-3. Fuel cost for 2-batch and online refueling as function of UF6 price (left) and SWU price (right)

5.2.3. Simplified fuel cycle cost model

This section presents the approach used for the calculation of the overall fuel cost.

5.2.3.1. Separative work

The first step consists of the calculation of the number of separative work units needed for the selected uranium enrichment (19.75% in the reference case; 9% as a secondary option below 10% limit). In the following equations, x_p describes the target uranium enrichment (19.75%), x_f is the weight enrichment of the feed material (assumed to be 0.711% [25]) and x_w is the enrichment of the waste product ("tails"), assumed to be about 0.2% [25]. The enrichments of feed, product and waste material are used to calculate the feed input rate F, the product output rate P and the tails output rate W, using the following correlations [37]:

$$F = P + W \quad (21)$$

$$x_f F = x_p P + x_w W \quad (22)$$

Feed to product and tails to product ratios can then be computed according to the following equations:

$$\frac{F}{P} = \frac{x_p - x_w}{x_f - x_w} \quad (23)$$

$$\frac{W}{P} = \frac{F}{P} - 1 \quad (24)$$

The enrichments are also needed for the calculation of the separation potential V, describing the distance in terms of enrichment between the final product and the feed material. The separation potential can be calculated using the following formula:

$$V(x_i) = (2x_i - 1) * \ln\left(\frac{x_i}{1 - x_i}\right) \quad (25)$$

The potential, along with the uranium processing rates, is used for the calculation of the separative work required to achieve a specific product enrichment. The SWU factor S is measured in SWU per kg of enriched product and it can be calculated using the following formula:

$$S = V(x_p) + \frac{W}{P} * V(x_w) - \frac{F}{P} * V(x_f) \quad (26)$$

The SWU factor is used for the calculation of fuel cost per unit mass

5.2.3.2. Fuel cost per unit mass of uranium

The calculation of the fuel cost per unit mass is made of four components:

1. Cost of uranium, computed from the uranium price PU [$/kgU] in U3O8 form;
2. Cost of conversion to UF6, computed from the price of conversion PC [$/kgU] to UF6;
3. Cost of enrichment, based on the separation price per SWU (PS) and the overall separation work S;
4. Cost of fabrication, computed from the fabrication price PF [$/kgU].

With reference to the fabrication cost, note that it is assumed here that it can be represented as cost per unit mass of Uranium; this simplifying assumption does not hold in general, because the cost of fabrication of some components of the fuel assembly, such as supporting structures and structural materials, are not directly proportional to the amount of uranium in the assembly. However, this study makes this simplifying assumption for two main reasons; first, the cost assumed here has been shown to be higher than average fabrication cost estimates performed in other work [26]; second, it has been shown that the driving factor for fuel fabrication cost is the fabrication of TRISO particles [26], which is proportional to the amount of uranium loaded.
Accounting for losses during the conversion (lc) and fabrication process (lf), the overall fuel cost per unit mass is given by the following formula:

$$P\ [\$/kgU] = \left[\frac{PU}{(1-l_c)(1-l_f)} + \frac{PC}{1-l_f}\right] * \frac{F}{P} + \frac{PS}{1-l_f} * S + PF \quad (27)$$

If the losses are assumed to be negligible, the fuel cost per unit mass becomes:

$$P\ [\$/kgU] = [PU + PC] * \frac{x_p - x_w}{x_f - x_w} + PS * S + PF \quad (28)$$

The price of uranium plus conversion and the price of enrichment are provided in section 5.2.2. the price of fabrication is relatively unknown at the present state of knowledge, due to the novel assembly design. For this reason, parametric studies have been conducted in order to establish a reasonable estimate of the fabrication cost. It has been assumed that a base fabrication cost for this type of fuel is on the order of 4000 $/kgU [38].

5.2.3.3. Linear reactivity model (LRM)

The linear reactivity model (LRM) has been adopted for the conversion of the fuel cost per uranium mass to fuel cost per unit energy; the LRM involves the calculation of the cycle length and discharge burnup for multiple number of batches. Note that it has been shown [1] that LRM for liquid salt cooled reactors does not work as well as for LWRs, and non-linear models should be adopted for better performance. Numerical studies on depletion analysis of AHTR fuel [39] have shown that second order polynomials provide better accuracy in fitting the reactivity curve, whereas higher orders do not provide any substantial improvement; with respect to LRM, the improvement in prediction of multi-batch discharge burnup is on the order of 3 percent or less. For this reason, LRM has been chosen as a first approximation for this study.

Given a multibatch fuel cycle organized in N batches, the discharge burnup (BU) and the cycle length (T, time distance between 2 refueling intervals) is given by the following formulas, with respect to the straight burn (single batch):

$$BU_N = \frac{2N}{N+1} BU_1 \quad (29)$$

$$T_N = \frac{2}{N+1} * T_1 \quad (30)$$

Where BU is the burnup and T is the cycle length (the subscript index is the number of batches). The equation for discharge burnup is needed for the conversion of cost from dollars per mass of uranium to dollars per energy; the equation for the cycle length is needed to compute the cost increase due to the refueling outage.

The LRM is a very simplified model that allows a quick comparison between different fuel cycle options.

Figure 5-4 shows the resulting estimate of the gain in terms of discharge burnup for online refueling, with respect to the number of batches in multi-batch cycles. The plot shows the burnup ratio between a multi-batch cycle and a single-batch cycle, derived from equation (29); the curve asymptotically approaches 2.0 for an infinite number of batches, but it is above 1.9 for number of batches equal or larger than 19. The second curve on the right axis shows the loss in terms of discharge burnup with respect to the ideal online refueling cycle (infinite batches); the loss is 50% for once-through and rapidly decreases, going below 5% at about 20 batches.

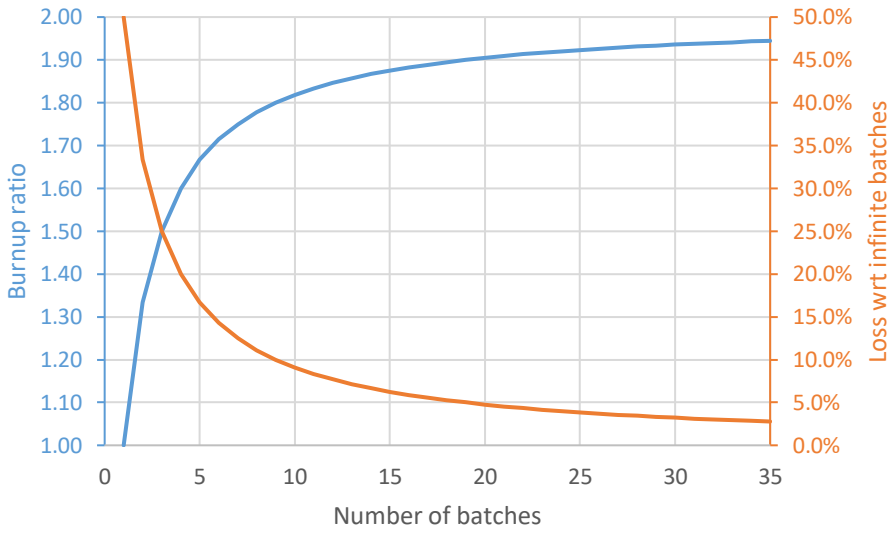

Figure 5-4. Burnup ratio (left axis) and loss with respect to infinite batches (right axis) as function of number of batches

5.2.3.4. Fuel cost per unit energy

The ultimate parameter that characterizes the economic aspect of the fuel cycle is the fuel cost per unit energy. The fuel cost per unit energy depends on two contributions: the fuel cost per unit mass and the cost of the refueling outage.

Note that an accurate evaluation of the refueling outage cost (OC, in $/outage) for the AHTR has yet to be performed, so a fixed outage cost has been assumed and more information about the choice of its value is presented in the parametric studies section. Another aspect that should be reminded here is the potentially large difference in refueling outage cost between a standard multibatch fuel cycle and the online refueling: the refueling outage cost is expected to be much lower for the latter, otherwise, due to the large number of refueling operations, the cost would be prohibitive.

The fuel cost (FC, in $/MWhe) can be expressed in the following form:

$$FC\left[\frac{\$}{MWh_e}\right] = \frac{P}{BU_N * eff} + \frac{OC}{pwr * eff * T_N} \quad (31)$$

Where pwr is the rector thermal power and eff is the efficiency of conversion to electric energy. The first term on the RHS of the equation represents the fuel cost per unit energy (electric) delivered to the grid; the electric energy produced per unit mass of uranium is computed by multiplying the discharge burnup by the power conversion efficiency (45% for the AHTR).

The second term on the RHS of the equation represents the contribution of the refueling outage. The cost per unit energy of outages is computed by dividing the fixed cost of the refueling outage by the electric energy produced over a single cycle length, since one refueling operation is executed at the end of each cycle.

Two more factors will be taken into consideration later on:

1. Maintenance outages. For regular multibatch, maintenance operations are performed during normal refueling operation, limiting the amount of time lost for maintenance. For online refueling, the reactor does not need to be shut down during refueling operations, so, if maintenance is needed, the reactor needs to be shut down. This difference might affect the overall fuel cost and attractiveness of the online refueling option.

2. Higher plant availability. For online refueling, the reactor remains online during refueling operations, so the availability of the plant is substantially higher, making the reactor potentially more profitable. On the other side, more advanced and specific equipment and upgrades to the reactor design will be required in order to make online refueling a viable approach; this aspect partially counterbalances the higher plant availability.

The methods presented in this section are very simplified and can potentially be refined; however, they are capable of providing preliminary insight into economic advantages or disadvantages of online refueling.

5.3. Preliminary evaluations on the economic model

The methodology presented in section 5.2.3 has been implemented in MATLAB.

Table 5-2 shows the initial parameters for the fuel cost model. Fabrication and outage cost are best estimate guesses derived from experience with LWRs and potentially both costs can be higher; parametric evaluations are presented in the following sections.

Cycle length and discharge burnup are computed for optimized fuel at 19.75% enrichment and their values are relatively high; results for 9% and 5% are also presented. Prices for uranium are derived from averaging data in the last decade.

Figure 5-5 shows the fuel cost as a function of the number of batches for 19.75% (left frame) and 9% (right frame) enrichment. The blue line represents the traditional multibatch refueling, accounting for refueling outage costs. The red line represents the fuel cost computed using the same approach and neglecting the refueling outage cost. The yellow line, representing the online refueling option, is the fuel cost for 253 batches neglecting the refueling outage cost. The plot serves as a gross comparison between the minimum cost for multibatch refueling (minimum for the blue line) and the cost of online refueling (yellow line); the cost saving derived from online refueling is about 40% of the minimum multibatch cost. This is a preliminary estimate using best guess parameters; further analysis will clarify the choice of these parameters.

Table 5-2. First guess parameters for fuel cost model

Parameter	19.75% enriched	9% enriched	Units
Single batch cycle length	815	355	Days
Single batch discharge burnup	139.31	60.68	GWd/MTU
Price of UF6 (including conversion)	104.26	104.26	US$/kgU
Price of SWU	92.75	92.75	US$/kgU
Fabrication cost	4000	4000	US$/kgU
Outage cost	20	20	Million US$

The savings increase for the 9% enrichment case, and become even more significant for 5% enrichment, as illustrated in Table 5-3. It is possible to conclude that for lower enrichment, since the relative savings remain about constant (or become even larger), the absolute advantage in terms of costs coming from online refueling is more substantial; as a rough estimate, the implementation of online refueling seems to provide about 50% fuel cost reduction.

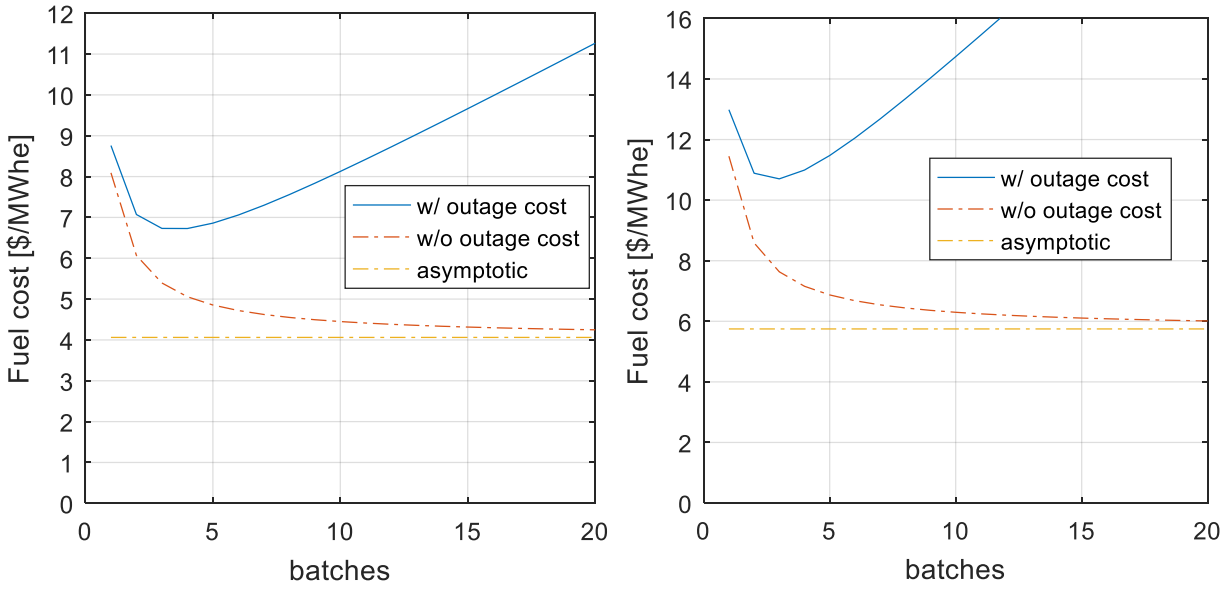

Figure 5-5. Fuel cost as a function of number of batches for 19.75% (left frame) and 9% (right frame). The cost for online refueling is represented by the asymptotic yellow line

Table 5-3. Online refueling savings for different initial fuel enrichments

Initial Enrichment	Multibatch minimum cost [$/MWhe]	Online refueling cost [$/MWhe]	Savings [$/MWhe]	Savings [%]
19.75%	6.8	4.0	2.8	41%
9%	10.8	5.8	5.0	46%
5%	25.0	12.0	13.0	52%

5.3.1. Cost of assembly fabrication

In order to provide an estimate of the cost of fabrication for the assembly, the cost model has been used to calculate the contributions of different cost factors to the overall cost.

Unit costs presented in Table 5-2 are used in this section; Table 5-4 presents reference parameters for baseline cost calculation. The mass of enriched uranium for the assembly is on the order of 80 kg and the cost per assembly strongly depends on the enrichment level, which is 19.75% in this configuration. The mass of uranium is computed assuming that four layers of TRISO particles are present in each fuel stripe, for a total of about 198 million particles per assembly; the mass density of uranium in the kernels is assumed to be 9.75 g/cm^3, derived from an overall kernel mass density (UCO) of about 10.9 g/cm^3.

Table 5-5 presents the cost splitting for uranium, enrichment and fabrication; with the assumed prices, the three components take about equivalent shares of the total cost. The overall cost is about $950,000, $300,000 per cost component.

Note that the uranium and enrichment cost strongly depend on the final enrichment; in other words, if the target enrichment is reduced, the cost of these two components is reduced by a similar factor. For 9% enrichment, the cost of uranium and its enrichment reduce to about $150,000 $ per assembly, which is about half the values for the 19.75% enrichment. Similar considerations can be derived for the 5% enrichment case: uranium and enrichment cost are roughly proportional to enrichment. This means that for low enrichment, fabrication costs probably become the cost driving parameter; this is particularly true in this case, where a relatively high fabrication cost has been assumed.

Table 5-4. Reference parameters for baseline cost calculation

Parameter	Value	Units
Mass of U per assembly	78.753	kg
Product enrichment – xp	19.75	%
Feed enrichment – xf	0.711	%
Tail enrichment – xw	0.002	%
Feed ratio – F/P	38.26	-
Tail ratio – W/P	37.26	-
Product potential – Vp	0.848	SWU/kg
Feed potential – Vf	4.869	SWU/kg
Tail potential – Vw	6.188	SWU/kg
SWU factor – S	45.118	SWU/kg

Table 5-5. Cost shares for fuel assembly fabrication

Cost:	Per kgU [$/kgU]	Percent [%]	Per assembly [US$]
U cost and conversion to UF6	3989	33	314130
Enrichment	4185	34	329560
Fabrication	4000	33	315010
TOTAL:	12174	100	958700

5.3.2. Parametric studies

A series of parametric studies has been conducted to evaluate the impact of different parameters on the overall fuel cost.

The main reason for these parametric studies is the lack of reliable information on the actual fabrication cost of the AHTR fuel assembly, which has a completely novel configuration, or on the cost of refueling outages for this specific type of reactor.

Parametric studies have been conducted on the fuel fabrication cost, the refueling outage cost and the total number of assemblies that will be utilized during the operational life of the plant.

5.3.2.1. Fabrication cost

Parametric studies have been performed on the fuel fabrication cost in order to evaluate its effect on the overall fuel cost. Two types of fuel cycle are considered in this analysis, the online refueling and a baseline 2-batches fuel cycle. The online refueling modeling assumes that the cost of outages can be neglected; the 2-batches fuel cycle assumes a 20 million $ refueling outage fixed cost and equation (31) shows how the refueling outage cost affects the total fuel cost.

Figure 5-6 shows the fuel cost as a function of fabrication cost (ranging from 1000 to 25000 $/kgU) for 2-batches (blue line) and online refueling (red line). The plot shows that fuel cost is reduced with online refueling due to the increased discharge burnup and the fact that less assemblies need to be used over the reactor lifetime, and this saving is higher at higher fabrication cost per kg of uranium.

Note that the order of magnitude of electricity retail price is 100 $/MWhe; at 4000 $/kgU fabrication cost, the fuel cost for 2-batches is about 7 $/MWhe and the fuel cost for online refueling is about 4 $/MWhe, for 19.75% initial enrichment.

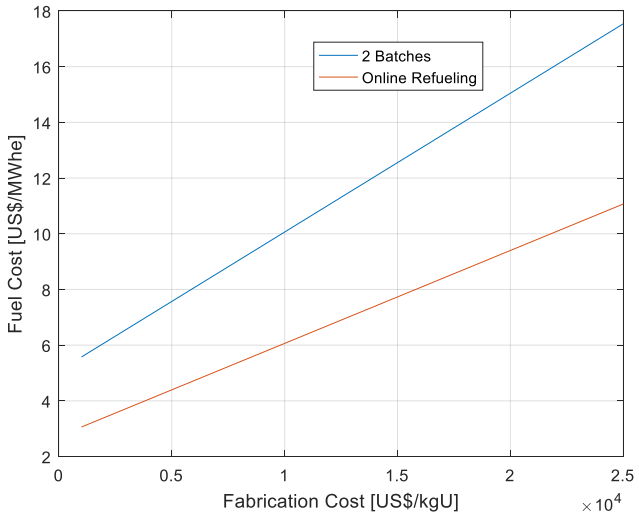

Figure 5-6. Fuel cost as function of fabrication cost for online and 2-batches fuel cycle for 19.75% initial enrichment

Figure 5-7 shows the percent cost reduction for the online refueling with respect to the 2-batches cycle as a function of the fabrication cost. The plot shows that for higher fabrication costs the percent gain given by online refueling decreases, even though the absolute gain increases (as shown in Figure 5-6); this behavior does not depend on the initial enrichment.

Figure 5-8 shows the fractional cost distribution as a function of fabrication cost for 2-batches (blue and orange) and online (yellow and purple) refueling. Each of the two cycles is represented by two curves, the sum of which is 100%: one curve represents the contribution of uranium, enrichment and outages, while the other curve represents the contribution of fabrication; all curves are function of fabrication cost.

Both fuel cycles show a crossover at a fabrication cost between 8000 and 10000 $/kgU: after the crossover the fabrication cost is the dominant cost factor; before the crossover the fabrication cost is not dominant. Note that the crossover value is similar for both cycles, and depends on uranium and enrichment cost. In particular, for low enrichment, the crossover value will be shifted to lower levels, due to the increased importance of the fabrication cost component.

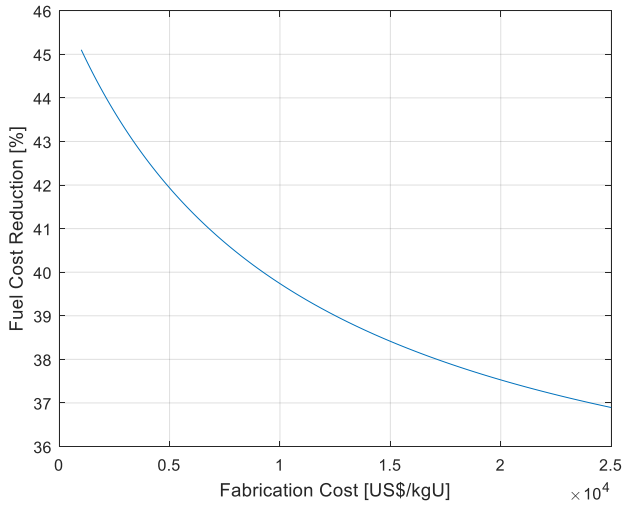

Figure 5-7. Fuel cost reduction from 2-batches to online refueling as a function of fabrication cost

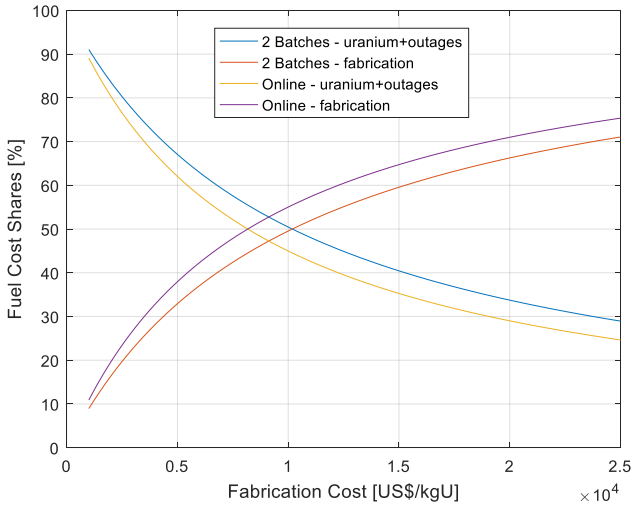

Figure 5-8. Fuel cost shares (fabrication and other costs) for online and 2-batches cycle as a function of the fabrication cost

5.3.2.2. Refueling outage cost

Parametric studies on the refueling outage cost have been performed in order to understand its effect on the fuel cost. Figure 5-9 shows the fuel cost (left) and cost shares (right) as a function of the outage cost for different number of batches.

The left frame shows the fuel cost as a function of refueling outage cost; the online refueling is modeled assuming that the refueling outage cost can be neglected (resulting in a horizontal curve), while the maintenance outage cost is the same in all cases and cancels out. For low outage cost high number of batches is more economical; for high cost of outage, low number of batches is more economical. For each value of refueling outage cost there is an optimal value for the number of batches, that minimizes the fuel cost.

The right frame shows the fractional cost splitting between refueling outage cost and other cost components (uranium plus fuel fabrication); curves are shown for online, 1-batch and 3-batches (2 curves per cycle). Note that online refueling again is represented by horizontal lines (at 0% and 100% for the outage and other cost, respectively), since there is no dependence on the refueling outage cost. The cross point is located at 50% and it moves towards the left as the number of batches increases. This is related to the fact that for higher number of batches the outage component of the overall cost tends to grow faster as the outage cost increases.

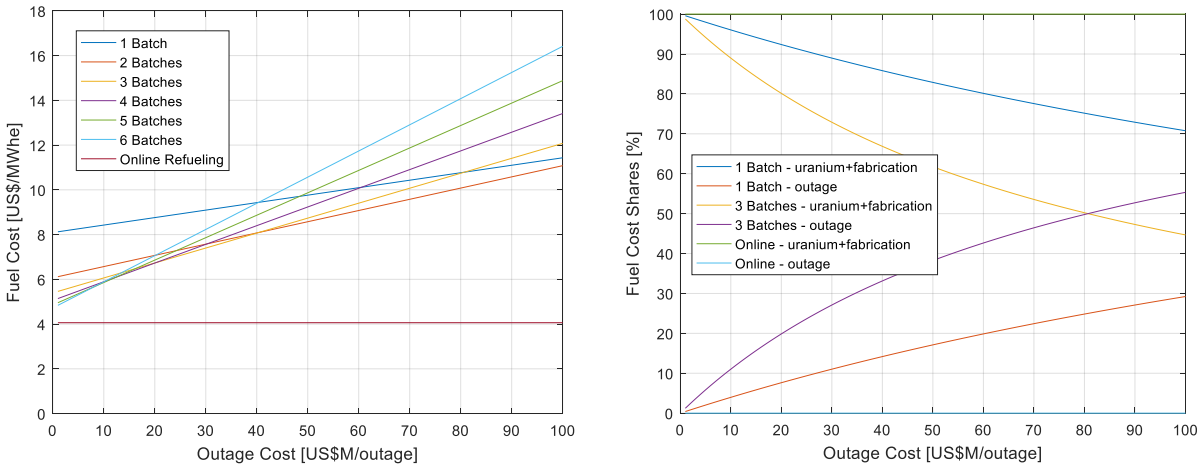

Figure 5-9. Fuel cost (left) and cost shares (right) for different number of batches as a function of the refueling outage cost

Figure 5-10 provides a representation of the optimal number of batches, that minimizes the fuel cost, as a function of the refueling outage cost. The two plots show the same quantity for two different ranges of outage cost: the outage cost for the left frame reaches $90 million per outage, while for the right frame the maximum cost is about 100,000 dollars. The plots show that if the outage cost is $43 million or more, 2-batches fuel cycle is optimal; 3-batches cycle is optimal between $22 and $43 million and 4-batches cycle is better for the $13-22 million range. These values are specific for the discharge burnup selected for the study, and they would change for different fuel enrichment and design.

Note that this calculation assumes that all outages are identical from the standpoint of the plant availability, the time lost for the single outage, which is related to the electricity generation lost because the reactor is shut down. With respect to this, if the retail price of electricity is 100 $/MWhe (10 cents/kWhe), the electricity not sold during a 3 days [2] refueling outage is about 11 million $, 3.5 million $ for every outage day. The yearly loss is about $11 million for a 1-year cycle and $22 million for a 6-months cycle, resulting in an overall loss over 60 years of $660 million and $1.32 billion, respectively. Note that this loss is only due to the fact that the plant is offline during refueling, so the electricity is not sold to the market. The cost of the refueling outage needs to be added to this.

The right frame of Figure 5-10 shows the optimal number of batches when the outage cost is low; the online refueling is expected to fall in this range. The plot shows that 253 batches, equivalent to online refueling, are optimal from the fuel cost standpoint if the outage cost is less than 8000 $/outage, otherwise it would be better to refuel in batches instead of single assemblies. Note that the terminology used here might lead to some confusion, because the term refueling outage is used for both online and multibatch refueling; for the online refueling case, the refueling outage can be considered as the series of operations needed to perform the refueling, which has an associated cost. In other words, both multibatch and online refueling have a refueling outage cost which might be caused by different aspects but that can be incorporated in the economic model using the same formulation under the term refueling outage cost.

Online refueling does not necessarily imply that one single assembly has to be removed per refueling operation. It implies instead that if two assemblies belong to the same batch, they are removed at the same time from the core. For the online refueling there is no strong reason to think that the removal cost would not be proportional to the number of assemblies removed. In other

words, online refueling does not need to be equivalent to 253 batches, but more than one assembly can be removed per each operation, keeping the cost proportional to the number of assemblies removed.

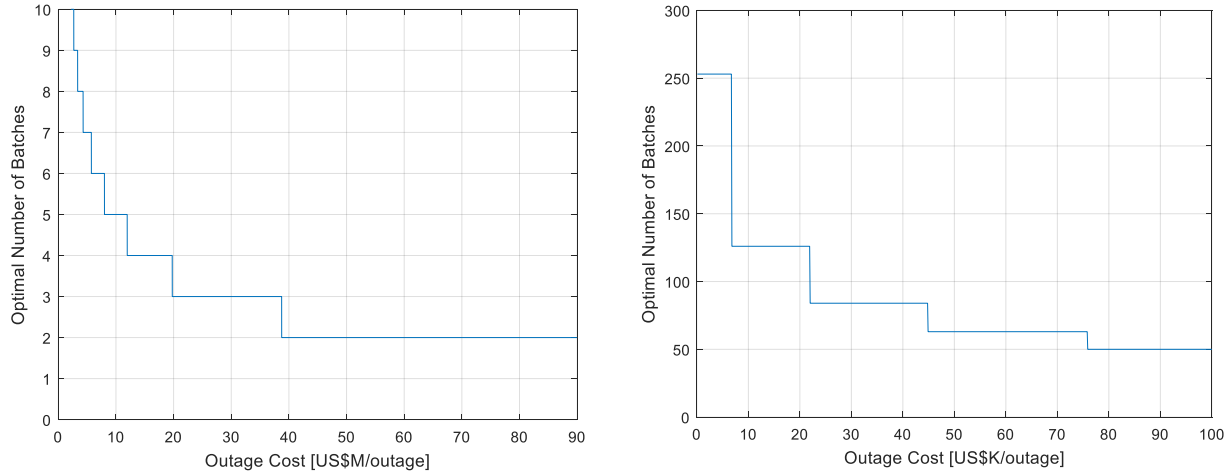

Figure 5-10. Optimal number of batches as a function of refueling outage cost for high cost (up to $90 million, left) and low cost (up to $100,000, right)

Figure 5-11 shows the minimized fuel cost as a function of the outage cost. The monotonic behavior of the curve tells us that it is desirable to have low refueling outage cost, because the optimal fuel cost is lower. Optimal condition for low outage cost is multibatch refueling, potentially each assembly removed singularly, in order to optimize fuel usage. On the other side, performing many refueling operations may introduce higher risk of accident, but as part of the design process this risk should be minimized and become negligible.

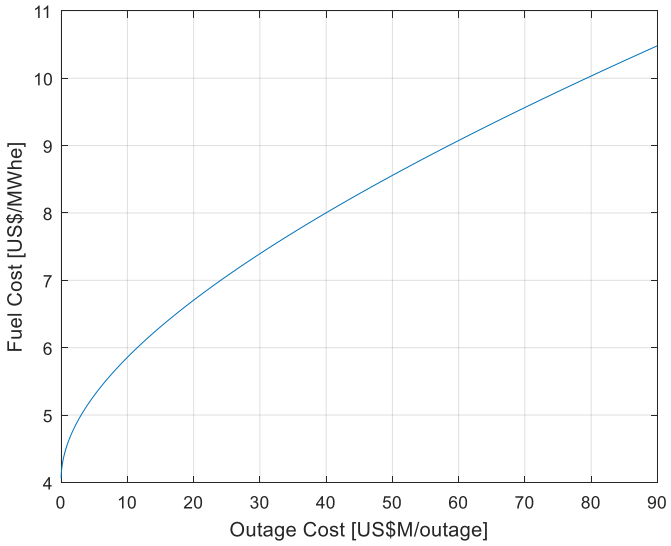

Figure 5-11. Optimal fuel cost as a function of refueling outage cost, minimized with respect to the number of batches

5.3.2.3. Total number of assemblies

Figure 5-12 shows the minimized number of assemblies needed over the reactor lifetime (60 years) as a function of the number of batches, for 19.75% enrichment. The plot shows that the total number of assemblies needed decreases with the number of batches and it reaches a steady value at about 50 batches. 5250 assemblies are needed for a 2-batches cycle and about 3700 for the online refueling with 253 batches, equivalent to about 29.5% reduction. For 9% initial enrichment, the 2-batch cycle requires about 12000 assemblies, while the online needs about 8000, about 33.3% reduction.

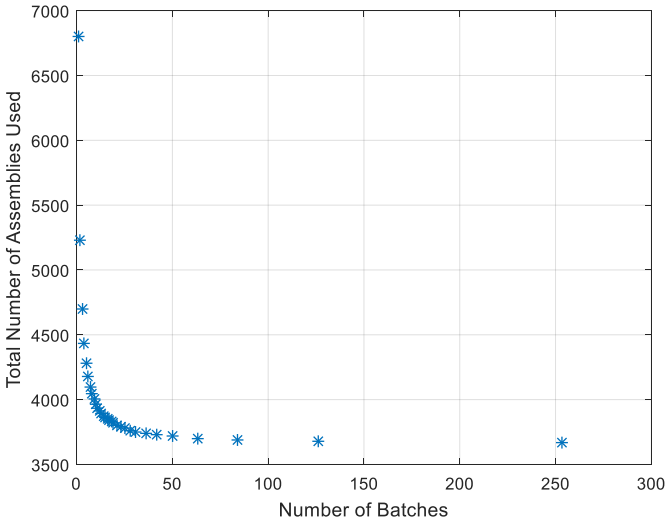

Figure 5-12. Total number of assemblies needed over the reactor lifetime (60 years) as a function of the number of batches

5.4. Considerations on refueling outages

The refueling outages impact the retail price of electricity in two ways:

- One aspect is the increase in fuel cost due to the fixed cost that needs to be paid at each refueling operation (section 5.3.2.2).
- The second aspect derives from the fact that during the refueling operation the power of the plant might need to be reduced or, for standard multibatch, the reactor would need to be shut down. This section provides some insight on the effects of this factor on the price of electricity.

The following cases are considered here for comparison purposes:

- Traditional 2-batches fuel cycle:
    - the reactor is offline;
    - each refueling operation requires 3 days;
- Online refueling:
    - 253 batches;
    - Each refueling operation requires half hour;
    - The power level during the refueling operation is 90% of nominal;

With these assumptions the overall amount of money lost during the reactor lifetime due to the reactor shutdown is equal to 433 million $ for 2-batches and 26 million for online refueling; note that the model neglects the time value of money.

Redistributing this amount of money over the total electric energy produced by the reactor over its lifetime, the 2-batch fuel cycle shows a loss 0.54 $/MWhe and the online refueling cycle has a loss of 0.03$/MWhe; as a term of comparison the fuel cost is in the range of 4-8 $/MWhe, and the retail price of electricity is about 100 $/MWhe.

The evaluation of the loss due to the outage depends on 2 factors, the power level and the duration of the outage. Note that this loss does not account for the money spent to perform the outage (included instead in the refueling outage cost).

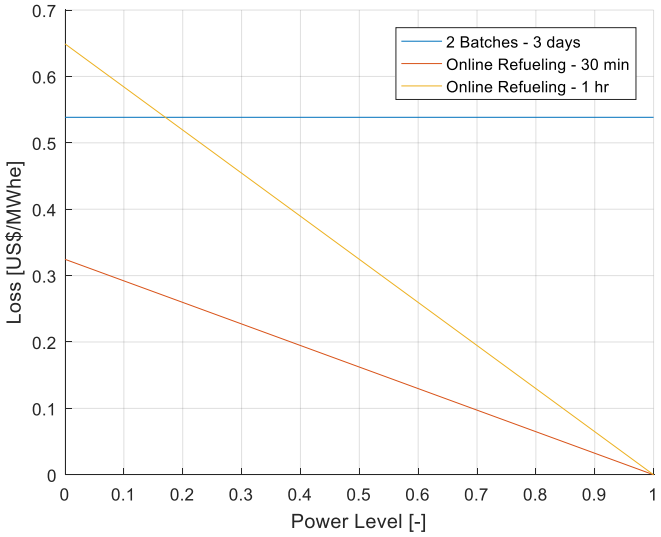

Figure 5-13. Loss due to shutdown or reduced power time as a function of the outage power level

Figure 5-13 shows the loss due to the outage as a function of the power level during the refueling operations. The 2-batches option assumes that the power level is equal to zero, so the curve is horizontal; the other two curves represent online refueling for outage duration of 30 minutes and 1 hour. The power level ranges from 0 to 100% of the nominal power. For duration less than about 1 hour, the loss is always lower than that for the 2-batches cycle; if the duration is longer, the power level needs to surpass a certain threshold in order to maintain the loss below the 2-batches reference.

If the power level is sufficiently high, the duration of the outage becomes less important; ideally, if the power level is 100%, the duration of the refueling operation does not affect the cost.

Figure 5-14 shows the loss due to outage as a function of the outage duration; for 2-batches cycle the duration has been assumed to be 3 days (design value for AHTR) and the curve is constant. Two other curves represent the online refueling for 80% and 90% power level; if the power level is above 80% and the duration is less than 4 hours, the online refueling option will perform better than 2-batches option. Note again that 100% power has zero loss, regardless of the outage duration. Assuming a 90% refueling power, a duration of 30 minutes will result in negligible losses for online refueling.

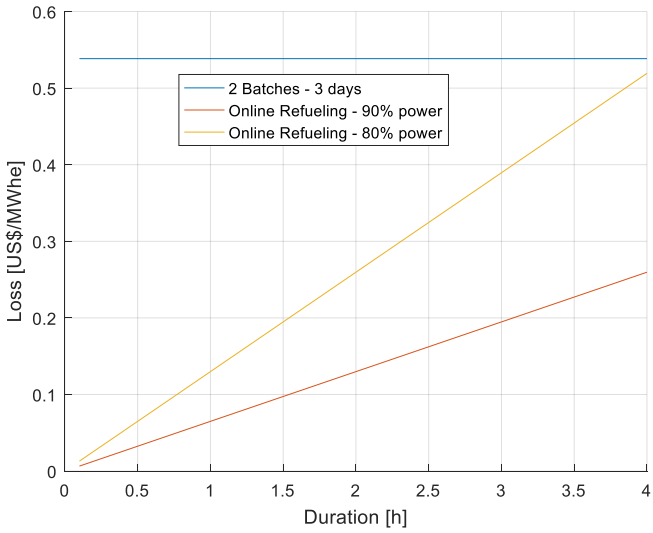

Figure 5-14. Loss due to shutdown or reduced power time as a function of the outage duration

5.4.1. Refueling machines

A preliminary economic evaluation on the cost of refueling machines has been performed at ORNL [40]. This evaluation accounts for remote in-vessel fuel handling system, fuel transfer pool hardware, fuel handling tools and equipment, service platforms, fuel storage, cleaning and inspection equipment and fuel storage racks; the total cost for these components has been estimated around $51 million. Assuming that the implementation of online refueling doubles the cost of refueling machines, the penalty for online refueling is on the order of 51 million $. If this amount is distributed over the reactor lifetime (60 years), the penalty is on the order of 0.06 $/MWhe. Since this penalty is at least one order of magnitude smaller than other cost components presented in Table 5-8, it has been neglected in the overall cost evaluation.

5.5. Considerations on maintenance outages

The maintenance outages affect the overall electricity price produced by the reactor and they might play a role in the computation of the fuel cost differences between the standard multibatch and online refueling for the AHTR.

Figure 5-15 shows the loss per unit energy (left frame) and total over reactor lifetime (right frame) as a function of the maintenance outage cost and duration. The calculation accounts for energy loss due to plant shutdown for maintenance and depends on two contributions: the actual cost for the maintenance operation and the penalty due to the electricity not sold during the outage. Note that in this case the reactor needs to shut down also for the online refueling option. The plots assume a maintenance interval of 3 years.

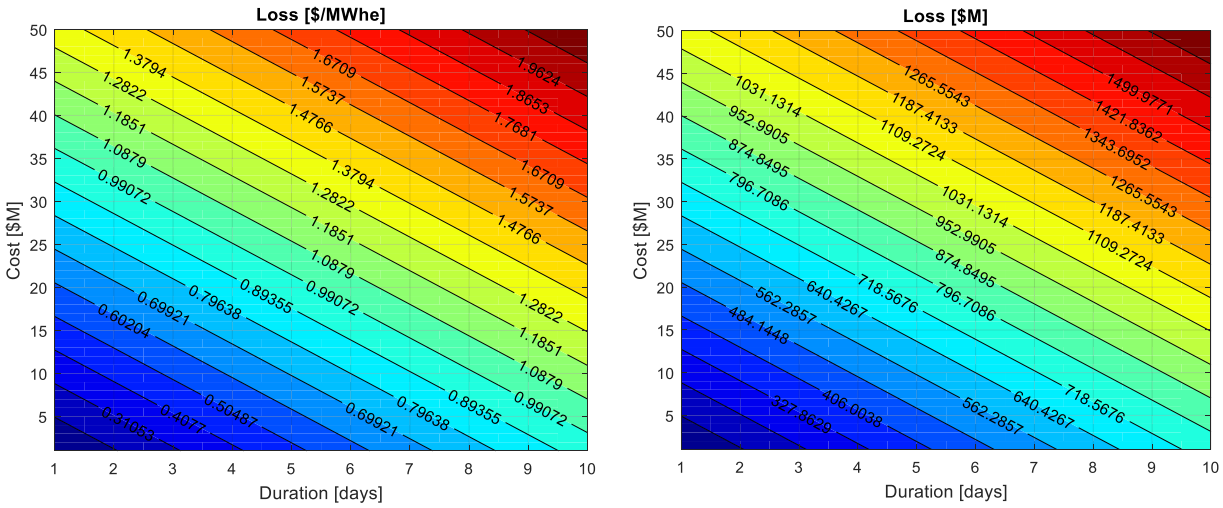

Figure 5-15. Loss due to maintenance outage as a function of the outage duration and cost

For a 3-day outage and 20 million $/outage cost the loss is about 0.78 $/MWhe equivalent to about 610 million $ over the reactor lifetime; this value is the same for both online and multibatch, assuming that both cases need to perform maintenance at the same intervals and costs. Note that the maintenance characteristics, such as duration and cost, cannot be easily estimated at this stage of the design.

With respect to maintenance outages, the difference between multibatch and online refueling is that multibatch fuel cycle can dilute some of these maintenance operation over the other refueling

outages, thus avoiding the need for outages specifically performed for maintenance reasons; on the other side, online refueling fuel cycle would need to shut down at a specific frequency to perform maintenance, thus reducing the advantage due to being able to keep the reactor online during refueling outages.

One way for accounting for this would be to assume that the cost of maintenance outages for multibatch is lower than the maintenance outage cost for online refueling. If for instance the outage cost is assumed to be 5 million $ instead of 20, the loss for multibatch would be estimated around 0.41 $/MWhe or 330 million $ over reactor lifetime.

The analysis on maintenance cost shows that maintenance operations reduce the advantage of the online refueling fuel cycle option, but the loss is minimal if compared to advantage factors in favor of online refueling.

5.6. Potential economic advantages from online refueling

The various contributions to the fuel cost can be put together in order to evaluate the cost advantage of online refueling over the 2-batch fuel cycle option. Table 5-6 shows the reference parameters used for a preliminary evaluation. A cost of 1000 $/outage has been assumed for each refueling operation for the online refueling option, as well as a 90% power level.

Table 5-6. Reference parameters for calculation of online refueling cost advantage

	2-batches cycle		Online refueling	
Parameter	Value	Units	Value	Units
Refueling outage cost	20	Million $	1000	$
Power level during refueling outage	0.0	%	90	%
Refueling outage duration	3	Days	30	Mins
Maintenance outage time interval	3	Years	3	Years
Maintenance outage duration	3	Days	3	Days
Maintenance outage cost	5	Million $	20	Million $

Table 5-7 shows the contribution to overall cost of manufacturing, outage and maintenance cost components, providing a comparison between a 2-batch reference fuel cycle and the online

refueling option. The major contributor to the difference is the fuel cost; the outage and maintenance losses tend to cancel out. The overall cost advantage is in favor of online refueling and it is of the order of 3.14 $/MWhe.

Considering the overall reactor lifetime (60 years), the approximate estimate of the electric energy produced by the reactor is of the order of 800 TWhe. If the overall cost advantage for online refueling is about 3 $/MWhe, the total amount saved over the reactor lifetime is of the order of 2.4 billion $, about 40 million $ per year.

Table 5-7. Online refueling cost advantage results for 19.75% initial enrichment

	2-batch	Online	2-batch minus online	Units
Fuel cost	7.071	4.066	3.005	$/MWhe
Outage loss	0.538	0.033	0.505	$/MWhe
Maintenance loss	0.398	0.771	-0.373	$/MWhe
TOTAL:			3.137	$/MWhe

Table 5-8 shows similar evaluations for 9% initial fuel enrichment. The maintenance losses remain unchanged, while the other two cost components increase in favor of online refueling. The fuel cost component increases for both 2-batch and online in a proportional manner, so the difference between the two quantities also increases; the outage loss increases substantially for the 2-batch cycle because of the larger number of refueling outages needed.

As expected, online refueling becomes more advantageous at lower enrichments.

Table 5-8. Online refueling cost advantage results for 9% initial enrichment

	2-batch	Online	2-batch minus online	Units
Fuel cost	10.889	5.758	5.131	$/MWhe
Outage loss	1.254	0.075	1.179	$/MWhe
Maintenance loss	0.398	0.771	-0.373	$/MWhe
TOTAL:			5.937	$/MWhe

This analysis is preliminary and lacks an accurate estimate of some contributions or completely neglects others, but it shows that the overall economic advantage obtained by the online refueling can potentially be significant.

6. INTEGRATION, FUTURE WORK AND CONCLUSIONS

6.1. Integration of various aspects

The models developed and presented in the previous sections have been integrated to provide a global assessment of the online refueling procedure. In particular, the results of the neutronic analysis have been integrated with the thermal-hydraulic models in order to correctly describe the power behavior of the core. Figure 6-1 provides a graphical representation of the interaction among different components of the modeling process. The implementation of online refueling affects the behavior of the system and its features on different time scales, ranging from seconds for fuel maneuvering operations up to months for refueling patterns and fuel management. On the short time scale (seconds to hours), relative to assembly and control rod extraction or insertion, flow and flux sudden variation are the most important parameters to be controlled. For medium time scales, on the order of hours, core reactivity management becomes the relevant aspect. For larger time scales (weeks and months), fuel usage and refueling pattern approach become the dominant parameters, directly affecting the economics of the entire fuel cycle.

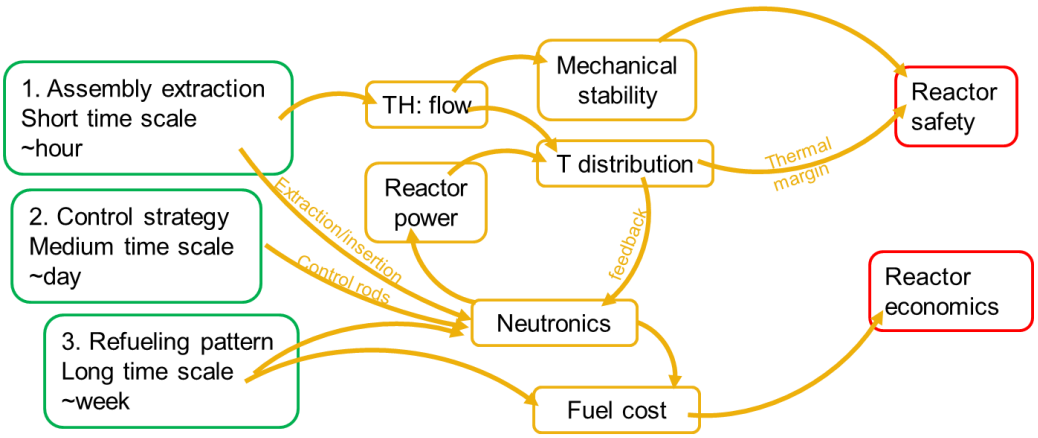

Figure 6-1. Integration of modeling aspects

The central portion of Figure 6-1 depicts the interaction among different components of the modeling approach. Three main interaction areas need to be highlighted:

1. Neutronics and thermal hydraulic coupling during refueling operation. This interaction accounts for the neutronic feedback on the reactor power and thermal parameters.
2. Effects of flow variation on mechanical stability of the refueling operation.
3. Neutronics and depletion effects on the economic evaluations.

This work has analyzed these interaction, providing a preliminary picture of the online refueling implementation that gives advantageous economic conditions and maintains adequate safety with respect to standard multi-batch cycles.

The analysis of interaction mechanisms for the online refueling involved the modeling of the transient variation of temperature distribution in the extracted assembly; the insertion of the control rod and the partial to full extraction of the element cause effects on the neutronic properties of the system, affecting the power in the removed assembly as well as the power in the rest of the core. This type of coupling has been accounted for in the modeling approach developed in this work.

From a thermal hydraulic standpoint, the flow change also affects the stability of the assembly during the refueling operation. This coupling has been used to evaluate the effects of flow on the force acting on the assembly as a function of the elevation of the extracted assembly, directly related to the mechanical stresses on the supporting mechanisms.

The effects of reactivity changes on the overall system have been evaluated using the output from the neutronic studies and the thermal hydraulic system model. Note that the approach used in this work does not utilize full coupling, instead it adopts a multiple iteration procedure: the temperature distribution is calculated from nominal parameters, the neutronic simulations are run to estimate the reactivity changes using the thermal parameters from previous analysis, then the derived reactivity profiles are fed back into the thermal hydraulic system solver with neutronic feedback to evaluate the response of the system. In other words, the work developed here does not feature full coupling, for which more intensive computational requirements are demanded.

Finally, the neutronic analysis is used to address the coupling problem between the economic evaluations and the depletion and fuel cycle simulations.

6.2. Future work

The present work addresses several challenges in the analysis of the online refueling for the AHTR, but reveals a strong need for further work on the development of modeling tools and approaches for Fluoride salt cooled reactors.

This section addresses some of the challenges that emerged along the development of this work that need to be addressed in the future.

1. Integration between CFD/thermal analysis and Monte Carlo, particularly for depletion calculations. Both Monte Carlo codes and CFD codes present several challenges in terms of computational requirements; for Monte Carlo, this is particularly true for depletion simulations, which cannot be easily performed in full core configuration. A better interface between the neutronic and thermal hydraulic calculation is needed in order to perform accurate simulations.
2. Need for development of nodal/diffusion models for the AHTR that allow accurate and fast calculation of flux distribution and neutronic parameters. This would support a more comprehensive study of the refueling pattern options for the online refueling. A basic methodology has been established for the neutronics analysis in this work, which is limited in terms of exploration of configurations for fuel cycle options. Some work has already been performed in this direction [34], but more work is needed to develop more adequate tools.
3. Advancements in the modeling and simulation capabilities for the flow distribution at the assembly level and for plenums and vessel. This aspect is particularly important in terms of design development for liquid salt reactors.
4. Study of mechanical stability and mechanical requirements on the mechanisms that perform the refueling operation.
5. Finalization of the core and vessel redesign approach to make the online refueling viable. Several options have been presented in this work, ranging from small changes to more substantial redesign of the core. A more exhaustive analysis is needed to explore all options and select those that maximize safety and economic advantage.
6. Improvements in the economic model, including a full implementation of the non-linear reactivity model, a more accurate fabrication cost modeling, as well as an evaluation of

refueling and maintenance outage cost. Potentially include more advanced tools, such as nodal codes, for a more detailed evaluation of the fuel cycle cost.

The proposed studies for future work directly impact the modeling capability for the online refueling, but they also have immediate relations to modeling capabilities for Liquid salt cooled reactors in general.

6.3. Conclusion

The on-line refueling is an attractive option for the improvement of the fuel utilization in the AHTR core; potentially, it can save on the order of $40M each year, or about $2.4B over a 60-year reactor lifetime. The operational transient associated with on-line refueling is very unique in many aspects, which can potentially challenge the operation and safety of the reactor. This work provided insight into several of these aspects.

This analysis has developed a multi-physics methodology for the study and optimization of the thermal-hydraulic transient and the flow distribution in the AHTR core. It also provided an appropriate method for the characterization of the neutronics of the reactor during the transient, as well as mechanical, technical and economic aspects.

The models developed in this work will provide benefit to safety analysis and transient studies for the study of FHR reactors. For instance, the studies on flow distribution in the lower and upper plenum, as well as along the channel of the removed assembly, constitute a basis on which a deeper analysis of temperature distributions and flow characteristics in the upper plenum can be developed.

This work proves that the online refueling ultimately may be a solution for the fuel utilization issue of FHR reactors.

7. APPENDIX

7.1. MATLAB input: plate-wise axial heat conduction

```
% Evaluation of the effect of axial heat conduction in the fuel assembly

clear all;
close all;
clc;

% general data for z
Ha=5.5;
Nz=27500;
dz=Ha/Nz;
z=dz/2:dz:Ha;
zb=0:dz:Ha;     % for power
He=7.0;
% general data for x
l=0.23;
xfs=0.007;      % rounded at 3rd digit
xgm=0.013;      % rounded at 3rd digit
Nfp=65;
% adapt geometry
dx=xgm/Nfp;
Nfs=round(xfs/dx);
Ngm=Nfp-Nfs;
xfs=dx*Nfs;
xgm=xfs+dx*Ngm;
Nx=Nfp+1;        % includes the point for the coolant temperature
Npartial=Nfp*Nz;      % number of points of the fuel plate mesh
N=Nx*Nz;    % includes the vector for the coolant temperature

% position and direction vector
xm(1:Nz,1:Nfp)=0;
zm(1:Nz,1:Nfp)=0;
for ix=1:1:Nfp
```

```
    for iz=1:Nz
        xm(iz,ix)=dx/2+(ix-1)*dx;
        zm(iz,ix)=dz/2+(iz-1)*dz;
    end;
end;

% material type matrix
% 1->fuel
% 2->meat
% 3->coolant
mat(1:Nz,1:Nx)=3;
for ix=2:(Nfs+1)
    mat(:,ix)=1;
end;
for ix=(Nfs+2):Nx
    mat(:,ix)=2;
end;

% conductivity matrix
k(1:Nz,1:Nx)=15;
for ix=1:Nx
    for iz=1:Nz
        if (mat(iz,ix)==3)
            k(iz,ix)=1.1;
        end;
    end;
end;

% power density matrix
% for now uniform axial profile
q3(1:Nz,1:Nx)=0;
P=3400e6;
Na=252;
Npl=18;
Afuel=xfs*l;
Vol=Afuel*Ha;
powerdensity=P/Na/Npl/2/Vol;
for iz=1:Nz
```

```
    pd(iz)=powerdensity;
end;
% cosine profile
La=zb(end);       % active length
Le=He;
norm1=2*Le/pi*sin(pi/Le*La/2);
for i=2:length(zb)
    cd(i-1)=Le/pi*(sin(pi*(zb(i)-La/2)/Le)-sin(pi*(zb(i-1)-La/2)/Le))/norm1;
end;
pd=pd.*cd/mean(cd);
% end of cosineprofile
for iz=1:Nz
    for ix=1:Nx
        if (mat(iz,ix)==1) q3(iz,ix)=pd(iz); end;
    end;
end;

% coolant channel
Tin=650;
rho=1950;
cp=2415;
mu=6e-3;
kcool=1.1;
Pr=mu*cp/kcool;
deltaTc=50;
m=P/cp/deltaTc/Na/Npl/2;
h=7500;     % this is an average value, approximation.

% build the matrices
b=zeros(N,1);
a2c=b; a1c=b; a2l=b; a1l=b; a2r=b; a1r=b; a2ll=b; a2rr=b; a1ll=b; a1rr=b;
for iz=1:Nz
    for ix=1:Nx
        i=ix+(iz-1)*Nx;
        co=k(iz,ix);
        po=q3(iz,ix);
        % centralnode
        if (ix>2)&&(ix<Nx)&&(iz>1)&&(iz<Nz)
```

```
    a2c(i)=2*co*(1/dx^2+1/dz^2);
    a1c(i)=2*co/dx^2;
    a2l(i)=-co/dx^2;
    a1l(i)=a2l(i);
    a2r(i)=-co/dx^2;
    a1r(i)=a2r(i);
    a2ll(i)=-co/dz^2;
    a2rr(i)=-co/dz^2;
    b(i)=q3(iz,ix);
% right boundary
elseif (ix==Nx)&&(iz>1)&&(iz<Nz)
    a2c(i)=co*(1/dx^2+2/dz^2);
    a1c(i)=co/dx^2;
    a2l(i)=-co/dx^2;
    a1l(i)=a2l(i);
    a2ll(i)=-co/dz^2;
    a2rr(i)=-co/dz^2;
    b(i)=q3(iz,ix);
% top boundary
elseif (ix>2)&&(ix<Nx)&&(iz==Nz)
    a2c(i)=co*(2/dx^2+1/dz^2);
    a1c(i)=2*co/dx^2;
    a2l(i)=-co/dx^2;
    a1l(i)=a2l(i);
    a2r(i)=-co/dx^2;
    a1r(i)=a2r(i);
    a2ll(i)=-co/dz^2;
    b(i)=q3(iz,ix);
% low boundary
elseif (ix>2)&&(ix<Nx)&&(iz==1)
    a2c(i)=co*(2/dx^2+1/dz^2);
    a1c(i)=2*co/dx^2;
    a2l(i)=-co/dx^2;
    a1l(i)=a2l(i);
    a2r(i)=-co/dx^2;
    a1r(i)=a2r(i);
    a2rr(i)=-co/dz^2;
    b(i)=q3(iz,ix);
```

```
% left boundary (fuel)
elseif (ix==2)&&(iz>1)&&(iz<Nz)
    a2c(i)=co*(1/dx^2+2/dz^2)+h/dx;
    a1c(i)=co/dx^2+h/dx;
    a2l(i)=-h/dx;
    a1l(i)=a2l(i);
    a2r(i)=-co/dx^2;
    a1r(i)=a2r(i);
    a2ll(i)=-co/dz^2;
    a2rr(i)=-co/dz^2;
    b(i)=q3(iz,ix);
% left boundary (coolant)
elseif (ix==1)&&(iz>1)&&(iz<Nz)
    a2c(i)=m*cp/(dx*dz*l)+h/dx;
    a1c(i)=a2c(i);
    a2r(i)=-h/dx;
    a1r(i)=a2r(i);
    a2ll(i)=-m*cp/(dx*dz*l);
    a1ll(i)=a2ll(i);
% top right corner
elseif (ix==Nx)&&(iz==Nz)
    a2c(i)=co*(1/dx^2+1/dz^2);
    a1c(i)=co/dx^2;
    a2l(i)=-co/dx^2;
    a1l(i)=a2l(i);
    a2ll(i)=-co/dz^2;
    b(i)=q3(iz,ix);
% low right corner
elseif (ix==Nx)&&(iz==1)
    a2c(i)=co*(1/dx^2+1/dz^2);
    a1c(i)=co/dx^2;
    a2l(i)=-co/dx^2;
    a1l(i)=a2l(i);
    a2rr(i)=-co/dz^2;
    b(i)=q3(iz,ix);
% low left corner (fuel)
elseif (ix==2)&&(iz==1)
    a2c(i)=co*(1/dx^2+1/dz^2)+h/dx;
```

```
            a1c(i)=co/dx^2+h/dx;
            a2l(i)=-h/dx;
            a1l(i)=a2l(i);
            a2r(i)=-co/dx^2;
            a1r(i)=a2r(i);
            a2rr(i)=-co/dz^2;
            b(i)=q3(iz,ix);
        % top left corner (fuel)
        elseif (ix==2)&&(iz==Nz)
            a2c(i)=co*(1/dx^2+1/dz^2)+h/dx;
            a1c(i)=co/dx^2+h/dx;
            a2l(i)=-h/dx;
            a1l(i)=a2l(i);
            a2r(i)=-co/dx^2;
            a1r(i)=a2r(i);
            a2ll(i)=-co/dz^2;
            b(i)=q3(iz,ix);
        % low left corner (coolant)
        elseif (ix==1)&&(iz==1)
            a2c(i)=h/dx+2*m*cp/(dx*dz*l);
            a1c(i)=a2c(i);
            a2r(i)=-h/dx;
            a1r(i)=a2r(i);
            b(i)=2*m*cp/(dx*dz*l)*Tin;
        % top left corner (coolant)
        elseif (ix==1)&&(iz==Nz)
            a2c(i)=h/dx+m*cp/(dx*dz*l);
            a1c(i)=a2c(i);
            a2r(i)=-h/dx;
            a1r(i)=a2r(i);
            a2ll(i)=-m*cp/(dx*dz*l);
            a1ll(i)=a2ll(i);
        end;
    end;
end;

% exact solution of 1D temperature
dll=[a1ll((Nx+1):end); zeros(Nx,1)];
```

```
dl=[a1l(2:end); 0];
dc=a1c;
dr=[0; a1r(1:(end-1))];
drr=[zeros(Nx,1); a1rr(1:(end-Nx))];
diagonals1=[dll dl dc dr drr];
a1=spdiags(diagonals1,[-Nx -1 0 1 +Nx],N,N);
sol1=a1\b;

% % exact solution of 2D temperature (for coarse mesh (~1 mm))
% dll=[a2ll((Nx+1):end); zeros(Nx,1)];
% dl=[a2l(2:end); 0];
% dc=a2c;
% dr=[0; a2r(1:(end-1))];
% drr=[zeros(Nx,1); a2rr(1:(end-Nx))];
% diagonals2=[dll dl dc dr drr];
% a2=spdiags(diagonals2,[-Nx -1 0 1 +Nx],N,N);
% sol2=a2\b;

% iterative (Gauss-Seidel) solution of 2D temperature (for fine mesh (~0.1
mm))
sol2=sol1;  % initial guess: 1D solution
Nit=100;     % number of iterations
err=zeros(Nit,1);
'start iterations'
clock=tic;
for it=1:Nit
    it
    sol2temp=sol2;
    sll=[zeros(Nx,1); sol2(1:(end-Nx))];
    sl=[0; sol2(1:(end-1))];
    sr=[sol2(2:end); 0];
    srr=[sol2((Nx+1):end); zeros(Nx,1)];
    sol2=(b-a2ll.*sll-a2l.*sl-a2r.*sr-a2rr.*srr)./a2c;
    err(it)=norm(sol2-sol2temp);
end;
timeit=toc(clock);
'end iterations'
```

```
s1=zeros(Nz,Nx);
s2=zeros(Nz,Nx);
for iz=1:Nz
    for ix=1:Nx
        i=ix+(iz-1)*Nx;
        s1(iz,ix)=sol1(i);
        s2(iz,ix)=sol2(i);
    end;
end;
Tc1=squeeze(s1(:,1));
Tc2=squeeze(s2(:,1));
dTc=Tc2-Tc1;
T1=s1(:,2:end);
T2=s2(:,2:end);
dT=T2-T1;

Nzp=1100;          % for plot
zlow=0.1;
zup=Ha-0.05;
dzp=(zup-zlow)/Nzp;
zp=(zlow+dzp/2):dzp:zup;
clear xmp zmp
xmp(1:Nzp,1:Nfp)=0;
zmp(1:Nzp,1:Nfp)=0;
for ix=1:1:Nfp
    for iz=1:Nzp
        xmp(iz,ix)=dx/2+(ix-1)*dx;
        zmp(iz,ix)=zlow+dzp/2+(iz-1)*dzp;
    end;
end;
T1p=interp2(xm,zm,T1,xmp,zmp);
T2p=interp2(xm,zm,T2,xmp,zmp);
dTp=interp2(xm,zm,dT,xmp,zmp);

% plots
figure(1)
[~,h]=contourf(xmp*1000,zmp*100,T1p,50);
xlabel('x [mm]');
```

```
ylabel('z [cm]');
title('Temperature distribution T1 [C]');
colorbar;
set(gcf,'units','centimeters','position',[10 10 20 10]);
set(h,'edgecolor','none');

figure(2)
[~,h]=contourf(xmp*1000,zmp*100,T2p,50);
xlabel('x [mm]');
ylabel('z [cm]');
title('Temperature distribution T2 [C]');
colorbar;
set(gcf,'units','centimeters','position',[10 10 20 10]);
set(h,'edgecolor','none');

figure(3)
[~,h]=contourf(xmp*1000,zmp*100,dTp,50);
xlabel('x [mm]');
ylabel('z [cm]');
title('Temperature distribution difference T2-T1 [C]');
colorbar;
set(gcf,'units','centimeters','position',[10 10 20 10]);
set(h,'edgecolor','none');

figure (4)
plot(zm(:,1)*100,dTc);
grid on;
xlabel('z [cm]');
ylabel('T [C]');
axis tight;
title('Coolant temperature distribution difference T2c-T1c [C]');
set(gcf,'units','centimeters','position',[10 10 20 10]);

save('results.mat');
```

7.2. MATLAB input: 3D assembly flow and temperature distributions

```
% Horizontal heat conduction of one plate
% Approximation: no axial heat conduction

clear all;
close all;
clc;

results_filename='TempDistr.dat';
% general data for z
Ha=5.5;
Nzs=40;
Nz=Nzs+1;
dz=Ha/Nzs;
z=0:dz:Ha;
zmed=[0 dz/2:dz:Ha Ha];
zplot=[dz/2:dz:Ha];
He=7.0;
% general data for x and y
xbw=0.01*2/sqrt(3);
xfp=0.24;
xys=xfp+0.02*2/sqrt(3);
yc1=0.0035;
ygm1=yc1+0.007;
ygm2=ygm1+0.011;
yc2=ygm2+0.007;
ytop=yc2+0.0035;
Nsy=30;          % # of segments for the portion of one plate
% adapt geometry
dy=ytop/Nsy;
dx=dy*2/sqrt(3);
Ny=Nsy;          % points, vertical
h1=dy/3;
h2=dy-h1;
Nsyc=round(0.0035/dy);
Nsyf=round(0.007/dy);
```

```
Nsyg=Ny-2*Nsyc-2*Nsyf;
yc1=Nsyc*dy;
ygm1=yc1+Nsyf*dy;
ygm2=ygm1+Nsyg*dy;
yc2=ygm2+Nsyf*dy;
ytop=yc2+Nsyc*dy;
% lower box wall and upper Y shape
ybw=0.01;
Nybw=round(ybw/dy);
ybw=Nybw*dy;
yws=0.02;
Nyws=round(yws/dy);
yws=Nyws*dy;
ylim=ybw+6*ytop+yws;
Ny=Nybw+6*Nsy+Nyws;
% horizontal direction
Nsx1=round(xbw/dx);
Nsx2=round(xfp/dx)-Nsx1;
Nsx3=round(xys/dx)-Nsx1-Nsx2;
Nsx2=Ny-Nsx1-Nsx3;
Nsx=Nsx1+Nsx2+Nsx3;
Nx=2*Nsx;       % points, horizontal
xbw=Nsx1*dx;
xfp=(Nsx1+Nsx2)*dx;
xys=(Nsx1+Nsx2+Nsx3)*dx;
xlim=xys;
N=Nx*Ny;        % total points

% position and direction vector
xm(1:Ny,1:Nx)=0;
ym(1:Ny,1:Nx)=0;
dir(1:Ny,1:Nx)=0;
    % downward
for ix=1:2:Nx
    for iy=1:Ny
        xm(iy,ix)=-dx/2*(iy-1)+(ix-1)/2*dx;
        ym(iy,ix)=h2+(iy-1)*dy;
        dir(iy,ix)=-1;
```

```
    end;
end;
    % upward
for ix=2:2:Nx
    for iy=1:Ny
        xm(iy,ix)=dx/2-dx/2*(iy-1)+(ix-2)/2*dx;
        ym(iy,ix)=h1+(iy-1)*dy;
        dir(iy,ix)=1;
    end;
end;

% material type matrix
% 1: graphite matrix
% 2: fuel stripe
% 3: box wall
% 4: Y shapre
% 5: coolant
mat(1:Ny,1:Nx)=4;
chanid(1:Ny,1:Nx)=0;
for ix=1:Nx
    for iy=1:Ny
        if (ym(iy,ix)<ybw)||(ym(iy,ix)<(sqrt(3)*(xbw-xm(iy,ix))))
            mat(iy,ix)=3;
        else
            xref=xm(iy,ix);
            yref=ym(iy,ix);
            if (yref<(sqrt(3)*(xfp-xref)))&&(yref<(ybw+6*ytop))
                i=ceil((yref-ybw)/ytop);
                yref=yref-ybw-(i-1)*ytop;
                if (yref<yc1)||(yref>yc2)
                    mat(iy,ix)=5;
                    if (yref<yc1)
                        chanid(iy,ix)=i;
                    else
                        chanid(iy,ix)=i+1;
                    end;
                end;
                if (yref<yc2)&&(yref>yc1)
```

```
                    if (yref<ygm2)&&(yref>ygm1)
                        mat(iy,ix)=1;
                    else
                        mat(iy,ix)=2;
                    end;
                end;
            end;
        end;
    end;
end;

% conductivity matrix
k(1:Ny,1:Nx)=15;
for ix=1:Nx
    for iy=1:Ny
        if (mat(iy,ix)==5)
            k(iy,ix)=0;
        end;
    end;
end;

% power density matrix
% for now uniform axial profile
q3(1:Nzs,1:Ny,1:Nx)=0;
P=3400e6;
Na=252;
Npl=18;
Afuel=(xfp-xbw)*(ygm1-yc1);
Vol=Afuel*Ha;
powerdensity=P/Na/Npl/2/Vol;
profile_factor=cosdistr(z,He)/mean(cosdistr(z,He));
for iz=1:Nzs
    pd(iz)=powerdensity*profile_factor(iz);
end;
for iz=1:Nzs
    for ix=1:Nx
        for iy=1:Ny
            if (mat(iy,ix)==2) q3(iz,iy,ix)=pd(iz); end;
```

```
        end;
    end;
end;

% channels
Tin=650;
mfract=0.005;       % fraction of the total mass flow rate that flows in the
inter-assembly channels
rho=1950;
cp=2416;
mu=0.006;
kcool=1.1;
Pr=mu*cp/kcool;
deltaTc=50;
mtot=P/cp/deltaTc/Na/3;
mitot=(1-mfract)*mtot;
mo=mfract*mtot;
% split the mass in the internal channel
fsmall=1.0;     % factor for increasing the thickness (yc1) for the two
smaller channels: 1.0 for standard design
As=(xys-xbw)*(yc1)*fsmall;
Al=(xys-xbw)*(yc1)*2;
pbs=2*(xys-xbw)+2*yc1/cos(pi/6)*fsmall;
pbl=2*(xys-xbw)+4*yc1/cos(pi/6);
hds=4*As/pbs;
hdl=4*Al/pbl;
vs=0.1;
Res=rho*vs*hds/mu;
fs=skinfc(Res);
pdrops=4*fs*0.5*rho*vs^2*Ha/hds;
vl=(mitot/rho-2*vs*As)/5/Al;
Rel=rho*vs*hdl/mu;
fl=skinfc(Rel);
pdropl=4*fl*0.5*rho*vl^2*Ha/hdl;
while pdrops<pdropl
    vs=vs+0.00001;
    Res=rho*vs*hds/mu;
    fs=skinfc(Res);
```

```
    pdrops=4*fs*0.5*rho*vs^2*Ha/hds;
    vl=(mitot/rho-2*vs*As)/5/Al;
    Rel=rho*vs*hdl/mu;
    fl=skinfc(Rel);
    pdropl=4*fl*0.5*rho*vl^2*Ha/hdl;
end;
ms=vs*As*rho;
ml=vl*Al*rho;
hs=kcool/hds*NuFunction(Res);
hl=kcool/hdl*NuFunction(Rel);
ycco=0.0175;
Ao=(xlim+xlim+ycco/sqrt(3))*(ycco/2)/2;
pbo=(xlim);
hdo=4*Ao/pbo;
vo=mo/rho/Ao;
Reo=rho*vo*hdo/mu;
ho=kcool/hdo*NuFunction(Reo);
ic(1:Nz,1:7,1:2)=0;
oc(1:Nz,1:2)=0;
maxT(1:Nzs,1)=0;
maxTloc(1:Nzs,1:2)=0;
ic(1,1:7,1)=Tin;
oc(1,1)=Tin;
ic(1:Nz,2:6,2)=hl;
ic(1:Nz,1,2)=hs;
ic(1:Nz,7,2)=hs;
oc(1:Nz,2)=ho;
mch(1)=ms;
mch(2:6)=ml;
mch(7)=ms;

% output file and output variables initialization
fileid=fopen(results_filename,'w');
mystr='TITLE = "Temperature Distribution"\n';
fprintf(fileid,mystr);
mystr='VARIABLES = "X" "Y" "Z" "Temperature" "Material"\n';
fprintf(fileid,mystr);
```

```
mystr=['ZONE I=' num2str(Nx,'%d') ', J=' num2str(Ny,'%d') ', K='
num2str(Nzs,'%d') ', DATAPACKING=POINT\n'];
fprintf(fileid,mystr);
fclose(fileid);
xtemp=reshape(xm',[],1);
ytemp=reshape(ym',[],1);
mattemp=reshape(mat',[],1);
ztemp=ytemp;

% iterations along z
for i=1:Nzs
    ['Iteration #' num2str(i) ' out of ' num2str(Nzs) '; Level: '
num2str(z(i+1)*100) 'cm']

[q1o,q1i,T]=onethirdfunction(xm,ym,dir,mat,chanid,k,squeeze(q3(i,:,:)),squeez
e(ic(i,:,:)),squeeze(oc(i,:)));
    for j=1:7
        ic(i+1,j,1)=ic(i,j,1)+q1i(j)*dz/cp/mch(j);
    end;
    if mo>0
        oc(i+1,1)=oc(i,1)+q1o*dz/cp/mo;
    else
        Tavg=(sum(T(:,1))+sum(T(1,:)))/(length(T(:,1))+length(T(1,:)));
        oc(i+1,1)=Tavg;
    end;
    % find maximum temperature value and location, as a function of z
    [maxcol,iline]=max(T);
    [maxT(i),maxTloc(i,2)]=max(maxcol);
    maxTloc(i,1)=iline(maxTloc(i,2));
    % write results to the output
    'Start writing'
    Ttemp=reshape(T',[],1);
    ztemp(:)=z(i)+dz/2;
    Mtemp=[xtemp,ytemp,ztemp,Ttemp,mattemp];
    dlmwrite(results_filename,Mtemp,'-append','delimiter',' ');
    'Finish writing'
end;
```

```
% plot the temperature distribution of the channels as a function of z
figure(1)
plot(z,oc(:,1),'Color',[0 1 0.5]);
hold on;
grid on;
plot(z,ic(:,1,1),'Color',[1 0.8 0]);
plot(z,ic(:,2,1),'b');
plot(z,ic(:,3,1),'b');
plot(z,ic(:,4,1),'b');
plot(z,ic(:,5,1),'b');
plot(z,ic(:,6,1),'b');
plot(z,ic(:,7,1),'r');
xlabel('z [m]');
ylabel('T [C]');
legend('external','int1','int2','int3','int4','int5','int6','int7');
title('Temperature distribution [C]');
axis tight;
set(gcf,'units','centimeters','position',[10 10 20 10]);

% plot the temperature at a z location
figure(2)
ztemp=3.5;  % plot at this elevation
itemp=round(ztemp/Ha*Nz);
if itemp<1 itemp=1; end;
if itemp>Nz itemp=Nz; end;
[q1o,q1i,T]=onethirdfunction(xm,ym,dir,mat,chanid,k,squeeze(q3(itemp,:,:)),sq
ueeze(ic(itemp,:,:)),squeeze(oc(itemp,:)));
[~,h]=contourf(xm*1000,ym*1000,T,50);
xlabel('x [mm]');
ylabel('y [mm]');
mystr=['Temperature distribution [C] at z= ' num2str(zplot(itemp)) ' m'];
title(mystr);
colorbar;
axis equal;
axis tight;
set(gcf,'units','centimeters','position',[10 10 20 10]);
set(h,'edgecolor','none');
set(gca,'xTick',[0:10:xlim*1000]);
```

```
% plot the maximum temperature distribution as a function of z
figure(3)
plot(zplot,maxT,'r');
grid on;
xlabel('z [m]');
ylabel('T [C]');
title('Maximum XY temperature [C] as a function of Z');
axis tight;
set(gcf,'units','centimeters','position',[10 10 20 10]);
```

```
% Horizontal heat conduction of one plate
% Approximation: no axial heat conduction
% Function

function [q1o,q1i,T]=onethirdfunction(xm,ym,dir,mat,chanid,k,q3,ic,oc)

% general data
xbw=0.01*2/sqrt(3);
xfp=0.24;
xys=xfp+0.02*2/sqrt(3);
yc1=0.0035;
ygm1=yc1+0.007;
ygm2=ygm1+0.011;
yc2=ygm2+0.007;
ytop=yc2+0.0035;
Nsy=30;          % # of segments for the portion of one plate
% adapt geometry
dy=ytop/Nsy;
dx=dy*2/sqrt(3);
Ny=Nsy;          % points, vertical
h1=dy/3;
h2=dy-h1;
Nsyc=round(0.0035/dy);
Nsyf=round(0.007/dy);
Nsyg=Ny-2*Nsyc-2*Nsyf;
yc1=Nsyc*dy;
ygm1=yc1+Nsyf*dy;
ygm2=ygm1+Nsyg*dy;
yc2=ygm2+Nsyf*dy;
ytop=yc2+Nsyc*dy;
% lower box wall and upper Y shape
ybw=0.01;
Nybw=round(ybw/dy);
ybw=Nybw*dy;
yws=0.02;
Nyws=round(yws/dy);
yws=Nyws*dy;
ylim=ybw+6*ytop+yws;
```

```
Ny=Nybw+6*Nsy+Nyws;
% horizontal direction
Nsx1=round(xbw/dx);
Nsx2=round(xfp/dx)-Nsx1;
Nsx3=round(xys/dx)-Nsx1-Nsx2;
Nsx2=Ny-Nsx1-Nsx3;
Nsx=Nsx1+Nsx2+Nsx3;
Nx=2*Nsx;       % points, horizontal
xbw=Nsx1*dx;
xfp=(Nsx1+Nsx2)*dx;
xys=(Nsx1+Nsx2+Nsx3)*dx;
xlim=xys;
N=Nx*Ny;        % total points
% evaluate boundary conditions
bcl(1:N,1:5)=2;
bcc(1:N,1:5)=2;
bcr(1:N,1:5)=2;
for iy=1:Ny
    for ix=1:Nx
        i=(iy-1)*Nx+ix;
        ichan=round((ym(iy,ix)-ybw)/ytop)+1;
            % left bc
            if ix==1
                bcl(i,1)=1;
                bcl(i,2)=oc(1);
                bcl(i,3)=oc(2);
                bcl(i,4)=dx;
                bcl(i,5)=0;
            else
                if (mat(iy,ix)==4)&&(mat(iy,ix-1)==5)
                    bcl(i,1)=1;
                    bcl(i,2)=ic(ichan,1);
                    bcl(i,3)=ic(ichan,2);
                    bcl(i,4)=dx;
                    bcl(i,5)=ichan;
                else
                    if (mat(iy,ix)~=5)
                    bcl(i,1)=0;
```

```
            bcl(i,2)=-1;
            bcl(i,3)=k(iy,ix)/2+k(iy,ix-1)/2;
            bcl(i,4)=2*h1;
            bcl(i,5)=dx;
            end;
        end;
    end;
    % right bc
    if ix==Nx
        bcr(i,1)=2;
    else
        if (mat(iy,ix)==3)&&(mat(iy,ix+1)==5)
            bcr(i,1)=1;
            bcr(i,2)=ic(ichan,1);
            bcr(i,3)=ic(ichan,2);
            bcr(i,4)=dx;
            bcr(i,5)=ichan;
        else
            if (mat(iy,ix)~=5)
                bcr(i,1)=0;
                bcr(i,2)=1;
                bcr(i,3)=k(iy,ix)/2+k(iy,ix+1)/2;
                bcr(i,4)=2*h1;
                bcr(i,5)=dx;
            end;
        end;
    end;
    % central bc
    if (dir(iy,ix)==1)&&(mat(iy,ix)~=5)&&(1<iy)
        if (mat(iy-1,ix-1)==5)
            bcc(i,1)=1;
            bcc(i,2)=ic(ichan,1);
            bcc(i,3)=ic(ichan,2);
            bcc(i,4)=dx;
            bcc(i,5)=ichan;
        else
            bcc(i,1)=0;
            bcc(i,2)=-2;
```

```
                    bcc(i,3)=k(iy,ix)/2+k(iy-1,ix-1)/2;
                    bcc(i,4)=2*h1;
                    bcc(i,5)=dx;
                end;
            end;
            if (iy==1)&&(dir(iy,ix)==1)
                bcc(i,1)=1;
                bcc(i,2)=oc(1);
                bcc(i,3)=oc(2);
                bcc(i,4)=dx;
                bcc(i,5)=0;
            end;
            if (dir(iy,ix)==-1)&&(mat(iy,ix)~=5)&&(iy<Ny)
                if (mat(iy+1,ix+1)==5)
                    bcc(i,1)=1;
                    bcc(i,2)=ic(ichan,1);
                    bcc(i,3)=ic(ichan,2);
                    bcc(i,4)=dx;
                    bcc(i,5)=ichan;
                else
                    bcc(i,1)=0;
                    bcc(i,2)=2;
                    bcc(i,3)=k(iy,ix)/2+k(iy+1,ix+1)/2;
                    bcc(i,4)=2*h1;
                    bcc(i,5)=dx;
                end;
            end;
    end;
end;
% build matrix
a(1:N,1:5)=0;
b(1:N,1)=0;
for ix=1:Nx
    for iy=1:Ny
        i=(iy-1)*Nx+ix;
        r(1,1:5)=bcl(i,:);
        r(2,1:5)=bcc(i,:);
        r(3,1:5)=bcr(i,:);
```

```
        b(i)=q3(iy,ix)*dx*dy/2;
        for j=1:3
            r1=r(j,1);
            r2=r(j,2);
            r3=r(j,3);
            r4=r(j,4);
            r5=r(j,5);
            % conduction
            if r1==0
                a(i,3)=a(i,3)+r3*r5/r4;
                a(i,(3+r2))=a(i,(3+r2))-r3*r5/r4;
            end;
            % convection
            if r1==1
                a(i,3)=a(i,3)+r3*r4;
                b(i)=b(i)+r3*r4*r2;
            end;
        end;
        % coolant
        if (mat(iy,ix)==5)
            ichan=round((ym(iy,ix)-ybw)/ytop)+1;
            a(i,3)=1;
            b(i)=ic(ichan,1);
        end;
    end;
end;
A=spdiags(a,[(-Nx-1) -1 0 1 (Nx+1)],N,N+1);
A=(A(:,1:(end-1)));
% connect right and top
ix=Nx-1;
iy=Ny;
count=0;
while (ix>0)&&(iy>0)
    count=count+1;
    ih(count)=(Ny-1)*Nx+ix;
    iv(count)=(iy-1)*Nx+Nx;
    ix=ix-2;
    iy=iy-1;
```

```
end;
for i=1:count
    A(ih(i),ih(i))=A(ih(i),ih(i))+k(end,end)/(2*h1)*dx;
    A(iv(i),iv(i))=A(iv(i),iv(i))+k(end,end)/(2*h1)*dx;
    A(ih(i),iv(i))=A(ih(i),iv(i))-k(end,end)/(2*h1)*dx;
    A(iv(i),ih(i))=A(iv(i),ih(i))-k(end,end)/(2*h1)*dx;
end;
% solve
Tv=A\b;
for ix=1:Nx
    for iy=1:Ny
        i=(iy-1)*Nx+ix;
        T(iy,ix)=Tv(i);
    end;
end;
% calculate power delivered per unit length
q1i(1:7)=0;
q1o=0;
for iy=1:Ny
    for ix=1:Nx
        i=(iy-1)*Nx+ix;
        r(1,:)=bcl(i,:);
        r(2,:)=bcc(i,:);
        r(3,:)=bcr(i,:);
        for j=1:3
            if r(j,1)==1
                if r(j,5)==0
                    q1o=q1o+dx*r(j,3)*(T(iy,ix)-r(j,2));
                else
                    q1i(r(j,5))=q1i(r(j,5))+dx*r(j,3)*(T(iy,ix)-r(j,2));
                end;
            end;
        end;
    end;
end;
```

7.3. Visual Basic input: assembly channel pressure drop as function of mass flow rate

```
Function ChPdrop(elev, mflow, gapPdrop, bypmflow)

' Properties and general data
rho = 1950
Aint = 0.02837101
Abyp = 0.02918159
mu = 0.006
hdint = 2 * 0.007
hdbyp = 2 * 0.018
hlsp = 0.35
hassy = 6.35
hbyp = hassy - elev

' Compute friction presssure drop in lower support plate
vel = mflow / rho / Aint
Re = rho * vel * hdint / mu
If Re < 2000 Then
    ff = 4 * 24 / Re
ElseIf Re < 4000 Then
    ff = 4 * (0.00000042721 * Re + 0.011146)
Else
    ff = 4 * (2.821096 * Re ^ (-0.710987) + 0.00510267)
End If
dplsp = 0.5 * rho * vel ^ 2 * ff * hlsp / hdint

' Compute friction presssure drop in bypass channel
vel = bypmflow / rho / Abyp
Re = rho * vel * hdbyp / mu
If Re < 2000 Then
    ff = 4 * 24 / Re
ElseIf Re < 4000 Then
    ff = 4 * (0.00000042721 * Re + 0.011146)
Else
    ff = 4 * (2.821096 * Re ^ (-0.710987) + 0.00510267)
End If
```

```
dpbyp = 0.5 * rho * vel ^ 2 * ff * hbyp / hdbyp

' Compute friction presssure drop between lower plate and lifted assembly
dpinterm = gapPdrop

ChPdrop = dplsp + dpinterm + dpbyp

End Function

Function bypPdrop(elev, mflow, bypmflow)

' Properties and general data
rho = 1950
Abyp = 0.02918159
mu = 0.006
hdbyp = 2 * 0.018
hassy = 6.35
hbyp = hassy - elev


' Compute friction presssure drop in bypass channel
vel = bypmflow / rho / Abyp
Re = rho * vel * hdbyp / mu
If Re < 2000 Then
    ff = 4 * 24 / Re
ElseIf Re < 4000 Then
    ff = 4 * (0.00000042721 * Re + 0.011146)
Else
    ff = 4 * (2.821096 * Re ^ (-0.710987) + 0.00510267)
End If
bypPdrop = 0.5 * rho * vel ^ 2 * ff * hbyp / hdbyp

End Function


Function intPdrop(elev, mflow, bypmflow)

' Properties and general data
```

```
rho = 1950
Aint = 0.02837101
Abyp = 0.02918159
mu = 0.006
hdint = 2 * 0.007
hdbyp = 2 * 0.018
hlsp = 0.35
hassy = 6.35
hbyp = hassy - elev

' Compute friction presssure drop in internal channel
vel = (mflow - bypmflow) / rho / Aint
Re = rho * vel * hdint / mu
If Re < 2000 Then
    ff = 4 * 24 / Re
ElseIf Re < 4000 Then
    ff = 4 * (0.00000042721 * Re + 0.011146)
Else
    ff = 4 * (2.821096 * Re ^ (-0.710987) + 0.00510267)
End If
intPdrop = 0.5 * rho * vel ^ 2 * ff * hassy / hdint

End Function

Function corePdrop(mflow)

' Properties and general data
rho = 1950
Aint = 0.02837101
Abyp = 0.02918159
mu = 0.006
hdint = 2 * 0.007
hdbyp = 2 * 0.018
hlsp = 0.35
hassy = 6.35 + 0.35

' Compute friction presssure drop in internal channel
vel = (mflow - bypmflow) / rho / Aint
```

```
Re = rho * vel * hdint / mu
If Re < 2000 Then
    ff = 4 * 24 / Re
ElseIf Re < 4000 Then
    ff = 4 * (0.00000042721 * Re + 0.011146)
Else
    ff = 4 * (2.821096 * Re ^ (-0.710987) + 0.00510267)
End If
corePdrop = 0.5 * rho * vel ^ 2 * ff * hassy / hdint

End Function

Function RemovedElemPdrop(e, m)     ' elevation and mflow

' Properties and general data
rho = 1950
Aint = 0.02837101
Abyp = 0.02918159
mu = 0.006
hdint = 2 * 0.007
hdbyp = 2 * 0.018
hlsp = 0.35
hassy = 6.35
hbyp = hassy - elev

' Compute coefficients
coeff = (0.05843 * e ^ (-0.8497) + 2.541) + (1 + WorksheetFunction.Tanh(100 *
(e - 0.09107))) / 2 * (-0.3947 * e + 3.683 - (0.05843 * e ^ (-0.8497) +
2.541))
expn = (-14.11 * e ^ 2 + 2.159 * e + 1.73) + (1 +
WorksheetFunction.Tanh(44.15 * (e - 0.09))) / 2 * (0.0007237 * e ^ 2 +
0.008554 * e + 1.769 - (-14.11 * e ^ 2 + 2.159 * e + 1.73))
RemovedElemPdrop = coeff * m ^ expn

End Function

Function coefffun(e, m)     ' elevation and mflow
```

```
' Compute coefficients
coefffun = (0.05843 * e ^ (-0.8497) + 2.541) + (1 +
WorksheetFunction.Tanh(100 * (e - 0.09107))) / 2 * (-0.3947 * e + 3.683 -
(0.05843 * e ^ (-0.8497) + 2.541))

End Function

Function expnfun(e, m)     ' elevation and mflow

' Compute coefficients
expnfun = (-14.11 * e ^ 2 + 2.159 * e + 1.73) + (1 +
WorksheetFunction.Tanh(44.15 * (e - 0.09))) / 2 * (0.0007237 * e ^ 2 +
0.008554 * e + 1.769 - (-14.11 * e ^ 2 + 2.159 * e + 1.73))

End Function

Function FreeChPdrop(mflow, gapPdrop)

' Properties and general data
rho = 1950
Aint = 0.02837101
Abyp = 0.02918159
mu = 0.006
hdint = 2 * 0.007
hdbyp = 2 * 0.018
hlsp = 0.35
hassy = 6.35

' Compute friction presssure drop in lower support plate
vel = mflow / rho / Aint
Re = rho * vel * hdint / mu
If Re < 2000 Then
    ff = 4 * 24 / Re
ElseIf Re < 4000 Then
    ff = 4 * (0.00000042721 * Re + 0.011146)
Else
    ff = 4 * (2.821096 * Re ^ (-0.710987) + 0.00510267)
End If
```

```
dplsp = 0.5 * rho * vel ^ 2 * ff * hlsp / hdint

FreeChPdrop = dplsp + gapPdrop

End Function
```

7.4. MATLAB input: creation of SCALE full core model input file

```
%% This script writes the input for the scale full core model

function WriteScaleInputFunction()

clear all;
close all;
clc;

%% Define General Properties

% input file header
filename='FuCo_1975_p3_b200.scale';
%%%%%%%%******** REQUIRES INPUT
check=0; % 1 if yes, 0 if no                          %%%%%%%%******** REQUIRES
INPUT
arrays=1; % 1 if yes, 0 if no                          %%%%%%%%********
REQUIRES INPUT
mesh=0; % 1 if yes, 0 if no                           %%%%%%%%******** REQUIRES
INPUT
if check check=' (parm=check)';
else check='';
end;
title='Full core model';
fid=fopen(filename,'w');
str=['=csas6' check '\n' title '\nv7-238\n'];
fprintf(fid,str);
str=['\n''---- MATERIALS ----\nread composition\n'];
fprintf(fid,str);
fclose(fid);

% boundaries for the rings
ringid=(0:9)';
ringnum=[6*ringid];
ringnum(1)=1;
ringnum(end)=6*6;
```

```
ringbnd=[ringid*100+1 ringid*100+ringnum];
Nel=elix(936);

%% Definition of material configurations
% Define the temperatures for each type of material

% 1->Tfuel, 2->Tcladding, 3->Tflibe, 4->enrichment          %%%%%%%%%%%%%%%%
REQUIRES INPUT
matconf=[
1100    1000    950 0.001830341
1100    1000    950 0.002183306
1100    1000    950 0.002922619
1100    1000    950 0.004124714
1100    1000    950 0.005934502
1100    1000    950 0.008626211
1100    1000    950 0.012763904
1100    1000    950 0.019726371
1100    1000    950 0.034295526
1100    1000    950 0.114396243
];

Nmat=length(matconf(:,1));

%% Definition of groups of elements
% Classification by elevation and/or materials/subdivisions
% Define the groups, the utype and ud

% Ring bounds
% 001 101 201 301 401 501 601 701 801 901
% 001 106 212 318 424 530 636 742 848 936
% 1->1st el, 2->last el, 3->unit type id
%%%%%%%%%%%%%%%% REQUIRES INPUT
groups=[001 001 1
        101 106 2
        201 212 3
        301 318 4
        401 424 5
        501 530 6
```

```
        601 636 7
        701 742 8
        801 848 9
        901 936 10];
groupsord(:,1)=elix(groups(:,1));
groupsord(:,2)=elix(groups(:,2));
% Definition of unit types
% 1->elevation in cm, 2->number of intervals 3->starting interval of control
rod          %%%%%%%%******** REQUIRES INPUT
utype=[0.0 1 2
       0.0 1 2
       0.0 1 2
       0.0 1 2
       0.0 1 2
       0.0 1 2
       0.0 1 2
       0.0 1 2
       0.0 1 2
       0.0 1 2];
% int->right bound, m->material configuration type
%%%%%%%%******** REQUIRES INPUT
ud(1).int=[550];
ud(1).m=[1];
for i=1:10
    ud(i).int=[550];
    ud(i).m=[i];
end;
Nunits=length(utype(:,1));

%% Write Composition, CellData and Parameters

for id=1:Nmat
    WriteMaterial(filename,id,matconf(id,:));
end;

WriteMaterialSupport(filename);

fid=fopen(filename,'a');
```

```
str=['\nend composition\n'];
fprintf(fid,str);
fclose(fid);

WriteCellDataAndParm(filename,Nmat,mesh)

%% Write Geometry

fid=fopen(filename,'a');
str=['\n''---- GEOMETRY ----\nread geometry\n'];
fprintf(fid,str);
fclose(fid);

for u=1:Nunits
    Nelem=0;
    for j=1:length(groupsord(:,1))
        if (groups(j,3)==u)
        Nelem=Nelem+groupsord(j,2)-groupsord(j,1)+1;
        end;
    end;

WriteGeometry(filename,u,utype(u,1),utype(u,2),utype(u,3),ud(u).int,ud(u).m,a
rrays,Nelem);
end;

WriteGeometrySupport(filename);

fid=fopen(filename,'a');
str=['\nend geometry\n'];
fprintf(fid,str);
fclose(fid);

%% Write Array

fid=fopen(filename,'a');
str=['\n''---- ARRAY ----\nread array\n'];
fprintf(fid,str);
fclose(fid);
```

```
WriteArray(filename,groups,utype,ud,Nunits,arrays);

fid=fopen(filename,'a');
str=['\nend array\n'];
fprintf(fid,str);
fclose(fid);

%% Write Plots and BCs and Grid

strgrid=WriteGrid(mesh);

fid=fopen(filename,'a');
str=[ ...
    '\n''---- PLOTS ----\n' ...
    'read plot\n' ...
    '\n' ...
    'ttl="Full Reactor Core"\n' ...
    '  XUL=-550.0 YUL=550.0  ZUL=400.0\n' ...
    '  XLR=550.0  YLR=-550.0 ZLR=400.0\n' ...
    '  UAX=1 VDN=-1 NAX=12800 END\n' ...
    '\n' ...
    'ttl="Partial Reactor Core"\n' ...
    '  XUL=-30.0 YUL=30.0  ZUL=400.0\n' ...
    '  XLR=30.0  YLR=-30.0 ZLR=400.0\n' ...
    '  UAX=1 VDN=-1 NAX=12800 END\n' ...
    '  \n' ...
    'ttl="Partial Reactor Core"\n' ...
    '  XUL=-30.0 YUL=30.0  ZUL=400.05\n' ...
    '  XLR=30.0  YLR=-30.0 ZLR=400.05\n' ...
    '  UAX=1 VDN=-1 NAX=12800 END\n' ...
    '  \n' ...
    'end plot\n' ...
    '\n' ...
    ''''---- BOUNDARY CONDITIONS ----\n' ...
    'read bounds\n\n' ...
    '   surface(1)=vacuum\n' ...
    '    surface(2)=vacuum\n' ...
```

```
    '   surface(3)=vacuum\n' ...
    '\nend bounds\n' ...
    '  \n' strgrid...
    '\nend data\n' ...
    'end    \n' ...
    ];
fprintf(fid,str);
fclose(fid);

end



%% FUNCTIONS

function [id]=elid(ix)
% this function returns the index from the id

ringid=(0:9)';
ringnum=[6*ringid];
ringnum(1)=1;
ringnum(end)=6*6;
ringbnd=[ringid*100+1 ringid*100+ringnum];
ringbnd(:,1)=elix(ringbnd(:,1));
ringbnd(:,2)=elix(ringbnd(:,2));

ring=ix;
ring(:)=0;
pos=ix;
pos(:)=0;
id=ix;
id(:)=0;
for i=1:length(ix)
    if ((ix(i)>253)||(ix(i)<1))
        'error: invalid element index'
        return;
    end;
    for ir=1:10
```

```
        if ((ix(i)<=ringbnd(ir,2))&&(ix(i)>=ringbnd(ir,1)))
            ring(i)=ir-1;
            pos(i)=ix(i)-ringbnd(ir,1);
            id(i)=ring(i)*100+pos(i)+1;
        end;
    end;
end;

end

function [ix]=elix(id)
% this function returns the index from the id

ringid=(0:9)';
ringnum=[6*ringid];
ringnum(1)=1;
ringnum(end)=6*6;
ringbnd=[ringid*100+1 ringid*100+ringnum];

ring=id;
ring(:)=0;
pos=id;
pos(:)=0;
ix=id;
ix(:)=0;
for i=1:length(id)
    ring(i)=floor(id(i)/100);
    pos(i)=id(i)-ring(i)*100;
end;

for i=1:length(id)
    if ((id(i)>ringbnd(ring(i)+1,2))||(id(i)<ringbnd(ring(i)+1,1)))
        'error: invalid element id'
        return;
    end;
    for j=0:(ring(i)-1)
        ix(i)=ix(i)+ringnum(j+1);
    end;
```

```
    ix(i)=ix(i)+pos(i);
end;

end

function []=WriteMaterial(filename,id,T)

ids=num2str(id);
Tfu=num2str(T(1),'%4.2f');
Tcl=num2str(T(2),'%4.2f');
Tfl=num2str(T(3),'%4.2f');
en=T(4);
n=num2str(id*10+[1 2 3 4 5 6 7]');
%calculate aden in at/(b*cm)
ad235=en*9.75/235*6.022e23/1e24;
ad238=(1-en)*9.75/237.99*6.022e23/1e24*0.99838;
ad234=(1-en)*9.75/237.99*6.022e23/1e24*0.00162;

str=[...
'\n''*** Material list number ' ids ' ***\n' ...
''' ---- Fuel, ' num2str(en*100,'%.2f') '%% Enrichment ----\n' ...
' U-234       ' n(1,:) '  0  ' num2str(ad234,'%0.7f') '  ' Tfu '    end\n'
...
' U-235       ' n(1,:) '  0  ' num2str(ad235,'%0.7f') '  ' Tfu '    end\n'
...
' U-238       ' n(1,:) '  0  ' num2str(ad238,'%0.7f') '  ' Tfu '    end\n'
...
' O-16        ' n(1,:) '  0  0.0352829   ' Tfu '    end\n' ...
' C-graphite  ' n(1,:) '  0  0.0105760   ' Tfu '    end\n' ...
''' ---- Buffer, IPyC, Silicon Carbide, OPyC, Matrix Material ----\n' ...
' C-graphite  ' n(2,:) '  0  0.076304410   ' Tfu '    end\n' ...
' Si          ' n(2,:) '  0  0.003755145   ' Tfu '    end\n' ...
''' ---- Graphite Meat ----\n' ...
' C-graphite  ' n(3,:) '  0  7.97223e-02 ' Tfu '    end\n' ...
''' ---- Sleeve/Cladding on Plate ----\n' ...
' C-graphite  ' n(4,:) '  0  7.97223e-02 ' Tcl '    end\n' ...
''' ---- FLiBe Coolant (99.995%% enriched Li-7) ----\n' ...
' Li-6        ' n(5,:) '  0  1.38344e-06 ' Tfl '  end\n' ...
```

```
' Li-7        ' n(5,:) '  0  0.0237205    ' Tfl '  end\n' ...
' Be          ' n(5,:) '  0  0.0118609    ' Tfl '  end\n' ...
' F           ' n(5,:) '  0  0.0474437    ' Tfl '  end\n' ...
''' ---- Graphite in Fuel Block ----\n' ...
' C-graphite  ' n(6,:) '  0  9.82741e-02 ' Tfl '  end\n' ...
''' ---- Control Rod ----\n' ...
' c           ' n(7,:) '  0  5.1542508e-04 ' Tfl '  end\n' ...
' hafnium     ' n(7,:) '  0  4.1619918e-04 ' Tfl '  end\n' ...
' molybdenum  ' n(7,:) '  0  0.06368707517 ' Tfl '  end\n' ...
];

fid=fopen(filename,'a');
fprintf(fid,str);
fclose(fid);

end

function []=WriteMaterialSupport(filename)

Tin=num2str(650+273,'%4.2f');
Tout=num2str(700+273,'%4.2f');
Trefl=num2str(675+273,'%4.2f');
Tvessel=num2str(675+273,'%4.2f');

str=[...
'\n'' *** Support Materials ***\n' ...
''' ---- FLiBe Coolant at Inlet (99.995%% enriched Li-7) ----\n' ...
' Li-6        1  0  1.38344e-06 ' Tin '  end\n' ...
' Li-7        1  0  0.0237205   ' Tin '  end\n' ...
' Be          1  0  0.0118609   ' Tin '  end\n' ...
' F           1  0  0.0474437   ' Tin '  end\n' ...
''' ---- Graphite Lower Support Plate ----\n' ...
' C-graphite  2  0  8.72433e-02 ' Tin '  end\n' ...
''' ---- Graphite Reflector Block ----\n' ...
' C-graphite  3  0  8.72433e-02 ' Trefl '  end\n' ...
''' ---- Graphite Upper Support Plate ----\n' ...
' C-graphite  4  0  8.72433e-02 ' Tout '  end\n' ...
''' ---- FLiBe Coolant at Outlet (99.995%% enriched Li-7) ----\n' ...
```

```
' Li-6        5  0  1.38344e-06 ' Tout '  end\n' ...
' Li-7        5  0  0.0237205   ' Tout '  end\n' ...
' Be          5  0  0.0118609   ' Tout '  end\n' ...
' F           5  0  0.0474437   ' Tout '  end\n' ...
''' ---- Alloy 800H Clad in CR ----\n' ...
'  C-graphite 6 0  3.2210e-04  ' Tvessel '  end\n' ...
'  Al         6 0  6.7209e-04  ' Tvessel '  end\n' ...
'  Si         6 0  6.0263e-04  ' Tvessel '  end\n' ...
'  P          6 0  3.1225e-05  ' Tvessel '  end\n' ...
'  S          6 0  1.5081e-05  ' Tvessel '  end\n' ...
'  Ti         6 0  3.7884e-04  ' Tvessel '  end\n' ...
'  Cr         6 0  1.9530e-02  ' Tvessel '  end\n' ...
'  Mn         6 0  8.8022e-04  ' Tvessel '  end\n' ...
'  Fe         6 0  3.8092e-02  ' Tvessel '  end\n' ...
'  Ni         6 0  2.6777e-02  ' Tvessel '  end\n' ...
'  Cu         6 0  2.2830e-04  ' Tvessel '  end\n' ...
];

fid=fopen(filename,'a');
fprintf(fid,str);
fclose(fid);

end

function []=WriteCellDataAndParm(filename,Nmat,mesh)

str=[...
'\n''---- CELL DATA ----\n' ...
'read celldata\n' ...
];
fid=fopen(filename,'a');
fprintf(fid,str);
fclose(fid);

for i=1:Nmat
    fuel=num2str(i*10+1);
    matrix=num2str(i*10+2);
```

```
    str=[' latticecell sphsquarep fuelr=0.02135 ' fuel ' pitch=0.0926537 '
matrix ' end\n'...
        ' centrm data\n'...
        '   dan2pitch(' fuel ')=0.916\n'...
        ' end centrm\n'];
    fid=fopen(filename,'a');
    fprintf(fid,str);
    fclose(fid);
end;

str1='';
if mesh str1='  mfx=yes\n  pms=yes\n  pmv=yes\n'; end;
str=[...
'end celldata\n' ...
'\n''---- PARAMETERS ----\n' ...
'read parameter\n' ...
'  gen=150\n' ...
'  nsk=50\n' str1...
'  npg=100000\n' ...
'  sig=0.0001\n' ...
'  tba=100\n' ...
'  htm=yes\n' ...
'  plt=yes\n' ...
'end parameter\n' ...
];
fid=fopen(filename,'a');
fprintf(fid,str);
fclose(fid);

end

function []=WriteGeometry(filename,uid,elev,Nint,cr,int,mat,arrays,Nelem)

Hinlet=200.0;
Houtlet=600.0;

%***** Inlet
str=[...
```

```
'\n''*** Unit list number ' num2str(uid) ' ***\n' ...
'unit ' num2str(uid*1000+1) '\n' ...
'com="Flibe Inlet"\n' ...
' hexprism    1  23.375 ' num2str(Hinlet) ' 0\n' ...
' media 1 1 1 vol=' num2str(Nelem*3.7855053e5) '\n' ...
' boundary 1\n' ...
];
fid=fopen(filename,'a');
fprintf(fid,str);
fclose(fid);
index(1,:)=num2str(uid*1000+1);
level(1)=0.0;

%***** Lower Support Plate
str=[...
'unit ' num2str(uid*1000+2) '\n' ...
'com="Lower Support Plate 1"\n' ...
' parallelepiped 1  21.70837  2.944486  35.0       30        0        0\n'
...
' media 2 1 1 vol=' num2str(Nelem*2.4910351e4) '\n' ...
' boundary 1\n' ...
'unit ' num2str(uid*1000+3) '\n' ...
'com="Lower Support Plate 2"\n' ...
' parallelepiped 1  22.51666  22.51666      35.0       30        0
0\n' ...
' hole ' num2str(uid*1000+2) '   origin  x=0.606218 y=0.35  z=0\n' ...
' hole ' num2str(uid*1000+2) '   origin  x=2.482606 y=3.6   z=0\n' ...
' hole ' num2str(uid*1000+2) '   origin  x=4.358995 y=6.85  z=0\n' ...
' hole ' num2str(uid*1000+2) '   origin  x=6.23583  y=10.1  z=0\n' ...
' hole ' num2str(uid*1000+2) '   origin  x=8.111771 y=13.35 z=0\n' ...
' hole ' num2str(uid*1000+2) '   origin  x=9.98816  y=16.6  z=0\n' ...
' media 1 1 1 vol=' num2str(Nelem*8.0202631e3) '\n' ...
' boundary 1\n' ...
'unit ' num2str(uid*1000+4) '\n' ...
'com="Lower Support Plate 3"\n' ...
' hexprism    1  23.375 35.0 0\n' ...
'  hole  ' num2str(uid*1000+3) ' rotate a1=210 origin x=-2.000000
y=23.67136103   z=0.  \n' ...
```

```
'  hole  ' num2str(uid*1000+3) ' rotate a1=90  origin x=21.5        y=-
10.10362971  z=0.\n' ...
'  hole  ' num2str(uid*1000+3) ' rotate a1=330 origin x=-19.500000  y=-
13.56773132  z=0.\n' ...
' media 2 1 1 vol=' num2str(Nelem*1.4388202e4) '\n' ...
' boundary 1 \n' ...
];
fid=fopen(filename,'a');
fprintf(fid,str);
fclose(fid);
index(end+1,:)=num2str(uid*1000+4);
level(end+1)=Hinlet;

%***** Flibe, if assembly is lifted
if elev>0
    str=[...
    'unit ' num2str(uid*1000+5) '\n' ...
    'com="Flibe Volume"\n' ...
    ' hexprism    1  23.375 ' num2str(elev) ' 0\n' ...
    ' media 1 1 1 vol=' num2str(Nelem*elev*1.8927526e3) '\n' ...
    ' boundary 1\n' ...
    ];
    fid=fopen(filename,'a');
    fprintf(fid,str);
    fclose(fid);
    index(end+1,:)=num2str(uid*1000+5);
    level(end+1)=Hinlet+35.0;
end;

%***** Lower Reflector
str=[...
'unit ' num2str(uid*1000+6) '\n' ...
'com="Lower Reflector 1"\n' ...
' parallelepiped 1  21.70837  2.944486  25.0       30        0        0\n'
...
' media 2 1 1 vol=' num2str(2.4910351e4) '\n' ...
' boundary 1\n' ...
'unit ' num2str(uid*1000+7) '\n' ...
```

```
'com="Lower Reflector 2"\n' ...
' parallelepiped 1  22.51666  22.51666      25.0       30        0
0\n' ...
' hole ' num2str(uid*1000+6) '   origin  x=0.606218 y=0.35  z=0\n' ...
' hole ' num2str(uid*1000+6) '   origin  x=2.482606 y=3.6   z=0\n' ...
' hole ' num2str(uid*1000+6) '   origin  x=4.358995 y=6.85  z=0\n' ...
' hole ' num2str(uid*1000+6) '   origin  x=6.23583  y=10.1  z=0\n' ...
' hole ' num2str(uid*1000+6) '   origin  x=8.111771 y=13.35 z=0\n' ...
' hole ' num2str(uid*1000+6) '   origin  x=9.98816  y=16.6  z=0\n' ...
' media 1 1 1 vol=' num2str(8.0202631e3) '\n' ...
' boundary 1\n' ...
'unit ' num2str(uid*1000+8) '\n' ...
'com="Lower Reflector 3"\n' ...
' hexprism    1  23.375 25.0 0\n' ...
'  hole  ' num2str(uid*1000+7) ' rotate a1=210 origin x=-2.000000
y=23.67136103   z=0.  \n' ...
'  hole  ' num2str(uid*1000+7) ' rotate a1=90  origin x=21.5        y=-
10.10362971  z=0.\n' ...
'  hole  ' num2str(uid*1000+7) ' rotate a1=330 origin x=-19.500000  y=-
13.56773132  z=0.\n' ...
' media 2 1 1 vol=' num2str(1.4388202e4) '\n' ...
' boundary 1 \n' ...
];
fid=fopen(filename,'a');
fprintf(fid,str);
fclose(fid);
index(end+1,:)=num2str(uid*1000+8);
level(end+1)=Hinlet+35.0+elev;

%***** Assembly
for ii=1:Nint
    idu=1000*uid+10*ii;
    idm=10*mat(ii);
    if ii==1
        H=int(1);
    else
        H=int(ii)-int(ii-1);
    end;
```

```
    if arrays
        myline=[' array ' num2str(idu+2) ' 1  place 1 1 1 0.0463269 0.0463269
0.0463269\n'];
    else
        myline=[' media ' num2str(idm+1) ' 1 1 vol='
num2str(Nelem*H*5.014712727e2) '\n'];
    end
    if ii<cr
        crmat='0';
    else
        crmat=num2str(idm+7);
    end;
    str=[...
    '''Level ' num2str(ii) '\n' ...
    'unit ' num2str(idu+1) '\n' ...
    'com="TRISO Fuel Particle"\n' ...
    ' sphere 1  0.02135\n' ...
    ' cuboid 2  0.0463269  -0.0463269  0.0463269  -0.0463269  0.0463269  -
0.0463269\n' ...
    ' media ' num2str(idm+1) ' 1 1 vol='
num2str(Nelem*H*2.8607e2*0.05124984312) '\n' ...
    ' media ' num2str(idm+2) ' 1 2 -1 vol='
num2str(Nelem*H*2.8607e2*0.9487501569) '\n' ...
    ' boundary 2\n' ...
    '''\n' ...
    'unit ' num2str(idu+2) '\n' ...
    'com="Fuel Portion of Fuel Plate"\n' ...
    ' parallelepiped 1  21.47743  0.4272391992  ' num2str(H) '       30
0       0\n' ...
    myline ...
    ' boundary 1\n' ...
    '''\n' ...
    'unit ' num2str(idu+3) '\n' ...
    'com="Graphite center with fuel plates"\n' ...
    ' parallelepiped 1  21.47743  2.71354626519  ' num2str(H) '       30
0       0\n' ...
    ' hole ' num2str(idu+2) '  origin  x=0 y=0 z=0\n' ...
    ' hole ' num2str(idu+2) '  origin  x=1.143153533 y=1.98 z=0\n' ...
```

```
    ' media ' num2str(idm+3) ' 1 1 vol=' num2str(Nelem*H*4.070242364e2) '\n'
...
    ' boundary 1\n' ...
    '''\n' ...
    'unit ' num2str(idu+4) '\n' ...
    'com="Complete Fuel Plate"\n' ...
    ' parallelepiped 1  21.70837  2.944486  ' num2str(H) '       30        0
0\n' ...
    ' hole ' num2str(idu+3) '  origin  x=0.173205 y=0.1 z=0\n' ...
    ' media ' num2str(idm+4) ' 1 1 vol=' num2str(Nelem*H*8.791885636e1) '\n'
...
    ' boundary 1\n' ...
    '''\n' ...
    'unit ' num2str(idu+5) '\n' ...
    'com="Group of Six Fuel Plates"\n' ...
    ' parallelepiped 1  22.51666  22.51666      ' num2str(H) '       30
0        0\n' ...
    ' hole ' num2str(idu+4) '   origin  x=0.606218 y=0.35  z=0\n' ...
    ' hole ' num2str(idu+4) '   origin  x=2.482606 y=3.6   z=0\n' ...
    ' hole ' num2str(idu+4) '   origin  x=4.358995 y=6.85  z=0\n' ...
    ' hole ' num2str(idu+4) '   origin  x=6.23583  y=10.1  z=0\n' ...
    ' hole ' num2str(idu+4) '   origin  x=8.111771 y=13.35 z=0\n' ...
    ' hole ' num2str(idu+4) '   origin  x=9.98816  y=16.6  z=0\n' ...
    ' media ' num2str(idm+5) ' 1 1 vol=' num2str(Nelem*H*3.208105273e2) '\n'
...
    ' boundary 1\n' ...
    '''\n' ...
    'unit ' num2str(idu+6) '\n' ...
    'com="Fuel Assembly, 18 Fuel Plates, and Control Blade Slot"\n' ...
    ' hexprism    10 23.375 ' num2str(H) ' 0\n' ...
    ' hexprism    1  22.5   ' num2str(H) ' 0\n' ...
    '  hole  ' num2str(idu+5) ' rotate a1=210 origin x=-2.000000
y=23.67136103   z=0.\n' ...
    '  hole  ' num2str(idu+5) ' rotate a1=90  origin x=21.5        y=-
10.10362971  z=0.\n' ...
    '  hole  ' num2str(idu+5) ' rotate a1=330 origin x=-19.500000  y=-
13.56773132  z=0.\n' ...
```

```
    ' cuboid      2  10.  0.  0.5 -0.5 ' num2str(H) ' 0  rotate a1=-30.\n'
...
    ' cuboid      3  10.  0.  0.5 -0.5 ' num2str(H) ' 0  rotate a1=90.\n' ...
    ' cuboid      4  10.  0.  0.5 -0.5 ' num2str(H) ' 0  rotate a1=210.\n'
...
    ' cylinder    5  1.2  ' num2str(H) '  0\n' ...
    ' media ' crmat ' 1 2 -5 vol=' num2str(Nelem*H*8.835687818) '\n' ...
    ' media ' crmat ' 1 3 -5 vol=' num2str(Nelem*H*8.835687818) '\n' ...
    ' media ' crmat ' 1 4 -5 vol=' num2str(Nelem*H*8.835687818) '\n' ...
    ' media ' crmat ' 1 5 vol=' num2str(Nelem*H*4.523893455) '\n' ...
    ' media ' num2str(idm+6) ' 1 1 -2 -3 -4 -5 vol='
num2str(Nelem*H*4.054459091e2) '\n' ...
    ' media ' num2str(idm+5) ' 1 10 -1 vol=' num2str(Nelem*H*1.390512036e2)
'\n' ...
    ' boundary 10\n' ...
    ];
    fid=fopen(filename,'a');
    fprintf(fid,str);
    fclose(fid);
    index(end+1,:)=num2str(idu+6);
    if ii==1
        delta=0.0;
    else
        delta=int(ii-1);
    end;
    level(end+1)=Hinlet+35.0+elev+25.0+delta;
end;

%***** Upper Reflector
index(end+1,:)=num2str(uid*1000+8);
level(end+1)=Hinlet+35.0+elev+25.0+550.0;

%***** Outlet
str=[...
'unit ' num2str(uid*1000+9) '\n' ...
'com="Flibe Outlet"\n' ...
' hexprism    1  23.375 ' num2str(Houtlet-elev) ' 0\n' ...
' media 5 1 1 vol=' num2str(Nelem*(Houtlet-elev)*1.89275264e3) '\n' ...
```

```
' boundary 1\n' ...
];
fid=fopen(filename,'a');
fprintf(fid,str);
fclose(fid);
index(end+1,:)=num2str(uid*1000+9);
level(end+1)=Hinlet+35.0+elev+25.0+550+25.0;

%***** Assembled element
fid=fopen(filename,'a');
str=[...
'unit ' num2str(uid) '\n' ...
'com="Assembled Element"\n' ...
' hexprism    1  23.375 ' num2str(Houtlet+Hinlet+25.0+550.0+25.0+35.0) ' 0\n'
...
];
fprintf(fid,str);
for j=1:length(level)
    str=['  hole   ' index(j,:) ' origin x=0.0   y=0.0   z=' num2str(level(j))
'\n'];
    fprintf(fid,str);
end;
str=[...
' media 1 1 1 vol=0.0\n' ...
' boundary 1\n' ...
];
fprintf(fid,str);
fclose(fid);

end

function []=WriteGeometrySupport(filename)

Hinlet=200.0;
Houtlet=600.0;
Hrefl=550+35+2*25.0;
H=Hinlet+Houtlet+Hrefl;
```

```
str=[...
'\n''*** Reflector Block and Barrel ***\n' ...
'unit 995\n' ...
'com="Graphite Reflector Block - Inlet"\n' ...
' hexprism    1  23.375 ' num2str(Hinlet) ' 0\n' ...
' media 1 1 1 vol=4.7787447e+07\n' ...
' boundary 1\n' ...
'unit 996\n' ...
'com="Graphite Reflector Block - Graphite"\n' ...
' cylinder    1  2.0    ' num2str(Hrefl) ' 0\n' ...
' hexprism    2  23.375 ' num2str(Hrefl) ' 0\n' ...
' media 1 1 1 vol=9.1043355e+05\n' ...
' media 3 1 2 -1 vol=1.3647848e+08\n' ...
' boundary 2\n' ...
'unit 997\n' ...
'com="Graphite Reflector Block - Outlet"\n' ...
' hexprism    1  23.375 ' num2str(Houtlet) ' 0\n' ...
' media 5 1 1 vol=1.4336234e+08\n' ...
' boundary 1\n' ...
'unit 998\n' ...
'com="Graphite Reflector Block - Unit"\n' ...
' hexprism    1  23.375 ' num2str(H) ' 0\n' ...
' array 2 1 place 1 1 1 0 0 0 \n' ...
' boundary 1\n' ...
];

fid=fopen(filename,'a');
fprintf(fid,str);
fclose(fid);

%***** Barrel
str=[...
'global unit 999\n' ...
'com="Reactor Core"\n' ...
' cylinder   1 478 ' num2str(H) ' 0\n' ...
' array 1 1 place 13 13 1 0 0 0 \n' ...
' cylinder   2 480 ' num2str(H) ' 0\n' ...
' cylinder   3 513 ' num2str(H) ' 0\n' ...
```

```
' cylinder   4 518 ' num2str(H) ' 0\n' ...
' media 6 1 2 -1 vol=8.2765258e+06\n' ...
' media 1  1 3 -2 vol=1.4155192e+08\n' ...
' media 6 1 4 -3 vol=2.2268001e+07\n' ...
' boundary 4\n' ...
];
fid=fopen(filename,'a');
fprintf(fid,str);
fclose(fid);

end

function []=WriteArray(filename,groups,utype,ud,Nunits,arrays)

str=[...
'\n ara=1  nux=25 nuy=25 nuz=1 typ=hexagonal\n' ...
'   fill\n' ...
];
fid=fopen(filename,'a');
fprintf(fid,str);
fclose(fid);

loc=[ ...
    10  10  10  10  10  10  10  10  10  10  10  10  10  10  10  10  10  10
10  10  10  10  10  10  10;
       10  10  10  10  10  10  10  10  10  10  10  10  10  10  10  10  10  10
10  10  10  10  10  10  10;
         10  10  10  10  10  10  10  10  10  10  10  10  10  10  10  10  10  10
10  10  10  10  10  10  10;
           10  10  10  10  10  10  10  10  10  10  10  10  10  10  934 935
936 901 902 903 10  10  10  10  10;
             10  10  10  10  10  10  10  10  10  10  10  10  845 846 847 848
801 802 803 804 805 10  10  10  10;
               10  10  10  10  10  10  10  10  10  10  933 844 739 740 741
742 701 702 703 704 806 904 10  10  10;
                 10  10  10  10  10  10  10  10  10  932 843 738 634 635 636
601 602 603 604 705 807 905 10  10  10;
```

```
                  10  10  10  10  10  10  10  10  931 842 737 633 528 529
530 501 502 503 605 706 808 906 10  10  10;
                    10  10  10  10  10  10  10  930 841 736 632 527 423 424
401 402 403 504 606 707 809 907 10  10  10;
                      10  10  10  10  10  10  929 840 735 631 526 422 317
318 301 302 404 505 607 708 810 908 10  10  10;
                        10  10  10  10  10  928 839 734 630 525 421 316 212
201 202 303 405 506 608 709 811 909 10  10  10;
                          10  10  10  10  10  838 733 629 524 420 315 211
106 101 203 304 406 507 609 710 812 10  10  10  10;
                            10  10  10  10  837 732 628 523 419 314 210 105
001 102 204 305 407 508 610 711 813 10  10  10  10;
                              10  10  10  10  836 731 627 522 418 313 209
104 103 205 306 408 509 611 712 814 10  10  10  10  10;
                                10  10  10  927 835 730 626 521 417 312 208
207 206 307 409 510 612 713 815 910 10  10  10  10  10;
                                  10  10  10  926 834 729 625 520 416 311
310 309 308 410 511 613 714 816 911 10  10  10  10  10  10;
                                    10  10  10  925 833 728 624 519 415 414
413 412 411 512 614 715 817 912 10  10  10  10  10  10  10;
                                      10  10  10  924 832 727 623 518 517
516 515 514 513 615 716 818 913 10  10  10  10  10  10  10  10;
                                        10  10  10  923 831 726 622 621 620
619 618 617 616 717 819 914 10  10  10  10  10  10  10  10  10;
                                          10  10  10  922 830 725 724 723
722 721 720 719 718 820 915 10  10  10  10  10  10  10  10  10  10;
                                            10  10  10  10  829 828 827 826
825 824 823 822 821 10  10  10  10  10  10  10  10  10  10  10  10;
                                              10  10  10  10  10  921 920
919 918 917 916 10  10  10  10  10  10  10  10  10  10  10  10  10  10;
                                                10  10  10  10  10  10  10
10  10  10  10  10  10  10  10  10  10  10  10  10  10  10  10  10  10;
                                                  10  10  10  10  10  10  10
10  10  10  10  10  10  10  10  10  10  10  10  10  10  10  10  10  10;
                                                    10  10  10  10  10  10
10  10  10  10  10  10  10  10  10  10  10  10  10  10  10  10  10  10  10
...
    ];
```

```
for i=1:25
    for j=1:25
        for k=1:length(groups(:,1))
            if ((loc(i,j)>=groups(k,1))&&(loc(i,j)<=groups(k,2)))
                arr(i,j)=groups(k,3);
            end;
            if (loc(i,j)==10)
                arr(i,j)=998;
            end;
        end;

    end;
end;

for i=1:25
    str='    ';
    for k=1:(i-1)
        str=[str '  '];
    end;
    for j=1:25
        num=arr(i,j);
        if num<10
            str=[str num2str(num) '   '];
        elseif num<100
            str=[str num2str(num) '  '];
        elseif num<1000
            str=[str num2str(num) ' '];
        else
            str='***** error, check array 1 *****';
        end;
    end;
    fid=fopen(filename,'a');
    fprintf(fid,[str '\n']);
    fclose(fid);
end;
str=[...
'  end fill\n' ...
```

```
];
fid=fopen(filename,'a');
fprintf(fid,str);
fclose(fid);

% Array for reflector column

str=[...
    '\nara=2 nux=1 nuy=1 nuz=3 typ=hexagonal\n' ...
    ' com="Fuel Arrangement in Reflector Column"\n' ...
    '    fill\n' ...
    '          995\n' ...
    '          996\n' ...
    '          997\n' ...
    '    end fill\n' ...
    ];
fid=fopen(filename,'a');
fprintf(fid,str);
fclose(fid);

% Arrays for fuel plates

if arrays

    for uid=1:Nunits
        Nint=utype(uid,2);
        int=ud(uid).int;
        for ii=1:Nint
            triso=uid*1000+10*ii+1;
            array=triso+1;
            lleft=0.0;
            if ii>1
                lleft=int(ii-1);
            end;
            l=int(ii)-lleft;
            Nz=ceil(l/(2*0.0463269));

            str=[...
```

```
            '\nara=' num2str(array) ' nux=250 nuy=4 nuz=' num2str(Nz) '
prt=no typ=square\n' ...
            ' com="Fuel Arrangement in Plate"\n' ...
            '    fill\n' ...
            '          250r' num2str(triso) '\n' ...
            '          250r' num2str(triso) '\n' ...
            '          250r' num2str(triso) '\n' ...
            '          250r' num2str(triso) '\n' ...
            '          ' num2str(Nz-1) 'q1000\n' ...
            '    end fill\n' ...
            ];
            fid=fopen(filename,'a');
            fprintf(fid,str);
            fclose(fid);

        end;
    end;

end;

end

function [strgrid]=WriteGrid(mesh)

if mesh==0
    strgrid='';
else
    strgrid=[...
            '\n''---- VOLUMES ----\n' ...
            'read volume\n' ...
            'type=random\n' ...
            'end volume\n' ...
            '\n''---- GRID ----\n' ...
            'read gridgeometry 1\n'...
            'title="MyGrid"\n'...
            'tolerance=1e-006\nxlinear 20 -550 550\n'...
            'tolerance=1e-006\nylinear 20 -550 550\n'...
            'zplanes\n'...
```

```
            '0 200 250 300 350 400 450 500 550 600 650 700 750 800 850 900
1000 1200 1400 end\n'...
            'end gridgeometry\n'...
            ];
end;

end
```

7.5. MATLAB input: 2D fission density plotting from SCALE output

```
%% Extract fission densities from output and print
function []=FissionDensities()

clear all;
close all;
clc;

%% Input file Reading

filename='ten.out';
Np=300;                                  %%%% random points for MC sampling
spacing=2;                               %%%% spacing for the plotting grid
fnametemp1='FissionDensities.out';    %%%%%%%%%%%% INPUT REQUIRED
fid=fopen(filename,'r');
prec1='';
prec2='';
temp1=fopen(fnametemp1,'w');
print=0;
i=0;
 while ~feof(fid)
     str=fgetl(fid);
     if strcmp(prec2,'      global unit') && strcmp(str,'
999      1    0.000E+00     0.00          0.000E+00')
         print=1;
     end;
     if strcmp(str,'1full core model
') && strcmp(prec1,'                                                  9
0.000E+00     0.00          0.000E+00')
         print=0;
     end;
     if print
         c=strsplit(str);
         if length(c)>1
             if str2double(c{end})>0
                 fprintf(temp1,[str '\n']);
```

```
                i=i+1;
                fd(i)=str2double(c{end-2});
            end;
        end;
    end;
    prec2=prec1;
    prec1=str;
 end;
fd=fd';
fclose(temp1);
fclose(fid);

%% Definition of groups of elements
% Classification by elevation and/or materials/subdivisions
% Define the groups, the utype and ud

% Ring bounds
% 001 101 201 301 401 501 601 701 801 901
% 001 106 212 318 424 530 636 742 848 936
% 1->1st el, 2->last el, 3->unit type id
%%%%%%%******** REQUIRES INPUT
groups=[001 001 1
        101 106 2
        201 212 3
        301 318 4
        401 424 5
        501 530 6
        601 636 7
        701 742 8
        801 848 9
        901 936 10];
groupsord(:,1)=elix(groups(:,1));
groupsord(:,2)=elix(groups(:,2));
% boundaries for the rings
ringid=(0:9)';
ringnum=[6*ringid];
ringnum(1)=1;
ringnum(end)=6*6;
```

```
ringbnd=[ringid*100+1 ringid*100+ringnum];
Nel=elix(936);
% Definition of unit types                                    %%%%%%%%%%%%
INPUT REQUIRED
% 1->elevation, 2->number of intervals 3->starting interval of control rod
for i=1:10
    utype(i,:)=[0.0 1 2];
end;
% int->right bound, m->material configuration type
%%%%%%%%******** REQUIRES INPUT
Nunits=length(utype(:,1));
for i=1:Nunits
    ud(i).int=[550];
    ud(i).m=[1];
end

%% Associate Fission Density

count=0;
for u=1:Nunits
    for j=1:utype(u,2)
        count=count+1;
        ud(u).fd(j)=fd(count);
    end;
end

%% Define location of centers

elemix=(1:Nel)';
elemid=elid(elemix);
xc(1:Nel)=0;
yc(1:Nel)=0;
l=23.375;
h=l*cos(pi/6);
rot=[1/2 3^0.5/2; -3^0.5/2 1/2];
index=1;
for ri=2:10
    Nperring=ringnum(ri);
```

```
    Nperedge=Nperring/6;
    if ri~=10
        for i=1:Nperedge
            pos(1,i)=-(Nperedge/2-1)*2*h+(i-1)*2*h;
            pos(2,i)=3/2*l*(ri-1);
        end;
    else
        for i=1:Nperedge
            pos(1,i)=-(Nperedge/2-1/2)*2*h+(i-1)*2*h;
            pos(2,i)=3/2*l*(ri-1);
        end;
    end;
    if ri==10
        first=4;
    elseif (Nperedge/2-floor(Nperedge/2))>0
        first=(Nperedge+1)/2;
    else
        first=Nperedge/2+1;
    end;
    for i=first:Nperedge
        index=index+1;
        xc(index)=pos(1,i);
        yc(index)=pos(2,i);
    end;
    for k=1:5
        postemp=(rot^k)*pos;
        for i=1:Nperedge
            index=index+1;
            xc(index)=postemp(1,i);
            yc(index)=postemp(2,i);
        end;
    end;
    for i=1:(first-1)
        index=index+1;
        xc(index)=pos(1,i);
        yc(index)=pos(2,i);
    end;
end;
```

```
%% Random points

count=0;
while count<Np
    xr=h*rand;
    yr=l*rand;
    if (yr<(l-1/sqrt(3)*xr))
        count=count+1;
        yrec(count)=yr;
        xrec(count)=xr;
    end;
end;
xrec=[xrec  xrec -xrec -xrec];
yrec=[yrec -yrec -yrec yrec];


%% Build matrix

x=xrec;
y=yrec;
for el=2:Nel
    x=[x (xc(el)+xrec)];
    y=[y (yc(el)+yrec)];
end;
fdtemp(1:length(xrec))=0.0;
for i=1:Nel
    for j=1:length(groupsord(:,1))
        if (i>=groupsord(j,1)) && (i<=groupsord(j,2))
            unitid=groups(j,3);
            fdtemp(:)=ud(unitid).fd(1);
            if i==1
                fdd=fdtemp;
            else
                fdd=[fdd fdtemp];
            end;
        end;
    end;
```

```
end;
[xi,yi] = meshgrid(min(x):spacing:max(x),min(y):spacing:max(y));
fddi = griddata(x,y,fdd,xi,yi,'nearest');

%% DEFINE BOUNDARY

xr(1)=-6*h; xr(2)=-5*h; xr(3)=-4*h; xr(4)=-3*h; xr(5)=-2*h; xr(6)=-h;
xr(7)=0;
xr(8)=h; xr(9)=2*h; xr(10)=3*h; xr(11)=4*h; xr(12)=5*h; xr(13)=6*h;
xr(14)=6*h;
xr(15)=7*h; xr(16)=8*h; xr(17)=9*h; xr(18)=9*h; xr(19)=10*h;

yr(1)=14*l; yr(2)=14.5*l; yr(3)=14*l; yr(4)=14.5*l; yr(5)=14*l; yr(6)=14.5*l;
yr(7)=14*l;
yr(8)=14.5*l; yr(9)=14*l; yr(10)=14.5*l; yr(11)=14*l; yr(12)=14.5*l;
yr(13)=14*l; yr(14)=13*l;
yr(15)=12.5*l; yr(16)=13*l; yr(17)=12.5*l; yr(18)=11.5*l; yr(19)=11*l;

xb=xr;
yb=yr;

for i=1:5
    delta=rot^i*[xr;yr];
    xb=[xb delta(1,:)];
    yb=[yb delta(2,:)];
end;

for i=1:length(fddi(:,1))
    for j=1:length(fddi(1,:))
        if (~inpolygon(xi(i,j),yi(i,j),xb,yb))
            fddi(i,j)=0;
        end;
    end;
end;

%% PLOTS
figure(1)
[C,h]=contourf(xi,yi,fddi,50);
```

```
hold on;
xlabel('x [cm]');
ylabel('y [cm]');
title('Fission Density');
axis equal;
axis tight;
set(gcf,'units','centimeters','position',[10 10 20 10]);
set(h,'edgecolor','none');
colorbar
%set(gca,'xTick',[0:10:xlim*1000]);

end % of main function

%% FUNCTIONS

function [id]=elid(ix)
% this function returns the index from the id

ringid=(0:9)';
ringnum=[6*ringid];
ringnum(1)=1;
ringnum(end)=6*6;
ringbnd=[ringid*100+1 ringid*100+ringnum];
ringbnd(:,1)=elix(ringbnd(:,1));
ringbnd(:,2)=elix(ringbnd(:,2));

ring=ix;
ring(:)=0;
pos=ix;
pos(:)=0;
id=ix;
id(:)=0;
for i=1:length(ix)
    if ((ix(i)>253)||(ix(i)<1))
        'error: invalid element index'
        return;
    end;
    for ir=1:10
```

```
        if ((ix(i)<=ringbnd(ir,2))&&(ix(i)>=ringbnd(ir,1)))
            ring(i)=ir-1;
            pos(i)=ix(i)-ringbnd(ir,1);
            id(i)=ring(i)*100+pos(i)+1;
        end;
    end;
end;

end

function [ix]=elix(id)
% this function returns the index from the id

ringid=(0:9)';
ringnum=[6*ringid];
ringnum(1)=1;
ringnum(end)=6*6;
ringbnd=[ringid*100+1 ringid*100+ringnum];

ring=id;
ring(:)=0;
pos=id;
pos(:)=0;
ix=id;
ix(:)=0;
for i=1:length(id)
    ring(i)=floor(id(i)/100);
    pos(i)=id(i)-ring(i)*100;
end;

for i=1:length(id)
    if ((id(i)>ringbnd(ring(i)+1,2))||(id(i)<ringbnd(ring(i)+1,1)))
        'error: invalid element id'
        return;
    end;
    for j=0:(ring(i)-1)
        ix(i)=ix(i)+ringnum(j+1);
    end;
```

```
    ix(i)=ix(i)+pos(i);
end;

end
```

REFERENCES

[1] Holcomb D. E. at al., "Core and Refueling Design Studies for the Advanced High Temperature Reactor", ORNL/TM-2011/365, ORNL, September 2011.

[2] Varma V. K. et al., "AHTR Mechanical, Structural, and Neutronic Preconceptual Design", ORNL/TM-2012/320, ORNL, September 2012.

[3] https://www.ornl.gov/msr

[4] Greene S. R. et al., "Pre-Conceptual Design of a Fluoride Salt-Cooled Small Modular Advanced High-Temperature Reactor (SmAHTR)"; ORNL/TM-2010/199, ORNL, December 2010.

[5] http://fhr.nuc.berkeley.edu

[6] Chen K., "Status of the TMSR-SF1 Licensing Efforts"; ORNL, October 2015.

[7] Petrovic B., Maldonado I., "Fuel and Core Design Options to Overcome the Heavy Metal Loading Limit and Improve Performance and Safety of liquid Salt Cooled Reactors"; NEUP project, 2012.

[8] https://www.ornl.gov/division/rnsd/projects/development-fluoride-salt-cooled-high-temperature-reactors

[9] Yoder G. L. et al., "Advanced High Temperature Reactor Thermal Hydraulics Analysis and Salt Clean-up System Description"; ORNL/TM-2014/499, ORNL, September 2014.

[10] Avigni P., Petrovic B., "Fuel element and full core thermal-hydraulic analysis of the AHTR for the evaluation of the LOFC transient"; Ann. Nucl. Energy, Vol. 64, pp. 499-510, February 2014.

[11] Huang L. M., Petrovic B., "Automated MCDancoff Factor Generation for Liquid Salt Cooled Reactor Parametric Studies"; ANS 2015 Winter Meeting, Washington, DC, November 8-12, 2015.

[12] Avigni P., "Thermal Hydraulic Modeling of the Advanced High Temperature Reactor for the Evaluation of Steady State and Transient Conditions"; Master's Thesis, Politecnico di Milano, Milan, Italy, April 2015.

[13] RELAP5-3D code development team, "RELAP5-3D Code Manual Volume I: Code Structure, System Models and Solution Methods", INEEL-EXT-98-00834, INL, June 2012.

[14] "TRACE V5.0 Theory Manual", Office of Nuclear Regulatory Research, US NRC, Washington, DC.

[15] "ANSYS Fluent User's Guide", Release 15.0, ANSYS, Inc., Canonsburg, PA, US, November 2013.

[16] "ANSYS Fluent Theory Guide", Release 15.0, pp. 122-128, ANSYS, Inc., Canonsburg, PA, US, November 2013.

[17] "ANSYS Fluent Theory Guide", Release 15.0, pp. 46-56, ANSYS, Inc., Canonsburg, PA, US, November 2013.

[18] Avigni P., Petrovic B., "Pseudo-3D Steady State Thermal-hydraulic Modeling of the Advanced High Temperature Reactor"; NURETH16, Chicago, IL, August 30-September 4, 2015

[19] Avigni P., Petrovic B., "Preliminary 2D analysis of the AHTR fuel assembly removal transient"; ANS 2015 Winter Meeting, Washington, DC, November 8-12, 2015.

[20] Richard J., Wang D., Yoder G., Carbajo J., Williams D., Forget B. and Forsberg C., Implementation of Liquid Salt Working Fluids into TRACE. Proceedings of ICAPP 2014, paper 14214. Charlotte, USA, April 6-9, 2014.

[21] Glasstone S., Sesonske A., "Nuclear Reactor Engineering", Van Nostrand Reinhold Company, 1967.

[22] "ANSYS Mechanical User's Guide", Release 15.0, ANSYS, Inc., Canonsburg, PA, US, November 2013.

[23] https://www.mathworks.com/help/curvefit/index.html, MATLAB curve fitting toolbox application.

[24] ANSYS Fluids HPC Team, "ANSYS Fluent HPC 16.0 Update", December 2014.

[25] Lewis S. M., "Simplified Core Physics and Fuel Cycle Cost Model for Preliminary Evaluation of LSCR Fueling Options", Master's Thesis, May 2014.

[26] Kingsbury C. W., "Fuel Cycle Cost and Fabrication Model for Fluoride-salt High-temperature Reactor (FHR) Plank Fuel Design Optimization", Master's Thesis, December 2015.

[27] Huang M. L., Petrovic B., “Use of MCDancoff Factor Correction for Multi-Group Fuel Depletion Analyses of Liquid Salt Cooled REactors”, PHYSOR 2014, Kyoto, Japan, September 28-October 3, 2014.

[28] Bowman S. M., "SCALE 6: Comprehensive Nuclear Safety Analysis Code System," Nucl. Technol. 174(2), 126-148, May 2011.

[29] “Scale: A Comprehensive Modeling and Simulation Suite for Nuclear Safety Analysis and Design”, ORNL/TM-2005/39, Version 6.1, ORNL, Oak Ridge, TN, June 2011.

[30] Rearden B. T., Jessee M. A., “SCALE Code System”, ORNL/TM-2005/39, Version 6.2.1, ORNL, Oak Ridge, TN, 2016.

[31] Ilas D. et al., “Advanced High-Temperature Reactor Neutronic Core Design”, PHYSOR 2012, Knoxville, TN, April 15-20, 2012.

[32] Petti D., “Overview of the Advanced Gas Reactor Fuel Development and Qualification Program” ART Program Review Meeting, Germantown, MD, June 2016.

[33] Huang M. L., Petrovic B., “Automated MCDancoff Factor Generation for Liquid Dalt Cooled Reactor Parametric Studies”, ANS 2015 Winter Meeting, Washington, DC, November 8-12, 2015.

[34] Gentry C. A., “Development of a Reactor Physics Analysis Procedure for the Plank-Based and Liquid Salt-Cooled Advanced High Temperature Reactor”, Master’s Thesis, May 2016.

[35] Ux Consulting Company (UxC), https://www.uxc.com/.

[36] https://www.cameco.com/invest/markets/uranium-price.

[37] R. G. Cochran and N. Tsoulfanidis, “The Nuclear Fuel Cycle: Analysis and Management”, American Nuclear Society, 1990.

[38] D. E. Shropshire, et al., “Advanced Fuel Cycle Cost Basis”, INL/EXT-07-12107, INL, Idaho Falls, Idaho, April 2007.

[39] Cisneros A. T., Ilas D., “Neutronics and Depletion Methods for Parametric Studies of Fluoride-Salt-Cooled High-Temperature Reactors with Slab Fuel Geometry and Multi-Batch Fuel Management Schemes”, PHYSOR 2012, Knoxville, TN, April 15-20 2012.

[40] Holcomb D. E. at al., “Advanced High Temperature Reactor Systems and Economic Analysis”, ORNL/TM-2011/364, ORNL, September 2011.